Bergische Universität Wuppertal

Investigation of Charged Droplets Aspirated in the Electrospray Ionization Process

Dissertation

zur Erlangung des akademischen Grades
Doktor der Naturwissenschaften (Dr. rer. nat.)

vorgelegt von
Clara Markert

Bergische Universität Wuppertal
Fakultät 4 - Mathematik und Naturwissenschaften
Physikalische und Theoretische Chemie
unter der Anleitung von Prof. Dr. Thorsten Benter

April 2023

"*Klack-Klack*"
Die Maus aus der Sendung mit der Maus

Danksagung

Diese Arbeit war geprägt durch Planänderungen: Sei es durch die COVID-19-Pandemie, die unser aller Leben die letzten Jahre bestimmt hat, oder durch die thematischen Erweiterungen, die vorab gar nicht vorstellbar gewesen sind. Es steht auf jeden Fall fest, dass ohne die Unterstützung von vielen Menschen diese Dissertation nicht entstanden wäre.

Ich danke allen, die mich ermutigt haben weiterzumachen,
die mich forschend unterstützt und mit mir über das Thema diskutiert haben,
die mich zum Lachen gebracht und mich abgelenkt haben,
die mir eine starke Schulter geboten haben,
und generell allen, die mich während der Zeit begleitet haben. Danke!

Erklärung

"Ich versichere, die Arbeit selbständig verfasst zu haben, nur die in der Dissertation angegebenen Hilfsmittel benutzt und alle wörtlich oder inhaltlich übernommenen Stellen als solche gekennzeichnet zu haben, und dass die Dissertation in der gegenwärtigen oder einer anderen Fassung noch keiner anderen Fakultät, keiner Gesamthochschule und keiner anderen wissenschaftlichen Hochschule vorgelegen hat."

Abstract

This work marks the beginning of the investigation of charged droplets within mass spectrometers. It is organized into an experimental and a theoretical section. The experimental part presents the first evidence for signatures of charged droplets in mass spectra acquired with commercial mass spectrometers. In a variety of instruments, droplets and their fragments were observed in the spectra. In the SCIEX 6500 Triple Quadrupole instrument, a “droplet scan mode” has to be applied to observe droplet signatures: It puts the first mass selective quadrupole in RF only mode so that only ions above a certain low mass cutoff are transferred. The resulting mass spectra show a significant intensity above this cutoff, which is attributed to the occurrence of charged droplets. In an Agilent Q-TOF instrument, a similar scan routine can be applied. This also leads to observable signatures of droplets. In addition, in two different ion traps systems from Bruker, isolation of ions in the high mass range leads to similar observations. It is noteworthy, that the ion traps do not have to be set to a specific droplet scan routine, since the signatures appear in normal scan mode. This is important evidence for the existence of charged droplets deeply in the vacuum system of different mass spectrometers. In further experiments the variation of ion source and transfer parameters of the investigated instruments lead to alterations in the resulting mass spectra. The droplet signatures are influenced by a variety of parameters. Fully eliminating this signal, however, was not possible.

The second part of this work aims to establish a workflow for employing MD simulations to further investigate the charged droplets. Specifically, the simulation framework LAMMPS was used, which proved to be promising, as different molecular systems were successfully investigated with the available force fields. The simulated droplets behave as expected from basic theory and critical parameters as the Rayleigh Limit are reproduced. In further simulations the energy transfer to the droplet was examined. A relaxation time in the range of picoseconds was determined. Simulated mass spectra were produced upon analyzing the disintegration pattern of the droplets. The results of initial mobility calculations with IMoS yielded further evidence for charged droplets to enter the vacuum systems of instruments, as the calculated mobilities are in the same range as the mobilities of higher mass molecular analytes.

Contents

1 Introduction - Electrospray Ionization (ESI)

1.1 Principles of the ESI process

Electrospray Ionization (ESI) is a widely used ionization technique for mass spectrometry in the field of analytical chemistry [1–6]. A liquid solution containing analytes is sprayed from an ESI emitter in a strong electric field. A stream of charged droplets forms. They are guided through the ion source to the entrance of the mass spectrometer by the electric field present in the ion source chamber. By desolvating the droplets with heated background gas, gas-phase ions are released, which can be detected in a resulting mass spectrum. It is possible to ionize large macromolecules like proteins or polymers with ESI. These fragile molecules are prone to fragmentation with other ionization techniques. Thus, ESI is considered a soft ionization method. In 2002 John Fenn, who is one of the main developers of the method, was awarded with a Nobel prize for his advancements of ESI in the field of ionizing biomolecules [7]. The concept of ESI started with ionizing a large polymer in solution to analyze it. This concept was first presented by Dole et al. in 1968 [1]. He was able to transfer large macromolecules without fragmentation into the gas phase, where they could be detected with a mass spectrometer. Fenn and Yamashita introduced nitrogen in the ion source to remove neutral solvents from the charged droplets [2]. This improvement resulted in relatively clean mass spectra of different alcohols, ester and cyanides and their solvent adducts. As Fenn predicted, the ESI source would be a novel interface for LC-MS application. Whitehouse established this in his work 1985 [3]. The ESI process consists of three crucial steps [5, 8]:

1. First the charged droplets are produced at the ESI emitter tip.

2. Afterwards, the sprayed droplets are shrinking due to solvent evaporation by collision with the background gas or disintegration from Coulomb explosions.

3. At last, the gas-phase ions form, which can be detected with the MS.

The three steps are detailed in a simple scheme in Figure 1.1.

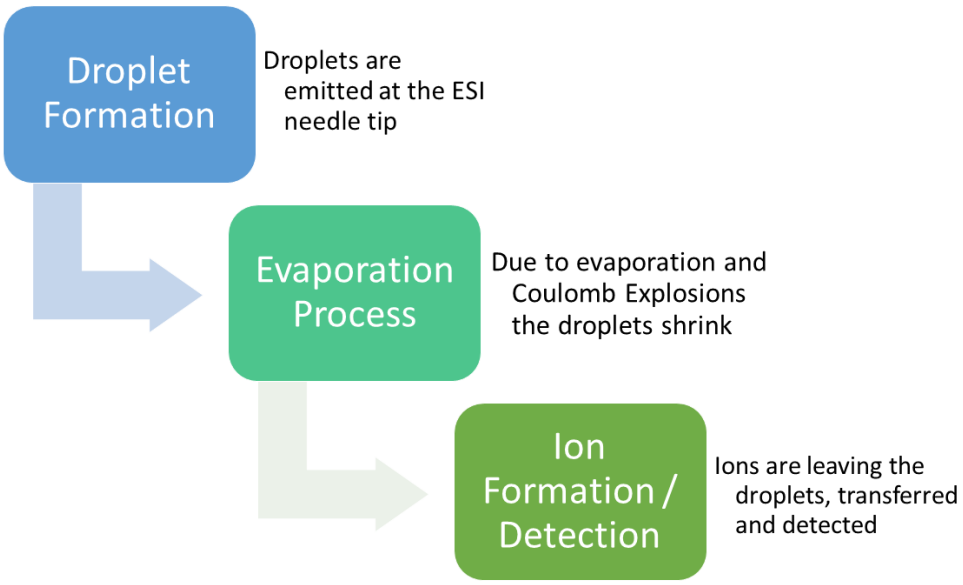

Figure 1.1: Scheme of the three major steps in the ESI process. Step 1: Droplet formation. Step 2: Evaporation process of the droplets. Step 3: Ion formation and detection.

In the following section, the major steps of ESI are described in more detail.

1.2 Step 1 – Droplet formation

The formation of charged droplets is the starting point of the ESI process. As described above, charged droplets are produced by applying an electric field to an analyte solution. The ESI emitter is placed near the entrance of the mass spectrometer (cf. Figure 1.2), which is realized as an orifice system or an entrance capillary [9, 10]. Typically, the voltage is applied directly to the ESI emitter. In different studies a variety of materials for ESI emitters are subject of investigation. Even non-conducting materials,

such as wood, are researched [11]. However, the most reported emitter material is glass or metal. The orifice plate or the metal end cap of the entrance capillary is used as counter-electrode. This creates an electric field within the ion source, in which the charged droplets are drifting through the background gas from the emitter to the mass spectrometer. Voltages of up to 5 kV are commonly applied to the emitter in commercial mass spectrometer systems [5]. The electric field induces polarization of the liquid within the ESI emitter. In positive spray mode a positive voltage is applied to the emitter. Positive ions are accumulating near the meniscus of the liquid, which deforms the surface of the liquid into a cone: The so-called Taylor-cone [12, 13]. At the tip of the Taylor-cone, the dynamical instability is the highest. In a process of balancing the net charge ratio, charged droplets are emitted into the ion source and a steady jet of nearly uniformly sized droplets is leaving the tip of the cone [14–16]. This process takes place if the Coulombic repulsion of the charges is higher than the surface tension of the liquid. The generated droplets have a positive net charge and drift through the atmospheric pressure ion source to the negative counter-electrode – the entrance of the MS. Figure 1.2 depicts an ESI emitter and the three steps in the ESI process schematically.
After emitting charged droplets, the meniscus of the liquid reaches a near spherical shape again, and the process of accumulating charges near the meniscus is repeated until a new cone is formed. A series of time-lapse images revealed that this successive process takes about 500 µs [17]. The time of this Taylor-cone oscillation can also be influenced by conditions in the ion source. In idealized theory this droplet generation mode, the so-called cone-jet mode, and the resulting emission of charged droplets is a stable process throughout the ESI experiment. However, in reality the spraying from the ESI emitter can fluctuate heavily in dependence to a variety of parameters. This results in different spray-modes, which can be observed experimentally [14]. Unstable spraying conditions can be the result of high surface tension of the solvent. In this case the applied voltage to the emitter has to be increased to apply a larger force on the liquid and to eject droplets from the meniscus. This can reach the electrical breakdown point of the gaseous background medium [18]. As a result, corona discharge, a common type of gas discharge, can be observed with the naked eye or simple monitoring equipment for the spray current [4, 19]. Therefore, corona discharge is a frequent occurrence in ESI experiments and can lead to a lower reproducibility of the resulting mass spectra. Adjusting and understanding the influence of the ion source parameters can lead to

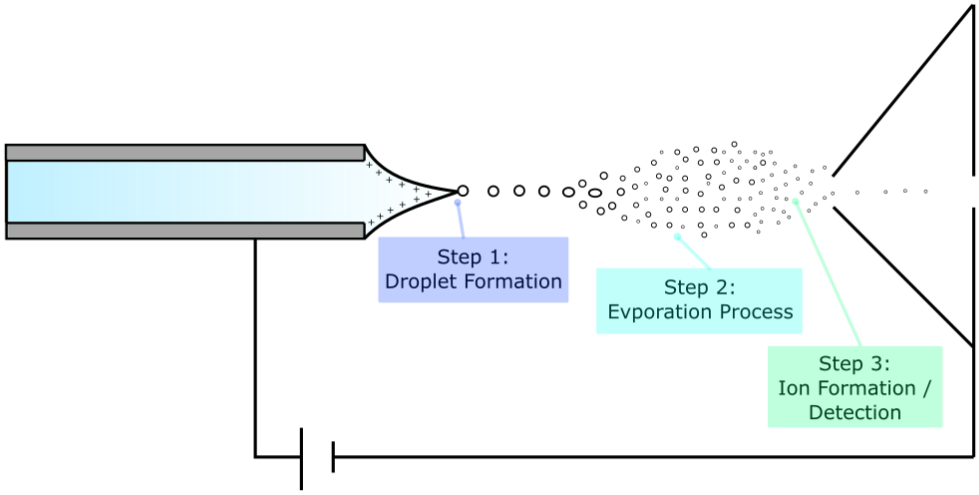

Figure 1.2: Scheme of an ESI emitter with its needle tip. A Taylor-cone is forming at the end of the tip due to the applied voltage. Droplets are leaving the Taylor-cone region in a monodisperse jet. The evaporation of solvent molecules leads to Coulomb explosion and shrinkage of the droplets. In the last step the ions are forming and entering the MS.

more favorable spraying conditions and in turn to a more uniform stream of droplets [4]. A more continuous generation of droplets is overall a more favorable state for an ESI experiment. The size of the emitted droplets is dependent on the Taylor-cone radius at the tip of the ESI emitter [14]. In common ESI experiments it can range between a few micrometers up to hundreds of micrometers. Droplet sizes were studied by different groups with a variety of methods, for example phase Doppler anemometry (PDA) [20–24]. Gomez and Tang (1994) investigated sizes of droplets consisting of heptane with PDA and shadowgraphy [22]. The size distribution of the emitted droplets reached the full measurement range of the PDA instrument, which was 1-200 µm. Smith et al. (2002) used an optical phase Doppler method to measure droplet sizes [20]. Additionally, the charges of the droplets were calculated by measuring the electrical mobility of the charged droplets. For droplets consisting of NaCl in water and methanol, the size distribution showed a maximum at 20-30 µm. Slightly larger droplets were emitted with acetonitrile as solvent (30-40 µm). The droplets contained $2 - 8 \times 10^6$ charges. These

droplets were observed for up to 0.25 s. The droplets underwent multiple discharge events in this time, in which the precursor droplets reached a charge near the Rayleigh Limit and then erupted in smaller droplets. The Rayleigh Limit describes the critical charge density at which a droplet is still stable. If the number of charges exceeds the Rayleigh Limit, it explodes into smaller droplets as described above. In the following section the equation to calculate the amount of charges for droplets is given and discussed as well as the shrinkage of the charged droplet. More results for droplet size measurements are given in Table 1.1.

Table 1.1: Observed droplet sizes in studies available in literature

Authors	Droplet diameter	Solvent
Abbas and Latham (1967) [25]	30-200 µm	water, aniline, toluene
Schweizer and Hanson (1970) [26]	15-40 µm	n-octanol
Taflin et al. (1988) [27]	ca. 43 µm	1-bromododecane
	ca. 27-40 µm	1,8-dibromooctane
	ca. 20 µm	dibutyl phthalate (DBP)
	ca. 32-35 µm	1-dodecanol
	ca. 28-65 µm	hexadecane
	ca. 29-36 µm	heptadecane
Davis and Bridges (1994) [28]	4-15 µm	aqueous solutions
	10-20 µm	1-dodecanol
Gomez and Tang (1994) [22]	1-200 µm	heptane
Feng et al. (2001) [29]	ca. 84 µm	methanol
Smith et al. (2002) [20]	30-40 µm	methanol, water, acetonitrile
Grimm and Beauchamp (2010) [21]	30-50 µm	methanol/2-methoxyethanol, methanol/tert-butanol, methanol/*m*-nitrobenzyl

The experimentally observed size distributions of the generated droplets vary significantly as the results of 1.1 show. In a widely accepted theoretical model of a typical evaporation process of charged droplets introduced by Peschke et. al. the initial droplet diameter was estimated to 0.15 µm [30], which is substantially smaller than the

experimentally observed initial droplet size. Due to the significant divergence of the estimated starting size of the droplets, it is questionable if this theoretical model is fully applicable to droplets emitted from a common ESI emitter. In the following section the evaporation process is detailed. In modern instruments mostly pneumatic assisted sprays are applied. In this type of ion source an assisting gas flow from the emitter is present, which assists the spray formation [4, 31, 32]. This method was primarily developed for the coupling between LC (liquid chromatography) and MS instruments. Because of the high liquid flows (tens to thousand µL per minute [4]) the ion evaporation is assisted by a so-called nebulizer. Applying a nebulizer to the ionization process partly decoupled the droplet formation from the actual charging of the droplets, which made balancing the voltages, flows, chemical composition of the liquid, etc. easier to handle. It led to a higher sensitivity and broad application of pneumatic assisted sprays in modern instruments. In recent years another technique is applied: nano-ESI [4, 33, 34]. In this ion source type the liquid flow is reduced as much as possible to increase the absolute sensitivity. Lesser liquid flows produce smaller droplets, which are easier to evaporate and thus are easier to transfer into the systems. Ion sources with these configurations are most likely operating in a pure cone-jet ESI mode, which is commonly described in literature.

1.3 Step 2 - Evaporation process

The second step of the idealized ESI process describes the shrinkage of the droplets. It occurs due to the evaporation of solvent molecules from the charged droplets. The absorbed heat for this process is taken from the surrounding atmosphere within the ion source. Usually, so-called "drying gas", a countercurrent, typically nitrogen, is applied from the direction of the MS [4]. Common instruments have an additional heater system for this gas to assist the evaporation. As solvent molecules evaporate, the charge density of the droplet increases. If it reaches a critical point, at which the repulsive forces of the charges are stronger than the surface tension of the liquid, the droplet disintegrates into smaller droplets, which have a lower charge density and are therefore more stable. This process is called Coulomb explosion and is repeated multiple times during the residence time of the droplet within the ion source. It was first studied by

Lord Rayleigh, in which he proposed an equation to predict the instability of charged droplets [35].

$$Q = 8\pi(\epsilon_0 \gamma r^3)^{1/2} \tag{1.1}$$

Equation 1.1 expresses the limit of charges Q a droplet can contain at a certain radius r. ϵ_0 is the vacuum permittivity and γ the surface tension of the liquid. With this equation the prediction of the point of instability, the so-called Rayleigh Limit, of charged droplet is possible. The fission of the droplets can be thought of as not an explosion into smaller droplets, but the ejection of droplet fragments in a jet like release from the mother-droplet as can be seen in the works of Gomez and Tang from 1994. This work contains pictures and shadowgraphs of the disintegrating droplets [22]. Notably, the experimentally observed droplets already start to disintegrate at about 70 % charge density of the calculated Rayleigh Limit. As mentioned above, in the work of Smith et al. discharge events were observed for water, acetonitrile, and methanol droplets. The disintegration of the droplets started for the different solvents at 80-100 % of their calculated Rayleigh Limit [20]. All of the droplets underwent three explosion events in the experiments. The diameter of the droplets shrank with the explosions to about 5 µm starting from 30-40µm. After a discharge event, the charge density of a droplet increased again to nearly their Rayleigh Limit due to additional solvent evaporation. The observed lifetime from the first detection of the charged droplets amounts to 0.14-0.25 second in this study. Similar observations were made by Grimm and Beauchamp in 2010 [21]. Droplets consisting of methanol (75 %) and 2-methoxyethanol (25 %) had an initial diameter of 30 µm. In one second of experimental observation time, they underwent at least six discharge events ending in droplets with a diameter of around 5 µm. The velocity of these aggregates was listed as well. At first the droplets had a speed of 55 cm/s. At the end of the experiment, they slowed down to 45 cm/s. A common ion source has a length of about 2-5 cm from the ESI emitter to the orifice. If the droplets of Grimm and Beauchamp have a lifetime of at least 1 second (the observation time of the experiment) and an end-velocity of 45 cm/s, the lifetime of the droplets exceeds the residence time in a typical ion source by far. The lifetime and electrical mobility of typical droplets is high enough for them to enter the vacuum system of MS instruments with ease. The electric mobility K is the quotient of the drift velocity (v_d)

and the electric field gradient. The reduced mobility K_0 is normalized by the pressure p and the temperature T [36]:

$$K = v_d / E \tag{1.2}$$

$$K_0 = K \left(\frac{273}{T} \right) \left(\frac{p}{760} \right) \tag{1.3}$$

In the experiment of Beauchamp and Grimm the field gradient was induced by eight steel rings to generate a linear field of 50 V/cm. With the reported initial drift velocity of 55 cm/s, a mobility for the droplets of 1.1 $cm^2\,V^{-1}\,s^{-1}$ can be calculated. In comparison, digitoxigenin was mass analyzed with electrospray ionization in a study by Bylda et al. [37]. Digitoxigenin is a steroid, which is a metabolite of the heart glycoside digitoxin and has a mobility of 1.6 $cm^2\,V^{-1}\,s^{-1}$, which was calculated from a list by Shumate et al. of reduced mobilities and temperatures [38]. This is evidence that bare molecular ions of larger analytes - like the aforementioned steroid - have a similar mobility like the highly charged droplets generated by a common ESI emitter. As larger analytes are obviously able to pass the entrance and transfer of the mass spectrometer with their electric mobility, charged droplets and their fragments will be able to do the same. This finding seems not to be common knowledge and appears to be overlooked often. Due to the comparison of the mobilities, the transport of charged droplets into the machines seems highly likely. In the next section the formation of ions from the charged droplets is discussed further.

1.4 Step 3 – Ion formation and detection

The third step of the ESI process details the formation of the actual bare gas-phase ions which are released from the droplets and detected by the instrument. Different proposed mechanisms of the ionization process were investigated by many groups [39–45]. Only a short overview of the large body of literature regarding this topic is given here, as the ion release mechanism is not the main focus of this work. Two models are commonly considered to be possible mechanisms for gas-phase ion formation in ESI experiments. The first is referred to as the charge residue model (CRM). It was first proposed by Dole. In this model, the analyte is released from very small droplets [1]. The small droplets only contain a single analyte molecule. If the remaining solvent

molecules evaporate fully from such an aggregate, only the charged analyte molecule is left and can be transferred into an MS. The very small droplets which are able to undergo such a process, have to be the result of multiple Coulomb explosions to achieve the required size range. This model is considered to be the main ionization mechanism for larger analytes [8]. The second model was introduced by Iribarne and Thomson [39, 42]. It is called the ion evaporation model (IEM). The gas phase ions are leaving larger, still multiple charged, droplets as the field strength on the surface of the droplets is assisting their release. The released analyte ions are still solvated by a few solvent molecules, which can be seen in actual mobility spectra [42]. This mechanism is commonly assumed for smaller analytes [8]. In addition to the two "classical" models described above, a new gas-phase ion release mechanism was proposed by Konermann et al.: A chain ejection model [46]. The ejections of larger peptides from charged droplets were modeled by in molecular dynamics (MD) simulations. The ions were leaving the droplets similar to a beaded chain. All of these models have one thing in common: They do not consider effects of expansion into vacuum and vacuum itself and therefore implicitly assume that the analyte containing droplets do enter the mass spectrometers. In addition, droplets that did not contain analytes from the beginning or are the remnants of releasing analytes into the gas-phase are still in the ion source and are still highly charged. As explained above, all these aggregates can potentially enter the vacuum systems of actual MS instruments due to their electrical mobility. First evidence that droplets leave traces in all regions of mass spectrometers was shown in the work of Kang et al. (2017) [47]. This publication clearly showed the disadvantages of using ESI for a longer period of time since contamination deeply in the MS instruments was observed. Additionally, personal conversations with different MS manufacturers raised the question, why these contaminations are occurring in the first place. All common models of the ESI process propose that only naked ions are transferred into the machine. However, these models do not consider the high mobility these charged droplets have allowing them to easily penetrate the mass spectrometer. Charged droplets are thus probably a main contributor to instrument contamination with ESI. The high electric mobility is an inevitable result of the large number of charges a droplet carries. The solution of installing a filtering device as for example a differential mobility spectrometer (DMS) [48, 49], is not as practical as it seems at first glance, considering the signal intensity loss typically connected to such a measure.

2 Observation of charged droplets in API MS

2.1 Introduction

The primary motivation for the investigation of charged droplets with different API MS instruments was the publication of Kang et al. [47]. The consequences of the contamination were shown in an impressive way. However, the signs for the aspiration of charged droplets into the MS system in the actual mass spectra were not investigated in detail in this publication. Reproducing the droplet scan method described in the publication of Kang et al. was the first step to observe charged droplets in an MS entrance stage. The analysis of the dynamics of these aggregates potentially gives clues how to mitigate their effects potentially adverse to analytical performance of a MS. As a SCIEX Triple Quad 6500 system was available, a first series of such experiments, was performed on this instrument.
In the following, the question raised if the aspiration of droplets is a unique aspect of the SCIEX Triple Quad 6500 with its entrance system and ion source or a common phenomenon. Different instruments equipped with different ESI sources were therefore investigated to answer this question which led to a new perspective on the scope of the phenomenon.

2.1.1 Droplet radius - Rayleigh Limit

The Rayleigh Limit describes the limit of the number of charges a droplet can carry before it fissions into smaller droplets due to the coulomb repulsion between the charges overcoming the surface tension of the liquid. This process is called Coulomb explosion and is described above. The equation for the Rayleigh Limit (cf. Equation 1.1) is shown

in section 1.3. The values of the surface tension and the vacuum permittivity to calculate the number of charges for three different solvents are given in Table 2.1. With the given density ρ of the three solvents in 2.1 and the equation to calculate the volume of a sphere and the density (cf. Equations 2.1), the mass of the droplet m for different radii becomes calculatable (cf. Equation 2.2):

$$V = \frac{4}{3}\pi r^3 \text{ and } \rho = m/V \tag{2.1}$$

$$m = \frac{4}{3}\pi r^3 \rho \tag{2.2}$$

Combined with the number of charges from the Rayleigh Limit the m/z of the droplets can be determined. In Figure 2.1 the m/z at the Rayleigh Limit for water, acetonitrile, and methanol is shown in dependence to the droplet radius. The shown radii serve as a lower limit, as the Rayleigh Limit represents the maximum number of charges of a droplet; a droplet with less charges or a larger radius is more likely to be stable.

Table 2.1: Values for the Rayleigh Limit calculation for different solvents

	Surface tension in mN/m	Density in g/cm	Vacuum pemittivity in F/m
Water	72.8	1.00	
Acetonitrile	29.0	0.786	8.85×10^{-12}
Methanol	22.7	0.791	

The calculated radii show that droplets at their Rayleigh limit with a radius of up to 2.5 nm are visible in mass spectrometers with a common mass range up to 3000. Although the calculation does not account for mixtures of different solvents, it is a useful first estimate of a lower limit size range of observable charged droplets.

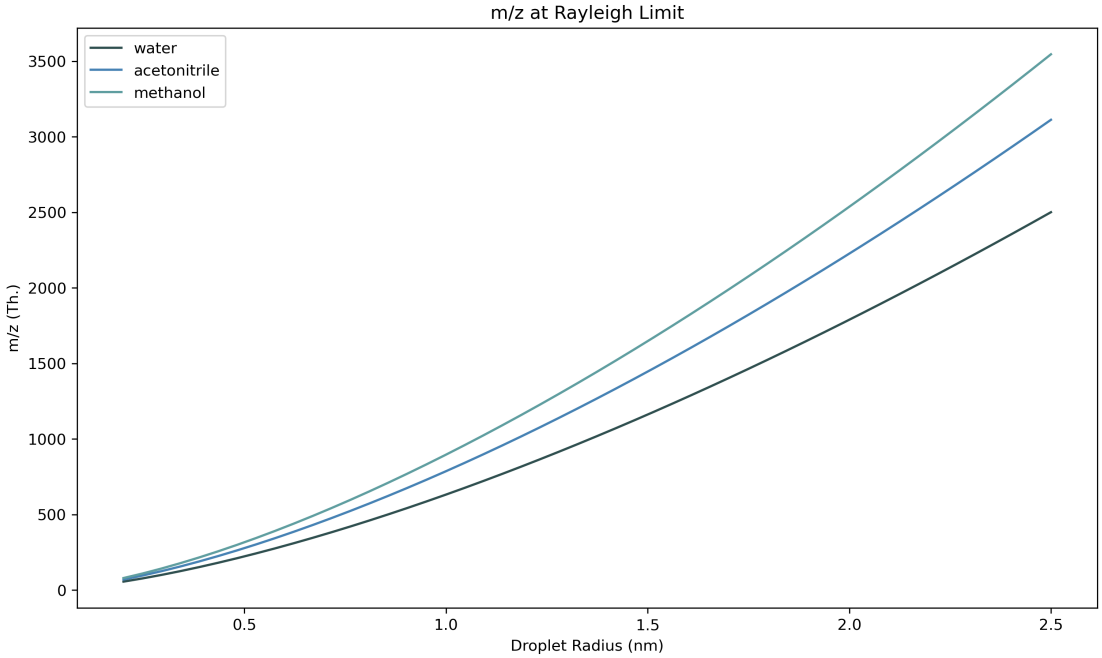

Figure 2.1: Calculation of m/z of charged droplets at their Rayleigh Limit in dependence to the droplet radius. The calculation was done for three different solvents (water, acetonitrile, and methanol). The m/z for droplets up to 2.5 nm is within common mass range of commercial mass spectrometer.

2.1.2 Chemicals

Experiments were performed with para-substituted benzylpyridinium ions (in the following referred to as thermometer-ions) and reserpine in different solvents [50–52].

Table 2.2: Masses of para-substituted benzylpyridinium-ions (thermometer-ions)

Ions	m/z (precursor ion)	m/z (primary fragment ion)
p-CH_3	184	105
p-F	188	109
p-Cl	204	125
p-CN	195	116
p-NO_2	215	136

The ions are dissociating in a specific pattern: A para-substituted toluene ion and a pyridine (shown in Figure 2.2) [50, 51]. The dissociation energies are depending on the substituent of the precursor ion. Due to their different stabilities these ions are used to detect effective ion temperatures and collision energies in ion transfer and mass analyzing devices.

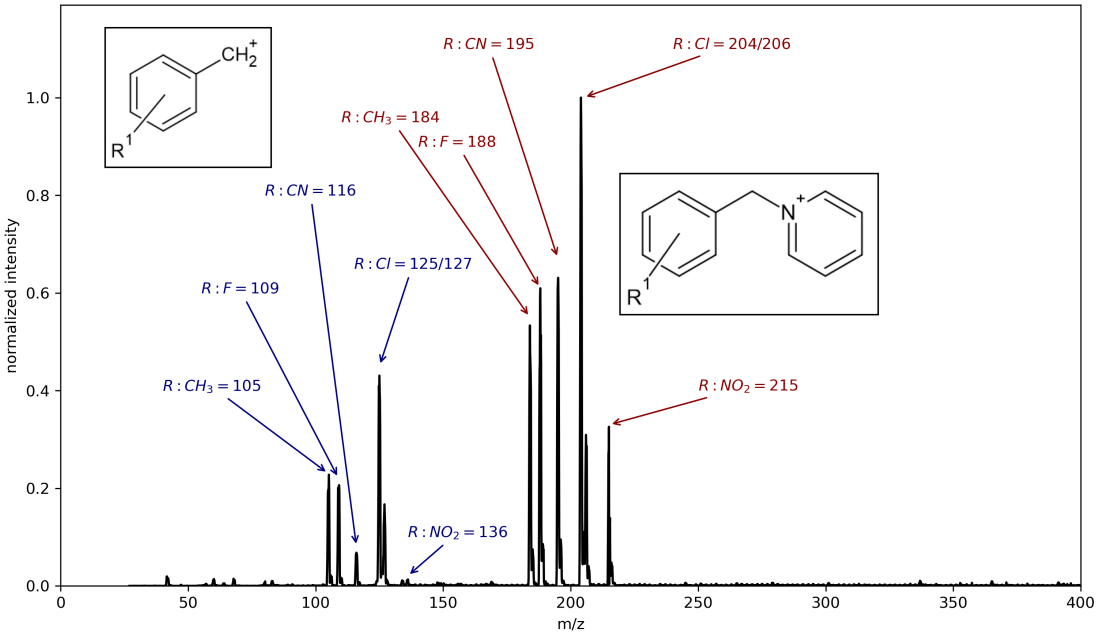

Figure 2.2: Overview spectrum of the thermometer ions and their fragments. Precursor ions: m/z 184-215 (shown with red annotations); fragments: 105-136 (shown with blue annotations). Para-substituted benzylpyridinium ions are breaking apart at a specific energy into a positive para-substituted charged toluene molecule and pyridine. The dissociation energy depends on the substituent.

The thermometer-ions were prepared in a one-pot synthesis by combining derivatized benzyl bromide (96-98 % purity; Sigma-Aldrich) with dry pyridine (> 99 % purity; J.T. Baker) in acetonitrile (HPLC grade; VWR chemicals) and water. The basic synthesis is described in Katritzky et al. [53]. The reaction is completed under constant stirring. The thermometer ions are re-crystallized in ethanol or diethyl-ether. The different benzylpyridinium species are mixed in a 1:1 ratio. As a second analyte-system reserpine was introduced. It is a drug for high blood pressure treatment. Today, it is a commonly

used analyte in MS experiments [52]. It has a m/z of 609 and its structure is shown in Figure 2.3. Reserpine was obtained in > 99 % purity from Sigma Aldrich.

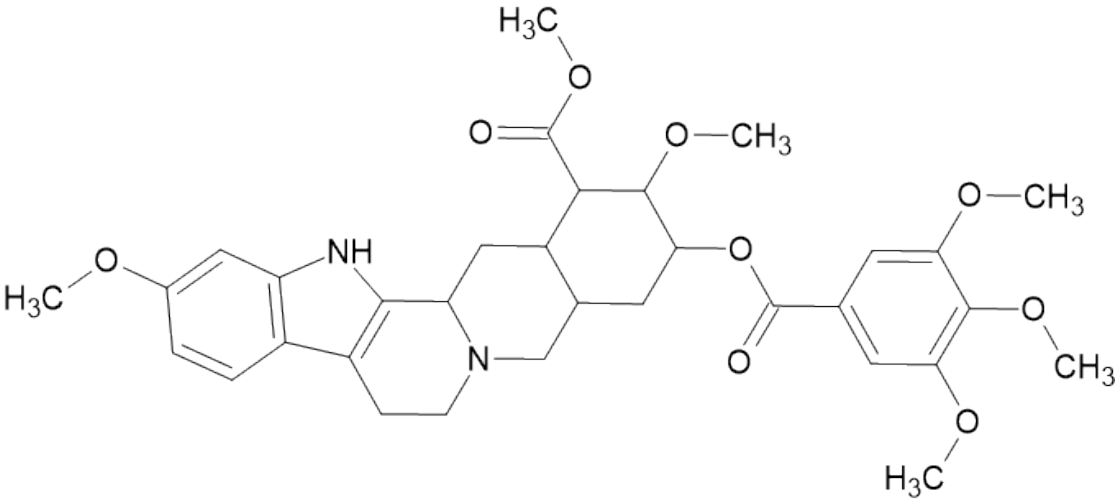

Figure 2.3: 2D structure of reserpine. It was used as an analyte with a higher m/z than the thermometer ions (m/z 609).

2.2 Experimental: SCIEX Triple Quad 6500

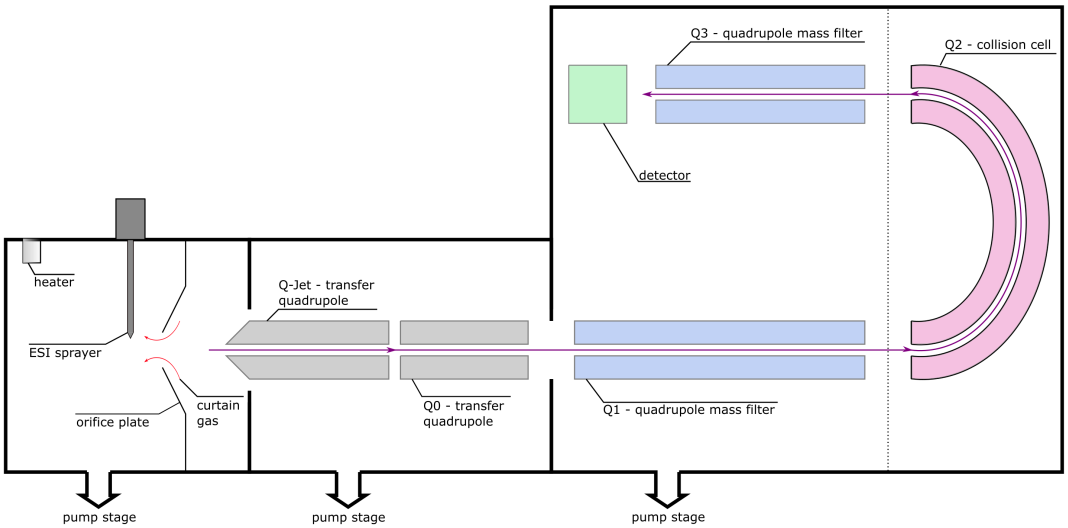

Figure 2.4: Scheme of the SCIEX Triple Quad 6500. The analyte solution is sprayed in the ion source. The ions are guided through the transfer quadrupoles (Q-Jet and Q0) into the first quadrupole (Q1). The collision cell (Q2) is bend. The ions are then guided into the last quadrupole (Q3) and detected.

As described above, initial experiments regarding charged droplets in API MS were done with a SCIEX Triple Quad 6500 System equipped with an IonDrive Turbo V ion source and operated with the TurbolonSpray ESI probe in ESI mode. A scheme of the instrument is shown in Figure 2.4. In contrast to other API MS systems, the SCIEX system has no inlet capillary as first pressure reduction stage but is equipped with a skimmer system leading straight into the first focusing quadrupole (Q-Jet) of the system, followed by another focusing quadrupole (Q0). It actively guides the ions into the first mass selective quadrupole (Q1) of the triple quadrupole configuration. The second quadrupole (Q2) acts as collision cell with nitrogen as collision gas. Characteristically, the collision cell of the SCIEX Triple Quad 6500 is bend and not linear as in previous systems. The third quadrupole (Q3), also a mass selective system, is situated behind the collision cell. The m/z range of the system is limited to 2000 in high mass-mode and 1250 in low-mass-

mode. To investigate charged droplets, which may have a much higher m/z range, a special “droplet-scan” mode was introduced in Kang et al. [47]. The first quadrupole is operated without DC potential on the rods (RF-only). In this mode the quadrupole operates as high-pass filter [54, 55]. Every charged species with a m/z higher than the low-mass cutoff (LMCO) is transferred through Q1 into the collision cell and can be mass analyzed by the third quadrupole (Q3). The LMCO in high-mass mode is approximately at m/z 1550 in this operation mode; in low-mass mode the LMCO is m/z 990. Everything above this LMCO is transmitted through Q1 into the collision cell, where the transferred ions are fragmented by collision induced dissociation (CID) with nitrogen. The collision gas pressure (CAD) can be controlled in the control software of the instrument. A typical value in a normal scan routine for the unitless CAD parameter is 6, which corresponds to a pressure of approximately 5×10^{-3} mbar. The effective energy of the collisions between ions and collision gas particles in the collision cell is controlled by the collision voltage, which is essentially the potential difference between Q0 and Q2. This defines the kinetic energy of the ions when entering the collision cell and thus the average collision energy. With the collision gas and voltage applied, CID fragments of the droplets can be mass analyzed in Q3 which generates a fragment mass spectrum. An automated collision voltage ramp can be set in the control software of the instrument to determine the fragmentation result in dependence on the average collision energy. A typical scan routine for the droplet scan is shown in Figure 2.5.

Figure 2.5: Scan sequence for the Sciex Triple Quad 6500 in droplet scan mode.

The voltage of the ESI needle was set to 5.5 kV, which resembles a common operating voltage for the triple quad instrument. The system has an integrated syringe pump, which was used to directly introduce the analyte solution into the ESI emitter with a flow rate of 7 µL/min, if not stated otherwise. As can be seen in Table 2.3 most of the parameters are given without a physical dimension or unit by the control software

of the system. In a second set of experiments, ion source parameters, like gas flow, temperature and liquid flow, were systematically varied.

Table 2.3: Default parameter for the ion source in the SCIEX Triple Quad 6500.

Control software	Definition	Default setting
Spray voltage	applied voltage	5.5 kV
Liquid flow	flow of the syringe pump	7 µL/min
CAD	collision gas, dimensionless	6 (approx. 5×10^{-3} mbar)
TEM	temperature of V-shaped heater in the ion source, dimensionless	0 (= room temperature)
GS 1	nebulizer gas, dimensionless	0-10
GS 2	gas stream from the V-shaped heater, dimensionless	0-10
CUR	curtain or dry gas, dimensionless	15-20
DP	declustering potential, dimensionless	100

2.2.1 Observation of droplet signatures with thermometer ions as analytes

The instrument was set up in droplet scan mode. The DC potential on the rods of the first quadrupole can be controlled by commands to the internal electronics of the instrument via a special serial interface and a terminal program, which was both provided by the manufacturer. The first experiments were done in high-mass mode, corresponding to a LMCO of m/z 1550. For the thermometer ion solution, the mass spectra show a wide signal structure above the LMCO at a collision voltage of 5 V (Figure 2.6 a). The signals of the bare analyte ions, which are around m/z 200, and additional unassigned signals have a low intensity at this collision voltage. It is noteworthy here that all detected light ions have to be generated after Q1, as everything under m/z 1550 is filtered out with Q1 in RF only mode. As the collision voltage is increased to 80 V, more analyte molecules and small fragments are released from the droplets and the signal below the LMCO increases in the mass spectra (Figure 2.6 b). At this point the LMCO appears not as sharp as before. When the collision voltage is increased to

155 V the bare analyte signals (m/z 184-215) are the most pronounced in the spectrum (Figure 2.6 c). The droplets, or the fragments of droplets, disintegrate almost entirely with this collision voltage. In addition, the fragmented thermometer ions (around m/z 100) are visible in Figure 2.6 c), which indicate even molecular fragmentation with the energy applied to the ions.

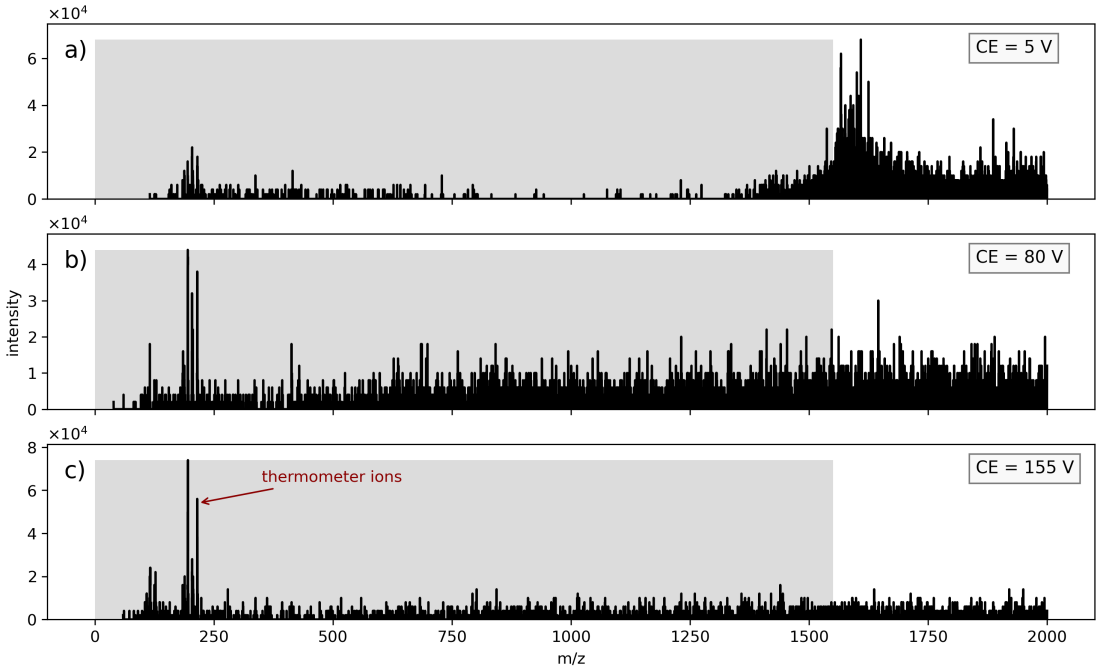

Figure 2.6: Droplet scan mode: Mass spectra of thermometer ions (in ACN/H2O) in dependence of the collision voltage. Signals below the LMCO of Q1 in RF-only mode (indicated by the grey shaded area), including bare thermometer ions, become visible with increasing collision voltage.

The declustering potential and curtain gas, which are applied to facilitate the evaporation and disintegration of large clusters, are set to values as in common analytical measurements (cf. Table 2.3). The declustering potential is defined as the potential between the orifice plate and the Q-Jet (cf. Figure 2.4). It influences the destruction of solvent cluster due to collision induced fragmentation. In addition, the curtain gas (cf. Figure 2.4) is generally assumed to generate smaller droplets as collisions with gas par-

ticles lead to a heat transfer, which assists the evaporation process. Thus, the droplet scan mode does not change the number of droplets entering the vacuum system of the MS; it makes the droplets reaching the collision cell observable in a mass spectrum. Furthermore, bare analyte ions, visible within the m/z range below the LMCO, must be transported within the charged droplet through Q1 and has to be released by the applied collision voltage and gas in the collision cell (Q2). The variation of collision gas is shown in the next section.

2.2.2 Collision gas pressure variation

The droplet scan mode can be applied to low-mass mode as well. A variation of the collision gas pressure in Q2 (CAD) was investigated. As described above, the recorded mass range is up to m/z 1250 and the LMCO in a droplet scan decreases to m/z 990 in low-mass mode. However, the mass resolution of the recorded mass spectra is higher compared to the high-mass mode. The unitless CAD parameter can be set from 0 to 12, which corresponds to approximately 1×10^{-3} mbar and 9×10^{-3} mbar of nitrogen within the collision cell. Figure 2.7 depicts mass spectra in dependence of CAD. The collision voltage was fixed to 12 V. Above the LMCO, intensive mass signals are generally visible, while the cutoff appears to be sharper with lower collision gas pressure, which is a result of the decreased collision frequency. At higher collision gas pressure, more signals below the LMCO emerge (cf. Figure 2.7) and the cutoff is blurred. This result shows that the fragmentation process of the droplets strongly depends on the collision voltage and collision gas pressure in the collision cell. This experiment was repeated in high-mass mode. Figure 2.8 shows the corresponding mass spectra. In contrast to the measurements in low-mass mode, the collision voltage was varied as well with the same parameter steps as depicted in Figure 2.6, although the liquid flow rate of the syringe pump was set to 10 µL/min which is a higher value as before (7 µL/min). At first glance it is obvious that the ion current and overall intensity above the LMCO is reduced for CAD = 12 (cf. Figure 2.8 a) and d). The analyte signal increases with higher collision gas pressure and voltage. The signals above the LMCO are smaller on average with higher collision gas pressure (cf. Figure 2.7 b) vs e). With the highest collision gas pressure and voltage, the unidentified signals around the analyte signals are reduced compared to the analyte signal (Figure 2.8 f). This is associated with the high energy

of the collisions happening in the Q2 under these conditions. The droplets appear to be completely fragmented as virtually no signal above the LMCO is visible.

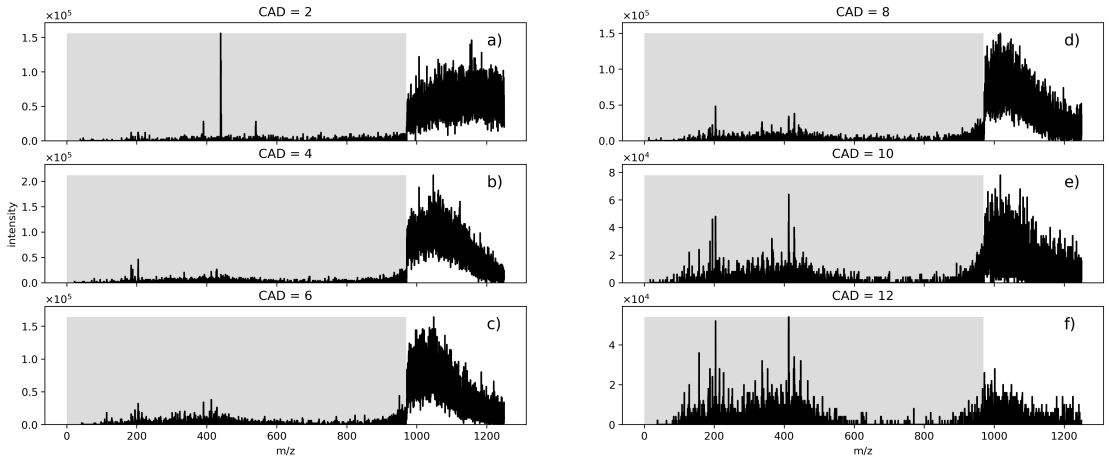

Figure 2.7: Droplet scan mode: Mass spectra of thermometer ions (in ACN/H2O) for different collision gas pressure values (CAD). With higher collision gas applied in the collision cell, fragment signals begin to appear, while the signal above the LMCO is decreases, particularly with high collision gas pressure (CAD=12). This measurement was performed in low-mass mode (m/z limit at 1250).

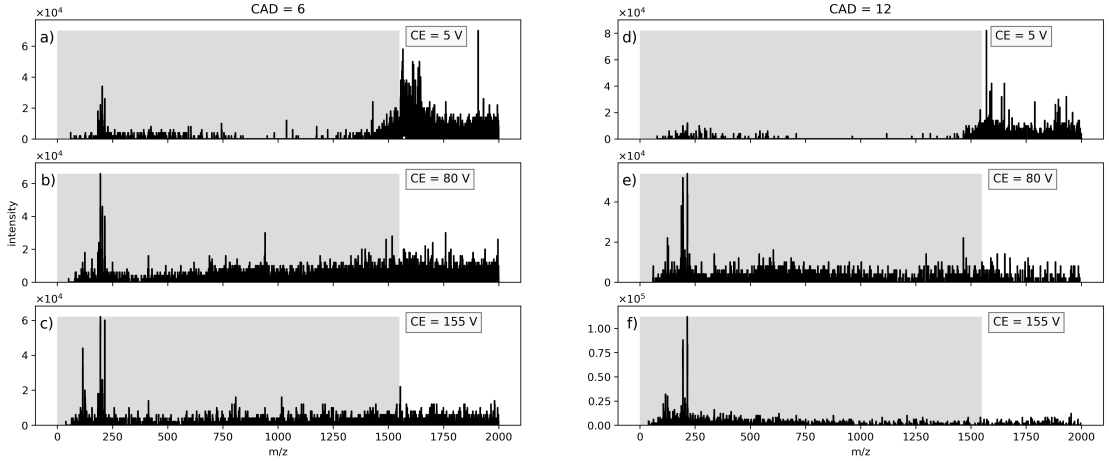

Figure 2.8: Droplet scan mode in high mass mode: Mass spectra of thermometer ions (in ACN/H2O) for varying collision voltages and pressure. The liquid flow was set to 10 µL/min for this measurement. With higher collision gas pressure, the broad signal above the LMCO is diminishing faster. However, the thermometer ions are less discernible at CAD = 12.

This first set of experiments with a solution of thermometer ions show that the fragments of droplets or charged droplets themselves can be detected with the SCIEX Triple Quad 6500. This observation strongly supports the notion of charged droplets entering the machine under common ion source conditions. The droplet scan method was applied to a solution of reserpine in isopropanol and water to investigate the effects of the chemical composition of the charged droplets. Variations of solvents and analytes are likely to influence the observed mass spectra significantly, since the internal dynamics of a droplet is strongly dependent on the interactions of the chemical components forming it.

2.2.3 Observation of droplet signature with reserpine as analyte

To examine the notion that chemical variation has a strong influence on the signatures of charged droplets observed in the droplet scan, reserpine was introduced as an analyte in a different solvent system. Reserpine is an aromatic molecule often used for calibration of mass spectrometers. The protonated mass signal is at m/z 609 and is filtered out by Q1 in droplet scan mode. Isopropanol and water were used as solvents. The system settings were applied as described before. The overall appearance of the mass spectra is similar to results of the measurements with thermometer ions. However, the shape of the signals above the LMCO is different. With reserpine as the analyte, the cutoff is sharper and diminishes abruptly to smaller m/z (Figure 2.9 a); in contrast, the mass spectra of the thermometer ions showed more of a smooth transition. This indicates less fragmentation of the thermometer ion solution droplets at a collision voltage of 5 V. An explanation could be the different choice of solvents. In contrast to acetonitrile, which was used with the thermometer ions, isopropanol is a protic solvent [56]. It is able to form hydrogen bonds with water molecules and produce more stable droplets compared to the acetonitrile/water droplets. With increasing collision voltage, the signals above the LMCO are decreasing strongly as the droplets are further fragmenting (Figure 2.9 b & c) and the bare analyte signal increases. These findings suggest that the choice of solvents has a notable effect on the resulting mass spectra and the fragmentation process of the charged droplets.

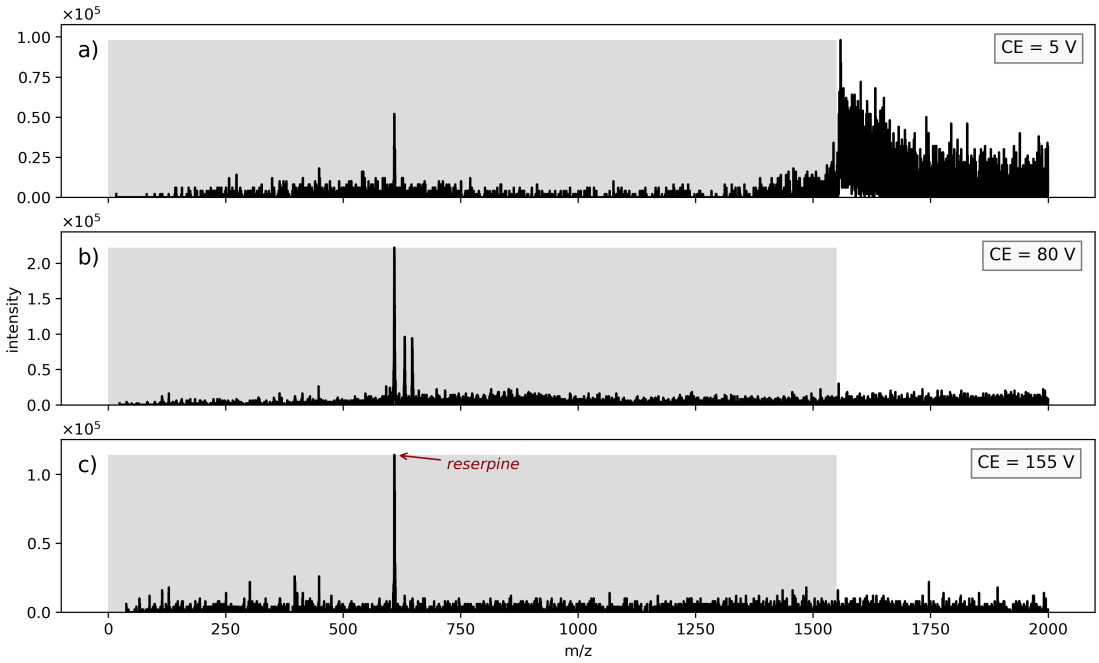

Figure 2.9: Droplet scan mode: Mass spectra for reserpine (in isopropanol/H2O) at different collision voltages. At low collision voltage (a) a broad signal can be observed above the LCMO. Additionally, a smaller analyte peak is visible at m/z 609. With higher collision voltages the analyte peak increases and the broad signal above the LMCO disappears. Fragments of the droplets can be seen in every spectrum.

Observing charged droplets worked as intended at the SCIEX Triple Quad 6500: Large charged aggregates, the droplets themselves or their large fragments, were visible in every performed measurement in droplet scan mode. This begs the question if the entrance stage of the SCIEX triple quad instrument is particularly prone to transfer large, charged aggregates due to its design, consisting of an orifice plate followed by two focusing quadrupoles. To investigate this aspect, experiments with different instruments are a useful subsequent step. A significantly different entrance stage is present in the Bruker amaZon speed ETD quadrupole ion trap (QIT). In this device, a glass capillary guides the ions into two ion funnels which are arranged off-axis to prevent direct transmission of particles along the line of sight. Ion funnels are used in atmospheric pressure ionization because of the drastic change in pressure regions [57–59]. The ions

are refocused by the funnels due to a fixed RF and electric potential. Otherwise, the ion beam would lose its narrow shape and a heavy loss of ion abundancy would occur. An observed capturing of droplets at this system would be additional evidence strongly indicating towards the common aspiration of droplets from ESI sources.

2.3 Experimental: amaZon speed ETD

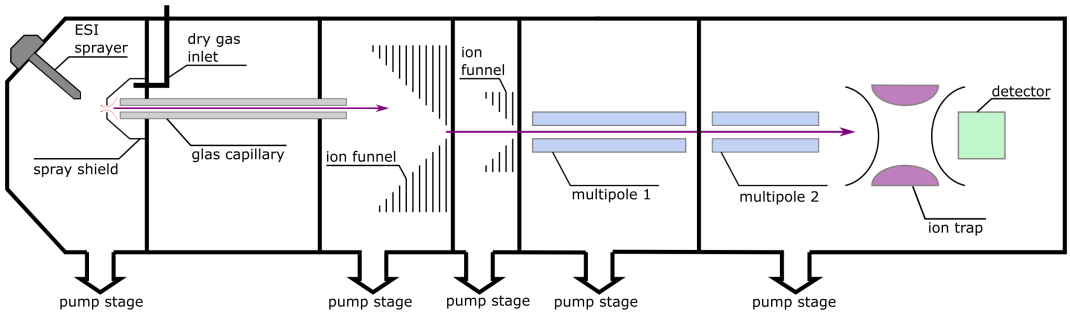

Figure 2.10: Scheme of the Bruker amaZon speed ETD. The spray is generated in the ion source and guided through a glass capillary. Two ion funnel focus the ions into two multipoles. The ion trap and the detector are situated behind the second transfer multipole.

To support the hypothesis that charged droplets are commonly aspirated from ESI ion sources into different instruments, subsequent experiments were performed with a Bruker Daltonics amaZon speed ETD quadrupole ion trap. In contrast to the SCIEX system, the amaZon speed trap uses a glass capillary as inlet stage. It is aligned off-axis relative to two ion funnels following downstream of the capillary, to reduce the transmission of neutral species deeper into the vacuum system. The transfer stage consists of two subsequent multipoles to further focus the ions. The ion trap mass analyzer is situated after the multipole assembly. Helium is used as trap gas. The instrument is equipped with a commercial Apollo Ion Source. A set of parameters can be varied in the ion source. The influence of these parameters, like the dry gas flow and temperature, nebulizer gas pressure and liquid flow from the syringe pump is investigated in another section of this work (cf. section 2.6.1). For the following measurement the spray voltage was set to 4.5 kV and the liquid flow was set to 4 µL/min. The default parameters are shown in Table 2.4.

The mass analysis process of the ion trap system consists of a sequence of steps: The ions are gated into the empty trap within a defined accumulation time (accu time). The accumulation time can be fixed by the user or the system is able to determine the time it requires to collect a defined number of charges. This operation mode is called ion

Table 2.4: Default parameter for the ion source in the amaZon speed ETD.

Control software	Default setting
Spray voltage	4.5 kV
Liquid flow	4 µL/min
Temperature	180 °C
Nebulizer pressure	0.5 bar
Dry gas flow	4 L/min
Isolation window	m/z 2500 (width 100 Da)

charge controlled (ICC). The trap is able to isolate certain masses with an additional applied RF potential. The isolated masses can be further fragmented by excitation in an RF field inducing energetic collisions with helium gas (collision induced dissociation: CID). A common mass analysis sequence consists of accumulating ions with ICC, isolating ions in a defined m/z range window (e.g., m/z 2500 ± 50) and fragmenting the ions in the isolated window with a defined fragmentation energy, which is defined by a relative amplitude factor for the excitation RF field (CID Amplitude). A schematic overview over the default mass analysis sequence is given in Figure 2.11. Droplets with m/z 2500 have a critical Rayleigh radius in the range of 2-2.5 nm (cf. Figure 2.1). To investigate the dynamic behavior of the charged droplets reaching the mass analyzer, the ion source and some transfer parameters were varied.

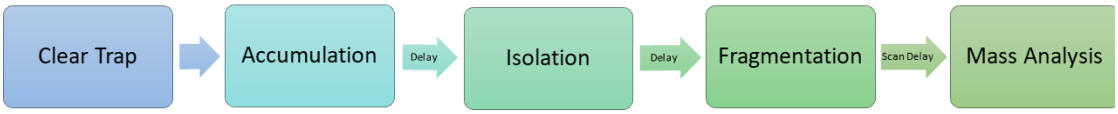

Figure 2.11: Default mass analysis sequence in amaZon speed ETD QIT

2.3.1 Observation of droplet signatures

The measurements were performed with the same thermometer ion solution as in the triple quad experiments. The molecular masses of the analytes and their primary frag-

ments are shown in Table 2.2. The dry temperature of the ion source was set to 50 °C. The gas flow of the ion source and transfer parameters were in normal operating mode. The experiment reveals a highly reproducible peak-structure in the isolated mass window of m/z 2500 ± 50 (cf. Figure 2.12 a). The broad structure at the isolation window is a strong indication that large, charged aggregates can be directly observed in the mass spectra obtained with the QIT. The signal seems to "bleed" over to smaller masses. With increasing accumulation time (Figure 2.12 b-c), the analyte signals at m/z 184-215, which are already visible at 40 µs accumulation time and are far away from the isolated m/z window, increase as well. Remarkably, the observed analyte ions have to be formed from something within the isolation window after the isolation step of the mass analysis sequence. This strongly indicates that the initially trapped large, charged aggregates, presumably droplets or droplet fragments, release analytes and smaller clusters in the trap.

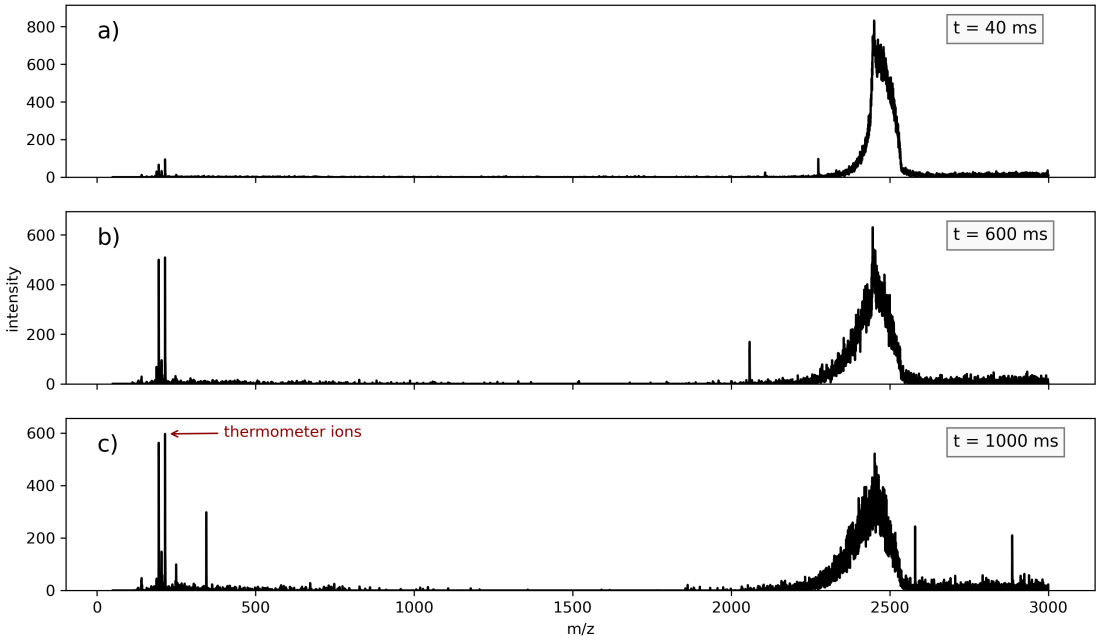

Figure 2.12: QIT Mass spectra for thermometer ions with varying accumulation time. A broad signal is observable in the isolation window (m/z 2500; width 100 Da). The thermometer ions signal (m/z 184 – 215) increases with longer accumulation time.

With the results of the QIT, a second mass spectrometer with an entirely different en-

trance system showed droplet signatures in the mass spectra. These observations are further, strong evidence that charged droplets can enter a variety of mass spectrometers. These results were a promising lead for further investigating charged droplets in a QIT.

2.3.2 Measurements with APCI

To verify that the observed mass signals are linked to the presence of charged droplets in the ion source originating from ESI, the amaZon speed ETD was equipped with an APCI (atmospheric pressure chemical ionization) source. In contrast to electrospray ionization, the APCI ionization process takes place in the gas phase [4]. It is an indirect ionization method: A corona discharge ionizes components of the background gas, which in return transfers its charge to analyte molecules via gas phase reactions. The very short mean free path at atmospheric pressure is an important factor for the ionization rate and contributes to the high ionization efficiency. A liquid solution of the volatile analyte and a solvent is pumped into a heated nebulizer, which vaporizes the solvent by contact with the heated surface. In contrast to ESI, no highly charged droplets result from this vaporization process in APCI. For this experiment dioctylamine was chosen as an analyte. It is commonly used for APCI experiments and shows its protonated form at m/z 242. This signal was clearly discernible in the mass spectra measured by the QIT with APCI (cf. Figure 2.13). Remarkably, the isolation windows (m/z 2500 with a width of 100 Da) were essentially empty with the experimental sequence described above. Subsequently it was also attempted to isolate smaller mass ranges. However, it was quickly determined the mass spectra contained no significant signals with the exception the bare analyte.
Due to the different ionization process of APCI, this experiment is strong evidence for the aspiration of charged droplets specifically from ESI sprayers.

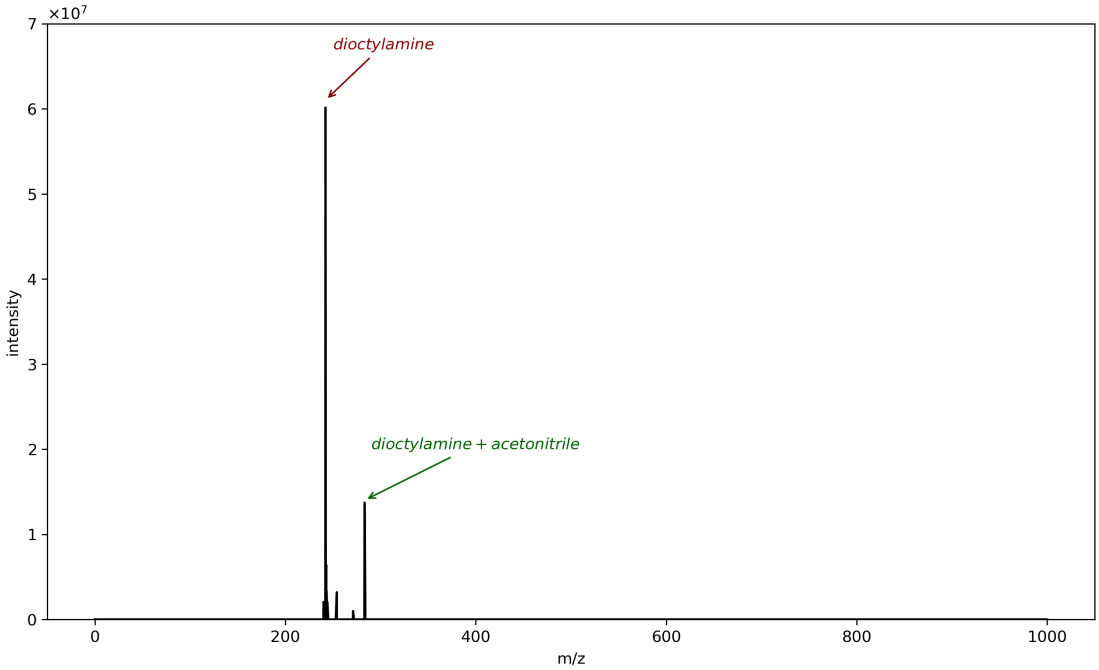

Figure 2.13: Mass spectrum in APCI mode. Dioctylamine is visible at m/z 242. Additionally, an adduct of one acetonitrile molecule and dioctylamine can be observed at m/z 283.

2.4 Experimental: Bruker esquire6000

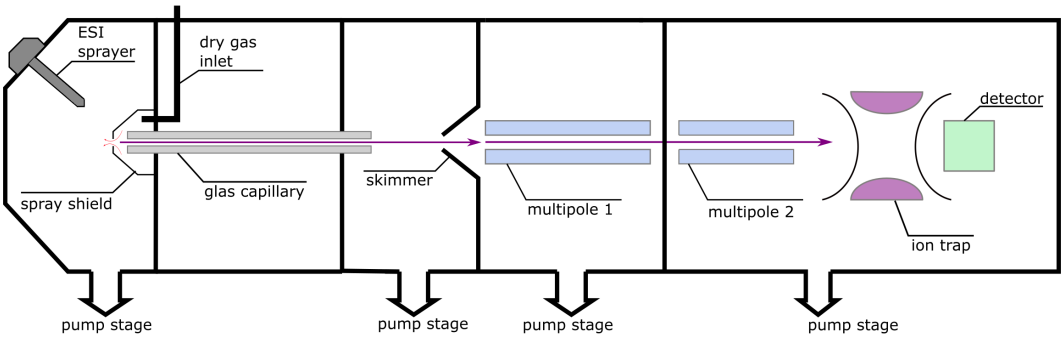

Figure 2.14: Scheme of the Bruker esquire6000. Instead of the ion funnels, a skimmer is built in the system.

Experiments with a Bruker esquire6000 instrument were performed to further extend the set of inlet stage configurations. This system is equipped with a glass capillary as well, but there are no downstream ion funnels: Here the ion stream passes a skimmer into the downstream multipole region, which is followed by the QIT. The skimmer is not oriented off-axis as it was the case in the Bruker amaZon speed ETD, which is the newer version within the instrument series. Due to the existence of a direct line of sight, this may lead to a transmission of charged droplets through the first entrance system stages with the Bruker esquire6000. The scan sequence shown in Figure 2.11 is repeated for the following experiment. Unfortunately, the system was not functioning properly: To acquire a usable mass spectrum, the instrument had to be set to negative spraying mode for a few minutes. With increasing time in positive mode, a broad signal at the end of the scannable mass range appears in every scan mode even if no analyte solution was sprayed. This strongly suggest a technical interference within the trap like an electrical discharge. This is obviously a problem for longer measurement routines and reproducing the same experiments done with the amaZon speed ETD. The reason for this behavior was not resolved during the course of experiments. Nevertheless, it was possible to record a spectrum with an isolation window set at m/z 2500 (cf. Figure 2.15). Before isolating this mass range, the transfer parameters were optimized automatically by the software for the transmission of ions with m/z 2500. The same thermometer ion

solution as before was used. The mass range of the recorded mass spectra was m/z 200 – 6000. The ESI voltage was set to 4.5 kV and the liquid flow was controlled by an external syringe pump to circa 5 µL/min. The other ion source parameter, which can be controlled in the control software, were kept the same as the parameters in the amaZon speed ETD. The parameter can be seen in Table 2.4. As Figure 2.15 shows, a double peak structure at the isolation window and smaller signals above it are clearly visible.

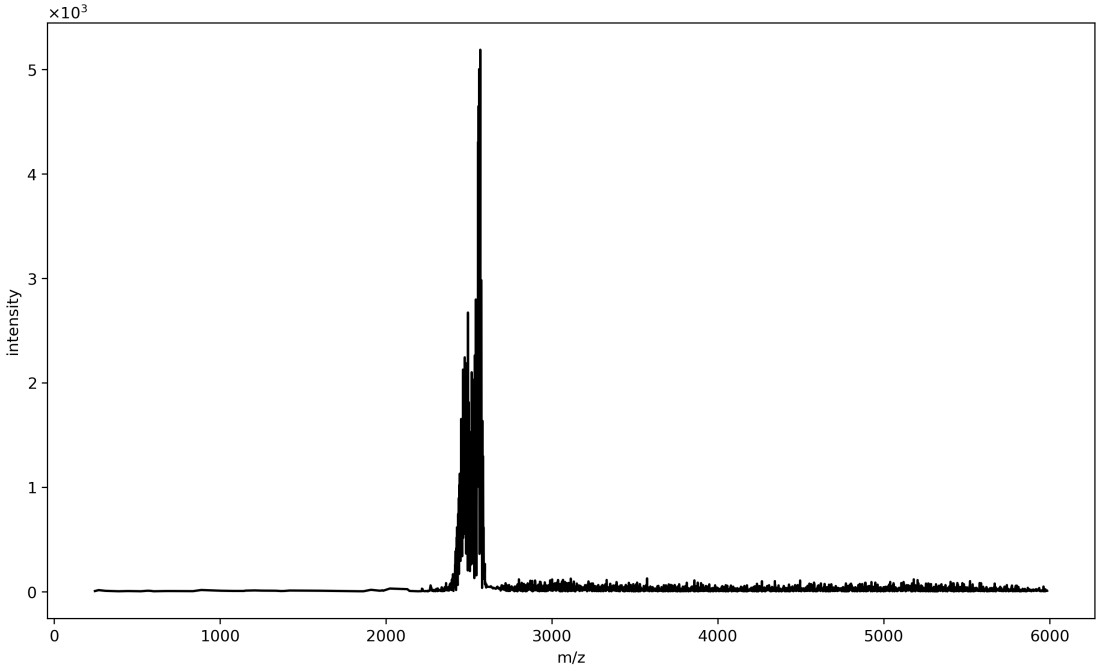

Figure 2.15: Esquire6000 spectrum of isolation at m/z 2500 (width 100 Da). A broader signal could be isolated. Above the isolation window smaller signals can be observed. Beneath the isolation window the spectrum appears to be empty.

The technical issues with the system hindered further systematic experiments. Nevertheless, the spectrum recorded is further supporting evidence that API MS systems are aspirating droplets from ESI sources irrespectively of the following inlet or transfer systems.

2.5 Experimental: Agilent 6538 UHD Q-TOF

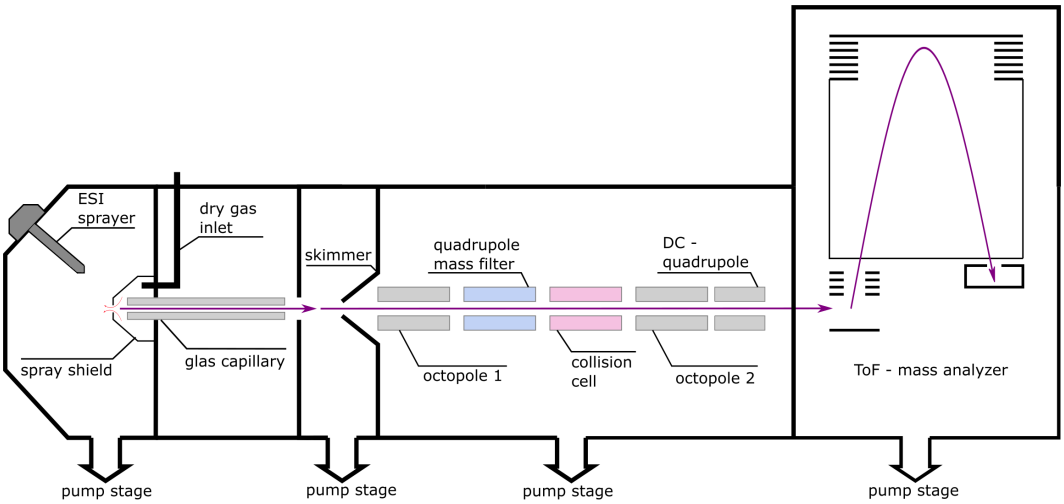

Figure 2.16: Scheme of Agilent 6538 UHD Q-TOF. The entrance stage is similar to the Bruker esquire6000 QIT and is followed by a series of different multipoles to transfer the ion beam into the ToF mass analyzer.

Further investigations of aspirated charged droplets were performed with the solution of thermometer ions in an Agilent 6538 UHD Q-TOF, a quadrupole-ToF instrument. Figure 2.16 depicts a scheme of the instrument. The basic design of the inlet stage is similar to the Bruker esquire6000: A glass capillary ends in a skimmer configuration which the ion stream passes into the quadrupole region and subsequently to the time-of-flight analyzer. The mass range of this system in this user mode reaches m/z 10000. The liquid flow into the ESI emitter was set to 8 µL/min with an ESI voltage of 2.9 kV. As the ion sources of the Bruker systems discussed before are quite similar to the source of the Agilent 6538 UHD Q-TOF, the values of the ion source parameters were applied in the same range as shown before (cf. Table 2.4). The DC bias of the mass selective quadrupole can be manipulated by the control systems and was switched off for this experiment. This generates an RF-only quadrupole with similar transfer properties as in the SCIEX Triple Quad 6500. A target mass of m/z 2500 was selected. Everything below this target mass is not transferred by the first quadrupole. Additionally, the Q-TOF is

equipped with a collision cell quadrupole. Different collision voltages can be applied, to fragment the ions in the collision gas bath in the cell which allows the recording of fragmentation spectra as described before for the SCIEX triple quad instrument.
As described above, the experiments were conducted with the thermometer ion solution. The collision voltage was increased in three increments: 0, 50 and 100 V. The mass spectra acquired in these experiments were not recordable in normal acquisition mode due to technical limitations of the instrument: The quadrupole can only be configured as “RF only” in a tuning mode of the instrument, unfortunately the control software does only allow the monitoring but not the recording of mass spectra in this mode. However, screenshots of the control program are shown below (Figure 2.17). For all collision voltages a broad signal at m/z 2000 and the bare analyte signal is visible. With increasing collision voltage, the analyte signal increases, which indicates the same release behavior of the analyte as was shown with the SCIEX Triple Quad 6500. As everything under m/z 2500 should be filtered out by the RF-only quadrupole, also the broad signal along with the analyte has to be fragments of larger aggregates. This additional experiment on a different instrument underlined the previous presented results: Charged droplet exist in a variety of ESI mass spectrometers and droplet signatures can be made visible in very different API MS systems.

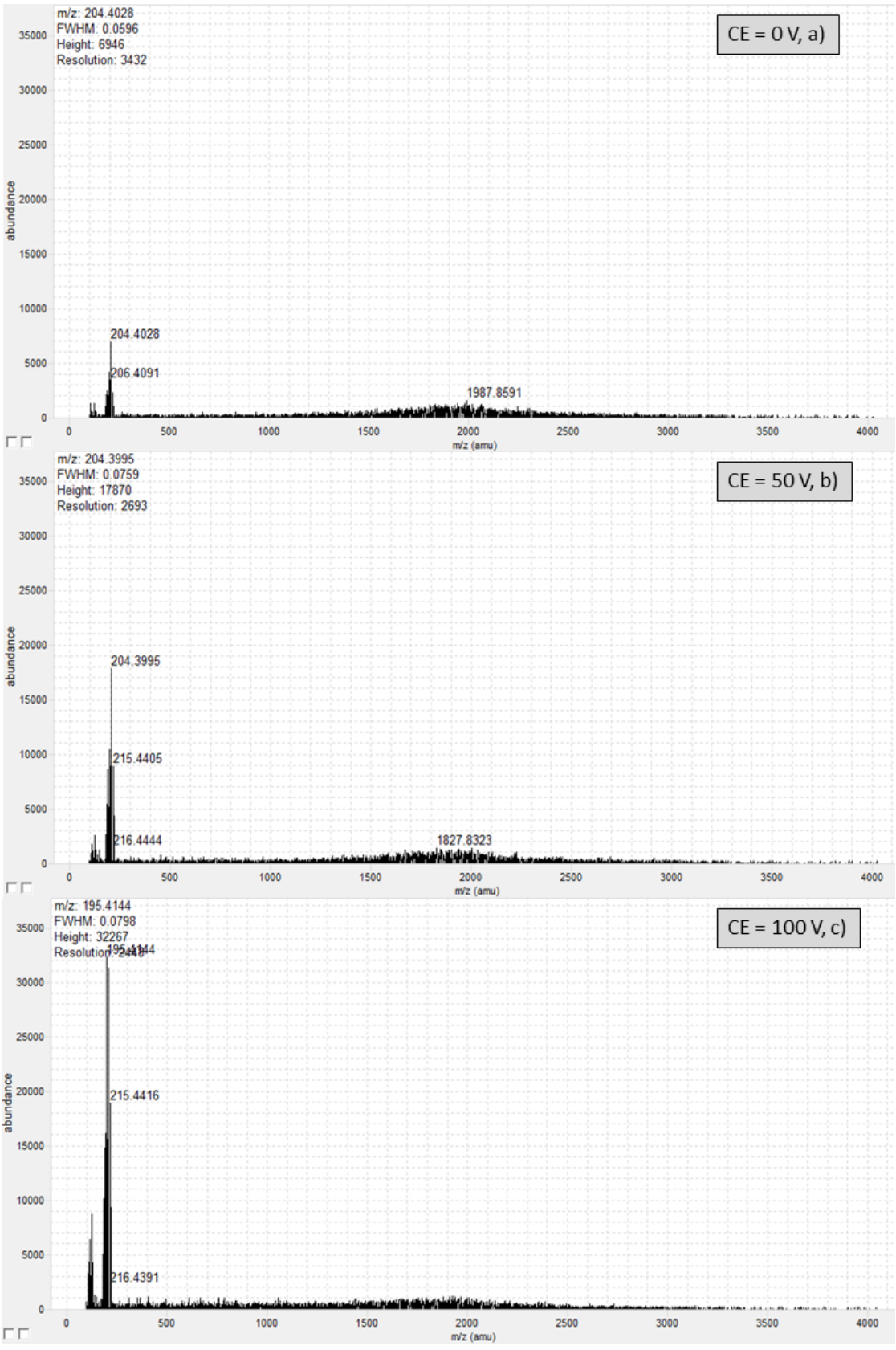

Figure 2.17: Droplet signatures at Q-TOF instrument. A broad signal is appearing at m/z 2000. The analyte is signal is increasing with higher collision voltage.

2.6 Variation of ion source parameters

2.6.1 Ion source parameters amaZon speed ETD

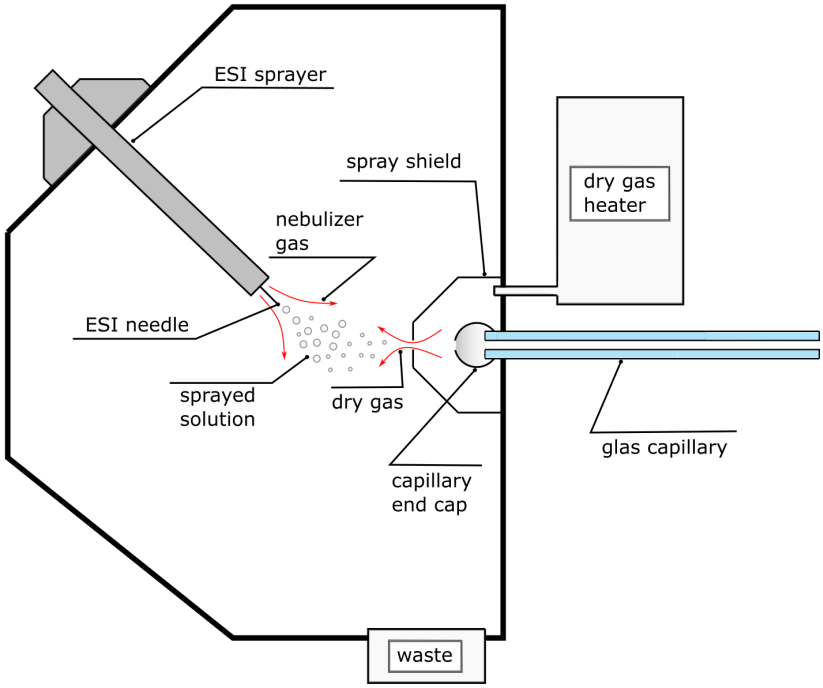

Figure 2.18: Scheme of the Bruker Apollo source. Different gas flows are indicated by arrows. The nebulizer gas is extruding from ESI sprayer itself, whereas the dry gas is applied from the spray shield as counter flow. The aspirated droplets are indicated as grey dots.

Strong evidence that charged droplets enter commercial systems was given in the previous chapter. The presented experiments and observations lead to the publication "Observation of charged droplets from electrospray ionization (ESI) plumes in API mass spectrometers" (2021) [60]. The droplet distribution present in the ion source depends on typical ion source parameters (gas flows and temperature, liquid flow) [4]. Therefore, also the characteristics of the droplets aspirated into the vacuum system are very likely to significantly depend on the ion source parameters. The amaZon speed ETD turned out to be a well-suited system to investigate the coupling of droplet signatures

and ion source parameters due to its minutely controllable parameters in the software and its reproducibility of the droplet signatures as shown in the previous chapter. In the Bruker Apollo ion source, Nitrogen is introduced as drying and nebulizing gas. This gas is applied as counter flow from the spray shield (cf. Figure 2.18). It is heated to induce a higher evaporation rate on the spray. The nebulizer gas is applied to the ESI needle assembly. It assists droplet formation in a constant stream at the end of the ESI needle as it directly interacts with the cone jet region of the spray [32]. As discussed above (cf. 1.2) due to the application of a nebulizer gas flow, the balance between the ionization voltage and the different flow parameter becomes easier to handle. For subsequent experiments, the transfer parameters of the QIT were optimized in instrument “smart mode” to m/z 2500. The isolation window was set to m/z 2500 with a width of 100 Da. It should be noted that droplets trapped at this range have a minimum size of about 2.5 nm (cf. Figure 2.1). The fragmentation amplitude was set to 0.5. As the analysis of the dynamics of the droplets needs more information than given by the mass spectra, the TIC (total ion count) and EIC (extracted ion count) is investigated as well. The TIC shows the overall intensity of the isolated signals, whereas the intensity of a specific mass range can be shown in the EIC. The default settings for the ion source parameters are shown in Table 2.4.

2.6.1.1 Nebulizer gas pressure variation – thermometer ions

The first experimental series is the variation of the nebulizer gas pressure. As described in the previous section, the nebulizer gas is introduced coaxially around the ESI capillary at the tip of the ESI emitter assembly (cf. Figure 2.18). Its purpose is to aid droplet formation by direct interaction with the cone jet region of the spray [4]. It is generally assumed that a higher pressure at the exit of the ESI needle leads to smaller droplets entering the system as droplet stream due to the turbulent aerodynamic forces at the ESI emitter exit [4]. As the droplet size is decreasing, the number of droplets should increase. The default setting for the nebulizer gas pressure is 0.5 bar. The dependence of the TIC of the isolated signal on the variation of the nebulizer gas flow is shown in Figure 2.19. The steps of the nebulizer gas pressure variation are indicated by the grey lines. Increasing the nebulizer gas flow has a notable influence on the TIC. Interestingly, the TIC does not increase as a higher flow of the pneumatic assistance gas at the ESI

needle tip would suggest. It decreases in three distinct steps at 0.5 bar, 0.75 bar and 1 bar. After setting the nebulizer gas pressure higher than 1.5 bar the TIC is not decreasing further. This possibly indicates that the droplet distribution does not change above a certain gas pressure at the ESI needle.

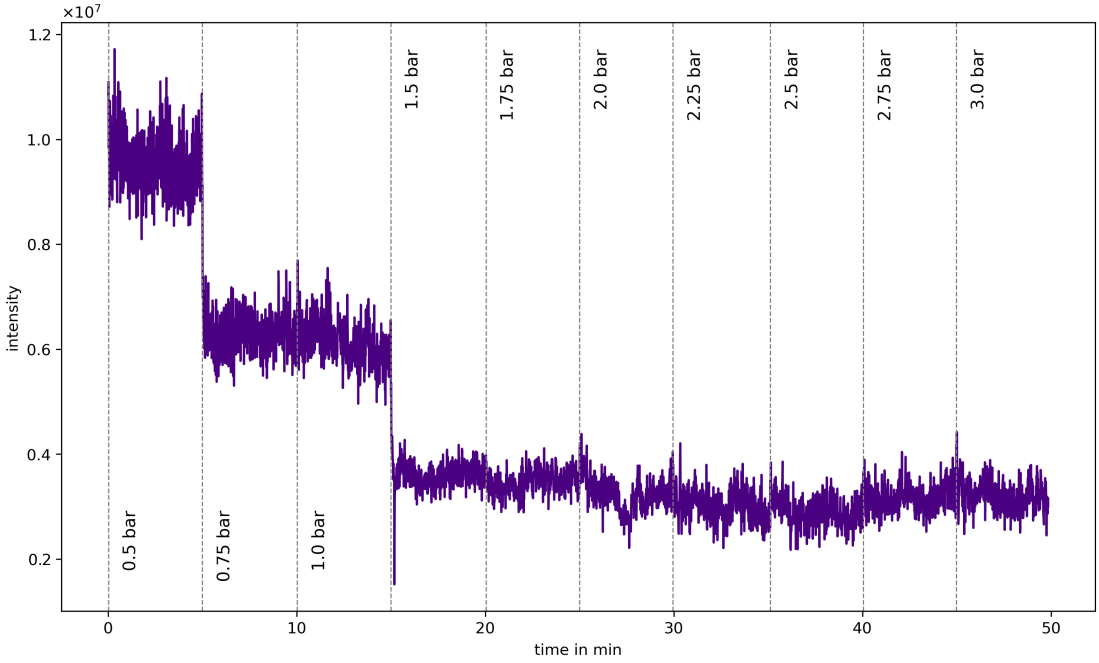

Figure 2.19: TIC for nebulizer gas pressure variation (thermometer ions) at the Bruker amaZon. The stepwise increments for the nebulizer gas pressure are indicated by grey lines. The TIC of the isolated droplet signal (isolation window m/z 2500 with a width of 100 Da) is shown in purple. Two steps are discernible in the observed TIC signal for this experiment at 0.5-0.75 bar and 1-1.5 bar.

Additionally to the analysis of the TIC, an extracted ion count (EIC) was set to the mass range of the bare thermometer ions (cf. Table 2.2). This means, that the range was set from m/z 184 to 215, which was chosen to have an indication of the release of thermometer ions over the course of the experiments. The EIC shows a noticeable burst of intensity of the thermometer ion the first increment at 0.5 bar (Figure 2.20), which is most probable an outlier. The first segment seems to have a slightly higher overall intensity. Another outlier is visible at 1.0 bar of nebulizer gas pressure. With nebulizer

gas flows higher than 1.5 bar, no further bursts of thermometer ions are visible and the EIC is evenly distributed until the end of the measurement. The burst may originate from less stable droplets transporting a higher number of analytes into the machine.

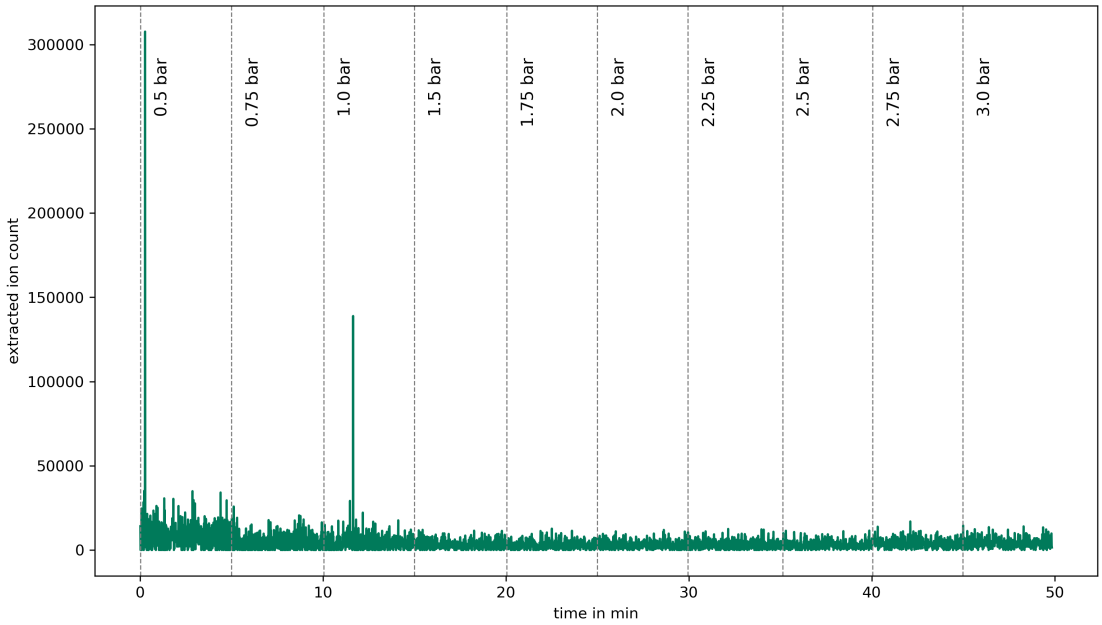

Figure 2.20: Extracted ion count of the mass range of thermometer ions (m/z = 184-215) for the nebulizer pressure variation (thermometer ions) at the Bruker amaZon. The increments for the nebulizer gas pressure are indicated as grey lines. The intensity of the EIC is shown in green. Two bursts with high intensity are visible at 0.5 bar and 1 bar.

In Figure 2.21 an enhanced depiction of the EIC is shown. In addition to Figure 2.20 the average of the signal was calculated for the different sections of nebulizer gas pressure in the experiment. The average is shown as a dashed line in red. The shape of the average variation of the EIC signal is similar as the shape of the TIC variation (cf. Figure 2.19). The variance of the averages could not be depicted in the same plot, as the values were orders of magnitudes larger than the average. This is due to the high noise level on the EIC, which is even more visible in the enhanced depiction in Figure 2.21.

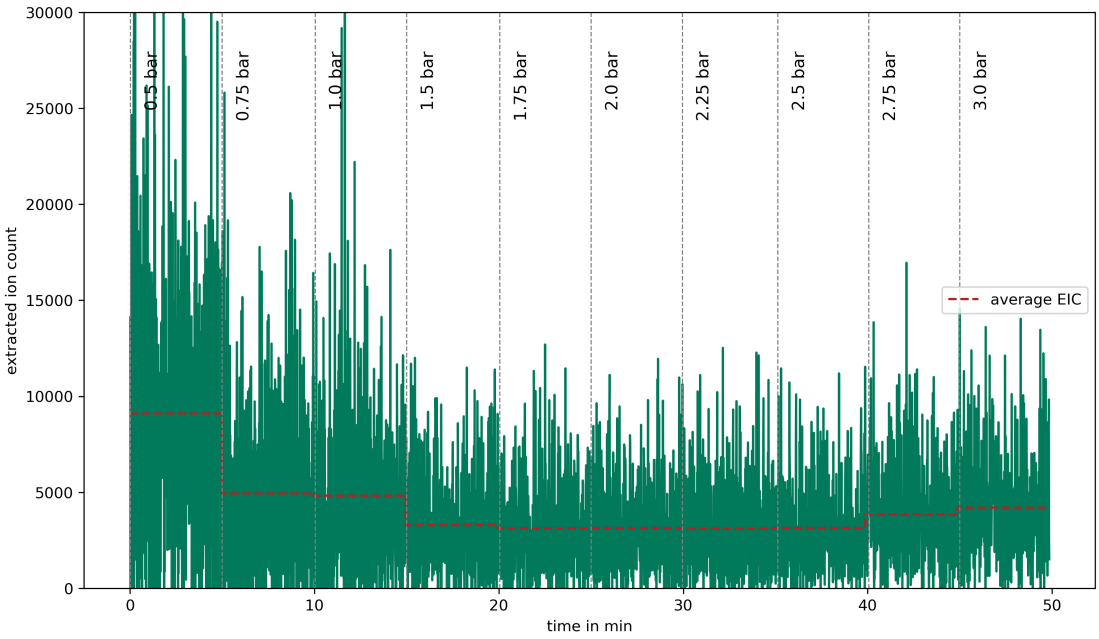

Figure 2.21: Enhanced depiction of the EIC of the thermometer ions (m/z 184-215). The dashed line represents the average of the signal in the different sections of the nebulizer gas pressure variation. The steps of the average are similar to the steps in the TIC.

The associated mass spectra are shown in Figure 2.22. All mass spectra are normalized to the spectrum of the series with highest intensity to emphasize the relative differences. A double peak structure in the isolation window corresponds to the trapped droplets. Except for the decreasing intensity, the mass spectra show no significant differences. The spectra are averaged over the duration of the specific nebulizer pressure segment (around 5 minutes each). Thermometer ion signals are absent in the mass spectra.

This set of experiments demonstrates that the nebulizer gas pressure has a minor influence on the shape of the resulting mass spectra, despite the obvious changes as shown in the chromatogram of the TIC. As the mass spectra are similarly shaped with the various nebulizer gas pressure values, it can be assumed that overall, and quite surprising, particles with similar fragmentation behavior are reaching the mass analyzer. The steps in the TIC signal is a result of different effectiveness of transporting the droplets. At a low nebulizer gas pressure value, a larger amount of droplets potentially

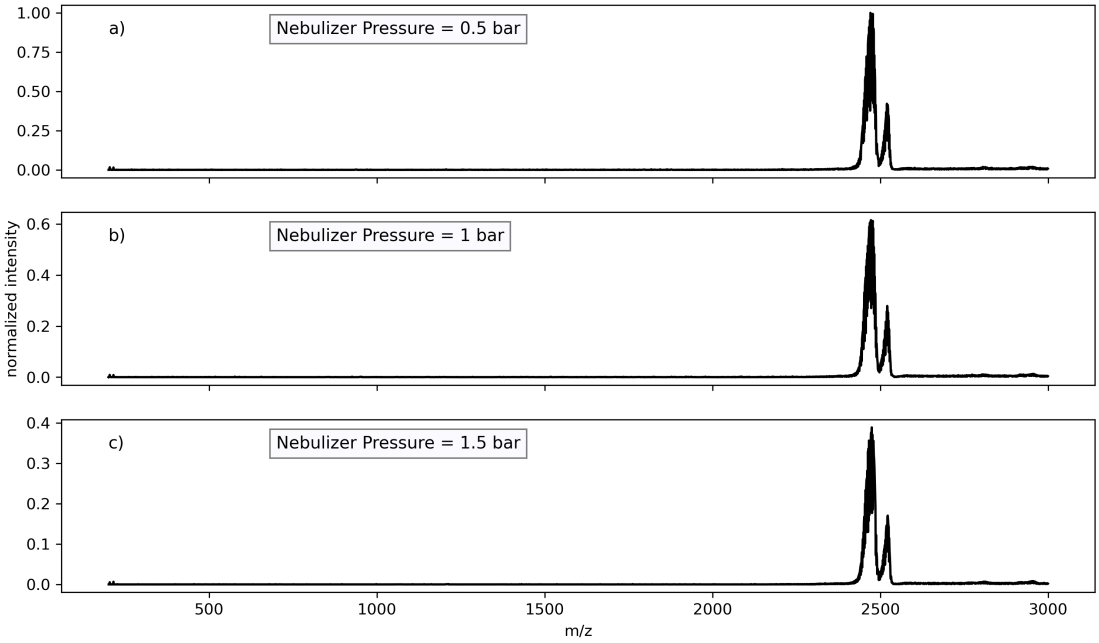

Figure 2.22: Mass spectra for three different nebulizer gas pressures (0.5 bar, 1 bar, 1.5 bar) at the Bruker amaZon. The intensity of the spectra are normalized to the one at the 0.5 bar segment. A double peak structure in the isolation window is visible.

enters the system and thus cause a larger intensity in the TIC. This could be, besides the obvious effect of the nebulizer gas on the pneumatical nebulization of the liquid solution, also due to the gas flow dynamics within the ion source, which inhibits droplets entering the inlet capillary at a high gas pressure. The EIC is shows the same overall variation, except for two brief intensive bursts of signal. In essence, the variation of nebulizer gas pressure has a small effect on the distribution of the aspirated droplets but does influence the transport of these aggregates. Thus, the dry gas flow was varied to further support the notion that the gas flow within the ion source influences the transport of the charged droplets.

2.6.1.2 Dry gas variation - thermometer ions

The dry gas flow is introduced into the ion source to desolvate droplets and cluster aggregates [4]. It also minimizes the entrance of neutral species into the vacuum system,

which would in turn lead to increased contamination. The heater for the dry gas flow was heated to 180 °C during the measurement series. The actual temperature of the gas entering the ion source is lower due to the distance between the heater and the ion source. A common setting of dry gas flow for an analytical experiment with thermometer ions is 4 L/min. The dry gas has potentially an influence on the size and stability of aspirated droplets, as the droplets have higher exposure to the hot gas, which leads to a higher average temperature within the droplet and a higher evaporation rate of the solvents. In Figure 2.23 the TIC is shown. It, again, represents the total intensity of the isolated signal. The segments of the dry gas flow variation are indicated by the grey lines. The chromatogram shows an expected general dependency: The TIC is decreasing with higher flow rates, presumably as less ions are entering the system due to the countering gas flow. Remarkably, the isolated droplet signal does not vanish entirely, even with very high dry gas flow rates.

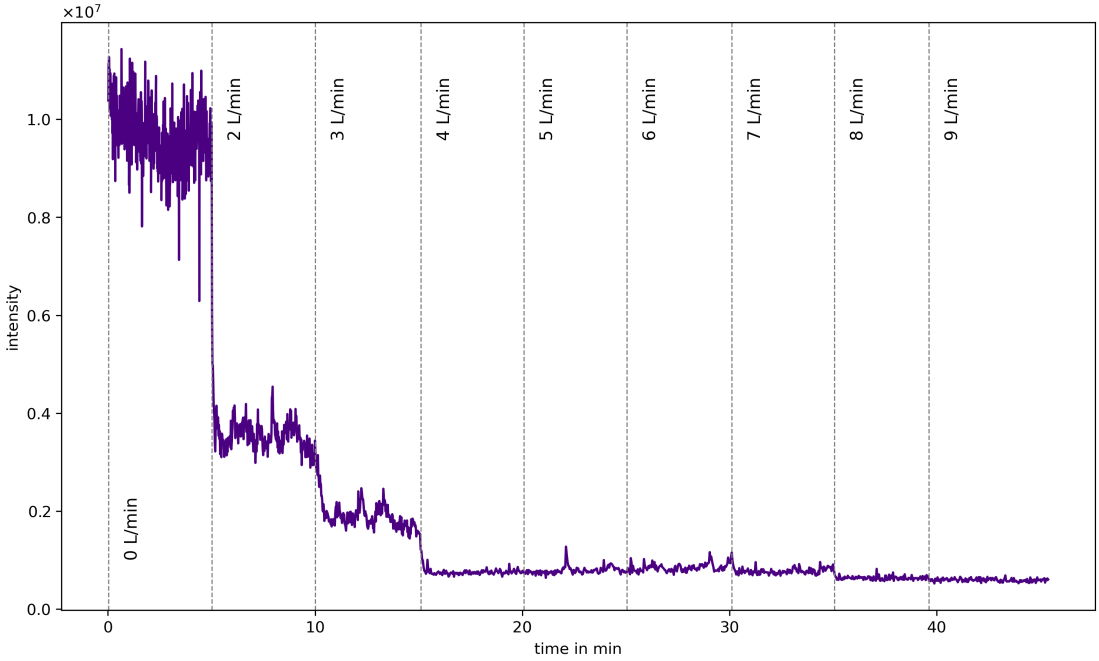

Figure 2.23: TIC of the isolated droplet signal during a dry gas flow variation at the Bruker amaZon. The grey lines represent the different increments of dry gas flow. A drastic decrease is visible from 0-2 L/min. Hereafter, the TIC decreases in smaller steps but does not vanish entirely.

Surprisingly, the EIC indicates that thermometer ions are released from the trapped droplets with a higher rate at a flow rate of 2 L/min (cf. Figure 2.24). The assumption that the droplets are desolvating more efficiently and are less stable with higher dry gas flow is contradicting with these results. At 0 L/min a very intensive burst of thermometer ions is visible, similarly to the previous measurement at varying nebulizer gas pressure values (cf. Figure 2.20). After increasing the dry gas flow up to 4 L/min the EIC stays at a comparably steady level.

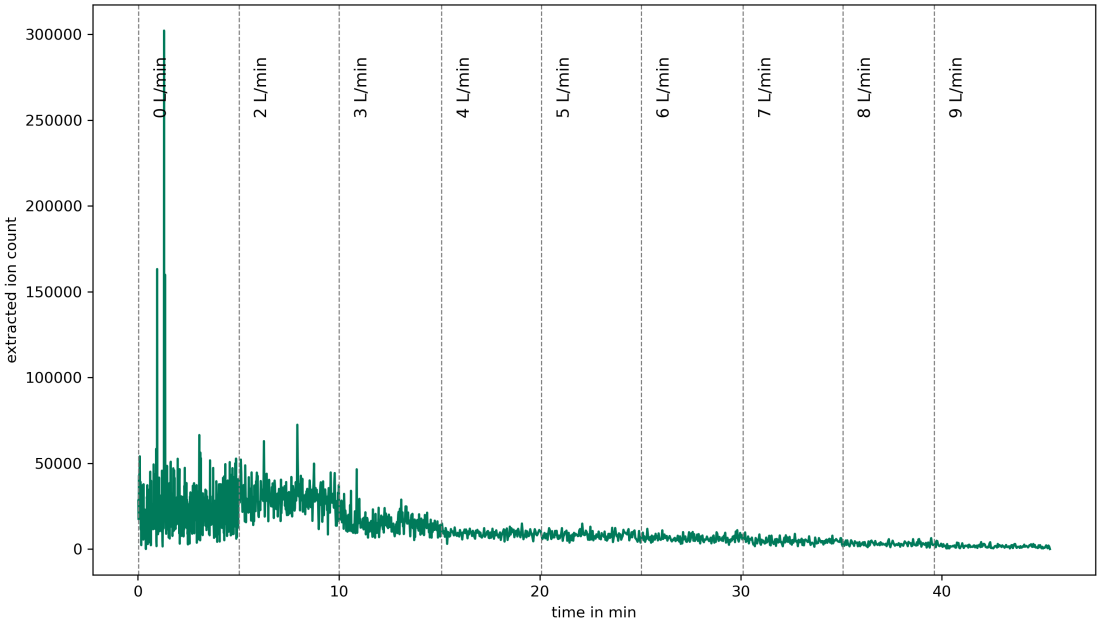

Figure 2.24: Extracted ion count of thermometer ions (m/z 184 – 215) generated by fragmentation originating from the isolated droplet signal for variation of the dry gas flow at the Bruker amaZon. The increments of dry gas flow are indicated by the grey lines. The EIC is shown in green. One large burst of signal is visible at 0 L/min. A slight increase can be observed at 2 L/min. At higher gas flow values, the EIC decreases.

The associated mass spectra of the isolated droplet signature show the same double peak structure as shown before (Figure 2.25). In contrast to the mass spectra obtained during the nebulizer gas pressure variation, the analytes are clearly visible in each mass spectrum. Due to the intensity loss with higher dry gas flow, signals close to but still outside of the isolation window - and particularly at higher m/z compared to the isola-

tion window - are more apparent. These structures above the isolation window indicate a loss of charge from the trapped droplets without strong mass loss. In Figure 2.26, a magnified version of spectrum d) of Figure 2.25 is shown. If one charged molecule leaves the droplet with only a small number of solvent molecules, the m/z value is increased and an additional peak above the droplet-peak appears. For example: When the primarily visible peak structure at m/z 2500 consists of a droplet with a mass of 12500 Da and 5 charges, a signal around m/z 2975 could be comprised of 11900 Da and 4 charges (cf. Figure 2.26 b). The difference in mass is only 600 Da, which is an indication that a few molecules of water and acetonitrile are leaving the droplet with an ion. The signal of the leaving molecules should also be visible in the mass spectrum at m/z 600, if they leave the droplet as compact cluster. Indeed, the background around this m/z is increasing in the last mass spectrum (cf Figure 2.26 a). Although it fits surprisingly well for this measurement, this proposed mechanism is highly hypothetical as the actual mass to charge ratio of the transferred droplets is currently unknown. Another interesting aspect of this measurement is that the double peak structure shifts its maximum from the left peak to the right peak at higher gas flow rates. The reason for this very interesting observation is also currently unknown.

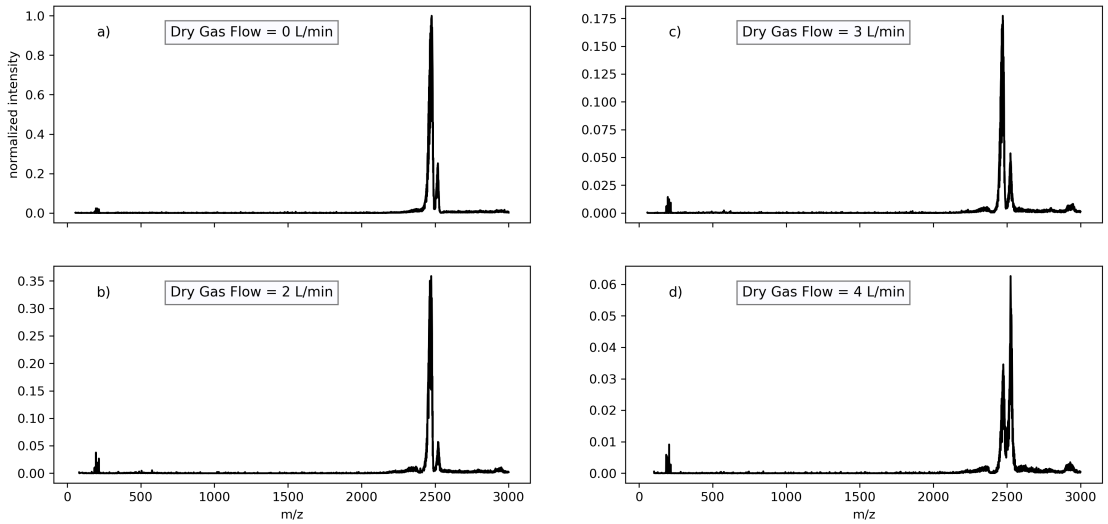

Figure 2.25: Mass spectra for four different dry gas flow values (0 L/min, 2 L/min, 3 L/min and 4 L/min) at the Bruker amaZon. A double peak structure at the isolation window can be observed. The intensity is decreasing with higher dry gas flow. Signals above the isolation window are visible.

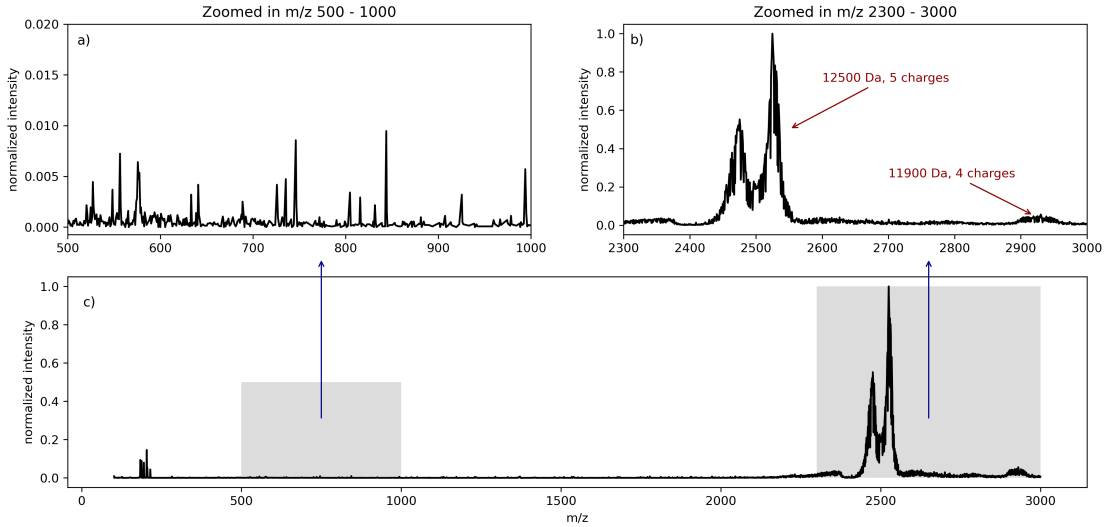

Figure 2.26: Mass spectrum for dry gas flow of 4 L/min at the Bruker amaZon. Two mass ranges are magnified (m/z 500 - 1000) and (m/z 2300 - 3000). In these zoomed in panels the signals above the isolation window are clearly discernible (b), as well as peaks below the isolation window (a), which are not attributed to the analyte and represent smaller charged cluster.

The observed decrease of the TIC was expected. Interesting were the changes in the EIC. The analytes are released more readily from the trapped droplet at 2 L/min, which indicates the isolation of a less stable droplet distribution containing the analyte. This suggests that the dry gas flow is notably affecting the stability of the entering droplets. The same double peak structure as before is isolated in the mass spectra. The increasing dry gas flow shifts the maxima of the described signal structure. Charge loss could be identified as signals at higher m/z next to the isolation window appeared. Another important parameter is the liquid flow of the syringe pump, which was varied in the next experimental series.

2.6.1.3 Liquid flow - thermometer ions

Gomez and Tang identified the liquid flow of the solution to be an important reason for different size distributions of droplets emitted from the ESI tip [22]. The size of charged droplets correlates with the number of charges the droplets can transport, which is limited by the Rayleigh Limit as described in section 1.3 [35]. An increasing liquid flow potentially leads to larger droplets with a higher total number of charges entering the system. It should be noted here that 4-5 µL/min considered a common analytical flow rate for ESI experiment at the ion trap system. The TIC of the isolated droplet ions is shown in Figure 2.27. The change of the liquid flow rate is indicated by grey lines. In contrast to previous measurements, the TIC varies widely over the course of the liquid flow rate and has even much more scatter than seen in earlier experiments (for example in Figure 2.23). It never reaches a plateau in the individual parameter segments, which suggests that an equilibrated state of the observed droplets is not reached. The parameter changes from 5-10 µL/min and from 15-20 µL/min show abrupt drastic decreasing intensity. It is unlikely that these two steps are pure coincidence, they occur directly in accordance with the change of the flow rate, which hints at a vastly different size distribution or transport phenomenon of the charged aggregates and thus a different stability of charged droplets at these flow rates. In the first two parameter segments a slow drift is visible, which is the result of another underlying, yet unknown process.

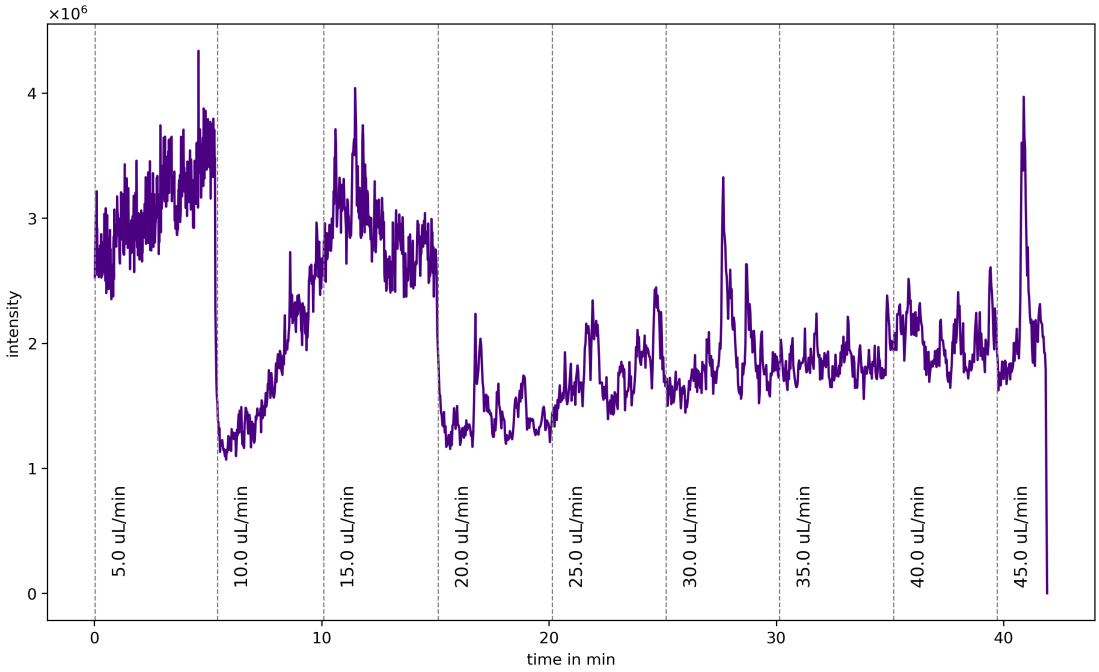

Figure 2.27: TIC of the isolated droplet signal with thermometer ions for the liquid flow rate variation at the Bruker amaZon. Variation of the liquid flow rate is indicated by grey lines. The TIC of the isolated droplet signal is shown in purple. In the first few segments a drift is visible. A higher fluctuation than at previous experiments can be observed.

The chromatogram of the extracted ion count (EIC) of the thermometer ions does not exhibit the same steps as visible in the EIC (Figure 2.28). The thermometer ion signals increase at higher flow rates. At 5 µL/min a similar burst of thermometer ion signal as described above is detected. Another burst is not visible in this experiment. At 10 µL/min the EIC is increasing steeper than at other rate changes. This is in accordance with the change of the TIC in the same parameter segment. The droplets aspirated with this flow rate could be less stable than droplets at different flow rates or they are more charged and thus larger droplets and therefore potentially more analytes are transported into the vacuum system. After 15 µL/min the thermometer ion signal becomes more stable and increases only slightly and evenly throughout the experiment.

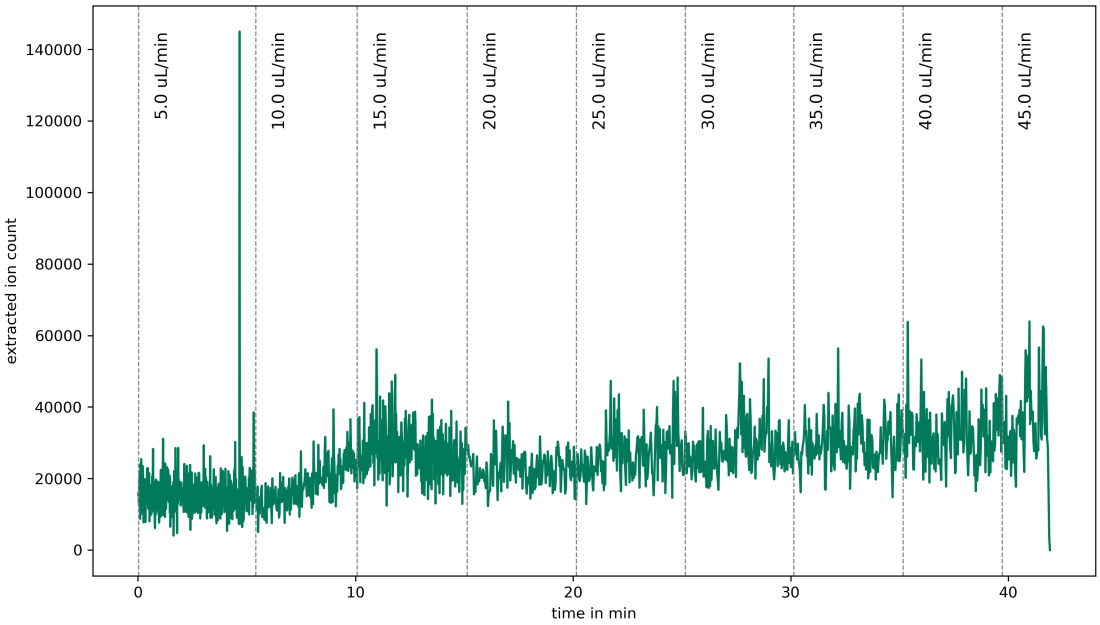

Figure 2.28: Extracted ion count of the mass range of the thermometer ions (m/z 184 – 215) generated from ions in the isolation window m/z 2500 (width 100 Da) for the liquid flow rate variation at the Bruker amaZon. The change of the liquid flow is represented by grey lines. The EIC is shown in green. An increase in signal at 10 µL/min is visible which correlates to the increase of the TIC (cf. Figure 2.27) in the same time segment.

The mass spectra depict the same double peak structure at the isolation window as described above (Figure 2.29). With higher flow rates, the double peak structure seems to get more distorted and the intensity ratio of the peaks changes. As seen before, the surrounding signals above the isolation window get more pronounced relative to the decreasing primary signal, which again indicates a charge loss of the trapped droplets as described above. The details of this presumed charge loss should be investigated in further simulations or experiments.

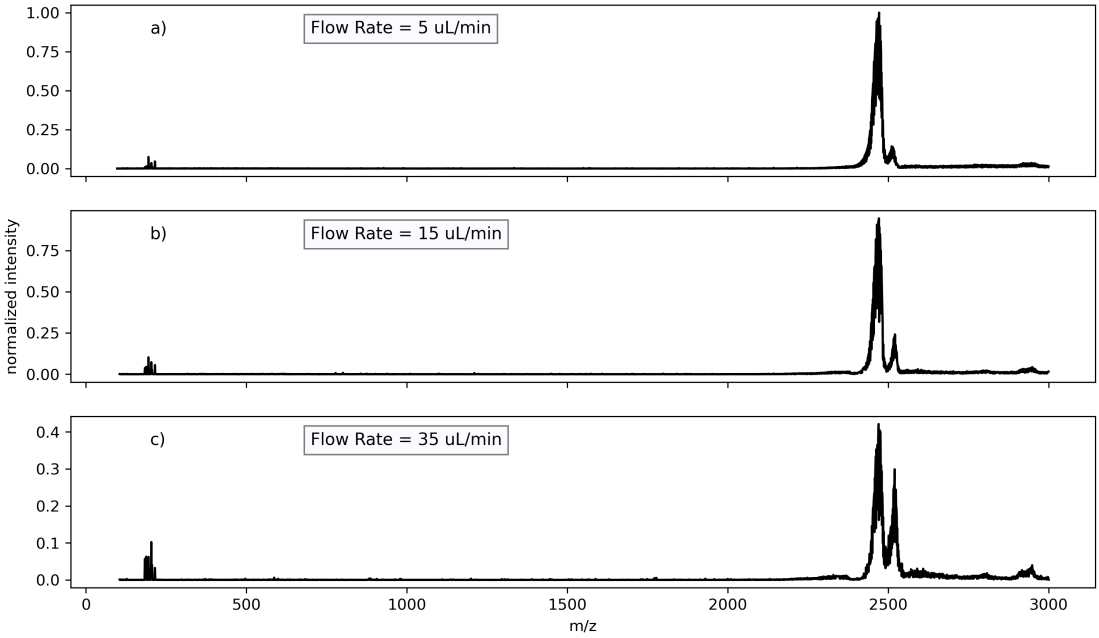

Figure 2.29: Mass spectra for three different liquid flow rate values (5 µL/min, 10 µL/min, 35 µL/min) with initial isolation at m/z 2500 (width 100 Da) at the Bruker amaZon. Thermometer ions were chosen as analyte. A double peak structure is visible in the isolation window. At higher flow rates the intensity decreases and secondary signals outside of the isolation window become much more apparent. Additionally, the ratio of the two double peak structure changes over the variation.

The observed effects are in accordance with the notion that the liquid flow influences the size of aspirated droplets of ESI sprays as described by Gomez and Tang [22]. The size of these droplets correlates with the numbers of charges in the droplets which influences the stability and the transport. In this experiment the TIC changed much stronger with variation of different gas flow parameters than observed before. It does not reach equilibrium in the individual measurement segments, although the liquid flow was not changed for about 5 minutes each. The EIC of the thermometer ions shows that the release of the analytes is slowly changing at 10 µL/min. The reason for this shift is yet unknown. The increase potentially indicates a different droplet stability or a better transport of these aggregates into the system at this flow rate. Additionally, bursts of thermometer ions can be detected at a normal flow rate of 5 µL/min. The corresponding

mass spectra show a shift in the intensity ratio of the double peak structure, charge loss and fragmentation of the isolated ions as signals at higher m/z and in the mass range of the bare analyte ions are apparent. The experiment demonstrates that the aspiration of droplets is influenced by the liquid flow rate of the solution. However, the overall effect is not as pronounced as speculated by the high flow rates. It has to be considered, that all of the flow rates are above the domain of a common ESI experiment without HPLC coupling except the first few segments. In the next experiment the temperature of the dry gas was varied.

2.6.1.4 Temperature variation - thermometer ions

Introduction of heated dry gas or curtain gas is generally assumed to lead to smaller aspirated droplets from the spray or even complete evaporation in the ion source [4]. The temperature of the gas presumably aids to evaporate solvent molecules and desolvate analyte ions in the ion source as collision of background gas particles with the droplets lead to a heat transfer. The following experimental series investigated the effects of the temperature of the dry gas. In this series, the dry gas flow was set to 4 L/min. A common temperature for analytical purposes is considered to be 180 °C. Important to note is that this measurement series has the lowest overall intensity. The detailed cause for that is still unknown. To compensate for the low intensity, the maximum accu time was increased from 200 ms to 600 ms. The TIC of the isolated signal for the temperature variation is shown in Figure 2.30. The changes of the dry gas temperature are indicated by the grey lines. Two steep increments are visible in the chromatogram at 50 °C and 250 °C. These steps hint towards significantly different droplet distributions entering the system at these two temperatures. The intensity is increasing constantly for all the other temperatures, which was also seen in the liquid flow variation. This drift hints towards an unknown mechanism independent of the increasing temperature, which slowly influences the experiment.

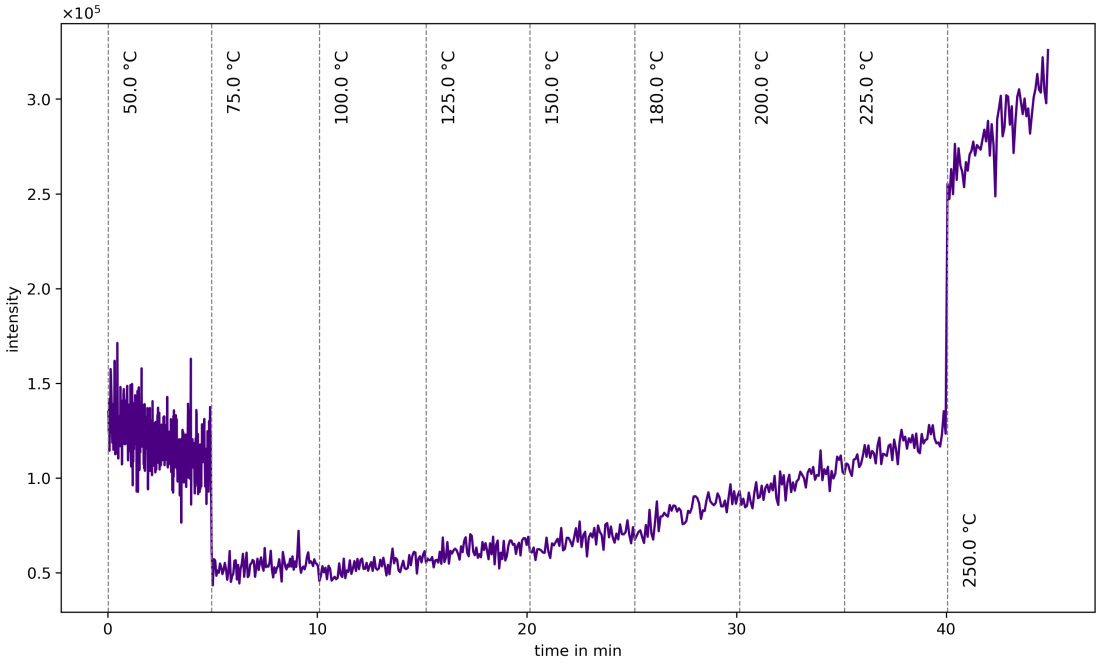

Figure 2.30: TIC of the isolated droplet signal (initial isolation range at m/z 2500 (width 100 Da)) for the dry gas temperature variation at the Bruker amaZon. The different temperatures are indicated by grey lines. The TIC of the isolated signal is shown in purple. The first and last segment (50 °C and 250 °C) have the highest intensity. Over the course of the other temperatures a slow drift can be observed.

The EIC of the thermometer ions indicates that the release of the thermometer ions is at its peak at 180 °C, which is a common temperature used analytically with this instrument (cf. Figure 2.31). The maximum is most likely attributed to the drift mentioned above, which is observable here as well. This again is the result of an underlying mechanism, which is independent from the dry gas temperature. Notably, the steps in the TIC cannot be found in the EIC in this experiment. The two plots are largely de-correlated. Bursts of thermometer ions are observed at low temperature. However, and remarkably, the following mass spectra show a clear change in accordance with the increasing temperature. Additionally, in clear correspondence to the temperature change from 50 °C to 75 °C a drastic change in the signal to noise ratio is visible. After the maximum at around 180 °C the signal of the thermometer ions is decreasing steadily. Surprisingly, the minima of the EIC are at 50 °C and 250 °C, which were also the segments with the

highest TIC. As discussed earlier, the exact position of the relative maxima and minima could be entirely the result of the obviously present drift of the EIC signal.

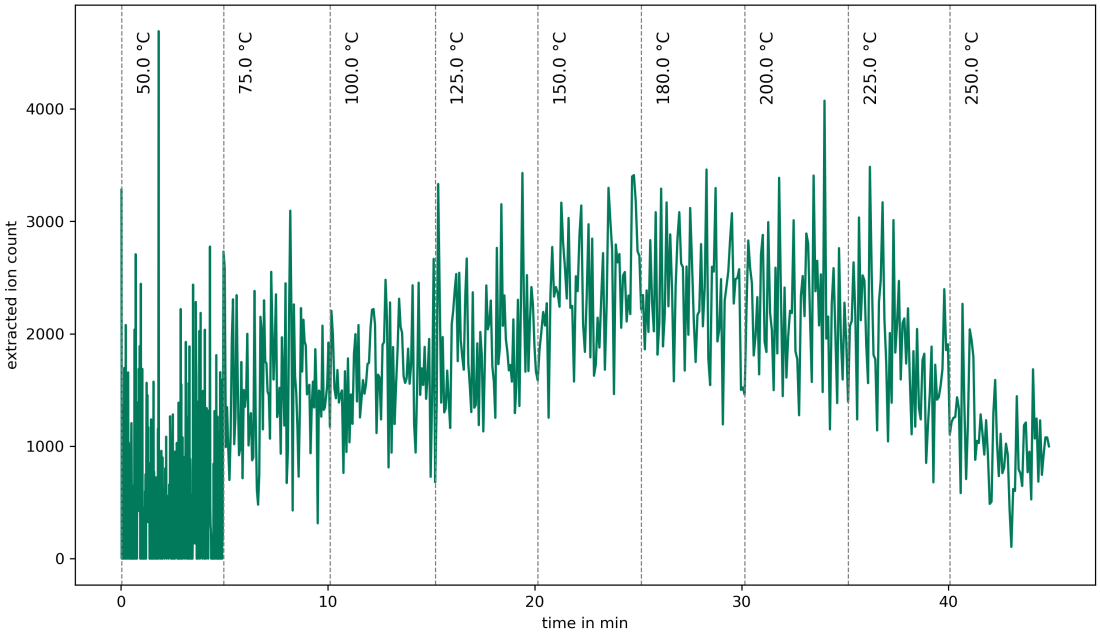

Figure 2.31: Extracted ion count of thermometer ions (m/z 184 – 215) for the dry gas temperature variation at the Bruker amaZon. The temperature variation is indicated by the grey lines. The EIC of the mass range of the thermometer ions is shown in green. The segment with the highest intensity of the analytes is at 180 °C. This is a common temperature chosen for analytical purposes at this machine.

In the related mass spectra, the double peak structure, which was present in all other measurements, is blurred to one broad signal at 50 °C and 250 °C. This is evidence for significant changes in the characteristics of the droplets entering the system. Particularly interesting is the mass spectrum at 250 °C, which has the highest intensity. Even at this high temperature, it was possible to isolate a signal similar to the lower temperatures, which hints at the high heat capacity of the droplets. Numerical modeling with MD simulations, described in the chapter 3, supports the notion of droplets which are able to store comparably large amounts of collisional energy in their internal degrees of freedom. The signal of the bare thermometer ions is highest at 180 °C, which becomes apparent in Figure 2.32 b). A defined double peak structure is occurring in the isolation

window under these conditions, although it looks more distorted than before.

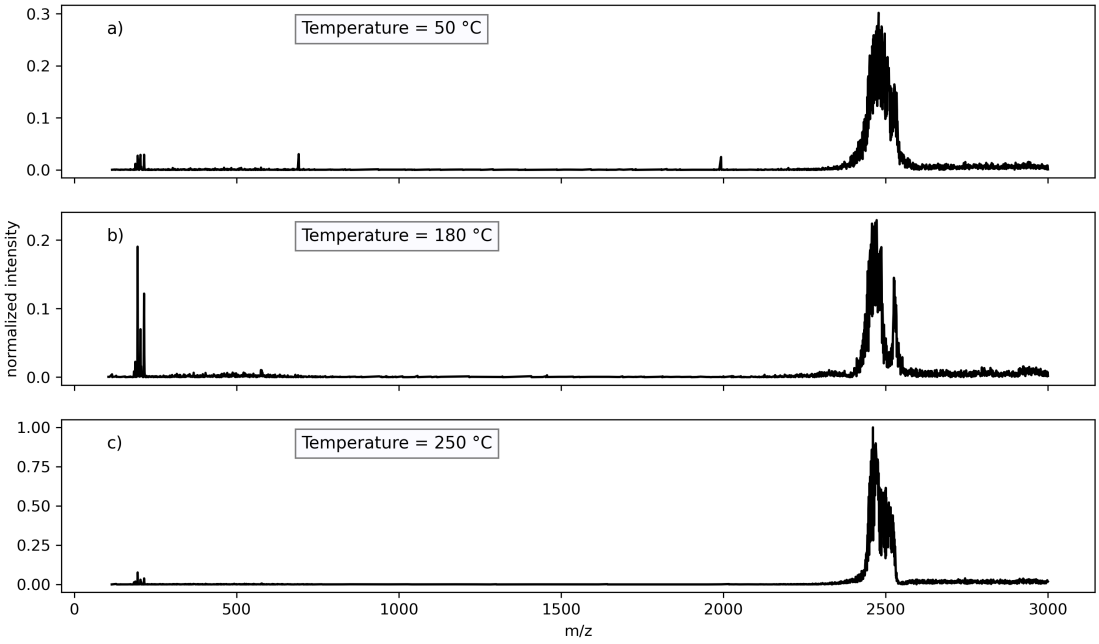

Figure 2.32: Mass spectra for three different dry gas temperatures (50 °C, 180 °C, 250 °C) at the Bruker amaZon. A fully defined double peak structure in the isolation window is only visible in the experiment with 180 °C. At different temperatures, the isolated signal shows a less defined broad behavior. The intensity is highest at 250 °C.

The TIC course of this measurement indicates significant changes in the characteristics of the droplet distributions entering the system at 50 °C and 250 °C. As the signal to noise ratio is changing as well, which is visible in the EIC, the entering droplets are influenced by the dry gas temperature. However, the slow drift, which is observable in the TIC and EIC is seemingly caused by a different mechanism unconditioned by the temperature. In the associated mass spectra, the bare analyte ions are most abundant at 180 °C. Additionally, the distinct double peak structure, which was observed in previous experiments, is only visible at 180 °C. This indicates that the temperature setting is a governing parameter for this phenomenon. The temperature variation concludes the investigation of the ion source parameters. As shown in the initial experiments, the chemical composition of the sprayed solution changes the results of the droplet scan examined in the SCIEX triple quad instrument. For the next experiments the analyte

and the solvents were changed.

2.6.1.5 Nebulizer gas pressure variation - reserpine in acetonitrile

As shown before, the chemical composition of the sprayed solution has a significant influence on the spectra of the SCIEX triple quad instrument (cf. Figure 2.9). To further evaluate this notion in the Bruker amaZon QIT, the analyte was changed to reserpine, which should be present at m/z 609 as protonated molecular ion. The solvent system was kept the same: Water and acetonitrile (1:1) with 0.05 % formic acid. The variation of the nebulizer gas pressure reveals only comparably small influence on the thermometer ion solution as shown in the previous section. In Figure 2.33 the TIC of the isolated droplet signal for the variation of reserpine in acetonitrile is shown. Although the intensity of the TIC is one order of magnitude less compared to the thermometer ions, the decrease of the TIC happens at the same pressure value increments. This indicates towards similar dynamic changes as described for the thermometer ions above.

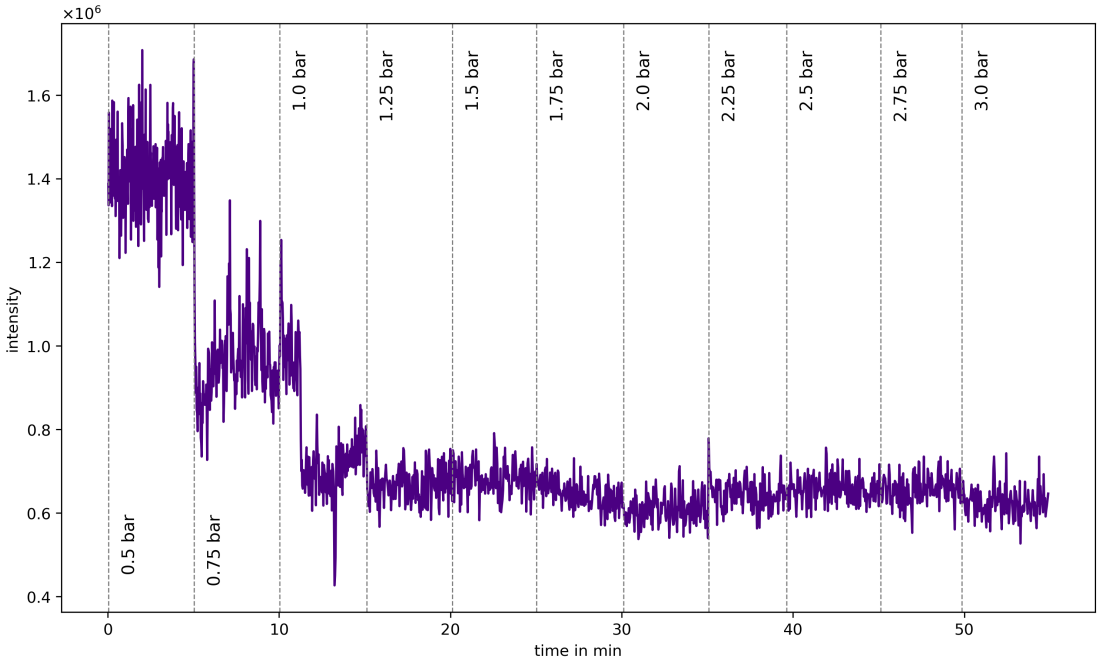

Figure 2.33: TIC for nebulizer gas pressure variation - reserpine in ACN/H2O at the Bruker amaZon. The TIC of the isolated signal is shown in purple. Three clear steps are visible at 0.5 bar, 0.75 bar and 1 bar. The intensity is remaining comparably stable and insensitive to nebulizer gas pressure changes with higher nebulizer gas pressures.

The extracted ion count for the m/z of 609 (cf. Figure 2.34) generated by fragmentation of isolated ions shows an entirely different behavior. The reserpine signal is detected much more scarcely and fluctuates much more than that of the thermometer ions. One reason is that the m/z range of the EIC for the thermometer ion variations was chosen much wider (ranging from the lightest precursor ion with m/z 184 to the heaviest with m/z 215). However, a similar result to the measurements with the SCIEX triple quad system described in section 2.2.3, could be shown here. In the SCIEX instrument all of the transported droplets were fragmented, which showed analyte signal appearing in the spectra. Even at high collision voltages, the reserpine was not as abundant in the mass spectra (cf. Figure 2.9). This speaks for a different transport of reserpine into the mass analyzer region of the instrument, compared to the transport of the smaller thermometer ions. The mass spectra solely contain bursts of signals, which vary in intensity. This indicates a presumably lesser release of the analyte from the trapped droplets, which

implies a more stable droplet system present or a smaller number of droplets containing analyte molecules transported into system. Reserpine is a larger aromatic molecule with different substituents (cf. Figure 2.3), which stabilized the droplet cluster due to inductive effects [61, 62].

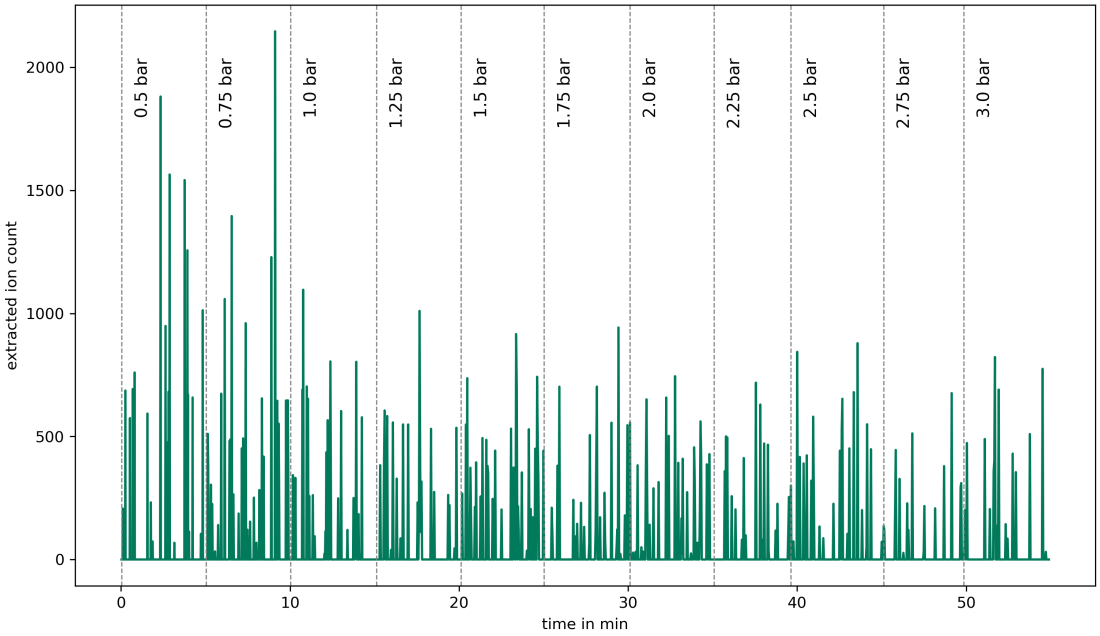

Figure 2.34: Extracted ion count (m/z 609) for nebulizer gas pressure variation for reserpine in acetonitrile / water at the Bruker amaZon. The analyte signal is only observable in very brief but comparably intensive bursts throughout the measurement. The exact cause for this result is still unknown, but the transport of single droplets into the mass analyzer is a potential explanation.

The associated mass spectra show the same phenomenon; reserpine cannot be detected, although the double peak structure from before is clearly visible. The right maximum of the double peak structure shrinks with increasing nebulizer pressure. However, besides that there is no drastic change in the mass spectra visible. In the last spectrum (cf. Figure 2.35 c) the relative intensity of the signals above the isolation window, slightly visible also with 0.5 and 1 bar pressure, increase. The observation of these signals is also evidence for charge loss of the trapped droplets.

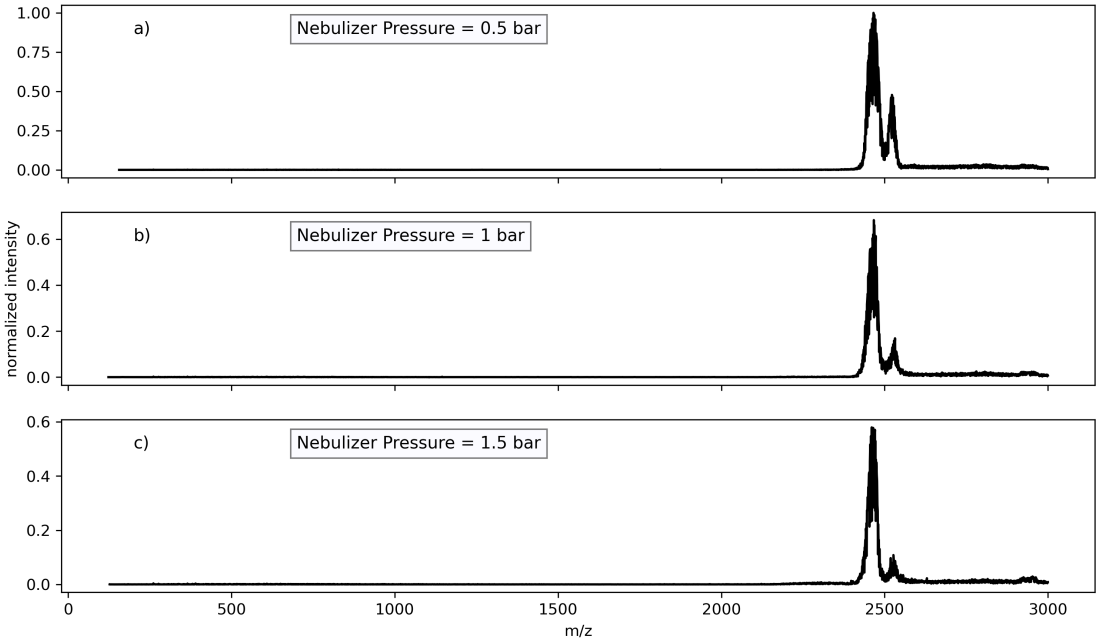

Figure 2.35: Mass spectra of reserpine in acetonitrile / water for three different nebulizer pressure values (0.5 bar, 1 bar, 1.5 bar) at the Bruker amaZon. A double peak structure is visible in the isolation window. The intensity of the right peak of this structure decreases with higher nebulizer pressure.

This experiment demonstrates that the two tested analytes in a similar solvent system does not strongly influence the results of the variation of the nebulizer pressure since the measurement with the thermometer ions shows a similar result as described in section 2.6.1.1. The EIC signal of the reserpine in acetonitrile and water is much scarcer, which indicates a different release mechanism of the analyte or different transport mechanism for the droplets containing reserpine. The associated mass spectra did not show significant changes, which implies that the nebulizer gas pressure does not have a strong impact on the observed dynamics of trapped droplets. This was also the case for thermometer ions as analyte. In the next experiment the solvent system was changed to a more protic solvent.

2.6.1.6 Nebulizer gas pressure variation – reserpine in methanol

To examine the hypothesis, that the solvent composition influences the droplets and their signatures significantly, the solvent system was changed to methanol and water (1:1) with 0.05 % formic acid. Methanol is a protic solvent; it forms hydrogen bonds between its alcohol group and water or the analyte. The analyte concentration was an order of magnitude higher (8 µmol/L) than in the previous experiment. The TIC with a variation of the nebulizer gas pressure for the isolated signal of the reserpine in methanol and water is shown in Figure 2.36. The overall course of the TIC shows a different development as with the acetonitrile / water solvent system before: It increases at 1.5 bar. This indicates differences in the characteristics of the observed droplet distribution. After this increase the TIC drops at 3 bar and stays comparably stable for the remaining experiment. Similar to the previous presented experiments, notable drifts of the signal within the parameter segments are visible. A clear drift in the first segment can be observed. It does stop at the change from 0.5 bar to 1 bar, which indicates a direct influence of the pressure on this underlying mechanism.

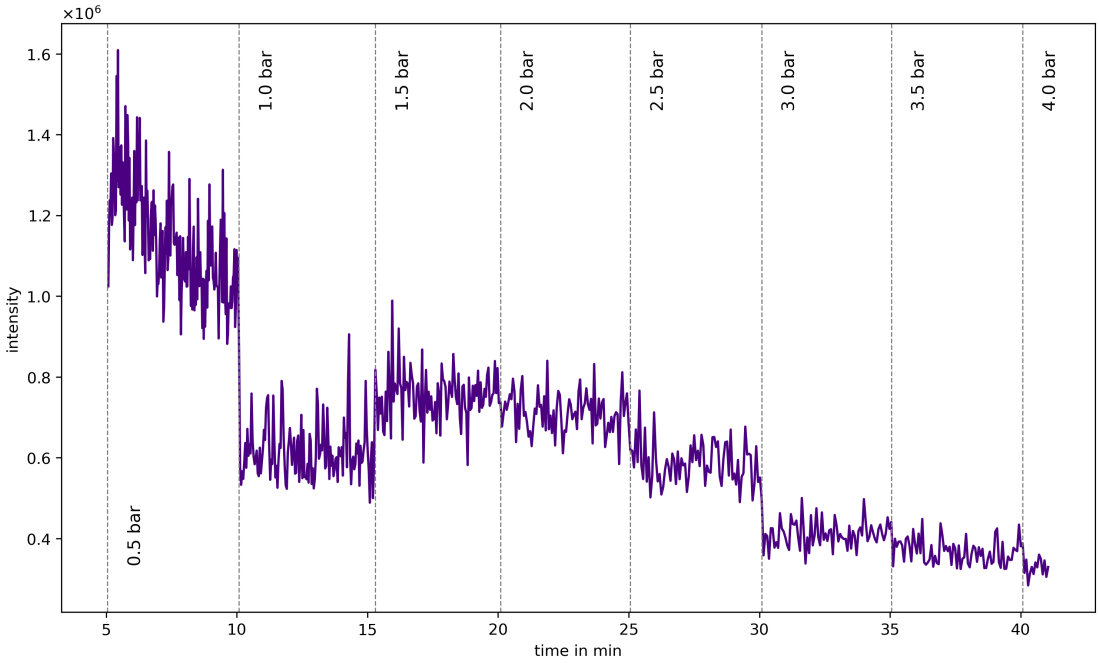

Figure 2.36: TIC for nebulizer gas pressure variation - reserpine in methanol / water at the Bruker amaZon. The TIC of the isolated signal is shown in purple. Different steps are visible in correspondence to changing the nebulizer pressure. A slight increase can be observed at 1.5 bar. A drift in the first segment signifies an underlying mechanism, which is influenced by the change of the nebulizer gas pressure.

The EIC of reserpine (m/z 609) is shown in Figure 2.37. The signals are as sparse as they were with the acetonitrile/water solution. Overall, the observed signal remains scarce for the variation of the nebulizer gas pressure. A few signal bursts with higher intensity are visible at the segment for 2.5 bar, which could be pure coincidence. However, particularly interesting is the detection of the dimer of reserpine. This implies that the dimer is transported within the droplets into the ion trap or (less likely) is forming in the trap. However, the mechanism as to how the dimer is transported or forming is currently not known in detail for these experiments. Dimers or even trimers are a common occurrence for ESI experiments with higher analyte concentration. The discernible signal of the dimer leads to questions about the mechanism in which they form and the chemistry within highly charged droplets.

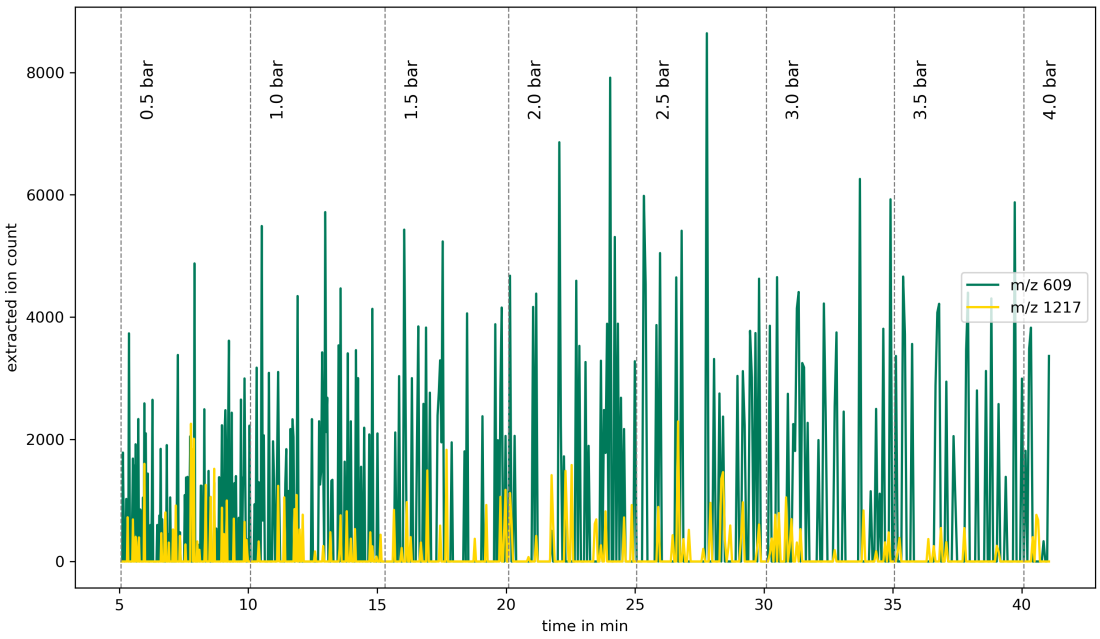

Figure 2.37: Extracted ion count for reserpine and its dimer (m/z 609 and 1217) in methanol /water for the nebulizer gas pressure variation at the Bruker amaZon. The reserpine signal is shown in green; the dimer is indicated in yellow. Both m/z are detected sporadically in this experiment.

The associated mass spectra show a much narrower signal in the isolation window and the double peak structure observed before has vanished (Figure 2.38). In the experiments before, generally two peaks slightly below and above the isolated m/z 2500 were visible. In this experiment the signal in the isolation window is appearing as one peak slightly below m/z 2500; the signal above m/z 2500 is not detected. This indicates that the double peak structure is not only dependent on the temperature; it is also dependent on the solvent. The two peaks of the double peak structure could possibly be a result of a specific charge/mass transition of acetonitrile and water clusters. Methanol and water presumably have significantly different cluster transitions, which could explain the missing peak above m/z 2500. In contrast to the experiment with acetonitrile, the analyte is observable at a pressure of 1 bar and 1.5 bar. The dimer is visible as well. As stated before, this indicates that the dimer of reserpine is transported into the ion trap within the droplet. Comparably strong signals above the isolation window are

visible for all nebulizer pressure values. These signals appear to be much more clearly structured compared to in the experiments before. This further supports the evidence for charge loss of the isolated droplets and of the existing of distinct transition reactions in the fragmentation / evaporation process of the droplets within the ion trap.

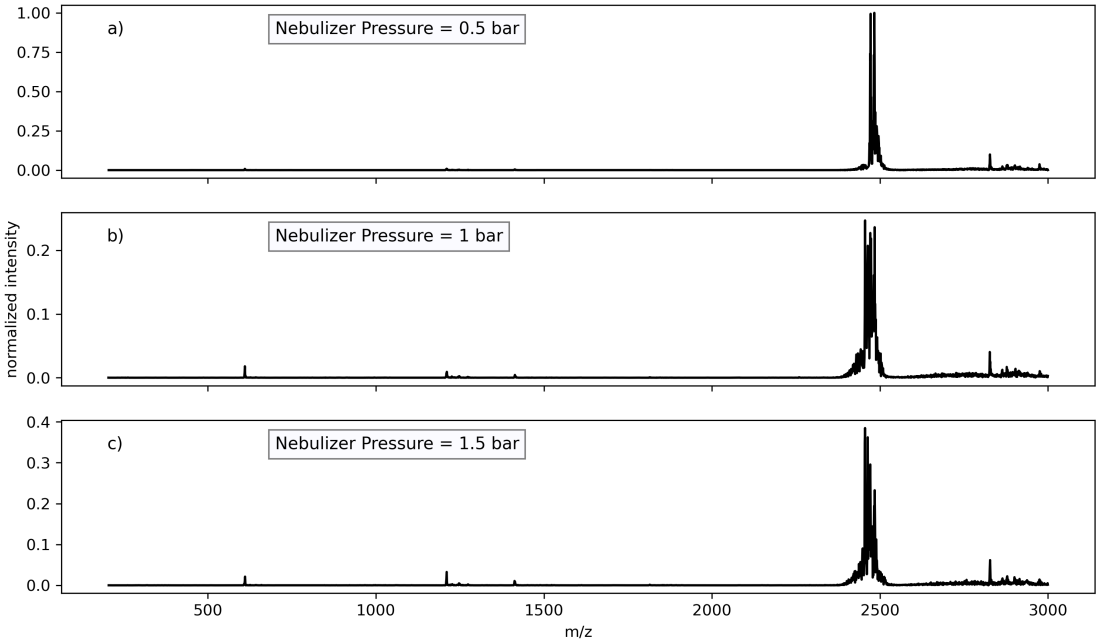

Figure 2.38: Mass spectra for three different nebulizer gas pressures (0.5 bar, 1 bar and 1.5 bar) of reserpine in methanol / water at the Bruker amaZon. A broader signal is visible slightly below the isolation window (m/z 2500 (width 100 Da)). A double peak structure, as was shown in the experiments before, is not detectable. Although, the isolated signal still appears distorted towards low m/z. Comparably clearly structured signals appear above the isolation window, indicating distinct charge loss reactions occurring in the ion trap mass analyzer.

In summary, this experiment investigated a different solvent system. The dependence of the TIC on the nebulizer pressure differs from the measurements discussed above: It shows an increase at 1.5 bar. This suggests towards a significantly different droplet stability with methanol as solvent. Since methanol is a protic solvent in comparison to acetonitrile, this is not surprising. The EIC of this measurement shows a similar sporadic dynamic of the bare reserpine signal as the experimental series above with thermometer ions. However, the dimer of reserpine at m/z 1217 is detected in this

experiment as well. This implies the transport of the dimer through the MS inlet stage into the ion trap within the droplets as already discussed for previous examples. The mass spectra did not show the double peak structure at the isolation window observed before: The mass signals in the isolation window appears as a narrow group of signals. The occurrence of the double peak structure is thus dependent on the solvent system, which indicates a direct linkage to cluster transitions of said systems. The liquid flow rate into the ion source shows a significant influence on the trapped droplet signal for thermometer ions as described in section 2.6.1.3. An investigation of the liquid flow on the reserpine / acetonitrile / water system appears as an obvious subsequent step.

2.6.1.7 Liquid flow - reserpine in acetonitrile

To investigate the effect of the liquid flow rate on the reserpine analyte-solvent system, the measurement described before was repeated with reserpine in acetonitrile and water with 0.05 % formic acid. The overall progression of the TIC with reserpine shows a different behavior than before (cf. Figure 2.33 and Figure 2.39). A strong signal drop in the segment with 5 µL/min is visible. This is most likely due to an external effect as the instrument was started shortly before the measurement. A comparably small step is visible at the change from 10 to 15 µL/min, which was also discernable at the measurement with thermometer ions. After that, the TIC is increasing uniformly for the rest of the experiment. Although a notable drift can be observed over the last few segments, which is most likely due to the high liquid flow that is drastically above the common flow for simple ESI-experiments without HPLC coupling at this system.

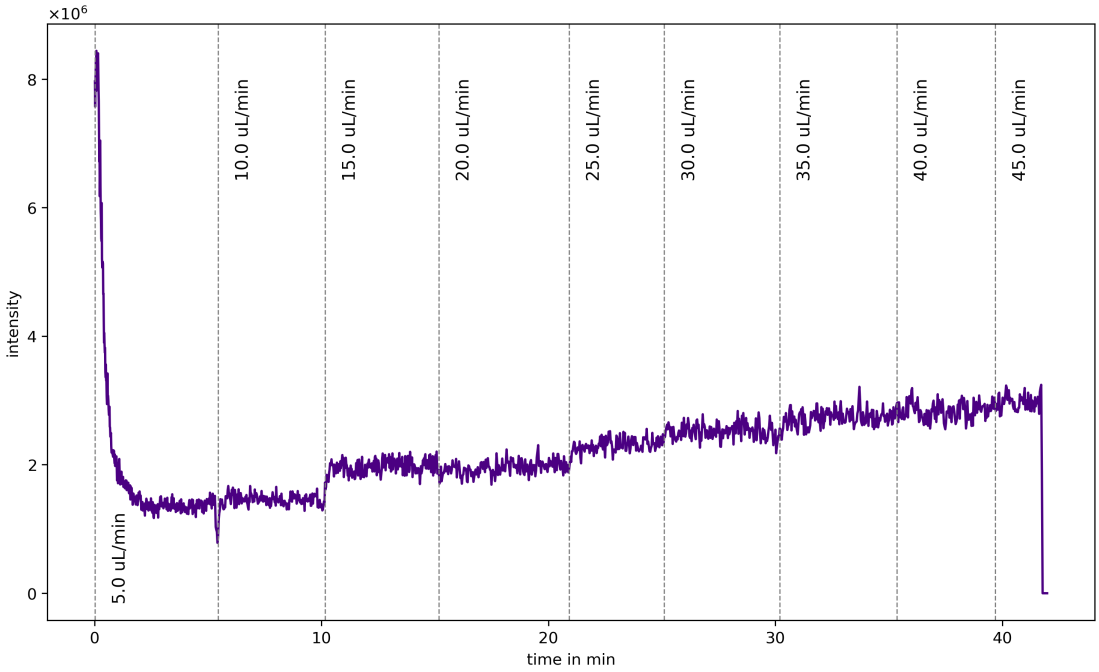

Figure 2.39: TIC for liquid flow rate variation for reserpine in acetonitrile / water at the Bruker amaZon. The TIC for the isolated signal is shown in purple. A steep signal decline can be observed in the first segment. In the last segments a drift is visible.

The extracted ion count (m/z 609) shows (cf. Figure 2.40) the same pattern of sporadic signal occurrence as the other measurements with reserpine. There is not a constant signal detectable but the individual signal bursts have significant intensity. At 5 µL/min, the reserpine signal is the least abundant. A comparably strong individual burst is visible at 40 µL/min.

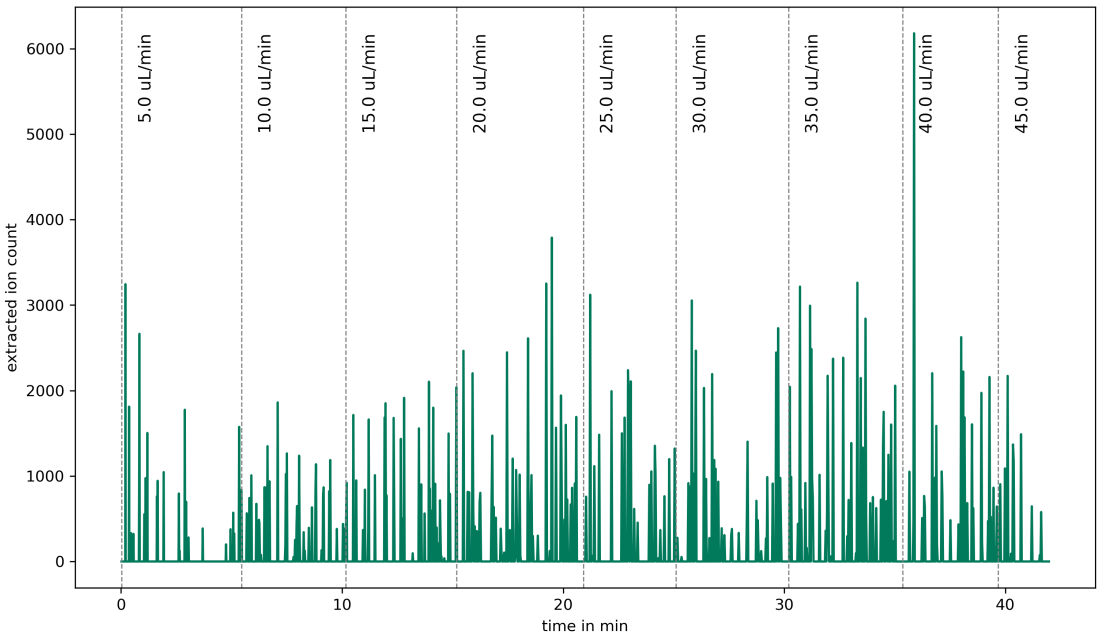

Figure 2.40: Extracted ion count for liquid flow rate variation for reserpine in acetonitrile / water at the Bruker amaZon. The EIC for m/z 609 is shown in green. The analyte, again, appears only sporadically over the course of this variation. In the segment of 40 µL/min a slightly higher intensity can be observed for a short time.

The associated mass spectra show no discernable reserpine signal (Figure 2.41). The double peak structure in the isolation window is visible again. This is strong evidence of influence of the solvent on this phenomenon, since all measurements with acetonitrile and water displays this feature. With increasing liquid flow rate, the right peak of the isolation window becomes slightly narrower. Signals above the isolation window are appearing stronger with higher liquid flow rate, which again implies charge loss of the trapped droplets. Besides that, the mass spectra do not show significant differences for the variation of the liquid flow rate.

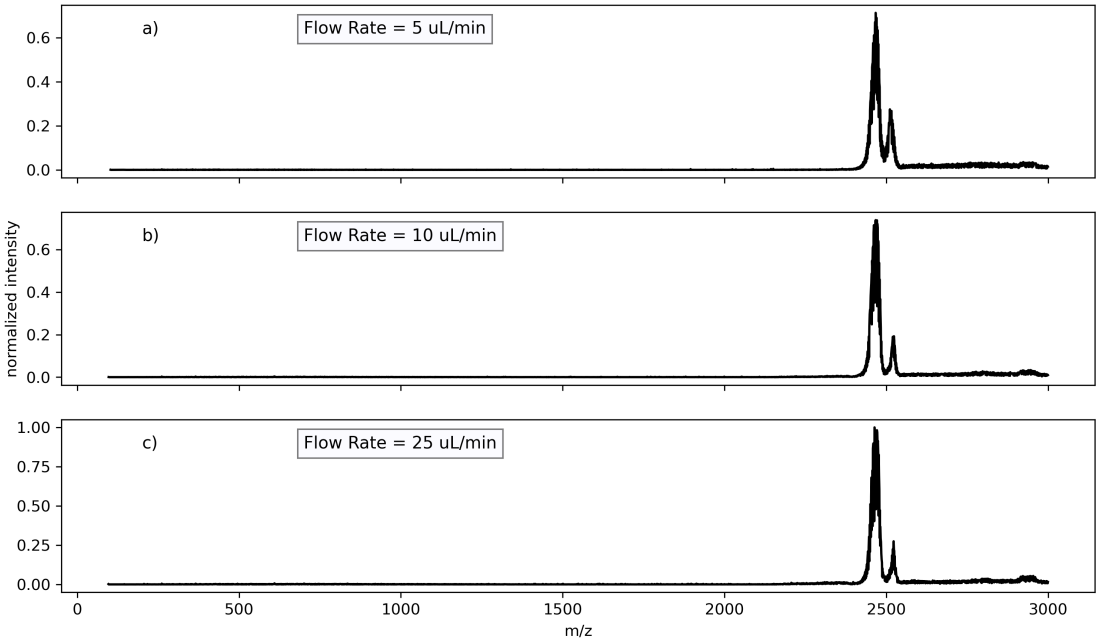

Figure 2.41: Mass spectra for three different liquid flow rates (5 µL/min, 10 µL/min, 25 µL/min) of reserpine in acetonitrile / water at the Bruker amaZon. The double peak structure is discernible again in the isolation window. Signals above the isolation window m/z are also reappearing at high flow rate.

Remarkably, the liquid flow has little influence on the observable results of the experiment with reserpine in acetonitrile and water. The TIC is steadily increasing, showing a long-time drift of the signal, with only a small step at 15 µL/min, which was also present in the measurement with thermometer ions in acetonitrile and water. The steep decrease at the beginning of the experiment is likely a run-in / stabilization effect since the instrument was started shortly before the measurement. The EIC shows a similar basic signal structure as before in the experiments with reserpine. The associated mass spectra show no strong differences for different flow rates, although the same charge loss pattern is presenting itself as signals above the isolation window. In summary, reserpine droplets appear to be more stable than the droplets forming with the thermometer ions or at least not releasing the analyte as much. This is implied by the mass spectra, which did not show reserpine signals as abundantly. The solely measurement in which reserpine was visible in the mass spectra is the experiment with methanol and

water as solvents. In MD simulations discussed in detail in chapter 3, methanol and water are mixed more evenly within the simulated droplet in comparison to acetonitrile and water. The simulation results show that acetonitrile forms a layer around the water droplet. This potentially leads to a layer protecting the inner droplet from direct interaction with the background gas. The subsequent section presents variations of ion source parameters with the SCIEX Triple Quad 6500.

2.6.2 Ion Source Parameters SCIEX Triple Quad 6500

The ion source of the SCIEX triple quad system can be easily detached without shutting down the instrument. The ionization method can also easily be changed from ESI to APCI as only the spraying needle has to be replaced. It became clear in conversations with the manufacturer, that this entails a higher gas flow into the ion source as in the Bruker systems. For the following experiments, the ESI needle was installed, and the ion source parameters (gas flow, liquid flow and gas temperatures) were varied. There are three gas flow parameters for the ion source which can be set in the control software. First, the “GS1” parameter is also called “sheath gas” and has the same purpose as the nebulizer gas in the Bruker systems. It is injected colinearly along the ESI needle and aids in the production of a constant droplet stream from the cone jet-region. The “GS2” parameter controls the gas flow through two high temperature heaters, which are placed in a V-shape in the upper half of the ion source. This is different from the Bruker ion source, which lacks such an additional gas flow into the ion source chamber. The curtain gas or “CUR” parameters has a similar function in the SCIEX triple quad instrument as the dry gas in Bruker instruments: It is directed from the spray shield into the source chamber to reduce neutral species from the spray entering the device and aid the evaporation of droplets. The indicated gas flow rates do not have the same units as in the Bruker system; the gas flows are set in the control software in arbitrary units. The temperature can be controlled by the “TEM” parameter. It has a range of room temperature to 750 °C in ESI spraying mode. The liquid flow is controlled by an integrated syringe pump. The default settings for these parameters are shown in Table 2.3. A schematic overview of the ion source and the names of the parameters in the control software is given in Figure 2.42.

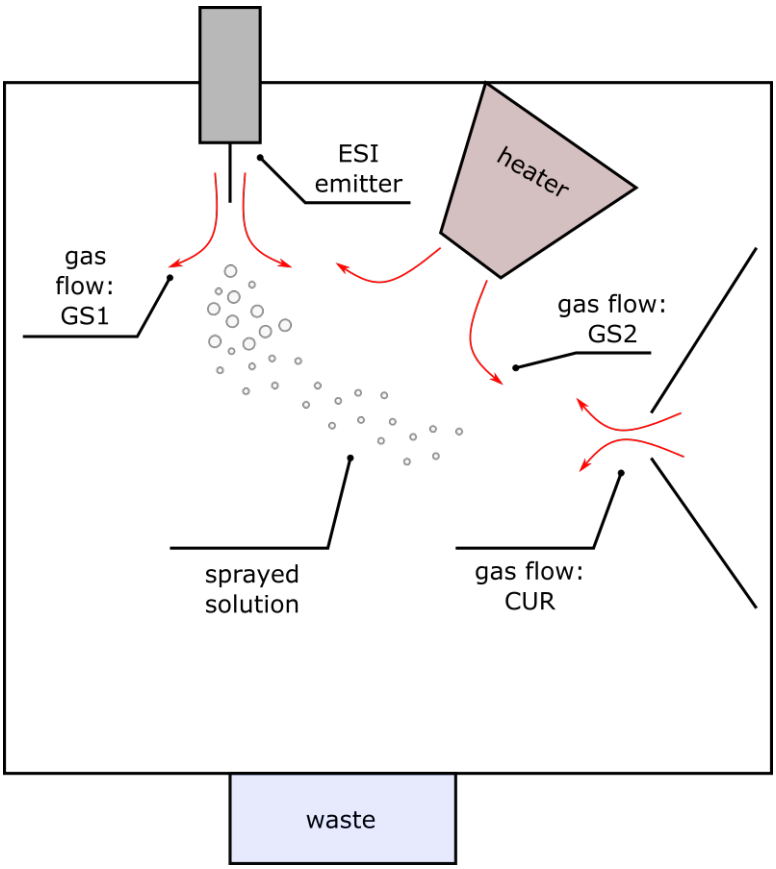

Figure 2.42: Schematic overview of the ion source of the SCIEX Triple Quad 6500. The parameter names are shown in the depiction.

As depicted in Figure 2.5, all of the following measurements were done in droplet scan mode. As described in detail earlier, the first quadrupole (Q1) is set to RF-only mode in this operation mode, which converts this part of the system into a high-pass filter. The second quadrupole (Q2) acts as collision cell as usual, in which the collision gas and voltage are applied. The third quadrupole (Q3) scans the fragments resulting from the fragmentation in the collision cell.

2.6.2.1 Temperature variation

In a first set of experiments the temperature of the gas heaters placed in a V-shape, which is named the “TEM” parameter in the control software, was varied. Four different

settings were investigated: room temperature, 250 °C, 500 °C and 750 °C. Thermometer ions in acetonitrile and water with 0.05 % formic acid was used as sprayed solution. Figure 2.43 shows the TIC against the collision voltages. Every TIC signal, for all individual temperatures, shows two maxima. The first one is constantly at 10 V. The second maximum seems to shift to lower collision voltages with higher temperature. The maxima in the plot represent a point at which the fragmentation of the transferred droplets in the collision cell is stronger which in return produces a higher intensity visible in the TIC. In addition, it is the indicator for a more efficient transport of these aggregates into the machine. If the second maximum is shifted to lower collision voltage, less collision energy is needed to fragment the transported droplets. This is in accordance with the notion that higher temperature leads to higher internal temperature in the droplets, which are thus more readily fragmented. To reinforce this hypothesis the associated mass spectra are shown in Figure 2.44, which compares different collision voltages (10 V and 50 V).

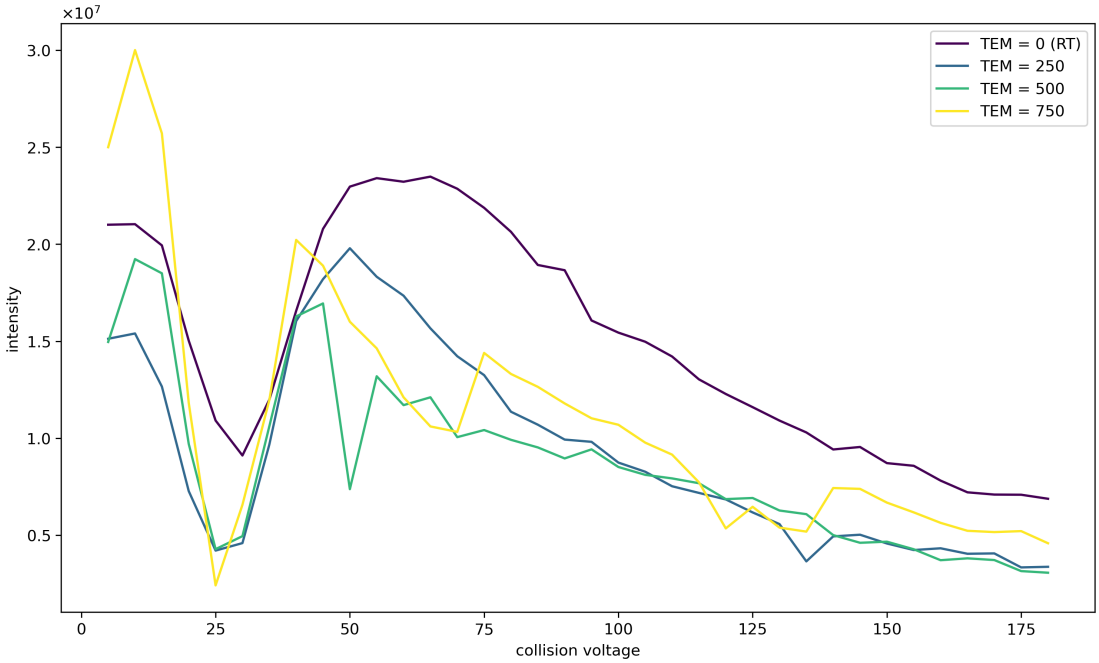

Figure 2.43: TIC against the collision voltage of the measurements of the thermometer ions at different temperatures at the SCIEX triple quad instrument. The different temperatures are indicated by different colors. At room temperature the maximum at higher collision voltage is the highest. For the highest temperature at 750 °C the maximum is visible at around 10 V collision voltage.

If the collision voltage is increased, the fragmentation process of the transmitted charged droplets described before occurs. The fragments of the larger aggregates (with m/z above the LMCO) can now be seen in the spectrum under the LMCO at approximately m/z 1550. With a low collision energy of 10 V, the cutoff becomes sharper with increasing temperature and the fragments of lower masses become scarcer. The analyte signals are only visible at room temperature for both collision voltages, which is surprising considering the TIC signals. The shift of the second maximum in Figure 2.43 therefore does not correspond to an easier fragmentation and higher amounts of fragments in the spectrum. It seems that the droplets are fragmenting less with increasing temperature or that high temperature are connected to less droplets entering the system, either due to transport effects / stronger evaporation in the ion source or due to a reduced droplet generation at the ESI needle. This is in accordance with the

results shown with the Bruker amaZon system, where the analyte was less likely to be released at the highest temperature of 250 °C (cf. Figure 2.32). In the SCIEX instrument, the temperature can be increased even higher, which again underlines the resilience of these aggregates: Charged droplets obviously enter the system, regardless of the applied temperature. The evidence for this is given by the mass spectra. In every mass spectrum a broad structure above the LMCO is visible, which is most likely caused by droplets entering the system. The increasing temperature does only slightly influence the structure above the LMCO.

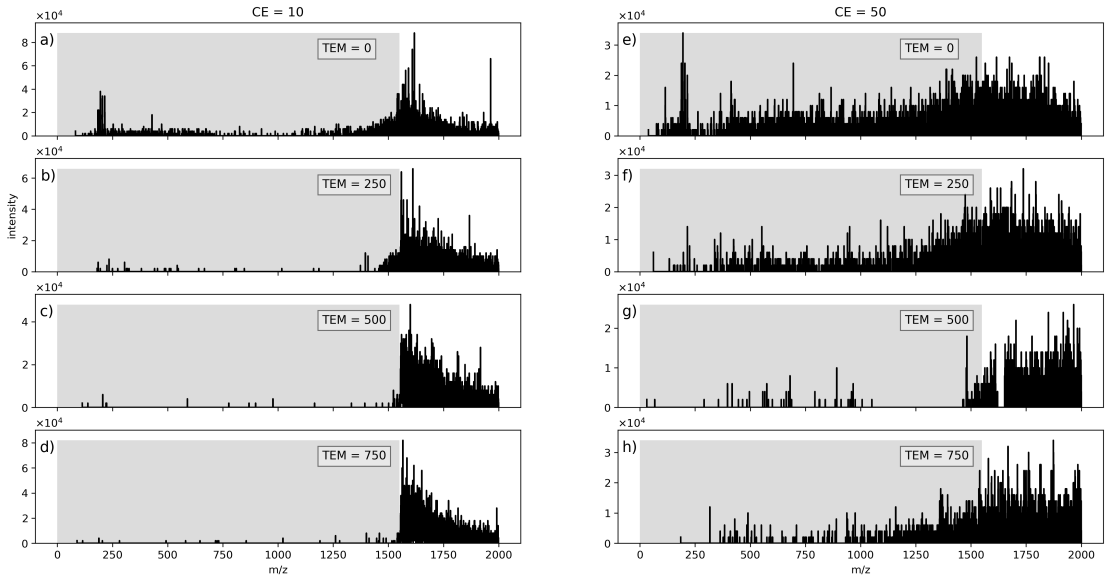

Figure 2.44: Comparison of different temperature settings at different collision voltages at the SCIEX triple quad instrument. On the left side mass spectra at the collision voltage of 10 V are shown with increasing temperature. On the right side the collision voltage is set at 50 V. The measurements done at room temperature show analyte signals as well as a broader structure above the LMCO. With increasing temperature, the analyte signals disappear and only the structure above the LMCO remains.

The comparison of the droplet scan with varied collision energies (CE = 5 V, 80 V, 155 V) described in section 2.2.1, which were performed at room temperature (TEM = 0), to the scan at a higher temperature shows a clear difference between the experiments (Figure 2.45) become apparent. As seen before, the thermometer ions are not as clearly

visible at TEM = 250, even though the collision voltage is increased in the same increments. Overall, there is a strong intensity loss with increasing collision voltage and temperature, which can be deduced from the TIC signal in Figure 2.43. Additionally, the structure above the LMCO is slightly different at room temperature compared to TEM = 250. The cutoff to smaller m/z is sharper (cf. Figure 2.45 a and d), which was also discernible in Figure 2.44. The signal structure above the LMCO (visible in all spectra as intensive signals outside of the grey box), is evidence that droplets are entering the system even at a higher temperature. However, the release mechanism of the analytes seems to change as the analyte signal is less pronounced in the associated mass spectra. This implies a different droplet stability.

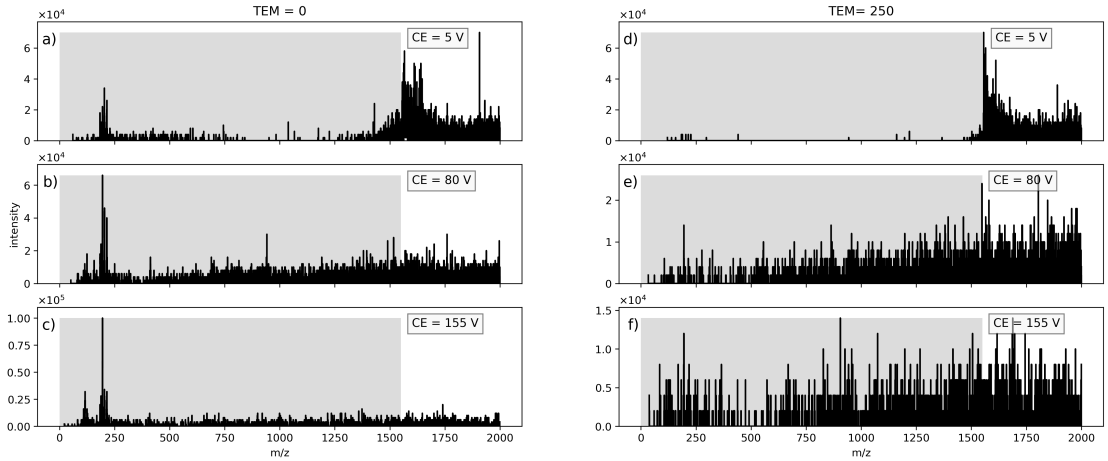

Figure 2.45: Comparison of three different collision voltages at room temperature (TEM = 0, left) and 250 °C (TEM = 250, right) at the SCIEX triple quad instrument. For an easier comparison, the collision voltages were set to the exact same values as in previously droplet scan experiments which are shown in Figure 2.6. The temperature has a clear influence on the droplet fragmentation. The mass spectra at TEM = 250 and a high collision energy have drastically smaller intensity.

The variation of the heater temperature does influence the droplet scan spectra. The second maxima of the intensity signals are drifting to smaller collision voltages with higher temperatures, which implies a different droplet stability. It seems as if the fragmentation pattern is changing with higher temperature, which becomes apparent by the disappearing distinct analyte and fragment signals at lower m/z. Because the in-

tensity loss is so significant (cf. Figure 2.45), the next spectra were acquired at the maxima in the TIC signal. In the subsequent experiments, the gas flow within the ion source was varied to investigate the results in comparison with the Bruker amaZon QIT data.

2.6.2.2 Gas flow variation

In a further series of experiments, the gas flow parameters in the ion source were varied, cf. Figure 2.42 for a schematic of the gas flows into the ion source. The GS2 parameter describes the gas flow from the heater fixtures. The GS1 parameter is comparable with the nebulizer gas pressure of the Bruker amazon QIT as this gas flow is injected from the ESI needle into the ion source. The CUR parameter describes the curtain gas, which is the gas that is applied from the direction of the spray shield to reduce neutral species accompanying the ion stream, comparable to the dry gas in Bruker instruments. Varying the gas flow potentially leads to a different overall different droplet distribution in terms of charge number and size detectable in the device due to different evaporation and fragmentation processes of the droplets. However, in a first set of experiments the variation of the GS2 parameter does not lead to a significant change in the droplet spectra and behavior. A common setting for this gas parameter is GS2 in the range between 0 and 10. The TIC maxima are at the same collision voltages on all settings (cf. Figure 2.46) at 10 V. The overall signal shape is the same except for decreasing intensity. In addition, the shape of the GS 2 = 0 variation indicates an underlying peak between 50 and 75 as a turning point seems to appear in this segment, which is not visible for the other GS2 parameter variations. The differences in the mass spectra at a collision voltage of 65 V are neglectable (cf. Figure 2.47); the same observation applies to the other gas parameters (GS1 and CUR). This is in contrast to the results from the QIT. Here, the gas flow within the ion source did influence the TIC, EIC and spectra.

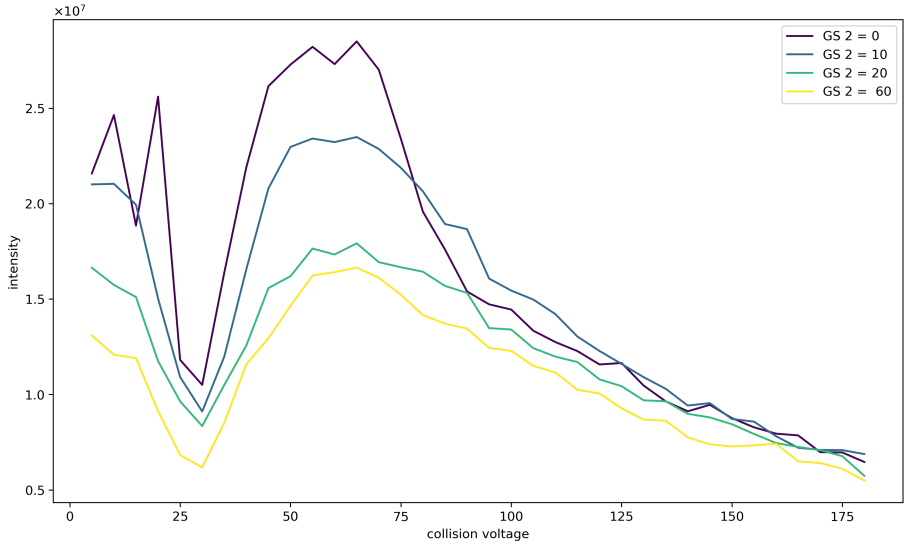

Figure 2.46: TIC of the GS2 variation at the SCIEX triple quad instrument. The different GS2 gas flows are indicated by different colors. Two maxima are visible in every development of the TIC: At a smaller collision voltage (5-10 V) and at around 65 V. The overall intensity is decreasing with higher GS2 flow.

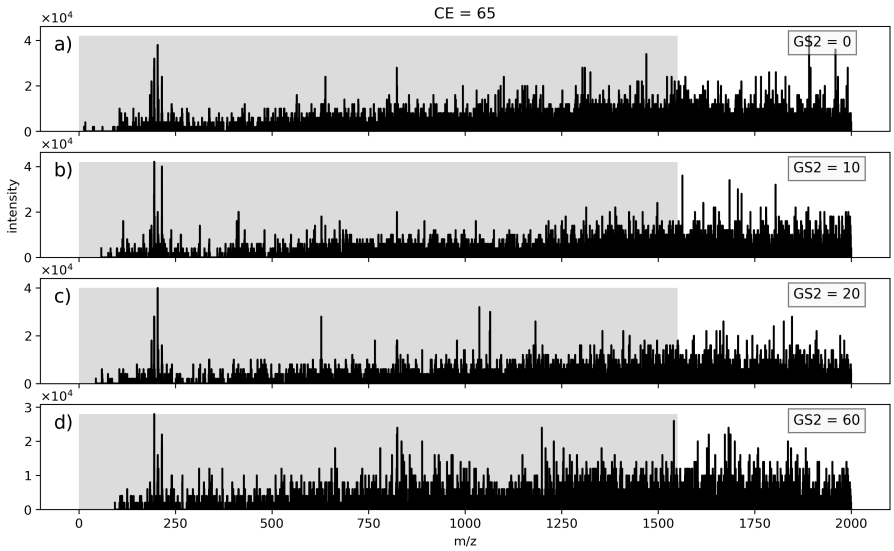

Figure 2.47: Mass spectra at 65 V collision voltage with varying GS2 parameter at the SCIEX triple quad system. GS2 = 10 is the default setting for the instrument. Overall, the mass spectra show no significant changes in their shapes with increasing gas flow in the ion source. Since the experiments were performed at a collision voltage of 65 V, the structure above the LMCO is mostly fragmented and the analyte is clearly visible.

Because the results shown in Figure 2.47 were not consistent with the observation of the influence of the gas flow on the droplets at the QIT, an additional series of investigations was performed: The gas flow (GS2) in the ion source was varied in combination with the temperature. When the collision voltage is small (10 V), the mass spectra for the different temperatures and the GS2 parameter appear to be very similar (Figure 2.48). The bare analyte signals are visible in all spectra. At TEM = 250 the fragments below the LMCO seem to follow a pattern with a minimum at m/z 1000. However, this was not the case for the simple temperature variation (cf. Figure 2.44) as in these spectra no signal was observed below the LMCO. Only at GS = 60 and TEM = 250 (Figure 2.48 f) the analyte signal nearly disappears. This implies that the combination of gas flow and higher temperature impacts the droplet stability in a complex fashion. If the collision voltage is increased, the temperature and the gas flow of the heater have a smaller effect on the mass spectra as visible in Figure 2.44.

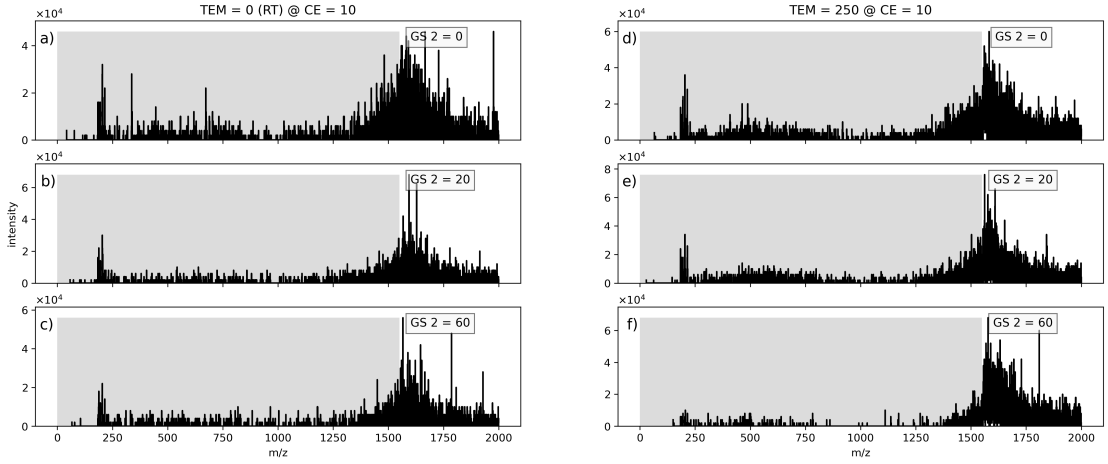

Figure 2.48: Variation of TEM and GS2 at collision voltage 10 V at the SCIEX triple quad instrument. The broad structure above the LMCO is visible in every mass spectrum. In combination the gas flow and the temperature give different results, than in an isolated variation. For higher temperatures mass spectra were mostly empty below the LMCO. Here smaller fragments of the transferred signals above the LMCO are visible.

At TEM = 250 and CE = 65 V (Figure 2.49 d, e, f) the structure above the LMCO is disappearing as was observed before while fragments of the transferred droplets are detectable below the LMCO. Besides that, no strong influence is discernable.

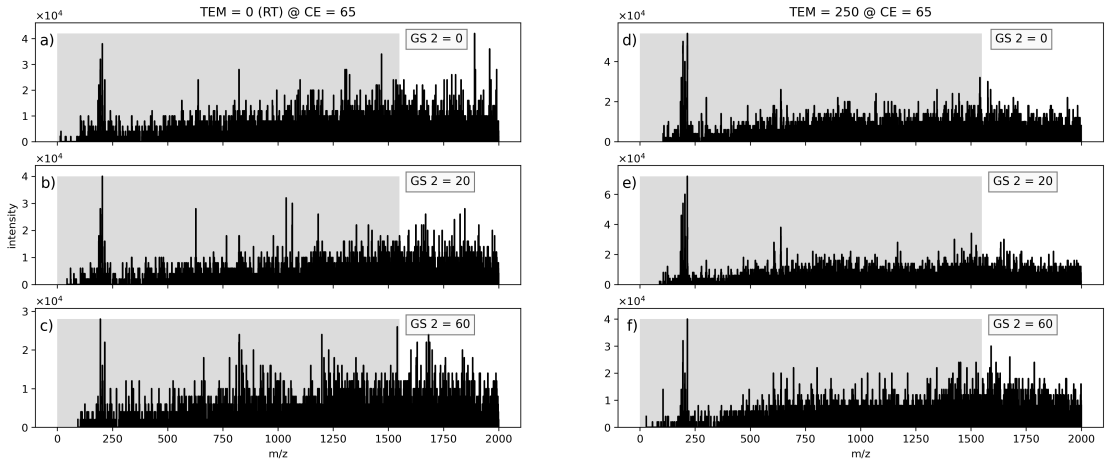

Figure 2.49: Mass spectra of the variation of the TEM and GS2 parameter at collision voltage 65 V at the SCIEX triple quad instrument. The measurement at room temperature and increasing GS2 gas flow is shown on the left side; on the right, the temperature is increased to 250 °C. The broad structure above the LMCO has vanished and the analyte signal is clearly visible. At the higher temperature the ratio of the analyte to fragment is higher and the analyte signal is more clearly pronounced.

The GS2 parameter alone did not strongly influence the spectra as initially expected. Nevertheless, in combination with increasing temperature within the ion source, the bare analyte signal was detectable again, which was not the case for the solely variation of the temperature. The GS2 and temperature parameter are coupled and influence the generation and transport of the droplets. Increasing the hot gas flow leads to different gas circulation and thus temperature distribution in the ion source. At higher collision voltages, the differences between the spectra become less significant. In the next series of experiments, which are presented in Figure 2.50, the influence of the curtain gas was investigated with different temperatures. The overall intensity decreases significantly with increasing curtain gas flow, which is not surprising, as it is applied from the spray shield in counter direction of the ion path. The variation of the curtain gas was limited, as it is coupled to an interlock which detects the incoming gas flow of the instrument. If the gas flow is too high or low, the system shuts down. A common setting for this parameter is in the range of CUR = 15–20. As observable below, the curtain gas flow has no strong visible effect at CE = 10 and room temperature (Figure

2.50 a–c). When the temperature of the V aligned gas heaters is increased to 250 °C the spectra change (Figure 2.50 d–f): The bare analyte signals are more pronounced in comparison to other fragments below the LMCO.

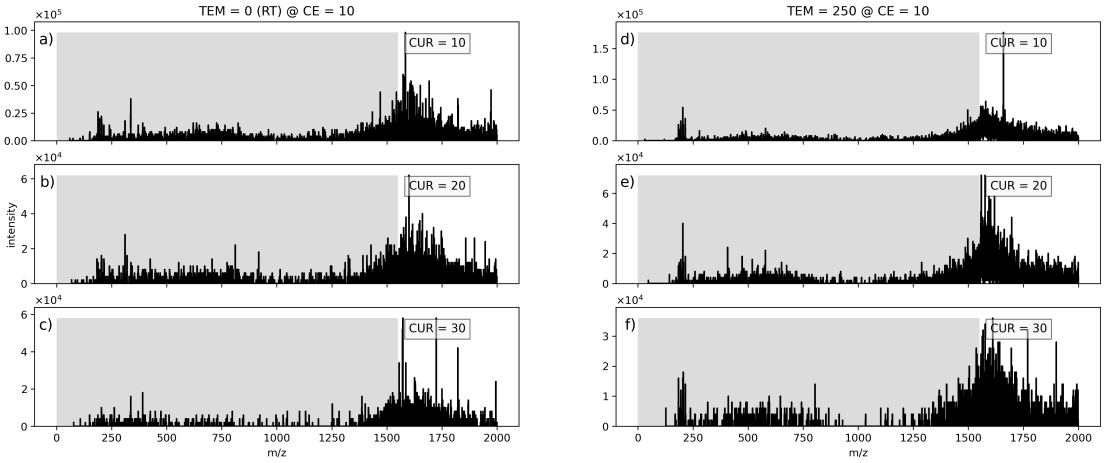

Figure 2.50: Mass spectra for the variation of TEM and CUR at collision voltage of 10 V at the SCIEX triple quad system. On the left side the spectra at room temperature are shown. On the right side the temperature was increased to 250 °C. The analyte signal is more visible at 250 °C in comparison to room temperature.

At a collision voltage of 65 V, the differences between the spectra are more apparent as visible in Figure 2.51. The particles with m/z above the LMCO are again fragmented to smaller m/z. At room temperature (Figure 2.51 a-c) those fragments are more evenly distributed over the m/z range, and the bare analyte signal is not clearly visible. In contrast, the bare analyte signal is discernible in comparison to the other fragments below the LMCO at TEM = 250 (Figure 2.51 d-f). This implies that also the curtain gas significantly influences the transferred droplets and their stability.

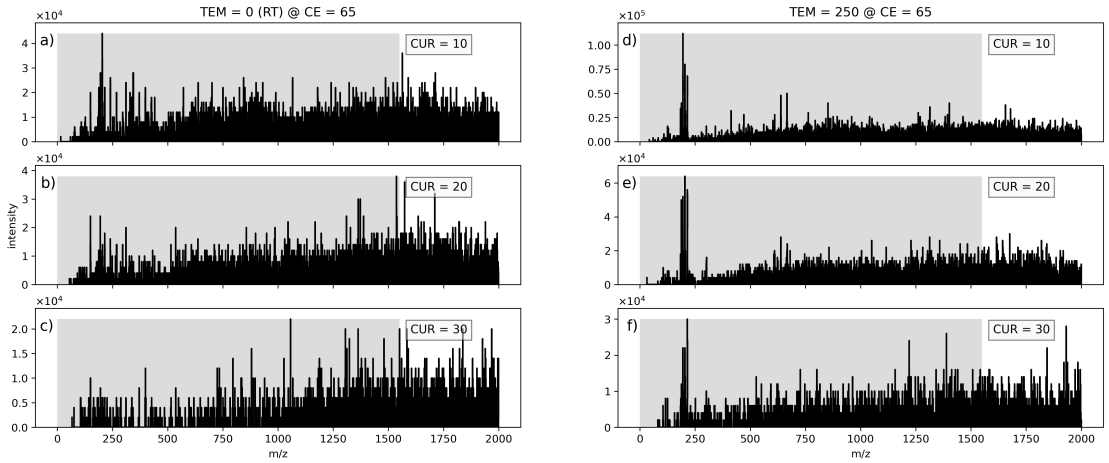

Figure 2.51: Mass spectra for the variation of the TEM and CUR parameter at a collision voltage of 65 V at the SCIEX triple quad system. The spectra for room temperature are shown on the left side. On the right side, the temperature is increased to 250 °C. The analyte signals become much more apparent when the temperature is increased.

As discussed above, the curtain gas flow alone did not strongly influence the results of the droplet scan. Droplets or at least large, charged clusters enter the system regardless of the applied curtain gas flow, indicated by the general occurrence of intensive mass signals above the LMCO. In combination with different “turbo-V" gas heater temperatures the droplets seem to be significantly influenced. However, the differences between the spectra are not as significant at small collision voltages as with increased collision voltage. The analyte signal is clearly detectable only at high gas heater temperatures at 65 V collision voltage. This implies a different fragmentation pattern of the transferred droplets for this temperature in combination with the curtain gas flow. In conclusion, it is apparent that the droplets can enter the SCIEX Triple Quad 6500 despite the applied gas flows. The gas flows at room temperature alone did not visibly influence the droplet signatures. However, the transferred droplets are affected in combination with increased gas temperature. The release mechanism of the analyte from said droplets is probably strongly connected to the droplet stability. This implies, that a higher temperature the interaction with the gas flows is destabilizing the aspirated droplets, as it led to a stronger analyte signal in all cases.

2.6.2.3 Liquid flow variation of the syringe pump

In a last set of experiments, the liquid flow from the syringe pump into the ESI source was varied. The results are shown in Figure 2.52. For a liquid flow of 5 µL/min the overall signal intensity in the mass spectra is comparably very low. The detector is reaching its detection limit and even the quantization of the digital signal recording system is clearly apparent, particularly in Figure 2.52 d). This indicates that the spraying conditions are not optimal with such a low flow and there is no constant stream of droplets entering the machine or that the spray does not produce droplets under these conditions. This changes when the flow is set to 7 µL/min, which is a typical value for the liquid flow at this instrument. The spectrum shows now the same phenomenon as the mass spectra presented for the experimental series above: A signal structure is visible above the LMCO, which breaks apart at higher collision voltages. If the liquid flow is increased further, the associated mass spectrum shows no additional effects, other than a slightly higher intensity. This is in contrast to the Bruker system, where an increasing intensity of bare analyte in the mass spectra and additional changes in the TIC are observable with increasing liquid flow. However, the liquid flow of the Bruker system was varied in higher increments, which was not possible for the SCIEX system due to limitations of the liquid flow parameter in the control software.

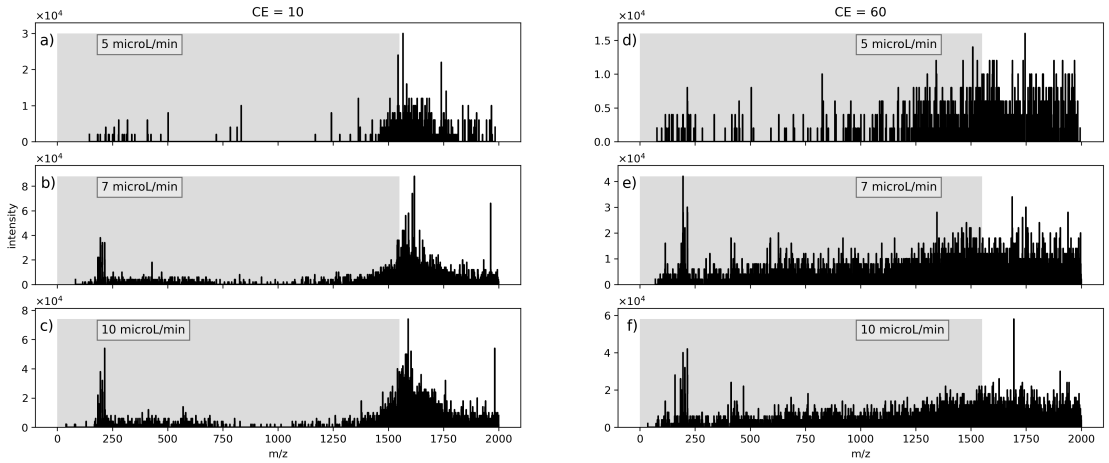

Figure 2.52: Mass spectra for the liquid flow variation from the syringe pump at a collision voltage of 10 and 60 V at the SCIEX triple quad system. At 5 µL/min the detector approaches its detecting limit. The intensity increases in accordance to the liquid flow. The thermometer ions are clearly visible in the spectra for 7 and 10 µL/min.

Due to the less pronounced differences for the droplet signatures, the liquid flow was not further investigated with the SCIEX Triple Quad 6500.

2.6.2.4 Special case: no collision gas

A special case became obvious on this system: The collision gas in the second quadrupole (the collision cell) can be turned off entirely. If this is done, a unique behavior becomes apparent. The TIC and the associated mass spectra are almost identically independent from other varied parameters. The TIC always is at its maximum at about 170 V collision voltage. As an example, the TIC is shown for different temperatures (Figure 2.53). If it is compared to the measurements done with CAD = 6, the differences are obvious: The TIC signal shape in the experimental series presented above always show more than one maximum at collision voltages of around 5-10 V and 50-65 V. These maxima varied slightly for different investigated parameters. However, the TIC signal for CAD = 0 presented in Figure 2.53 shows the same qualitative shape for every temperature. The mechanism behind this observation is not clear and needs more investigation. However, at this point changes in the transfer properties along the ion path through the Tripe Quad instrument in dependence on the collision voltage is

the most probably cause for the similar TIC signal shape.

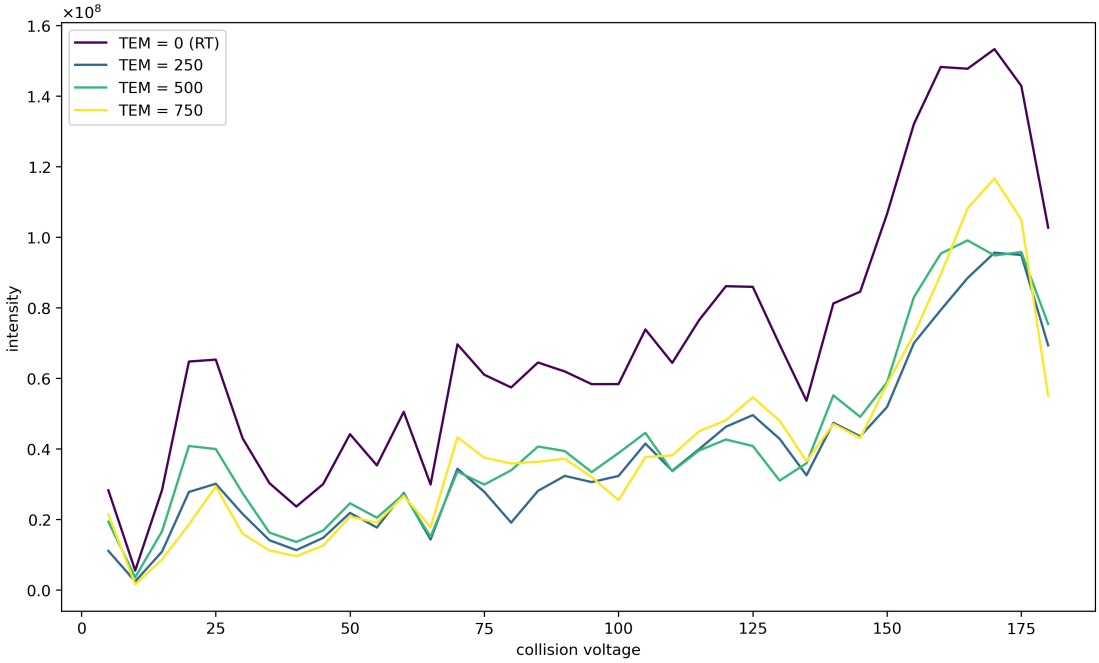

Figure 2.53: TIC for measurement with no CAD gas pressure at the SCIEX triple quad instrument. A variation of the ion source gas heater temperature is indicated by the different colors. The overall shape for the different measurements shows nearly the same maxima. The cause for these results is still unknown.

2.7 Variation of transfer parameter

The parameters of the ion transfer stage between ion source and mass analyzer of the different instruments were kept steady for all the experiments presented so far, but they obviously influence the droplets on their way to the mass analyzer. Therefore, an initial investigation of these parameters was performed.

2.7.1 Transfer stage of the amaZon speed ETD

The transfer stage of the amaZon speed ETD consists of two ion funnels and two multipoles as described on the schematic of the instrument in Figure 2.10. The amplitudes and frequencies of the RF ion guides are variable and controllable in the control software in addition to the trap drive, which is an important transfer parameter, as it controls the low mass cutoff of the transferred ions. The ions gated into the ion trap itself are trapped in the quadrupolar RF-field with a low basic amplitude, which is called trap drive in the control software of the Bruker QIT. For the droplet experiments, the analysis of a certain mass range is important. To select the best possible transfer parameters for a given mass range, the software offers a so called “smart-mode” as explained in section 2.6.1. The transfer parameters, e.g., trap drive, voltages, and RF on the funnel, are automatically optimized for the given mass in this mode. The influence of these parameters on analytes was investigated in detail by M. Thinius [63].

2.7.1.1 Isolation window variation for thermometer ions

The previous chapters show the results for choosing an isolation window at m/z 2500. This m/z was chosen based on preliminary test measurements which showed significant signal intensity in this range. To further investigate the occurrence of droplet signatures, the isolation window was varied. The goal for these measurements was to detect a maximum of the average ion signal in the mass range of the QIT, which ranges from m/z 200 – 6000 in Extended-Mass-Range-Mode. The information gained with this experiment potentially give a first indication to the size of the droplets entering the system. The experiments on the QIT presented in the sections above were done in the Xtreme-Scan-Mode, which only ranges to m/z 3000. The transfer parameters were optimized in smart mode as explained above for every isolation window, which leads,

for example, to different RFs amplitudes on the funnels and a different trap drive for every segment. To show this change of transfer parameters for the first experiment with thermometer ions the changing trap drive is shown in grey beneath the different m/z of the isolation window (cf. Figure 2.54). At first, a solution of thermometer ions in acetonitrile and water with 0.05 % formic acid was sprayed. Figure 2.54 shows the TIC in the individual isolation windows reaching from m/z 1500 to 6000. The TIC is decreasing almost evenly, only two distinct steps at an isolation window of m/z 2500 and m/z 5000 are visible. The ICC (ion charge control) was turned on, which induces the different noise-level on the signals in the different segments, because the intensities measured with ICC are scaled by a factor according to the accumulation time. The isolation width is changing for every isolation window setting, as it was always set to the highest width possible in the control software. At an isolation window of m/z 1500 the width is 60 Da. It increases at every window by 20 Da and reaches its maximum at the isolation window of m/z 6000 with a width of 240 Da.

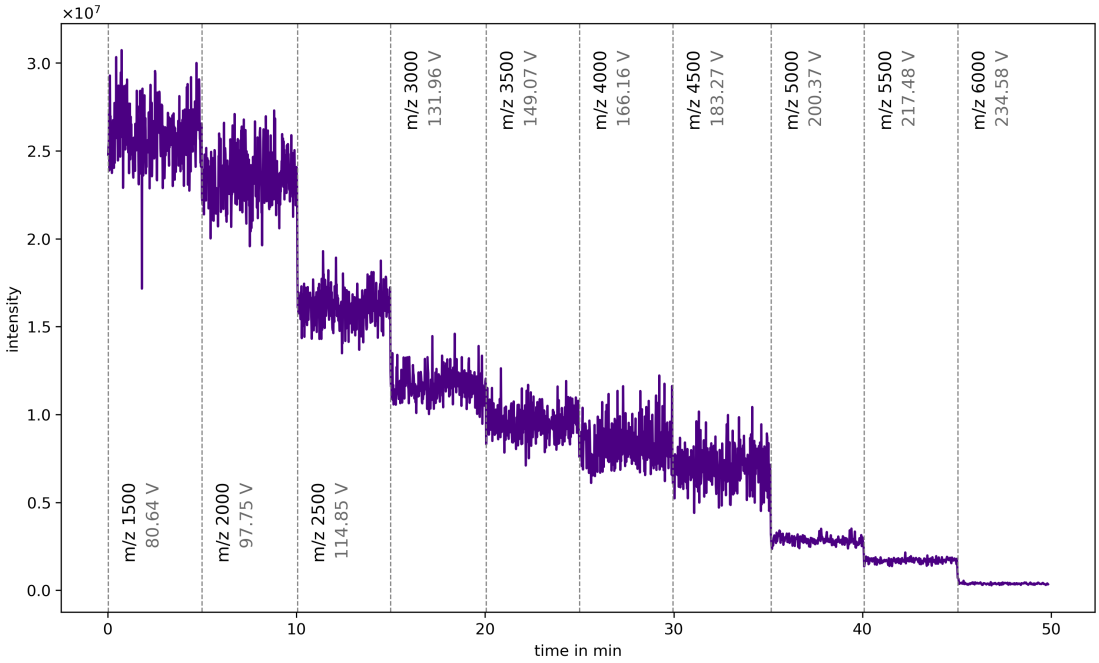

Figure 2.54: TIC of isolation window variation for the thermometer ions in acetonitrile at the Bruker amaZon. In grey the changing trap drive voltage is shown to represent the variation of transfer parameters with each isolation window. The width of the isolation window is changing (from 60 – 240 Da).

The averaged mass spectra for the individual isolation windows are shown in Figure 2.55. All the spectra show a clearly formed peak at the isolated m/z window. At m/z 2500 the same double peak structure as observed in the experimental series before appears again, which is another clue for the specific cluster transition of acetonitrile and water at this m/z. Interestingly, for smaller isolated masses, especially at m/z 1500 and 2000, a broad signal structure above the isolation window is visible (Figure 2.55 a-d). It reaches from m/z 2000 – 4500. As the trap is emptied in this m/z range after isolating the ions in the specified isolation window, the signals are forming from particles in the initial isolation window. The broad appearance of this signal implies that droplets size transitions happen continuously. The transition of different sizes could be instigated by clusters or charges leaving the droplets perpetually. Take up of clusters into charged droplets also contribute to this broad signal, but it is unknown currently how likely this process is. The signals above the isolated masses become more structured

at the isolation window of m/z 3500. This is also observable in the Xtreme-Scan-Mode measurements before (cf. Figure 2.25). There as well here, distinct charge loss reactions probably lead to the specific pattern observable in the mass spectra.

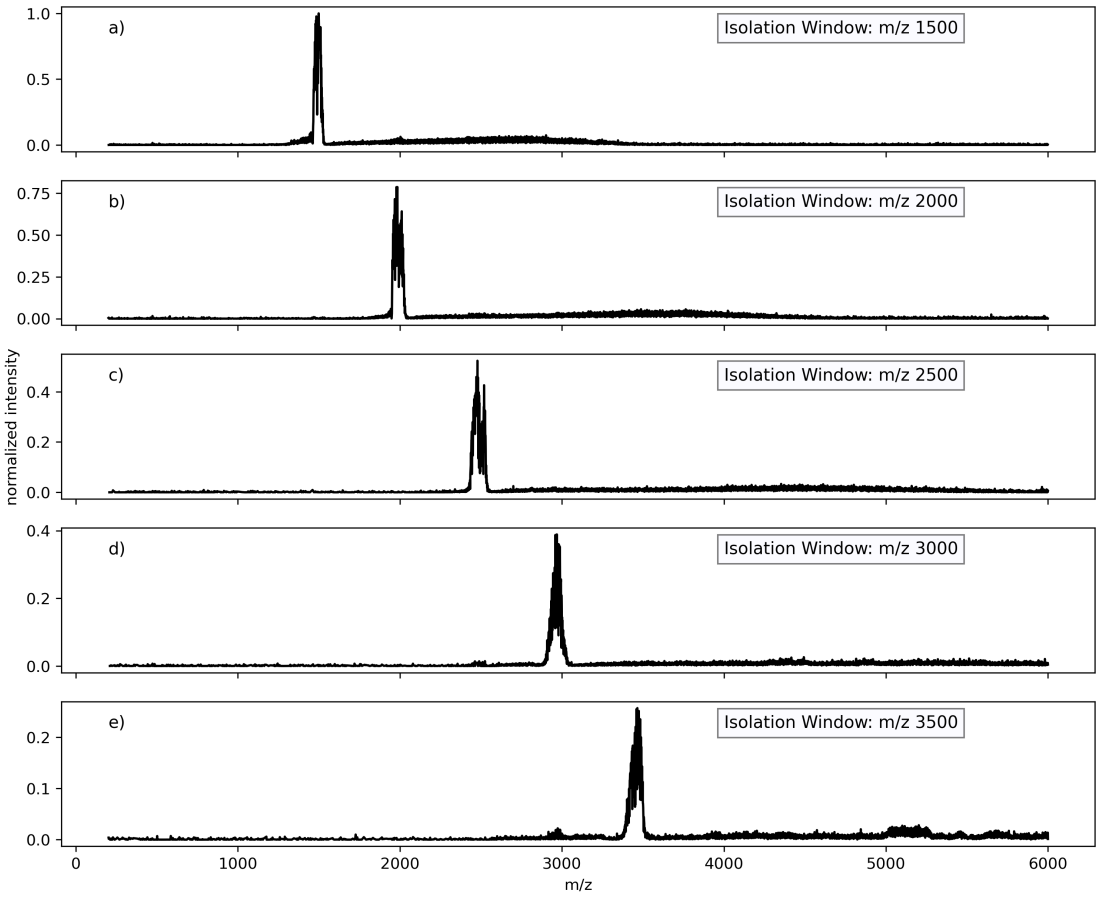

Figure 2.55: Mass spectra for different isolation windows m/z 1500 – 3500 at the Bruker amaZon. At every isolation window a broader signal distribution above the isolation window can be observed. At the isolation window of m/z 2500 the already observed double peak structure is visible. For the isolated mass range of m/z 3500 distinct signals above the isolation window are appearing.

At higher isolation windows (Figure 2.56) a wider range of more pronounced structures are appearing in the mass spectra. This is most notably for the isolation window of m/z 4500 and higher (Figure 2.56 g-i). Pronounced signal peaks form also below of the

isolated mass range in those scans. These structures appear again probably due to specific cluster or charge transitions, which are so abundant, that defined peaks are visible in the mass spectra. The underlying mechanism and numbers can in principle be modelled with specialized Monte Carlo simulations. Here, a statistical analysis of the simulated fragmentation process or the loss of charges can give more insight about the composition of the droplets observed in the experiments.

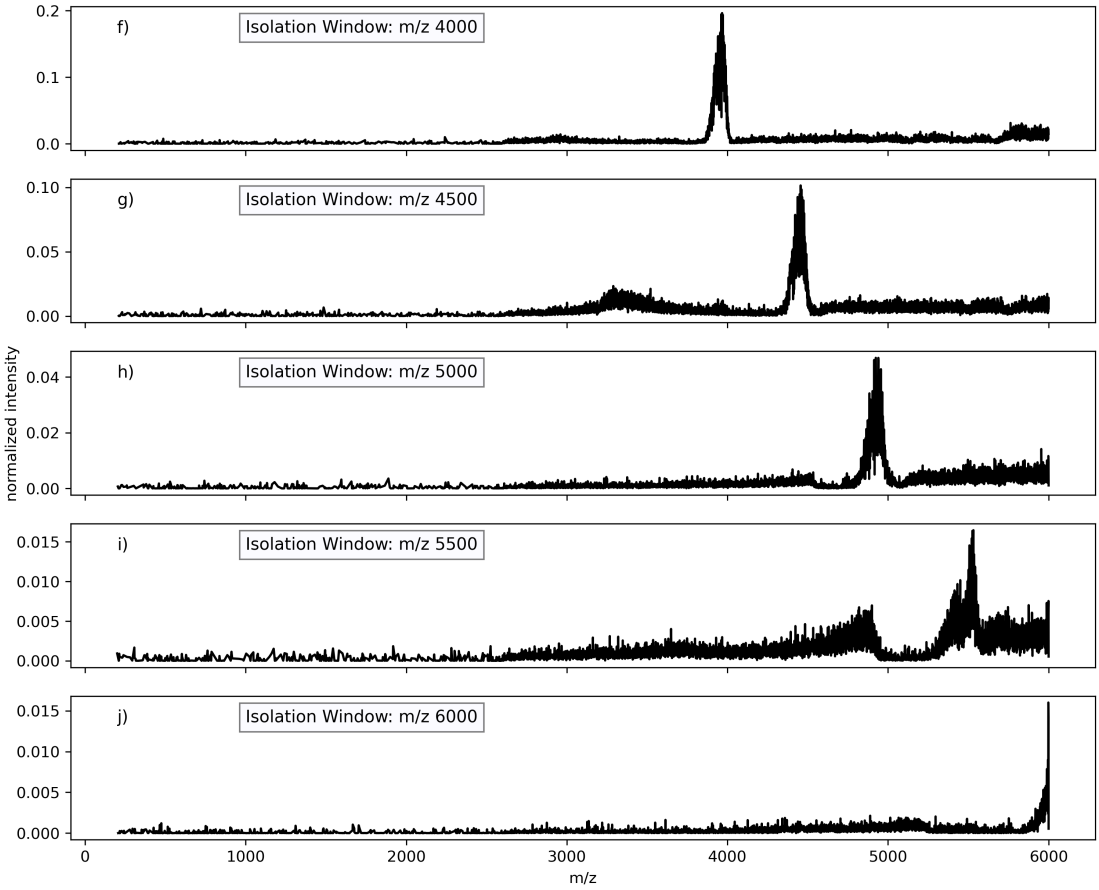

Figure 2.56: Mass spectra for isolation windows m/z 4000 – 6000 at the Bruker amaZon. With every isolation window a broad signal structure above and below the isolation window could be isolated, except for m/z 6000. This is due to the mass range limit of the machine.

To get a better comparison between the intensities, all mass spectra resulting from the individual isolation windows are plotted together in Figure 2.57. The signals with an

isolation window of m/z 5000 – 6000 (light green and yellow) are disappearing in the broad signal in the mass spectrum with an isolation window of m/z 1500 (dark purple). This underlines the high intensity of the signals in the mass spectra with low isolation windows.

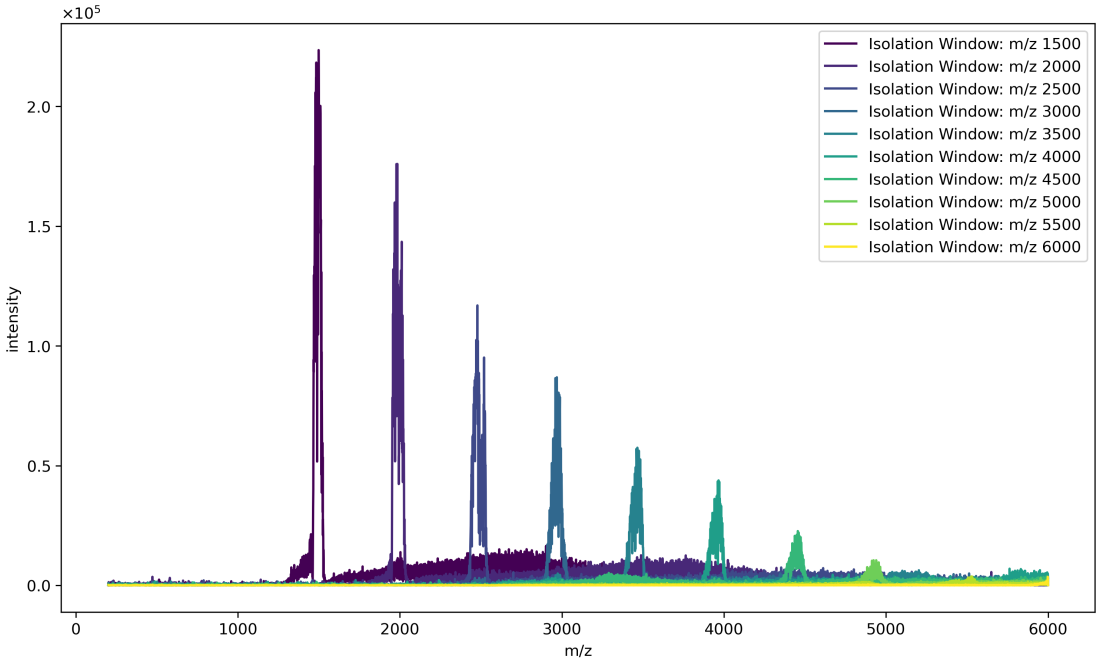

Figure 2.57: Overview spectrum of different isolation windows - thermometer ions at the Bruker amaZon. The different isolation windows are represented in different colors. The intensity loss at higher isolation windows becomes apparent in this plot.

2.7.1.2 Isolation window variation for reserpine

The same experiment was repeated for reserpine in different solvents. The TIC with variated isolation windows for reserpine in isopropanol and water with formic acid is shown in Figure 2.58. Again, the width of the isolation windows is ranging from 60 – 240 Da for every isolated mass range, as the maximum of this parameter for the individual isolation window position was set in the control software. The difference to the thermometer ion result is clearly visible: The TIC is drastically changing at different isolation windows and is not evenly decreasing as shown before. The TIC even increases

until it reaches a second maximum at m/z 4500 and drops after m/z 5500. The associated mass spectra potentially lead to more insight about the reasons behind this maximum.

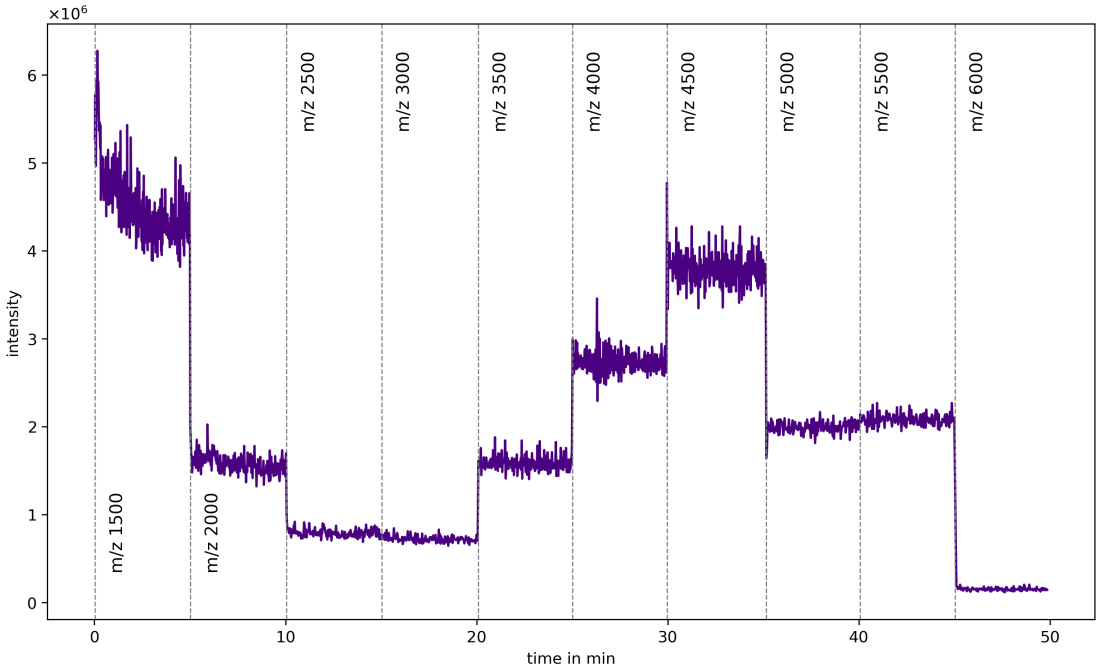

Figure 2.58: TIC of isolation window variation - reserpine in isopropanol at the Bruker amaZon. In contrast to the experiments with thermometer ions, a second maximum at m/z 4500 is discernible for this variation.

As seen before, a distinct droplet signature is discernible at every isolation window. In the mass spectra for an isolation window of m/z 1500, a broad continuous signal above the isolation window is visible again (Figure 2.59 a). At an isolation window of m/z 2500 a defined second peak structure below the isolation window can be observed. A cluster transition occurring after isolating the droplets appears to be particularly abundant at around m/z 2000 in the spectrum. Additionally, signals above the isolation window are discernible. The reason for this phenomenon is probably again the perpetual loss of charges. The increase in TIC, which could be seen in the figure above, is not as apparent in the mass spectra due to the wide mass signals in the spectra. However, in the spectrum at m/z 4500 particularly, additional signals below and above the isolation

window appear which have a particularly broad shape. The mass spectra are normalized to the maximum signal intensity in the whole spectrum series, which can be found in the first spectrum at an isolation m/z 1500. As the highest peak at the isolation of m/z 4500 is only 10 % as high, the increase in total ion current in Figure 2.58 reflects the obvious occurrence of very wide ion signals with medium peak intensity. The different peak structures are assumed to be the result of certain cluster size transitions, which is explained above in Figure 2.26. In the experiments above reserpine was not as easily released from the droplets, which implies a higher average droplet stability when reserpine is sprayed. Again, bare reserpine is not observed in the mass spectra, even at higher isolation windows. If reserpine exhibits a stronger attractive force with the solvent system due to its bigger aromatic structure, a different fragmentation process of the droplets is induced, which could be the reason for the high abundance of additional peaks at m/z 4500. It also could be the case, that reserpine is not transported in the droplets and the reason for the signals in the mass spectra are protonated solvent molecules. At the moment, the transport of reserpine in the droplets can only be assumed.

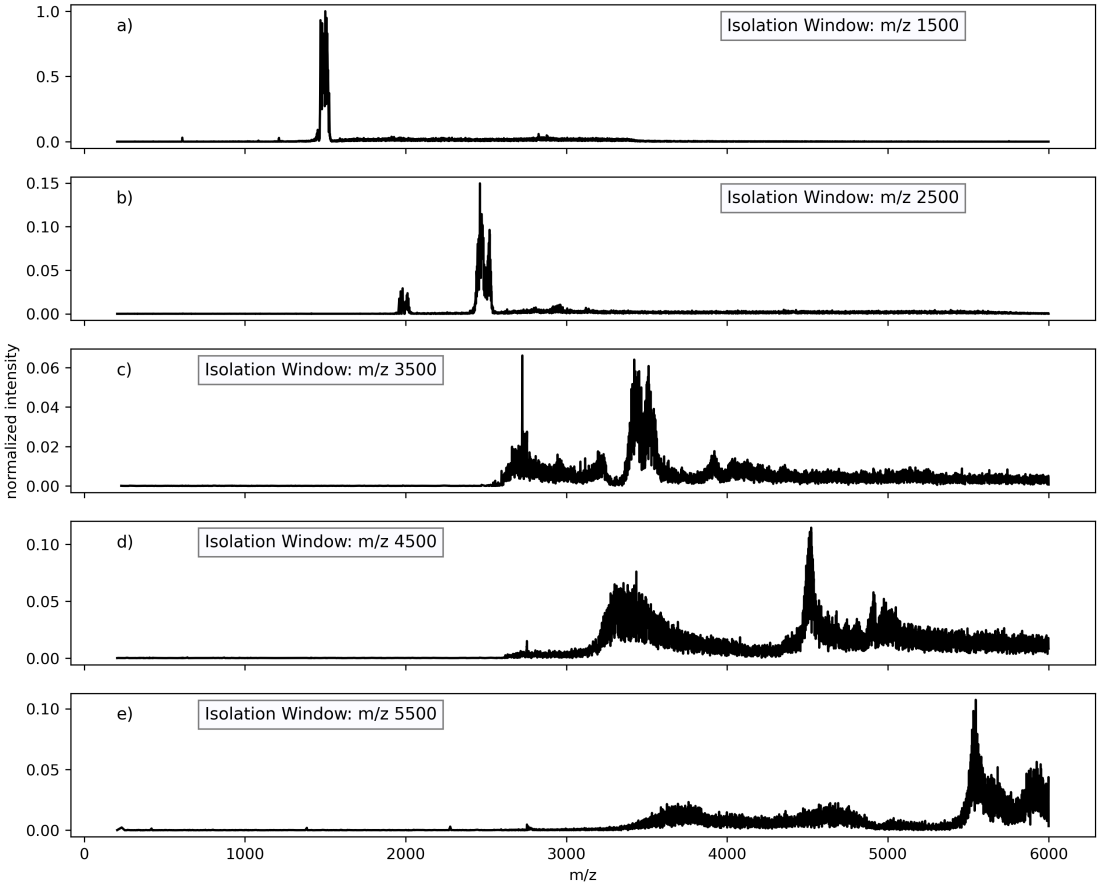

Figure 2.59: Selected mass spectra from the isolation window variation of reserpine in isopropanol and water at the Bruker amaZon. The mass spectra show a double peak structure for the isolation window at m/z 2500. Additional, broader signals are discernible in all of the mass spectra above the isolation window of m/z 1500.

To make the intensity ratios clearer, all the recorded mass spectra were also plotted together in one overview spectrum (Figure 2.60). The increase of the TIC at m/z 4500 can be observed as the green plot lines increase over the background, which underlines the differences between the two different analyte systems. In the experiment with thermometer ions, the peaks of the higher isolation windows were miniscule (cf. Figure 2.57), compared to the broad signal visible at m/z 1500 for reserpine.

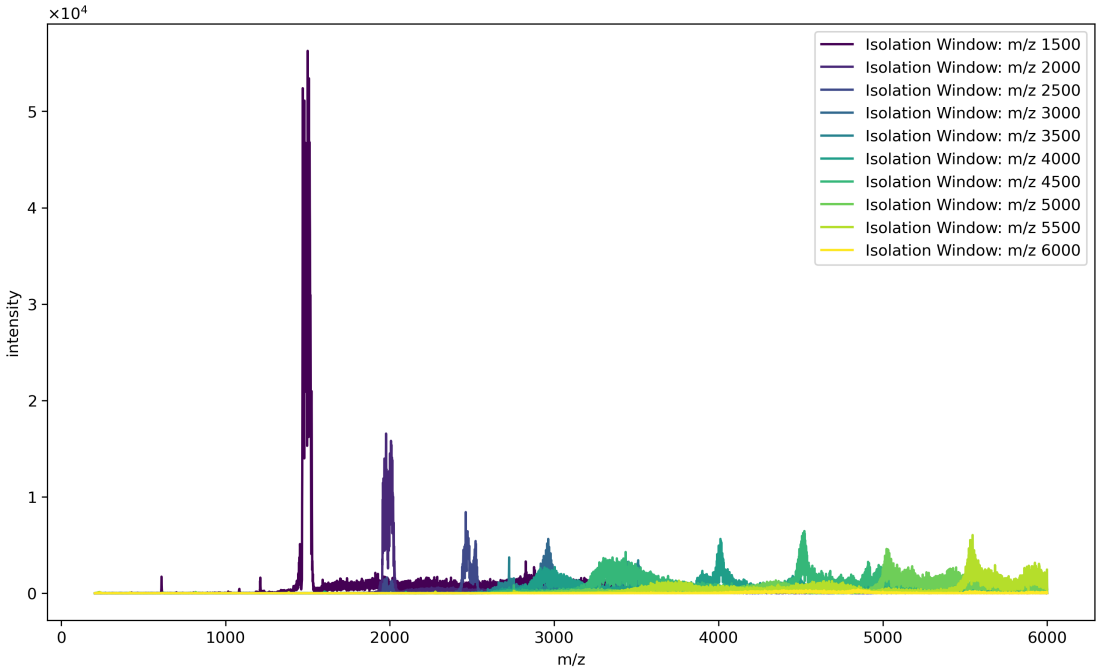

Figure 2.60: Overview spectrum of different isolation windows - reserpine in isopropanol. Different isolated mass ranges are indicated by different colors. The intensity increases again at the isolation window of m/z 4500 (green).

This experiment clearly shows that the choice of analyte and solvent does affect the distribution of droplets transferred in the mass spectrometer, as a completely different TIC shape with variation of the isolation window was observed. The increase at higher m/z of the isolation window can only be explained by the choice of analyte and solvent, as it was not discernible in the experiments before.

2.7.1.2.1 Reserpine in acetonitrile The variation of the isolation window was repeated for reserpine in acetonitrile and water with formic acid. The TIC shows the same pattern as with reserpine in isopropanol, although the second maximum is not as distinct (Figure 2.61). This is evidence that the analyte, specifically reserpine, strongly influences the transfer and observed mass spectra of charged droplets.

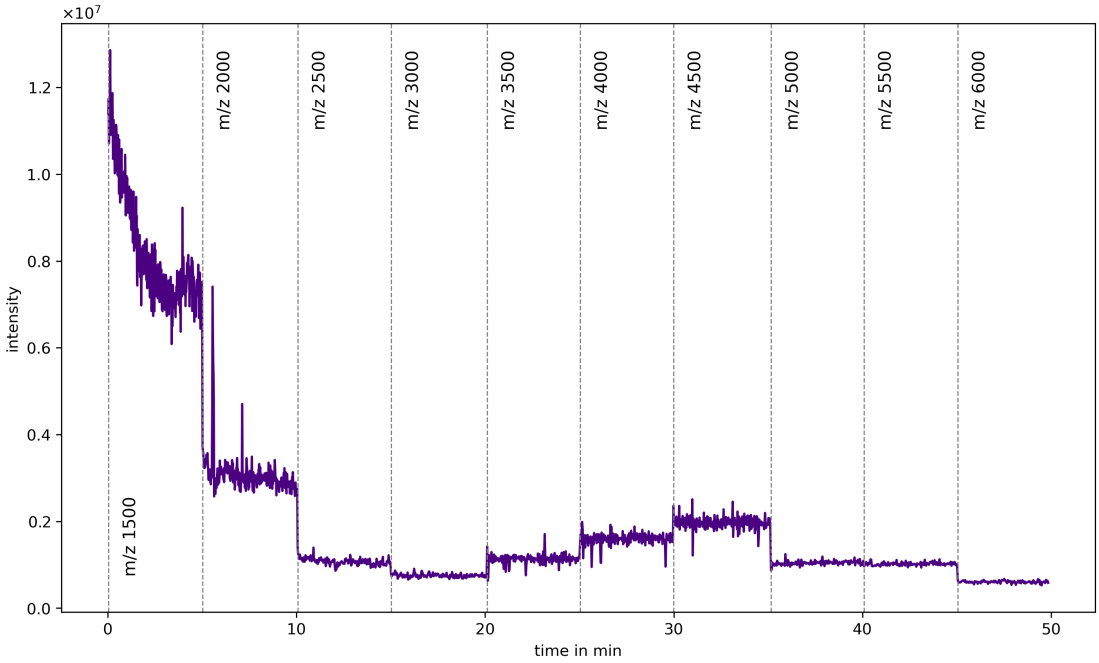

Figure 2.61: TIC of isolation window variation - reserpine in acetonitrile and water at the Bruker amaZon. A second maximum is discernible, again, at an isolation window of m/z 4500.

The associated mass spectra are similar to the already discussed spectra for reserpine in Figure 2.59. Below, an overview of all mass spectra of this experiment is given (Figure 2.62). Again, the broader signal above the isolation window of m/z 1500 is visible. Due to the declining intensity for higher isolation windows, the signal structure is not as distinct as for the results presented above (cf. Figure 2.59).

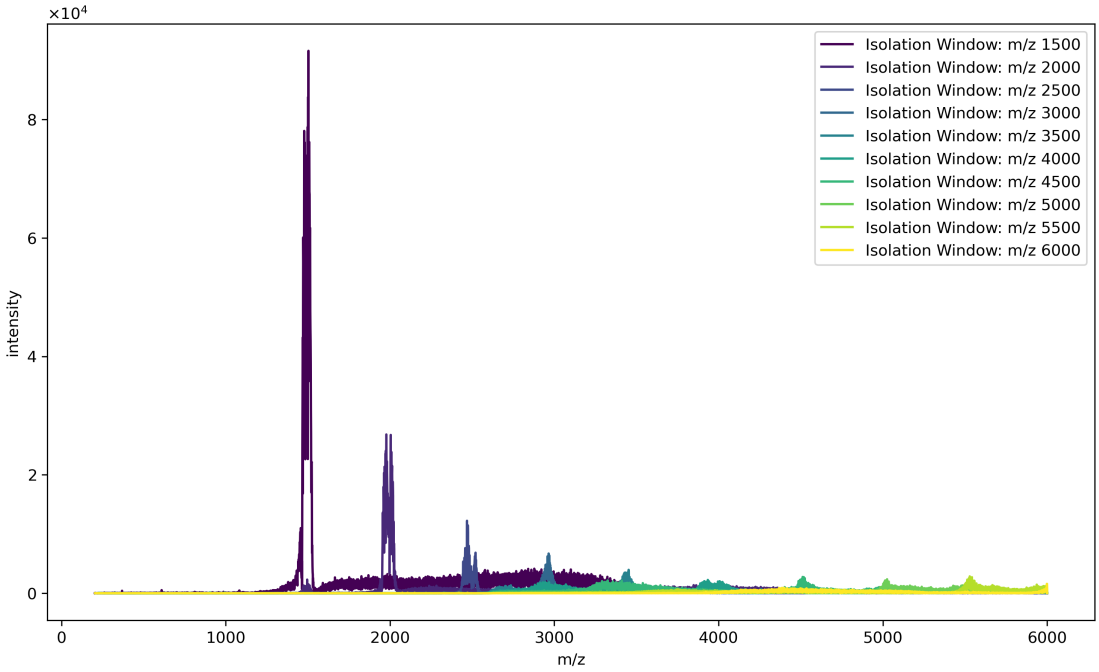

Figure 2.62: Overview spectrum of different isolation windows - reserpine in acetonitrile and water at the Bruker amaZon. The different isolated mass ranges are indicated by different colors. The spectrum overview illustrates the intensity loss at a higher m/z of the isolation window.

The chemical composition of the sprayed solution seems to have a significant influence on the transferred droplets and the abundance of their signatures in the isolation window. In summary, the experiments of the isolation window variation illustrate that the isolated droplets (or their fragments respectively) expose very different chemical behavior in dependence on their size, reflected in the isolation m/z, and on their initial chemical composition. To recall: In these experiments the transfer parameters were optimized according to the m/z of the isolation window in the control software by the so-called “smart-mode”. A depiction of the changing transfer parameter is shown in grey in Figure 2.54. The trap drive, which controls the low mass cutoff of the ion trap, is varying with every isolation window. The TIC is declining with increasing isolation window mass range in the measurement with thermometer ions. In every mass spectrum a defined peak structure at the isolated mass range is observed. In the first isolation

window of m/z 1500, a broad continuous signal appears above the isolation window. This implies the perpetual loss of charges and changing of the trapped droplet sizes. At higher isolated mass ranges, additional distinct mass signal structures appear, which are evidence for a specific fragmentation process of the droplets within the trap. As the experiment was repeated with reserpine as analyte in isopropanol and water as solvents, the TIC shows a drastically different pattern. It is not steadily declining with higher isolated mass ranges but is increasing to a second maximum at m/z 4500. The same pattern is observed for the measurement of reserpine in acetonitrile and water, which signals towards the chemical influence of the analyte on the transferred droplets. Properties of the analyte as proton affinity and intermolecular interactions probably have a strong influence on the stability of the analyte containing charged droplets. Such differences potentially lead to completely different fragmentation process of these aggregates. In further investigations, Monte Carlo simulations can help to understand the fragmentation events occurring in the QIT and give further information about the size range and charges of the droplets or droplet fragments reaching the mass analyzer region of the ion trap MS.

2.7.1.3 Declustering potential of the SCIEX Triple Quad 6500

To investigate the transfer parameters even further, the declustering potential of the SCIEX triple quad instrument, called “DP” in the control software, was varied. The inlet stage of the SCIEX Triple Quad 6500 consists of an orifice plate and two focusing quadrupoles, called “Q-Jet” and “Q0”. The Q-Jet was introduced by SCIEX to reduce the signal-to-noise ratio and the overall sensitivity. The Q0 is further focusing the ion beam for the first quadrupole. The declustering potential controls the voltage on the orifice plate as described in detail in Figure 2.4. It has an influence on the electrostatic focusing between orifice and Q-Jet. Additionally, solvent cluster can be reduced by this potential due to collision induced fragmentation. Because of these described properties it is an interesting parameter to study in an experiment using the droplet scan. The default setting for this parameter is DP = 100. A solution of thermometer ions in acetonitrile and water is sprayed. The associated mass spectra for different collision voltages applied are shown below (Figure 2.63 and Figure 2.64). The collision voltage (CE parameter) is calculated as the potential difference between Q0 and Q2 as described in section

2.2.1. The overall intensity does not strongly vary at different DP values. However, with higher DP, the boundary of the LMCO becomes much more pronounced, which indicates less fragmentation of the transferred droplets. This is underlined by a declining signal of the bare analyte. This is interesting as a higher DP should lead to more energy given to the entering aggregates, which would imply a stronger fragmentation.

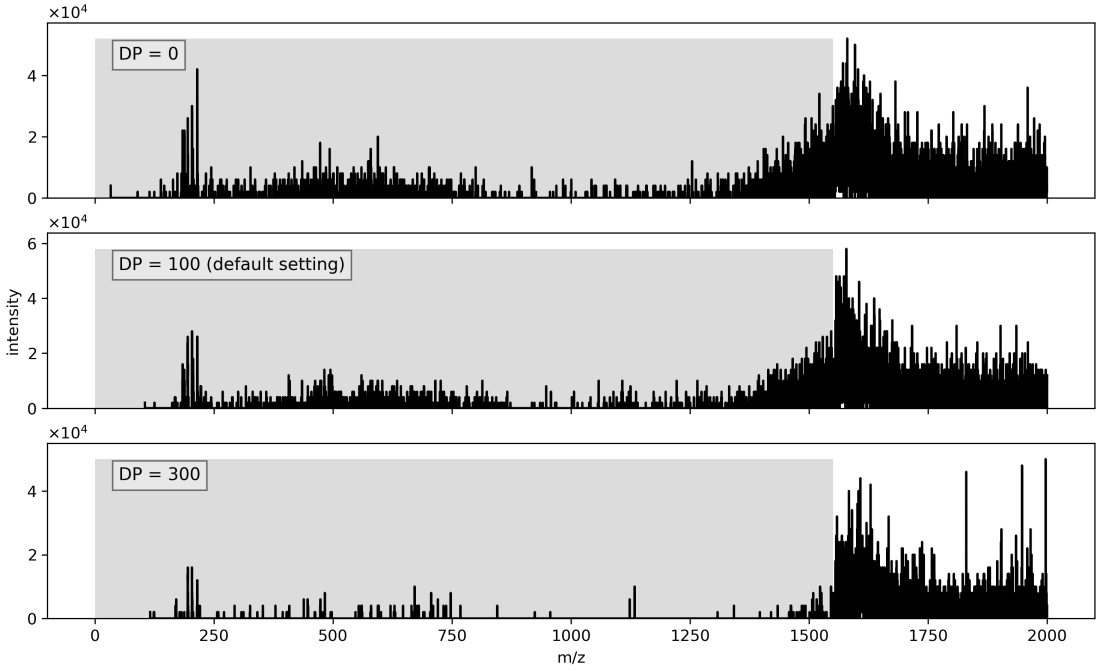

Figure 2.63: Mass spectra for the declustering potential (DP) variation at a collision voltage of 5 V in the SCIEX triple quad instrument. The default setting for this instrument is 100. If the DP is set to 0, the intensity is decreasing slightly in comparison to the default settings. If it is increased to 300, the mass spectrum contains fewer signals below the LMCO of Q1.

At higher collision voltage the droplets start to disintegrate in the same fashion (Figure 2.64) as was explained earlier for the previous droplet scans. The DP variation has an influence on the spectra: with increasing declustering potential, the bare analyte becomes much more discernible between the other signals of fragments. However, in comparison to the spectra above with less collision voltage, some of the thermometer ions are less abundant.

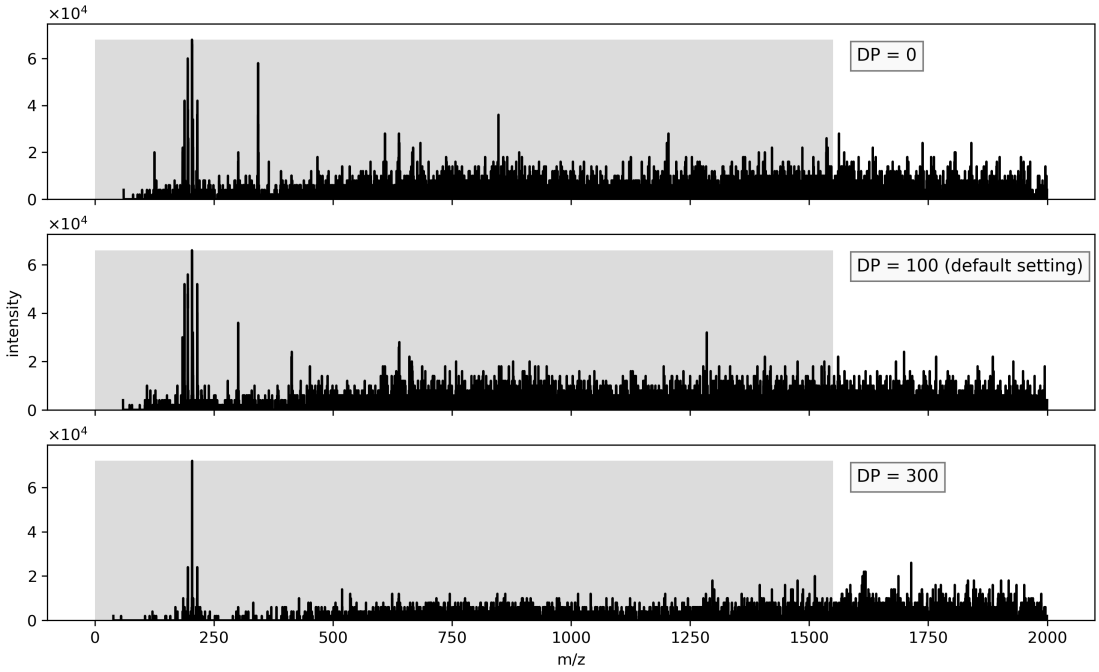

Figure 2.64: Mass spectra for the declustering potential (DP) variation at a collision voltage of 65 V in the SCIEX triple quad instrument. The default setting for this instrument is 100. The signal above the LMCO is not as pronounced as seen before (Figure 2.63), because all of the remnants of the droplets are fragmented.

It seems to be plausible, that a higher declustering potential leads to less droplet signatures in the mass spectra as the aspirated droplets are fragmented early in the transfer system of the instrument with high DP. However, it is demonstrated in this comparably brief experiment, that despite the highest value of the DP parameter, droplet signatures are visible in the spectra. At a collision voltage of 5 V the droplets seem to fragment even less than with no potential applied. For a collision voltage of 65 V the bare thermometer ions are more distinctly observed in the mass spectra with high DP. Though, the intensity ratio of all analytes is changing. All things considered, the declustering potential has much less influence on the droplets than initially expected.

2.8 Conclusion - Experiments

After the first experiments were done it was clear that the SCIEX Triple Quad 6500, despite its entrance system design with a skimmer arrangement, is not particularly prone to aspiration of charged droplets as it was assumed initially. The droplets or their fragments are visible above the LMCO as a broad signal structure, which reacts to higher collision voltages and collision gas pressures by increased fragmentation. In contrast, the Bruker amaZon speed ETD QIT has an inlet capillary and ion funnel configuration. This system does show strong droplet signatures as well. Isolating a signal at m/z 2500 (isolation window width 100 Da) produced a noticeable broad peak in the mass spectra. Remarkably, the QIT was in default analytical operation conditions when the experiments were done. This shows that the existence of charged droplets is common when ESI is used as the ionization method. Additionally, strongly different transfer stages were present in the systems used for the experiments. However, droplets aspirated from ESI sources are observable in all investigated MS-Systems which differ significantly in their basic configuration. In addition, evidence was given that the droplets transport a significant fraction of analytes through the transfer systems of the instruments. By fragmentation in the SCIEX Triple Quad 6500 with different collision settings, e.g., collision voltages and gas pressure, the analyte was released and strong analyte signals could be observed. This was also the case for the Agilent Q-TOF. An increase of the collision voltage showed similar results. The transport of analytes within the droplet could also be demonstrated in the in the Bruker amaZon speed ETD, in which an isolation window at m/z 2500 (width 100 Da) was usually chosen. However, the analyte signal was discernible far outside of this window, which means that ions generating this signal have to be formed after the isolation. The droplet signature above the LMCO was distinctively reproducible in the SCIEX Triple Quad 6500. However, the shape of the signal changed when a different solvent and analyte was used. The obvious conclusion is that charged droplets consist mainly of solvents. Thus, the configuration should be strongly influenced by the used solvent. The release mechanism of the analyte also most likely changes with different chemical compositions. Although an analyte solution is also sprayed in APCI, droplet signatures could not be detected when investigated at the Bruker amaZon speed ETD as isolating at different m/z produced entirely empty spectra. This underlines the significance of the perpetual issue with charged droplets

when using ESI as the ionization technique. Since ESI is one of the most important API methods, all unwanted effects from ESI, particularly contamination, have potentially a strong effect on routine analytical applications of ESI. Contamination of the instruments by the charged droplets may lead to downtime, which adversely impacts the efficiency of analytical methods. Additionally, the behavior and molecular dynamics of the charged droplets is hardly investigated yet. They influence the chemical background due to fragmentation and releasing large amounts of solvent molecules. The release mechanism of analyte from the charged droplets under different conditions within the entrance stages is also widely unknown. Thus, charged droplets and their influences on the chemical background have to considered as a factor in ESI experiments. To further investigate the droplets and their behavior, ion source parameter variations serve to be a good starting point. Ion source parameters, like gas flow or temperature and liquid flow, can influence the droplet signatures and thus give more insight about them and their dynamics. Interesting results were achieved with the Bruker amaZon speed ETD QIT, in which the transfer parameters were optimized for high m/z ranges. If thermometer ions in acetonitrile and water are sprayed, an intense double peak structure appears in the isolation window at m/z 2500. The nebulizer gas was studied in the QIT in a first set of experiments. It is injected from the tip of ESI needle assembly into the ion source. The experiments reveal that different nebulizer gas pressure values have only limited influence on the associated mass spectra. However, the total ion count (TIC) shows a decrease in three steps. The same pattern is observable for thermometer ions and reserpine in acetonitrile and water, which indicates that the solvent is accountable for this phenomenon. In Figure 2.65 the phenomenon is shown by three different mass spectra. The double peak structure is only visible in the acetonitrile / water experiments even if the analyte is changed from thermometer ions to reserpine. If the solvent system is changed to methanol / water, the double peak disappears.

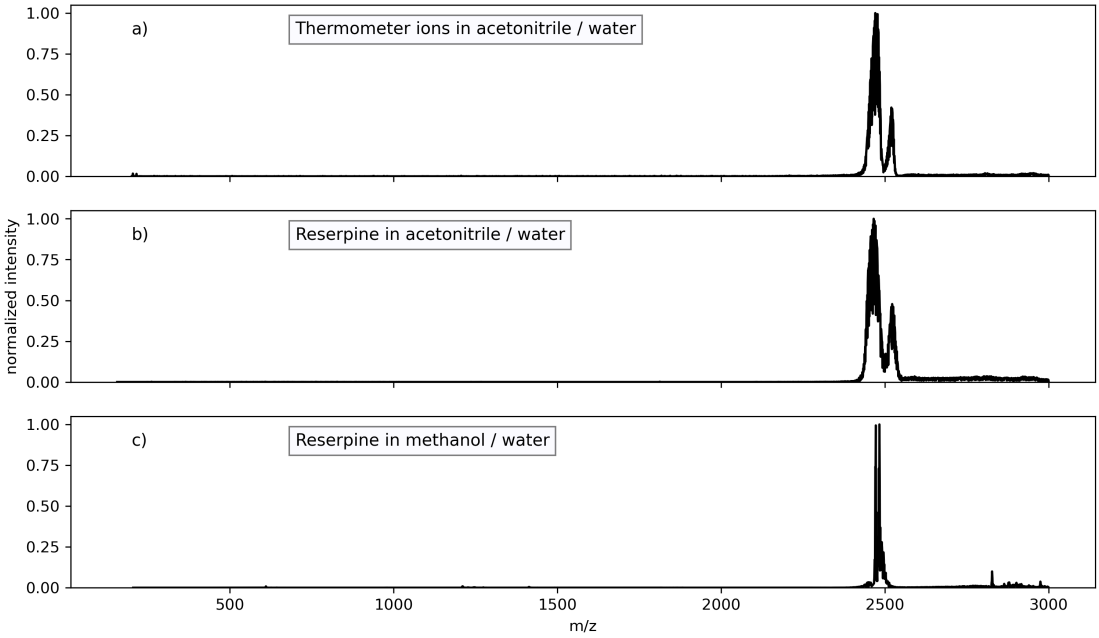

Figure 2.65: Mass spectra of different solvent systems (acetonitrile / water and methanol / water). The double peak structure is only clearly visible in the acetonitrile / water mass spectra. In the methanol / water spectrum the signal in the isolation window (m/z 2500) is sharper.

If the intensity changes as drastically, as it is seen in the TIC, it hints at a different transport efficiency of the droplets or entirely different droplet distributions entering the machine. Smaller intensity in the isolated spectra also imply smaller droplets, as higher nebulizer pressure should lead to smaller generated droplets by the spray as they are more rapidly ripped away. Experiments with methanol and water as solvent system led to a different TIC signal shape, which again suggests an influence of solvents on the aspirated droplets. Furthermore, with methanol no double peak structure in the isolation window is visible in the mass spectra. This indicates a defined cluster transition at m/z 2500 for the acetonitrile and water system. Additionally, the experiment with reserpine and methanol in particular show that dimers of analytes are transported into the ion trap within droplets, as they were detected in the associated mass spectra. This raises new questions about the chemistry in the aspirated droplets and how dimers are actually formed in ESI experiments. The effect of the dry gas flow rate was investigated in an additional set of experiments. The dry gas is applied as a counter

flow from the spray shield and has the purpose to hinder neutral species from entering the system and to support the desolvation of analytes. The EIC of thermometer ions show that the release rate of analytes from the droplets is increased at a certain dry gas flow. The release mechanism of the analyte is linked to the droplet stability and can thus be used as an indicator for that. Additionally, signals above the isolation window were regularly observed in the mass spectra. This suggests charge loss of the trapped droplets as the m/z increases. The exact mechanisms of charge loss reactions are still unknown. However, a simple reaction scheme was given above in Figure 2.26, which fits surprisingly well. The results obtained with the Bruker amazon are in stark contrast to the experiments on the SCIEX Triple Quad 6500. Variation of the gas flow does not lead to visible effects on the droplet scan in terms of the mass spectra or the chromatograms in experiments on this device. The gas flow pattern within the SCIEX Triple Quad 6500 seems to have less of an effect on the observed droplet signatures. Only in combination with increasing temperature, the analyte signal shows significant changes. The droplets interact with heated background gas in the ion source and heat from the gas particles is transferred to the droplets. The effects seen in the spectra could be a result of the higher internal temperature of the droplets. In the Bruker QIT the temperature is governed by heated dry gas, which is applied in counter flow direction from the spray shield. It could be determined that at every temperature setting droplets can be observed in the mass analyzer. The TIC signal shape shows two maxima, at the lowest and the highest temperature. The double peak structure at the isolation window observed regularly in previous experiments with the QIT is visible at 180 °C, which implies that the occurrence of this phenomenon is also linked to the temperature. Additionally, the EIC displays a maximum at 180 °C, which in return points at lower droplet stability. Interesting to note is that droplets can be trapped even at 250 °C dry gas temperature. This suggests a high heat capacity of the charged droplets. In addition, the results of the temperature variation with the SCIEX Triple Quad 6500 underlines this suggestion. At the triple quad instrument, the temperature of the heater placed in V-shape at the ion source chamber can be varied from room temperature to 750 °C. Even given the fact that the average ion source temperature is certainly well below the heater temperature in both instruments, it is remarkable that a droplet scan is possible at this high temperature with a similar signal pattern as described above. However, the bare analyte signal disappears at higher temperatures, which is an indication for a changed

droplet stability. The liquid analyte solution flow into the ESI emitter can be varied as well. The liquid flow influences the droplet size of the sprayed solution as it was already determined by Tang and Gomez [22]. The size in return should have a direct connection to the stability of the aspirated droplets. A variation of the liquid flow in the Bruker QIT also supports this notion. Differences in the EIC indicate a different stability of the droplets as well. In the SCIEX Triple Quad 6500 the variation range of the liquid flow is limited, but obviously the condition of the electrospray strongly depends on the liquid flow also in the SCIEX ion source as very low liquid flows lead to mass spectra with very low overall intensity. The experiments clearly show a dependency between the transfer dynamics of the droplets and the ion source parameters. Every new parameter leads to a new dimension to investigate, which makes it difficult to summarize the result in a compact way. Direct assertions of the size and charge state of transferred droplet are not possible at this moment after these initial experiments. However, an investigation of the presumed charge loss mechanism observed in the QIT could lead to a more detailed understanding about the actually isolated species. Additionally, the selected parameters of the transfer stages and the QIT mass analyzer were investigated. They also influence the droplet signatures in the mass spectra. The declustering potential in the SCIEX Triple Quad 6500 had much less influence than expected. Only a slight decrease in the intensity of droplet signals was observable. In contrast, the isolation window variations at the Bruker QIT revealed the actual shape and characteristics of the isolated charged aggregate distribution in a much broader fashion. Further investigations with this method, particularly of the most intensive regions of this particle distribution, seems to be very promising for future experimental efforts.

3 Simulation of charged droplets

3.1 Introduction

Substantial experimental evidence for the occurrence of droplet signatures in mass spectra from various API mass spectrometer is presented in the previous chapter. These first results were summarized in a publication from 2021 [60]. Particularly, the isolation of droplet species the mass range m/z 2500 in Bruker amaZon speed ETD was a promising confirmation that droplets can be transferred deeply into the machines and detected in the spectrum. The variation of different ion source parameters verifies that the dynamics and transfer of the droplets can be manipulated by external conditions. The results gave first indications about the thermal stability of these aggregates as it was possible to isolate them even as they underwent dry gas heating at temperatures as high as 250 °C in the Bruker system (cf. Figure 2.32). A first rough indication of the actual size of those droplets can be inferred from the Rayleigh Limit (cf. Figure 2.1). Thus, the calculated radii are a lower limit for a size estimation. By this simple estimation it was postulated that droplets of up to 2.5 nm radius can be observed in the instruments at m/z 2500. However, the droplets can obviously transport less charges than determined by the Rayleigh Limit, which would imply a broader size range. The distribution of the charges within the droplets and the overall composition remained unknown after analyzing the experimental results, which is why the goal of the following chapter is to answer some of the questions about these aggregates with numerical modelling approaches.

3.2 Methods to simulate droplets

There are different molecular modelling methods for chemists available nowadays. Choosing the right approach is the first step for dependable assertions about the sim-

ulated molecular systems. In simple terms, the droplets consist of charges and solvent molecules. The interaction between these molecules and charges has obviously a great influence on the dynamic / stability of the whole charged droplet and therefore in which state they are transferred into the machines. Interactions between atoms and molecules are modelled by a molecular dynamic simulation (MD) [64–69]. MD simulation can account for the interactions by different theoretical approaches. Either by calculating the electron density of every atom within the simulated system [70, 71] or by the interactions by a simplified classical set of potential functions, a so called “force field” [72, 73]. The choice between the different approaches does generally not only lie with the user alone as the performance of the available computer system is almost always a limiting factor. The following example exemplifies this: A droplet with a radius of 2.5 nm, estimated with the Rayleigh Limit calculation (cf. Figure 2.1), consisting of a 1:1 mixture of water and acetonitrile contains at least 1200 molecules and thus 5400 atoms. With this in consideration, the system size is orders of magnitude too large for common quantum mechanics approaches of calculating the electron density of every atom in the droplet to deduce the interactions between them at every timestep. The computational costs for a quantum-mechanical molecular dynamics simulation for a simple aromatic system with about 18 atoms can reach up to multiple days on current medium sized shared memory parallel computers, depending on the chosen accuracy; this makes it impossible to simulate a charged droplet with this approach on computer systems realistically available for such a task in an university environment. However, the dynamics of a system of this size can be calculated with a different approach: classical molecular dynamics simulations [67]. Classical MD simulations are more time efficient, as the forces and potentials between atoms or molecules are not calculated on the spot from the specific electron density. They are listed in so-called force fields, in which theoretical data for potentials between different atom types are compiled. Nowadays, many force fields for liquids and gases exist and are implemented in different MD codes [74–79]. In classical MD simulations Newtons equations of motion are solved numerically for particles in a specific simulation box, which results in a trajectory of the simulated particles over a specified time frame. For every timestep of the chosen time frame the potential energies between the particles are calculated [64]. This approach was chosen to answer questions about the stability and dynamic of the charged droplets.

3.2.1 Building droplets for MD simulation

There are a many MD codes available today. For this work LAMMPS (**L**arge-scale **A**tomic/**M**olecular **M**assively **P**arallel **S**imulator) was chosen [79]. Its development started 2004 to model materials on a parallelized computer system. The code was further developed to integrate different methods for fluid or solid simulations. It is completely open-source and can be changed to accommodate specific questions and needs of the user. Many common pre- and postprocessing tools are also open-source software. To construct the modeled molecules (solvents or analytes) the program Avogadro was used [80]. It is a molecule builder and simulation result visualization tool with a broad variety of features. The configurations of single molecular species can be exported in a LAMMPS data format to further prepare them for the actual simulation input files, which was achieved with moltemplate. Moltemplate is a script-based system to set-up the actual initial state of a MD simulation based on complex rules, which makes the placement of the modeled molecules within the simulation box much more accessible [81]. Processing the moltemplate scripts by the computer system only takes a few seconds, resulting in input files specifically for LAMMPS simulations. The choice of the used force field and the force field parameters are also part of this preprocessing step. As described above, the force fields are the backbone of a classical MD simulation, as the calculation of the interactions between particles is solely based on these lists of potential functions for a variety of functional groups or single atoms. OPLS (**o**ptimized **p**otentials for **l**iquid **s**imulations) is a common force field which was introduced by Jorgensen et al. in 1988 [82]. It was created for the simulation of proteins. Later, the force field was extended for organic molecules in an all-atoms (OPLS-AA) approach [83]. Force fields model all molecular interactions in a classical MD simulation. Thus, they contain the potentials for bonded and non-bonded interactions. Bonded interactions can entail bond-stretching and angle-bending or torsional deformation. Non-bonded interactions are commonly considered as Lennard-Jones and Coulomb terms. In OPLS-AA, the torsional and non-bonded interactions were derived by ab-initio calculations. The potentials for different functional groups of organic molecules were tested in Monte-Carlo simulations and compared to their structural and thermodynamical properties derived from experiments. The bonded interactions were gathered from the AMBER all-atoms force field [84]. Due to the extent of properties for organic molecules, like alcohols, ethers, alde-

hydes, etc., OPLS-AA was chosen for the simulation of charged droplets, which mainly consists of organic solvent molecules and water. Water is also described in OPLS-AA. It uses widely known water models, like TIP4P [85], TIP3P [86] or SPC [87]. The water model is chosen by the user when the simulation input is written in the same fashion as the parameters for other particles. The atoms of a specific molecules are searched in a list of parameters, which is unique for every force field. Additionally, simple ions like alkaline metals, alkaline earth metals as well as halogens are part of OPLS-AA. For example, ammonium (NH_4^+) is listed as a unified particle. Such united "atoms" are mostly used as a simplification of commonly used functional groups. The atoms within the group are not explicitly accounted for; rather the potential energy for the group is assumed as a one-core dummy atom. Another simplification to simulate charged droplets with OPLS-AA has to be made: Protons, which would account for the actual charges in a droplet, cannot be readily simulated in this approach. It is complicated to model protons in a classical MD simulation as they are effectively transported in liquid by charge transport through hydrogen bonds, which is fast and efficient [88]. However, bond forming and breaking cannot be simulated with classical force fields, which limits the simulation to use different charged atoms, like the described ammonium or alkaline metals. Overcoming this limitation requires at least specialized implementations of MD methods [89]. As the actual equilibrium geometry of the droplets is unknown before the simulation, all simulated droplets are set-up in a block structure at the center of a simulation box. This is done with the aforementioned program moltemplate. The distance between the individual molecules is crucial. It obviously determines the initial forces between the molecules and therefore the initial stability of the molecular system in this artificial non equilibrium state. For example, if the molecules are placed too close to each other, the forces placed on the molecules is unphysically large: The droplet "explodes" in consequence. If the molecules are placed too far apart, the attractive forces of the solvent molecules are too small, the molecules separate from each other over a few timesteps in the MD simulation and no droplet forms at all. Figure 3.1 shows a typical starting point of a droplet MD simulation after the processing of the moltemplate script.

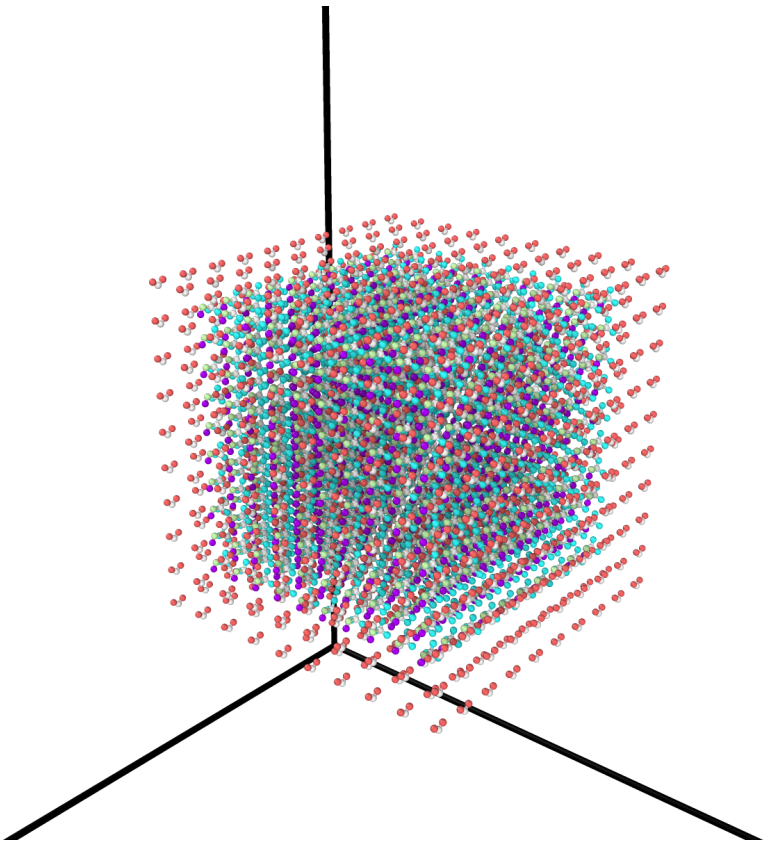

Figure 3.1: Typical starting point of a droplet simulation: The molecules are arranged in a block-shape around the center of the simulation box. The shown system consists of water, acetonitrile, and ammonium ions. The borders of the simulation box are depicted in black.

The visible inner cube contains acetonitrile which is shown in turquoise and purple. The outer, larger cube consists of water which is depicted in red and white. The spacing between the water molecules is slightly larger than the distance between the acetonitrile molecules which is the reason for the different block sizes. The actual spacing was found iteratively by iterating the MD simulation for a few timesteps to observe the motion of the molecules. If the molecules were drifting apart, the distance was adjusted to a new value in moltemplate. The resulting initial structure contains 1000 molecules of water and acetonitrile each. To complete a charged droplet, 12 ammonium ions, modeled as a united atom, were added to the structure. Due to their lower number, they are not visible in the figure. The spatial domain in which the simulated particles

are placed is called the simulation box. The borders of this box are visible in black in Figure 3.1. Typically, MD simulations are done with periodic boundary conditions. This means, that the borders of the simulation box are folded on the opposite boundary: If a molecule is forced out of the simulation box, it reenters from the opposing side. To represent this concept, Figure 3.2 shows a simple visualization.

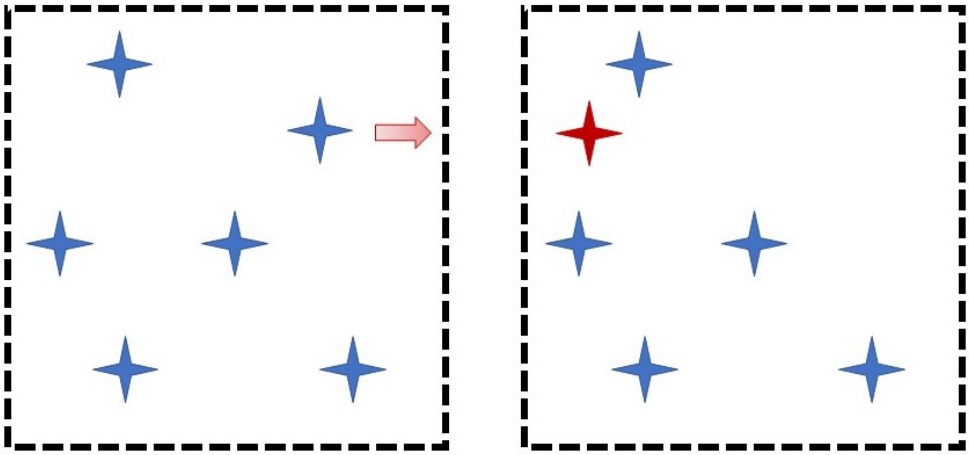

Figure 3.2: Simple two-dimensional example for periodic boundary conditions: On the left a first timestep of a simulation is shown. The red arrow represents the trajectory of the blue-star particle. The following timestep is shown on the right: The particle, now marked red, has crossed the border of the simulation box and reentered at the opposing side.

The blue stars represent simulated particles, the red arrow shows the trajectory of one of the particles. On the right the following timestep is shown: The particle has crossed the border of the simulation box accordingly to its trajectory. It enters the simulation box from the opposing side as if the borders of the simulation box are wrapped around, similar to the surface of a cylinder. Of course, this example is rather simplified as only one of the particles is moving and the example is only two dimensional. In a real simulation, obviously every particle moves due the interaction with the particles around it and MD simulations commonly take place in three-dimensional space. If the border

were assumed to be periodic other boundary conditions have to be imposed. For example, particles could be either reflected or just removed from the simulation if they reach the borders of the simulation box. If reflective walls are modeled, parameters for the reflection of particles by the walls have to be specified, as a metal is reflecting particles different to a fluid for example. This is not always practicable or possible. Losing particles as they reach the borders could cause numerical errors, if, for example, molecules are cut in half. Additionally, with a changing number of particles some properties of the resulting trajectory are not calculatable as another statistical ensemble has to be applied to the simulation. A microcanonical ensemble can be assumed for the simulations, which implies a constant number of particles, volume, and energy [90, 91]. This is the base for different temperature and pressure controlling functions, so called numerical thermostats and barostats, implemented in LAMMPS. Therefore, even if periodic boundary conditions of a comparably small simulation box obviously do not represent the true reality in a mass spectrometer, they are a feasible assumption for charged droplet simulations. To ensure a more efficient way of calculating the pair-wise interactions between particles, a cutoff radius is defined [69]. Only interactions of particles with a distance within this radius are calculated in the simulation. If particles are farther apart, the interaction is not considered in the calculation to increase numerical performance. This means, that before setting up a simulation run the radius has to be carefully chosen to balance the computational costs and the accuracy of the particle interactions. In case of simulating charged droplets, the cutoff radius of the particles has to be large enough, to ensure that the molecules on either side of the droplet can interact with each other. This ensures a stable energy development throughout the time frame of the simulation and represents interactions of a more realistic droplet. This has to be accompanied by simulating a sufficiently large simulation box, to prevent interactions between periodic images of the droplets. Important to note is the timescale at which MD simulations commonly take place. Simulation timesteps are usually in the range of femtoseconds. In case of biomolecular simulations, in which protein folding is the subject, the resulting simulated timeframe in the picosecond or nanosecond range is sufficient. For other problems, this timeframe can be too short to fully depict a process. However, to gain general information of the dynamic of a system, the timeframe is tolerable and can even depict spectroscopic data accurately [92]. This method of MD simulation is called steered MD (SMD). As this work aims to set a first insight into the

simulation of the dynamics of charged droplets, the short timeframe is reasonable at the moment.

3.2.2 Minimization

The block-shape of the moltemplate script output is obviously not an equilibrium geometry of a droplet (cf. Figure 3.1). A simple energy minimization by LAMMPS is preceding the first timestep of the simulation: A minimal energy for the starting geometry is searched by iteratively changing the coordinates of the atoms until the geometry shows a local minimum for the geometry or another stopping criteria e.g., steps of the minimization process, is reached. Specifically, the Polak-Ribiere conjugate gradient method is applied in the minimization in LAMMPS [93]. With this algorithm the force gradient is combined with the gradient from a previous step to find a new search direction in contrast to the previous direction. The minimization also ensures, that atoms are not overlapping. Figure 3.3a shows the geometry after this first energy minimization in the left panel. The arrangement of the molecules is still a general block shape but are the individual positions are not exactly aligned anymore.

3.2.3 Data analysis and visualization

The result of the simulation, a so called “trajectory” is saved to plain text output files by LAMMPS. The trajectory contains a list of properties for every particle for every time step. The particle properties which are recorded can be defined in the input file for LAMMPS. The coordinates, velocity, kinetic and potential energy for the particles have been tracked for every simulation performed for this work. To visualize the trajectories OVITO is used [94], which also allows basic analysis and post processing of LAMMPS trajectories. An important data analysis method for droplet simulations is cluster analysis: A cluster is defined by a certain radius around a molecule. It is a group of associated molecules, which is attached due to their molecular interactions. This analysis is a useful indication for the stability of different droplets. For further data analysis and interpretation self-written python programs are used.

3.3 Evaluation of critical simulation parameters

In section 3.2 the steps to construct initial conditions for droplet simulations was explained. As described, the droplet is in a block-like shape after processing the input script with moltemplate. However, if the classical MD simulation code LAMMPS and the chosen force field yield results which represent the real dynamics of charged droplets is not yet clear. Simple tests of typical physical properties could lead to an answer this question. In first simulations properties of different solvents were tested. To find an actual realistic initial equilibrium state of the droplet, it is "relaxed" with a numerical thermostat in a first MD simulation. LAMMPS implements (among others) the Nosé-Hoover thermostat [95, 96]. It is applied to the translational degrees of freedom for every simulated particle and updates their position and velocity in every timestep so that the ensemble averages of those parameters are in accordance with the specified temperature. The fundamental idea behind a numerical thermostat is the contact of the simulated system with an external heat bath, which has a fixed temperature. Figure 3.3 shows the starting and ending point of the initial relaxation MD simulation.

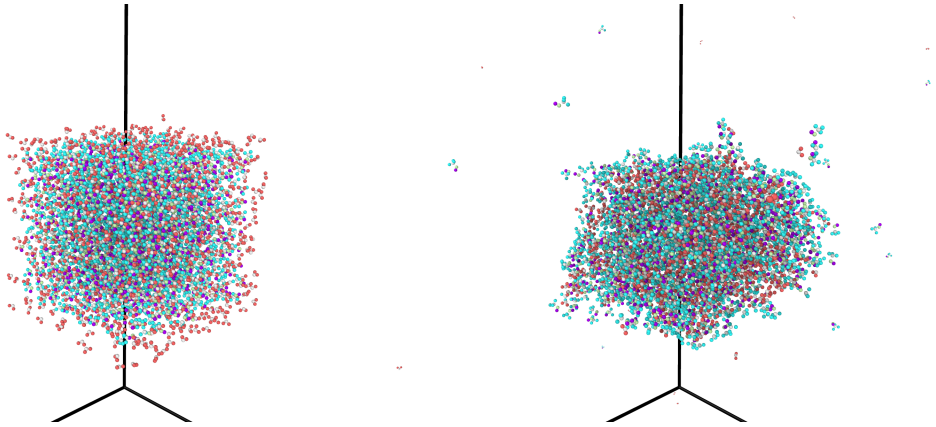

(a) Starting point after minimization **(b)** End point

Figure 3.3: Left panel: Starting point of a relaxation MD simulation of a droplet containing water, acetonitrile and lithium ions after the initial energy minimization. On the right: Droplet after 100 ps simulated time of the relaxation MD simulation with an applied thermostat with a specified temperature of 300 K.

In Figure 3.3 a temperature of 300 K was chosen for the thermostat. The relaxation

simulation is run for 100 picoseconds (10×10^{-10} s). After this simulated time, the droplet has an approximately spherical shape as expected for its equilibrium state. Relaxation simulations were repeated for different droplet compositions to evaluate if the described simulation approach is feasible for different solvent mixtures. Realistic behavior in terms of physical properties of the simulated droplets allow to assess the validity of the simulation approach. If the droplets show characteristics as expected from previous experimental and theoretical observations, MD simulations done with LAMMPS can be a primary method to describe dynamics of charged droplets seen in the experiments.

3.3.1 Comparison of different solvents and charges

A variety of solvents other than acetonitrile are used in ESI experiments. Commonly, water is diluted in a 1:1 mixture with an organic solvent. In addition to acetonitrile, methanol, ethanol, and isopropanol are frequently used. Furthermore, formic acid is added in a concentration 0.1 - 0.05 % to lower the pH of the solution and add more charge carriers. In the previous section the relaxation of a water / acetonitrile droplet in a MD simulation was presented. The relaxation process gives a spherical shape, which is expected as equilibrium state of the droplets. Additionally, solvent typical behavior can be observed: The outer layer of the droplets consists mainly of acetonitrile molecules and larger water clusters can be found enclosed by the organic solvent. Droplets of different chemical composition were simulated, to further validate the choice of a classical MD simulation approach to investigate the dynamics of different charged droplets. In the example of the acetonitrile and water droplet (cf. Figure 3.5) differences in polarization / permanent dipole moment of the molecules are responsible for the coordination of the molecules. For example, the partially negatively charged N-atom in acetonitrile, is almost always directed toward the inner droplet, due to the positive charges of the ions. In the same fashion the partial negatively charged O-atom is coordinated by the charge of the ions. Typical solvent behavior can also be observed, if the solvent is changed to methanol: In Figure 3.4 and Figure 3.5 two droplets are shown after a relaxation simulation. One consists of methanol and water (512 molecules each), the other of acetonitrile and water (again: 512 molecules each). Both droplets are charged by 9 lithium ions. The droplets are shaped spherical, and the

ions are placed randomly inside the solvent mixture.

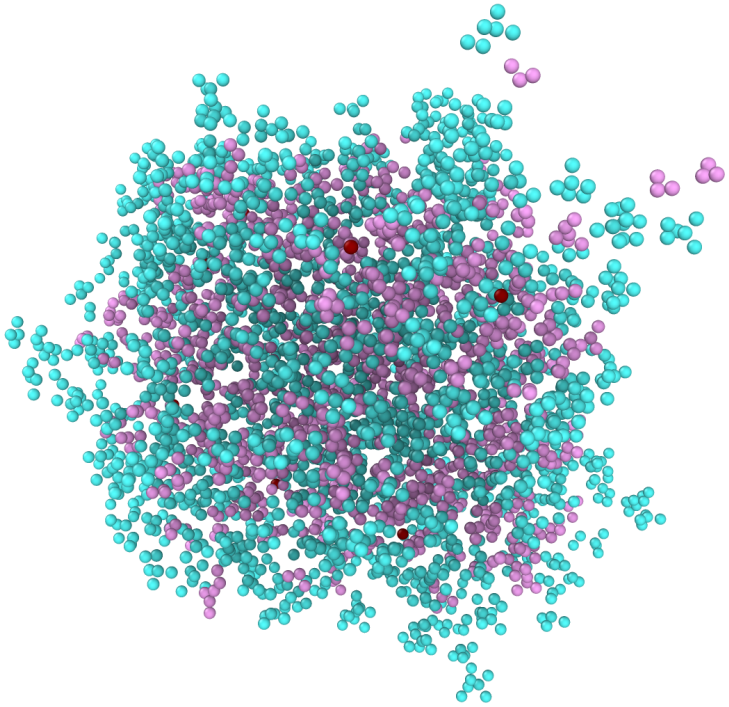

Figure 3.4: Charged droplet after a relaxation simulation for a simulated time of 100 ps. The droplet is a mixture of methanol / water droplet with lithium ions. It is shaped spherical, and the ions (dark red) are enclosed by the solvents.

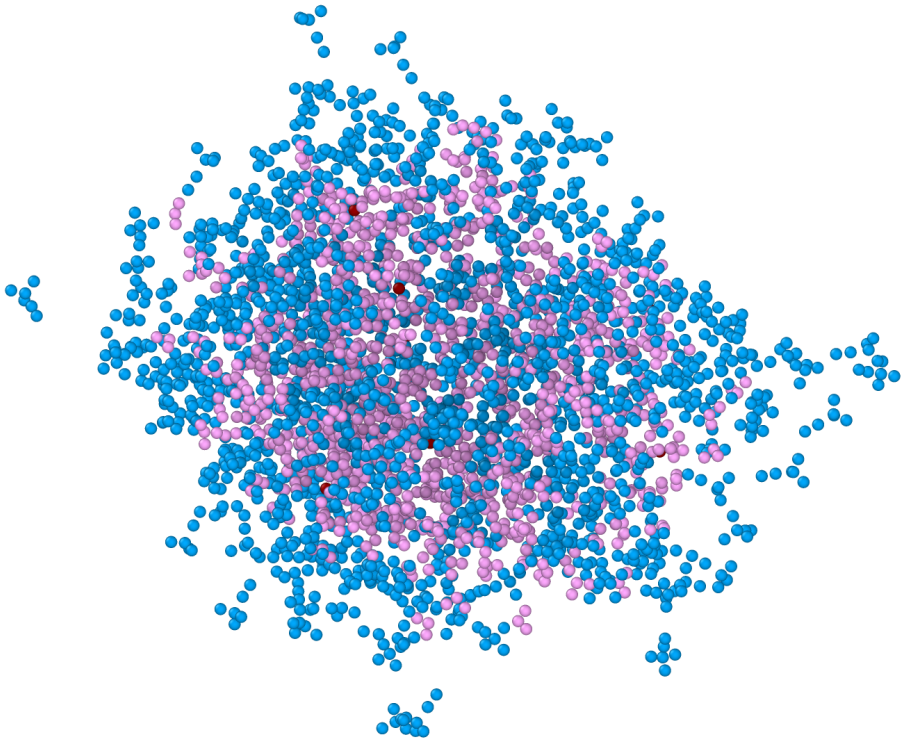

Figure 3.5: Charged droplet after relaxation simulation for 100 ps. In this simulation a mixture of acetonitrile and water droplet with lithium ions as charge carriers was investigated. Larger clusters of water are placed within the droplet. The ions (dark red) are enclosed by the solvents. The outer layer of the droplet consists almost entirely of acetonitrile molecules.

In Figure 3.4 and Figure 3.5 water molecules are colored pink, Methanol is colored turquoise, Acetonitrile is colored blue. The lithium ions are colored dark red. At first glance it appears as if the water / methanol droplet is mixed more uniformly whereas the droplet with acetonitrile / water contains larger clusters of water. The surface layer of the droplet seems to consist mainly of acetonitrile, as observable before in Figure 3.5. To confirm this notion the partial radial distribution function of water and the organic solvent is investigated.

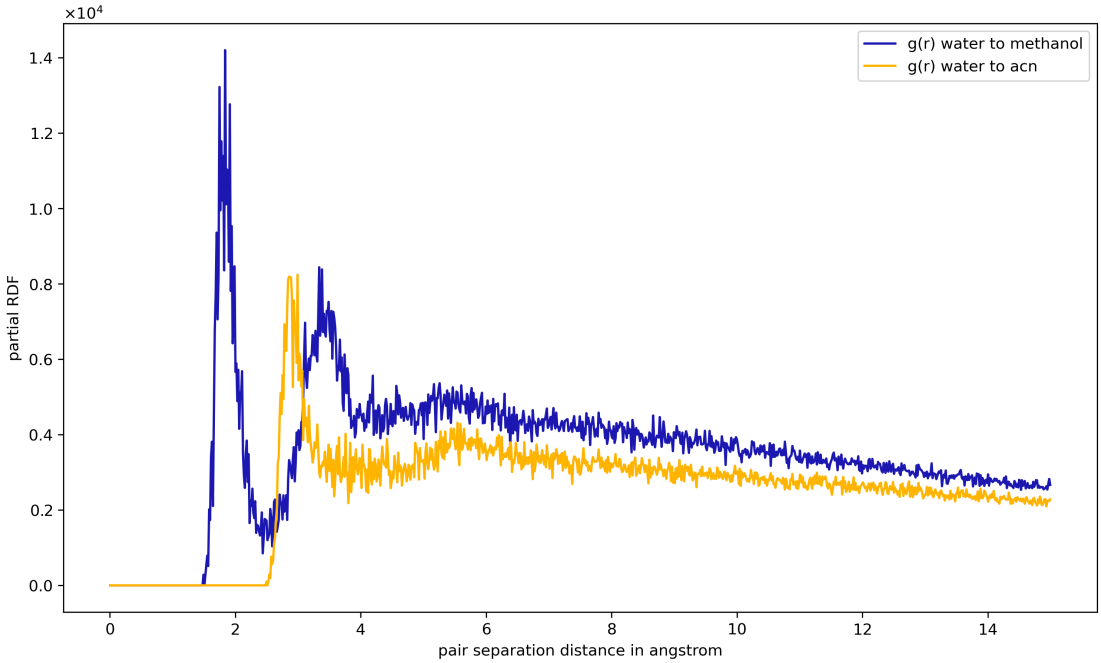

Figure 3.6: Partial radial distribution function of water and the respective organic solvent. The radial distribution function of a pair of atoms between water and methanol is shown in blue, the radial distribution function of a pair of atoms between water and acetonitrile is shown in yellow. The methanol / water pair shows a much higher probability to exist at a lower separation distance.

The radial distribution function $g(r)$ is the probability of an atom to occur in a specific separation distance r between a defined pair of atoms. Figure 3.6 shows the partial radial distribution function of water and the respective organic solvent in the two droplets. As analyzed particles pairs the O-atom of water and a specific atom in the organic solvent (H-atom of the alcohol function in methanol and the N-atom in acetonitrile) were selected. It shows a mean of the last ten timeframe of the simulated trajectory of the relaxation simulations. For water / methanol, the partial radial distribution function shows a pronounced maximum at around 2 Å: the pair has the highest probability to exist at this separation distance. In contrast, the separation distance between water and acetonitrile is larger in the other droplet, the first pronounced maximum is missing and the probability of the pair to exist is starting later, at around 3 Å. This again supports the theory that methanol and water mix more evenly.

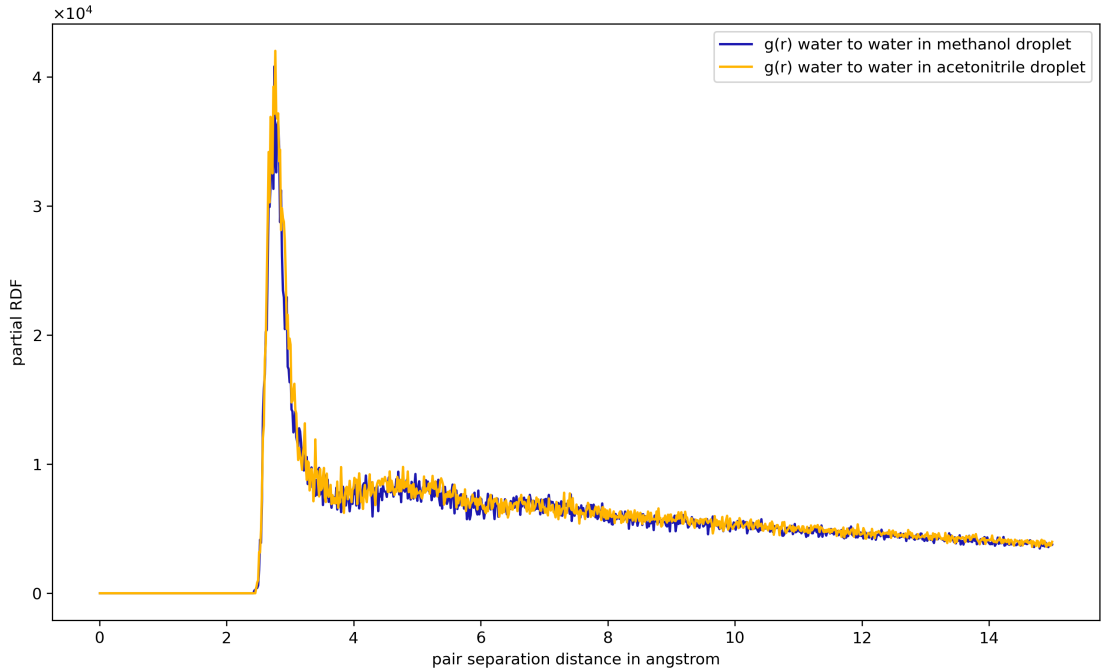

Figure 3.7: Partial radial distribution function for an acetonitrile / water (yellow) and a methanol / water droplet (blue). Here the pair separation distance between two water molecules is analyzed. The water molecules in an acetonitrile / water and the methanol / water are at exactly the same distance from each other.

The analysis of the coordination of water to other water molecules reveals a stark difference to the radial distribution between the solvent components (Figure 3.6 vs. Figure 3.7). The acetonitrile / water droplet and the methanol / water droplet exhibit nearly identical RDFs for the water molecules in both droplets. The probability of the distance of water molecules to each other seems to show no difference despite the change of organic solvent as the other component. Different alcohols (ethanol and isopropanol) show a very similar behavior in subsequent sets of simulations. These results for different mixtures are in accordance with the actual qualitative physical properties of their solubility, specifically their polarity, the approach to investigate the dynamics of charged droplets with the means of a commonly used MD code and force field seems even more promising [56]. Acetonitrile is less polar than methanol, which can be deduced from the first coordination analysis (cf. Figure 3.6). The water molecules have

a smaller distance to methanol than to acetonitrile. The geometries of the different droplets after the relaxation were used as initial configurations for further simulations.

3.3.1.1 Analytes in simulated droplets

In the previous section mixing / solubility properties of two different solvent systems in droplets were investigated. Since the calculations appear to reproduce qualitative experimental observations and expected behavior [56], subsequent MD simulations with LAMMPS of more complex systems are performed. Lithium or ammonium in a united atoms approach was chosen as charge carriers in the initial set of simulations. These model systems are far from the actual conditions in ESI experiments where droplets are charged by protons and charged analytes. In a second series of simulations which attempt to model the droplets closer to reality, analyte molecules were constructed and placed in the simulated droplets. Prior experimental work in our group investigated diaminooctane and its behavior in ESI processes [97].

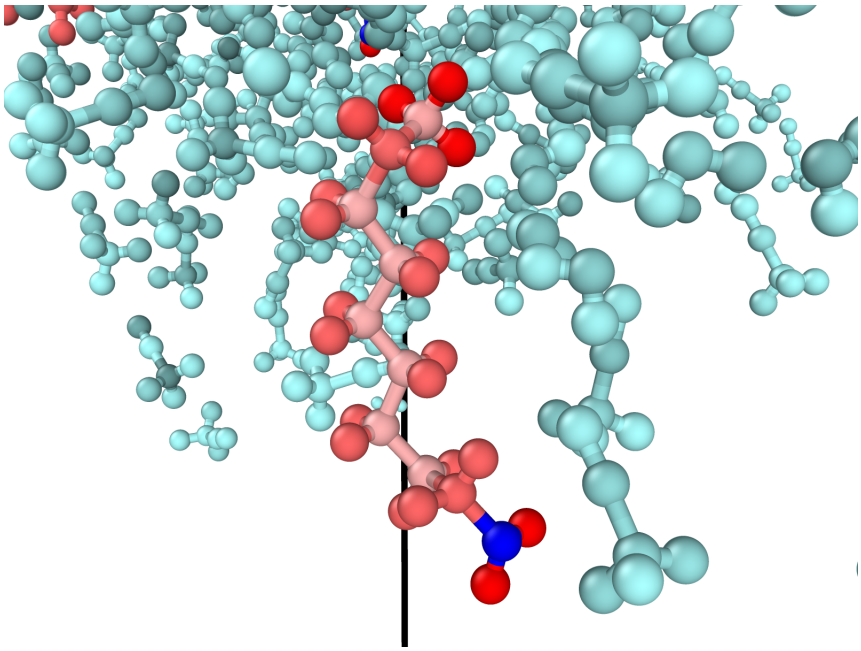

Figure 3.8: Diaminooctane in a charged droplet simulation: The atoms are colored by partial charges of the analyte. The highest positive charge is located on the farthest methyl-group from the amine-function. The N-atom of the amine-function is partially negatively charged and is facing away from the droplet center. The positively charged methyl-group is positioning itself into the center of the droplet.

Acetonitrile and water were chosen as solvent system. Diaminooctane as analyte can be present in its single or double charged state. To construct such a complex charged molecule with moltemplate with the consideration of the selected force field, a simplification had to be made. As described before, single protons are not catalogued in the force field, due to their different diffusion in contrast to other small ions. Other ions mostly exhibit Brownian diffusion, whereas water is in addition subject to Grotthuss diffusion [89]. This makes the mobility of protons 7 times higher than that of Na^+ and 5 times higher than that of K^+ and more difficult to describe them in a simple force field [98]. However, the analyte can be constructed as a hybrid of different listed molecule groups. In the case of diaminooctane: An uncharged amine and a charged amino acid. The body of the molecule is taken from the amine and the charged end is built with parameters from the charged amino acid. The sum of the partial charges of these atom

types leads to a decimal number, which is obviously not representing physical reality. But for the purpose of investigating the qualitative dynamic of the droplets interacting with a larger charged molecule, simulations with a hypothetical proxy molecule were deemed feasible. The singly charged proxy analyte molecule has a charge of +1.02, which is rounded to 1 and the doubly charged has charge of +2.04, which is rounded to 2. Figure 3.8 shows the analyte molecule within a simulation; the atoms of the analyte are colored with a color map according to the partial charges of the molecule. The positive charge is oriented towards the solvent molecules of the droplet, while the blue marked N-atom is partially negatively charged. The net charge of the molecule vanishes, the analyte is electrically neutral in total. The position and orientation of the analyte molecule is similar to surfactants, which also orient themselves on the surface of droplets similarly. The charged analyte was observed in a slightly bend and a linear structure (cf. Figure 3.9), which is also typical behavior of charged long-chained hydrocarbons and is therefore another indication, that MD simulations can produce realistic results of physical and chemical properties. However, due to the repulsive forces of the partial charges the linear structure is more common, which was investigated in more detail in the work of C. Polaczek [97].

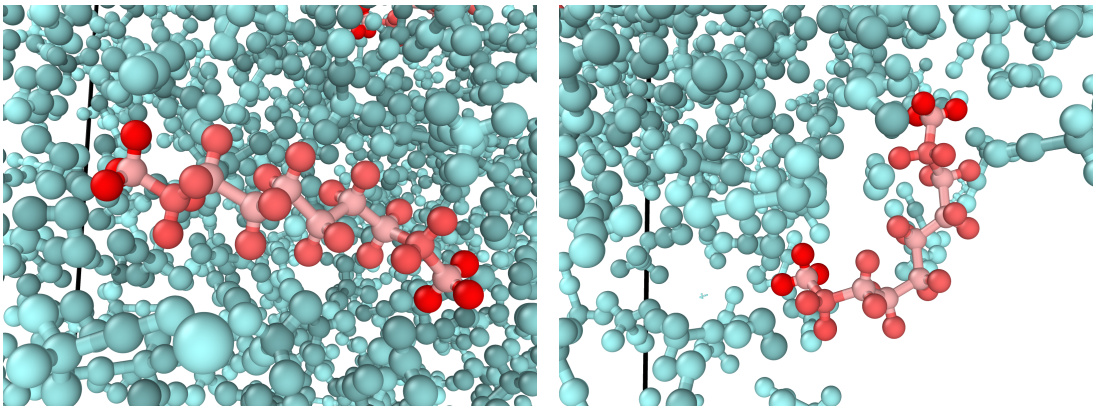

(a) Linear orientation **(b)** Bend orientation

Figure 3.9: Bend and linear structure for the doubly charged diaminooctane analog proxy molecule. The analyte is colored according to the partial charges of the atoms (red = positive). The solvent molecules are colored turquoise. The analyte can be seen to exist in both configurations within the droplet, which is typical behavior for long-chained hydrocarbons.

To compare the simulated droplets with simple atoms as charges and the simulated droplet with the more realistic proxy analyte, the partial radial distribution functions are shown in Figure 3.10.

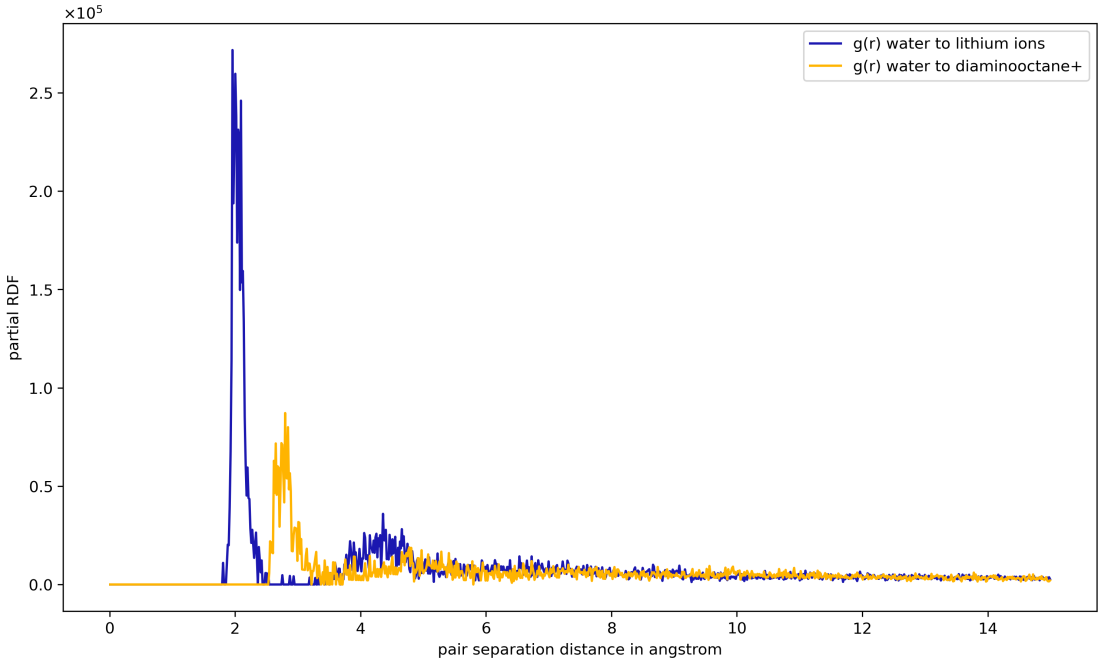

Figure 3.10: Partial radial distribution function for lithium and diaminooctane proxy analyte: g(r) for water and lithium ions is shown in blue, g(r) for water and diaminooctane is shown in yellow. The analyzed pairs were chosen as the positively charged end of the diaminooctane proxy and the O-atom in water and the distance between a lithium-atom and the O-atom in water.

The partial radial distribution function of water to the positively charged end of diaminooctane is shown in yellow; the distribution function for lithium to water is plotted in blue. Although the distributions have some visible differences, the maxima of the water coordination to the respective ions occur at a similar separation distance of 2 Å and 3 Å. This implies a similar mixing behavior of the ions and the water. These results show, that even if a crude simplification of simply constructing charged analytes as approximate proxies from initially unrelated chemical groups in the force field, they exhibit plausible behavior similar to simple charged particles. These simulations demonstrate

that more realistic analytes can be simulated by LAMMPS. More simulations in this direction seem promising for a future project. Particularly, thermometer ions and their fragments are interesting systems for further modeling efforts.

3.3.2 Rayleigh Limit in MD simulation of charged droplets

The Rayleigh Limit is an important parameter defining the dynamic behavior of charged droplets [35]. It determines the maximum number of charges a droplet can hold before undergoing a so-called Coulomb explosion, which is assumed as the crucial factor for droplet disintegration. As seen before, LAMMPS simulation results show physicochemical properties of different solvent systems and analytes. Therefore, MD simulations should also reproduce the Rayleigh Limit of charged droplets. In a work by Malevanets et al., the shape of droplets was investigated with NAMD [99], a classical MD code which is available free of charge for non-commercial applications. They observed the ejection of charges from a water droplet in a string-like fashion. The charges, Na^+ ions in their case, did leave the droplet when the charges were near the surface. The phenomenon was reproduced with LAMMPS: Figure 3.11 shows an example of such an ejection event.

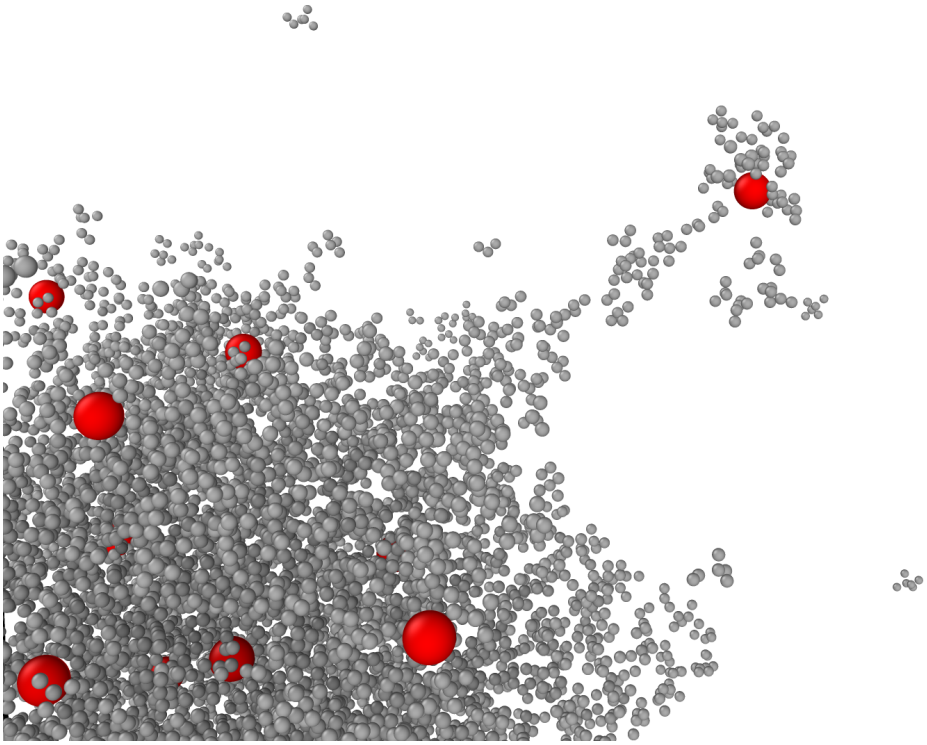

Figure 3.11: Ion ejection from water / methanol droplet. Solvents are colored gray, Ions colored red and their radius is increased for better representation. A jet consisting of a few solvent molecules forms and leaves the droplet with a charged particle. This behavior could be observed in multiple simulation runs.

The solvent molecules of the droplet are shown in grey while the radii of the ions (marked in red) were increased to improve visibility. A few solvent molecules are leaving the surface of the droplet with a charged atom. This could be observed frequently in different simulations of charged droplets. If an ion is near the surface of the droplet for a few timesteps, the probability of a solvent jet leaving the droplet is significantly higher. Malevanets et al. also investigated the overall shape of droplets, if the number of charges is increased. Protrusions of solvents and ions can be observed on the surface of the droplet. They performed the simulations with modified ions: The electrical charge and the radius of a Na^+ was increased [99]. This can be achieved by a simple

force-field parameter modification. The result of these simulations was so-called “star-shaped” droplets. The same protrusions are observable in LAMMPS simulations, notably even without modification of the force field parameter of the ions. Only the number of ions was increased, to reach a higher net charge closer to the Rayleigh Limit. Figure 3.12 shows a set of exemplary simulation results. The simulated droplets consist of 1000 water and 1000 methanol molecules and a varying number of charges. The unified (one particle) approximation of ammonium ions was chosen as charge carriers. The number of protrusions forming the “points” of the star shape is increasing with higher number of charges. The protrusions contain ions and solvent molecules. As observable in Figure 3.12, the protrusions even form a regular structure around the droplet with the highest number of charges. The phenomenon of the star-shaped droplets described in Consta et al. and later in Malevanets et al. can be reproduced with LAMMPS and different ions [45, 99]. The droplets have a charge density near the Rayleigh Limit, which increases their mobility and therefore the transmission in the MS systems becomes even more likely. Also with ion ejections happening, the droplets remain charged and thus detectable in the mass spectrum. LAMMPS, again, proves to be a capable tool to investigate notions of the charged droplets seen in ESI experiments.

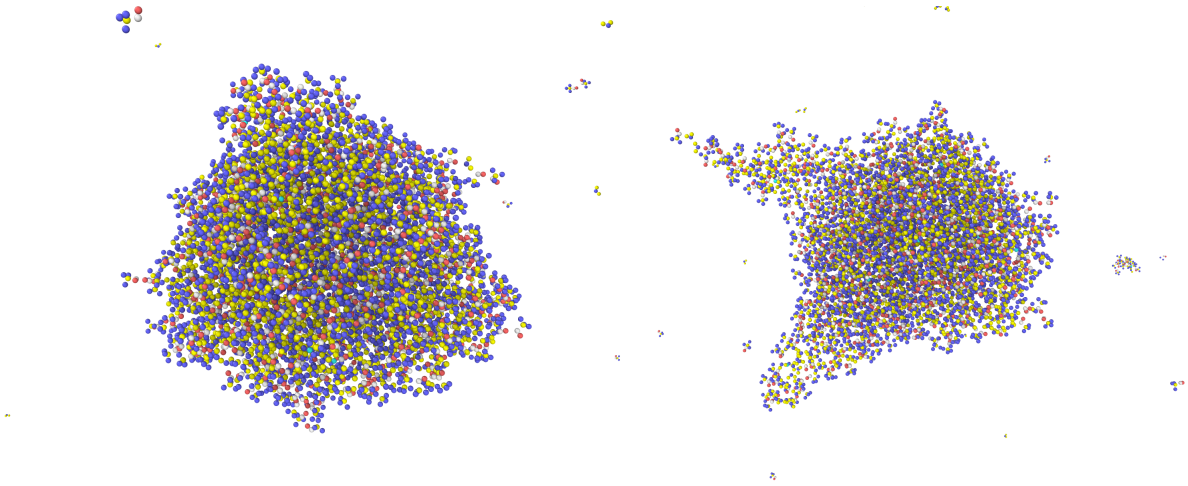

(a) Droplet with 12 ions

(b) Droplet with 27 ions

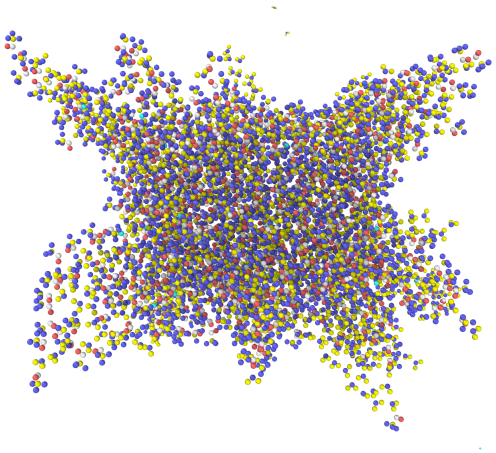

(c) Droplet with 64 ions

Figure 3.12: LAMMPS Simulation of a water / methanol droplet with increasing number of charges. Top left: 12 ammonium ions. Top right: 27 ammonium ions. Bottom: 64 ammonium ions. The droplets develop more protrusions with increasing net charge. The protrusions take a specific, aranged shape around the droplet according to the number of charges.

3.4 Internal energy transfer of simulated droplets

As discussed above, charged droplets are moving from the ion source to the entrance of the mass spectrometer through the neutral background gas due to the applied electric field. The collisions with the background gas particles potentially leads to a significant increase in internal energy of the droplets, as collision energy can be transferred to the droplets in inelastic collisions. In experiments this should lead to a higher evaporation rate or even fragmentation of the analytes. In the following, the energy transfer to the droplet was investigated with MD simulations to investigate how much the internal energy is increased by an energetic collision, how long the molecules of the droplets need to distribute the energy evenly within the droplet and if there is a limit for energy uptake from collision projectiles.

3.4.1 Collisions with projectiles

As first step to answer those questions, single impactors or projectiles were examined. In particular, argon was used as a projectile. Argon is also available in the OPLSAA force field and could therefore readily be considered in a MD simulation in addition to the droplet. The argon atom was placed in the simulation box and was initialized with a pre-defined velocity vector. Its trajectory was aimed directly at the droplet. The reason behind this approach was that the acceleration of droplets is not easily replicated due to the limits of MD simulations. The kinetic energy of the droplets can easily reach 20 eV or more in MS instruments due to the applied electric acceleration. To give a general overview of the dynamics of the charged droplets, they were investigated with the following projectile approach. The initial timestep of an impact simulation is shown in Figure 3.13. The argon projectile is oriented toward the droplet in x-direction. The velocity of the projectile is set according to the intended collision energy.

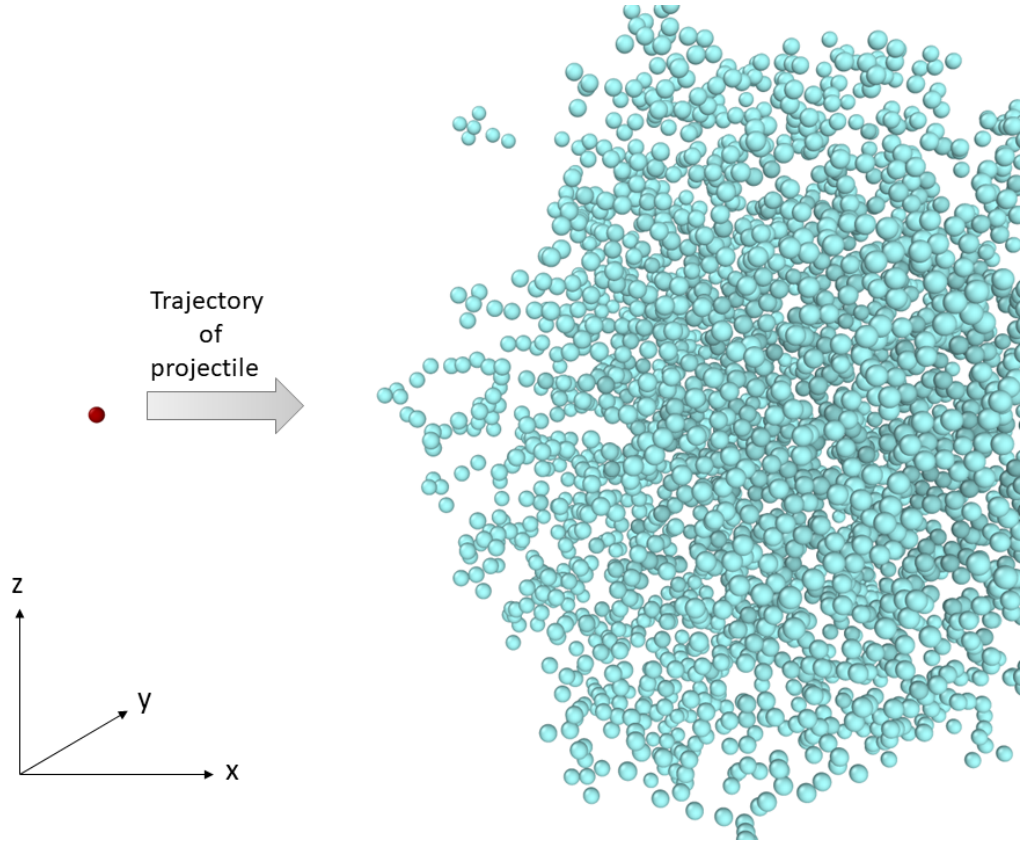

Figure 3.13: Acetonitrile / water droplet (turquoise) with argon projectile (red) in the initial time frame of a collision simulation. The argon projectile is oriented towards the surface of the droplet in x-direction. It will hit the droplet with a specific velocity according to the intended collision energy.

Figure 3.14 shows four frames of the simulations after the collision. The particles are colored according to their kinetic energy, which was calculated with the post processing capabilities of OVITO. Blue was chosen for a low kinetic energy in contrast to red, which symbolizes a higher kinetic energy. The projectiles radius was enhanced and the color of it was changed to orange, to make it more visible throughout the trajectory. The first timestep of the collision is shown in the upper left panel (Figure 3.14 a)). The droplet is entirely colored blue, because the collision event did not happen. The projectile is coming from the left side of picture. The first panel is followed by the frame in the upper right panel, in which the projectile just collided with the surface of the droplet

(Figure 3.14 b)). The impact leads to an energy transfer of the argon atom to the molecules close to the impact size apparent by the change of the color. The next frame is depicted in the lower left corner (Figure 3.14 c)). Some molecules are “sputtered” off the droplet surface due to the collision and are leaving the collision site. In the next frame, in the lower right panel, the energy is starting to distribute within the droplet and the projectile is reflected of the surface of the droplet (Figure 3.14 d)). The number of highly energetic particles in the frame is decreasing rapidly.

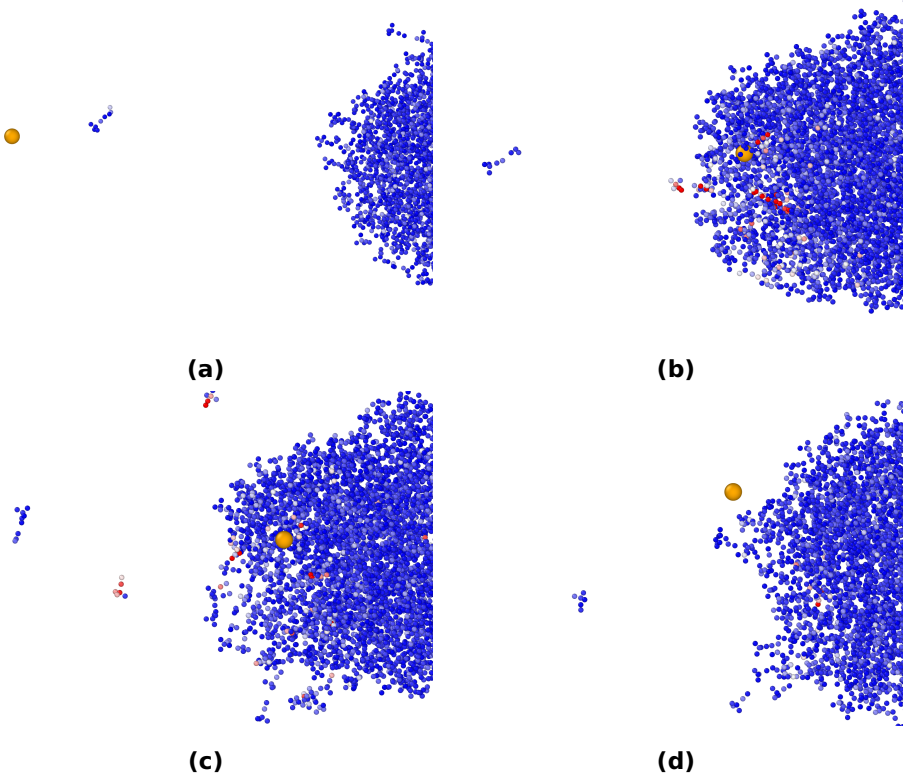

Figure 3.14: Collision event of argon projectile with a droplet. The particles are colored according to their kinetic energy. A low kinetic energy is depicted in blue and high kinetic energy in red. Immediately before the collision (upper left panel), only the argon projectile has high kinetic energy. Just after the collision, the molecules hit by the projectile see an energy increase, visible by their now red color (upper right panel). The energy of the projectile is distributed within the droplet or is leaving the droplet aggregate with sputtered molecules (bottom panels).

The visualization in Figure 3.14 show the behavior of the droplets during and after the collision event. The rapidly lowering number of atoms with high kinetic energies indicate a quick distribution of the energy within the droplet. To investigate this energy redistribution further, the total energy of all molecules within the droplet is plotted against the simulation time in Figure 3.15. The total energy is the sum of the potential and kinetic energy and can be recorded by LAMMPS for every simulated timestep and every atom. The collision event is clearly visible as energy step at approximately 50 ps simulation time. The projectile of this simulation had a kinetic energy of 20 eV. This energy is almost completely transferred to the droplet and immediately distributed. This simulation was repeated for a different kinetic energy of the projectile. Figure 3.16 shows a simulation result with to 45 eV collision energy. However, the general observation is very similar to the simulated collision with 20 eV: The kinetic energy of the projectile (45 eV) is again almost completely absorbed by the droplet.

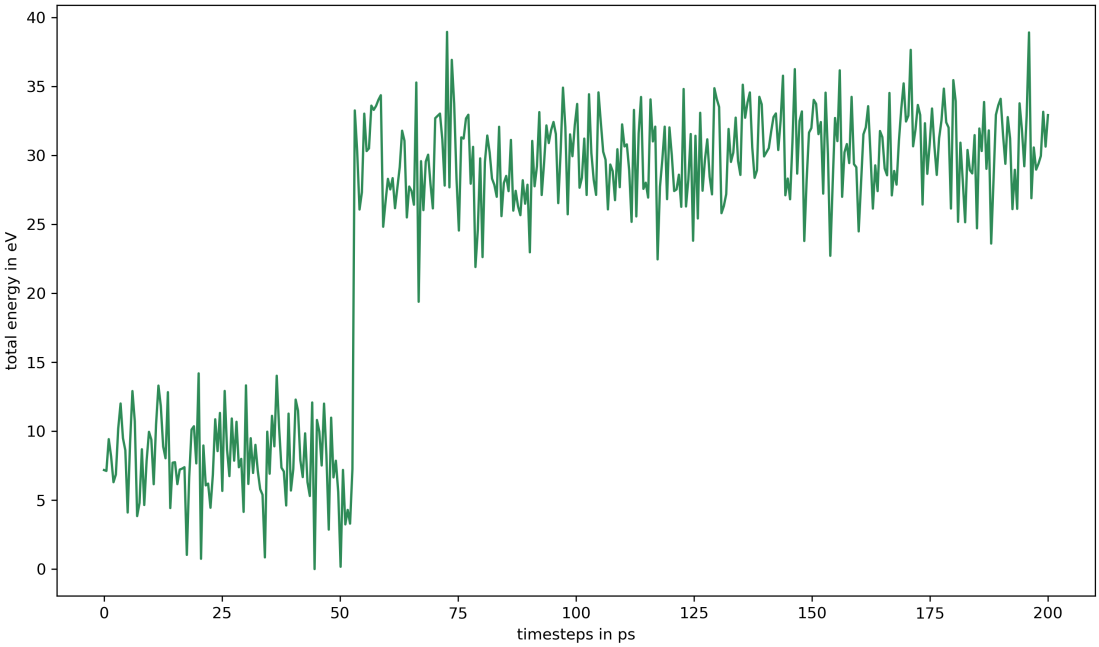

Figure 3.15: Total energy, which is the sum of potential energy and kinetic energy of all particles within the simulated droplet, for a collision event with a kinetic energy of 20 eV. The collision event happens at approximately 50 ps and is visible as strong energy step. The total energy of the particle increases according to the kinetic energy of the projectile, indicating that essentially the full collision energy is transferred to the droplet.

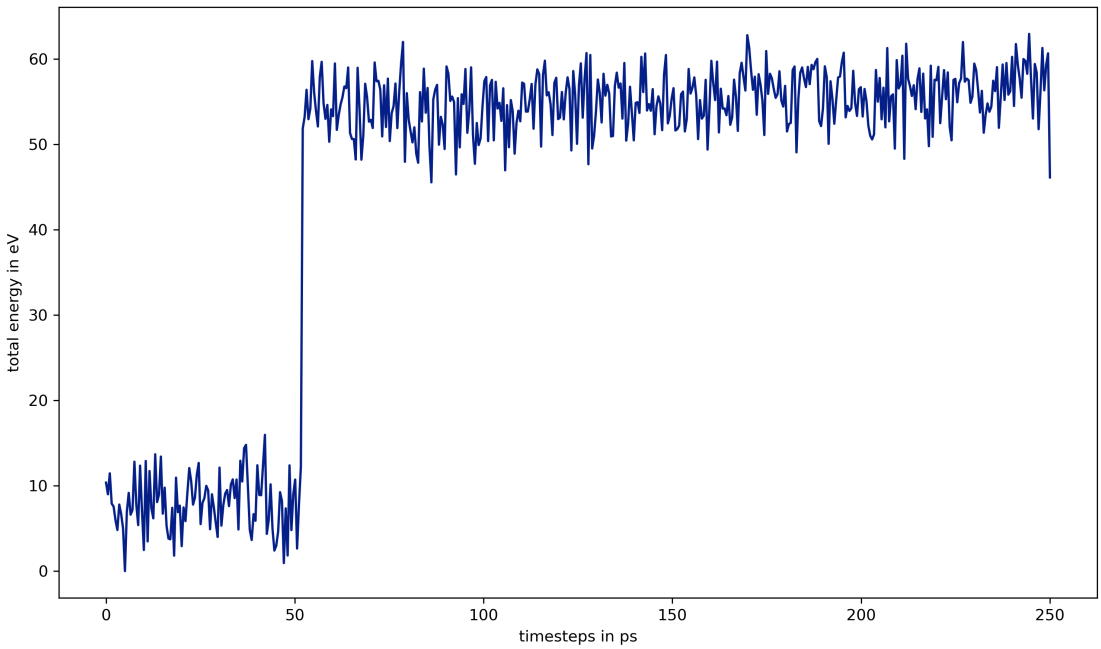

Figure 3.16: Total energy of the particles for a collision event of one argon projectile with an acetonitrile / water droplet. In this simulation the projectile had a kinetic energy of 45 eV. The collision happens approximately at 50 ps. The total energy of the particles in the droplet increases accordingly to the collision energy, demonstrating full energy transfer from the impactor to the droplet.

This begs the question, if there is a limit of energy uptake the droplet can absorb before it begins to behave differently, like disintegrate for example. In an attempt to assess this, multiple, successive collision events were simulated. Argon projectiles from different directions of the simulation box hit the droplet in one simulation run. Two runs are shown in Figure 3.17. The light blue plot represents the simulation of projectiles with a kinetic energy of 1 eV each. The droplet exhibits the same general behavior as before: The energy is completely absorbed and distributed within the droplet. A second run is shown in dark blue. The projectiles were initialized with a kinetic energy of 20 eV each. The collisions are clearly discernible as steps in the development of the total energy. The projectiles collided with the droplet 5 times. This leads to a total energy uptake into the droplet of around 110 eV during the simulation. Surprisingly, the droplet did not show any substantial change of behavior. It did not start to disintegrate or frag-

ment and there is no significant decrease in energy transfer into the droplet by impacts later in the simulation. To put this into perspective: Common electron impact ionization (EI) experiments are done by 70 eV electron energies to ionize almost every molecular analyte, which generally leads to fragmentation of most analytes [54].

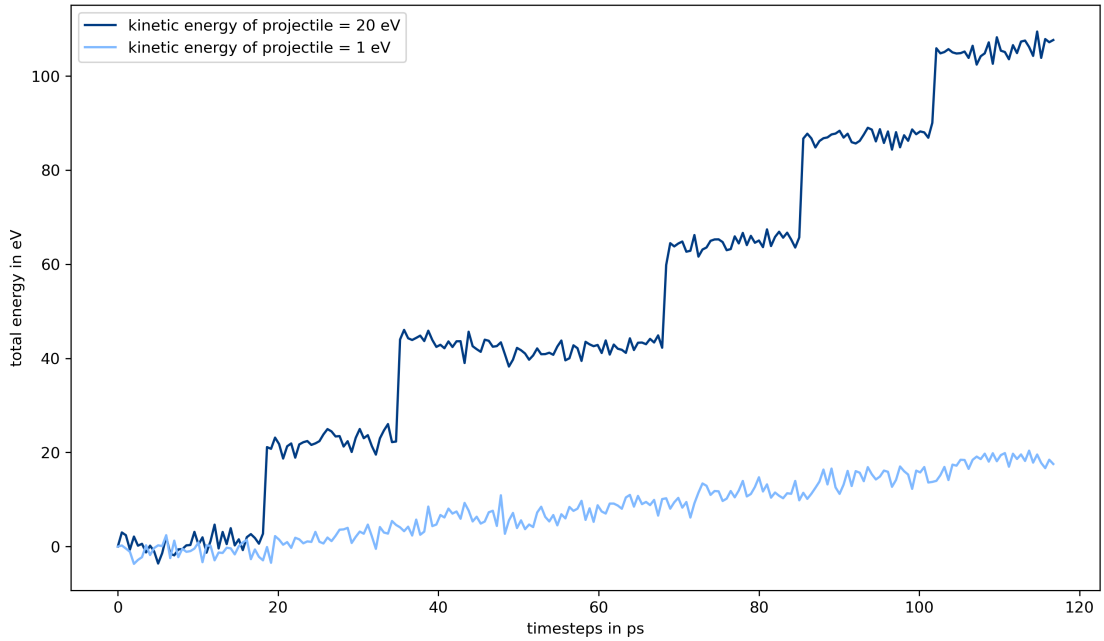

Figure 3.17: Total energy of simulated methanol / water droplets with multiple, successive collisions of argon atoms. The total energy increases according to the kinetic energy of the different projectiles. In light blue the total energy for 6 collision events with a kinetic energy of 1 eV is shown. The individual collisions are not discernible due to the comparably strong numerical fluctuations of the total energy but the general transfer of collision energy into the droplet is visible. In dark blue, the kinetic energy of the projectiles was increased to 20 eV. In this case, the five individual collisions are clearly visible. In this simulation one of the projectiles was inaccurately initialized so that it did not hit the droplet, resulting in the missing increase at around 50 ps.

This simulation was repeated with a different projectile to assess if this is a phenomenon specific to the structure of the projectile. However, the energy transfer of ammonium ions (in a united atoms model) as projectiles occurs in the same fashion. This is shown in Figure 3.18. The projectiles had a kinetic energy of 9.3 eV each, which is entirely

transferred to the droplet by the collision events also. After all collision events, the droplet had an energy uptake of 70 eV in total.

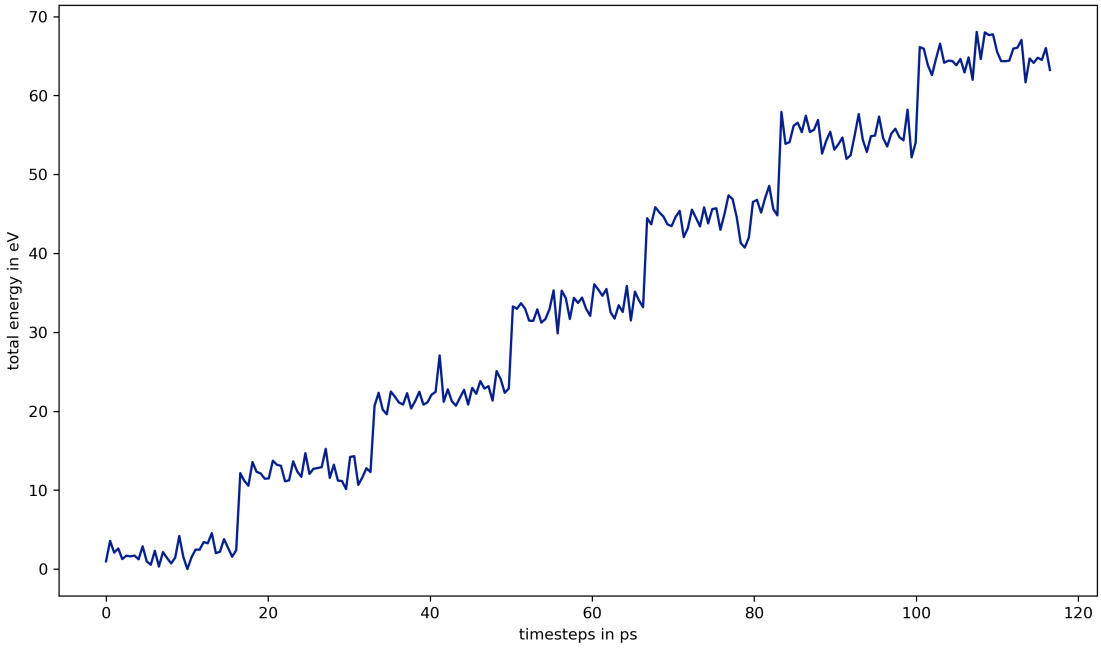

Figure 3.18: Total energy of multiple, successive collision events of NH_4^+ with a methanol / water droplet. The projectiles had a kinetic energy of 9.3 eV each. The total energy in the droplet, again, increases according to a transfer of the collision energy into the droplet.

The presented simulations are evidence for the high stability of the droplets when they are colliding with single or multiple particles. They do not disintegrate, even after multiple collisions. The distribution of the kinetic energy into the internal degrees of freedom of the droplet happen very quickly after the impact. As described, a disintegration of the droplet is not observable in the collision simulations. However, the collision event influences the droplets behavior in other ways. Figure 3.19 shows a droplet before and after a collision with a projectile of 45 eV kinetic energy. The point of view is not changed between the two frames, and a translation of the droplet is clearly visible: The droplet is moving to the right approximately 33 Å. In the figure, the atoms of the droplet are colored by their particle IDs, essentially just a running index for the individual particles. This shows that the droplet does not only move, but also rotates clockwise due

to the impulse transfer from the collision. Additionally, the molecules in the droplet appear to be packed more tightly in the last frame. This was investigated further by a coordination analysis with a radial distribution function.

(a) **(b)**

Figure 3.19: Droplet moving after the collision with a projectile with a kinetic energy of 45 eV: The droplet particles are colored according to their particle ID. The viewing perspective between the first frame (left) and the last frame (right) is not changed, which shows the translation and rotation of the droplet.

To recall, the partial radial distribution function provides information on the probability to find a certain pair in a specific distance. Figure 3.20 shows the partial radial distribution for the distances between the ions in the droplet for the first (light blue) and the last frame (dark blue). The radial distribution function was smoothed by an envelope function as the small number of ions produce a scarce signal otherwise. The pair separation distance between ions is decreasing from 6 Å to 4 Å after the collision event: The ions are positioned closer to each other. This could lead to an increase in repulsive forces and contribution to the total energy increase after the collision event.

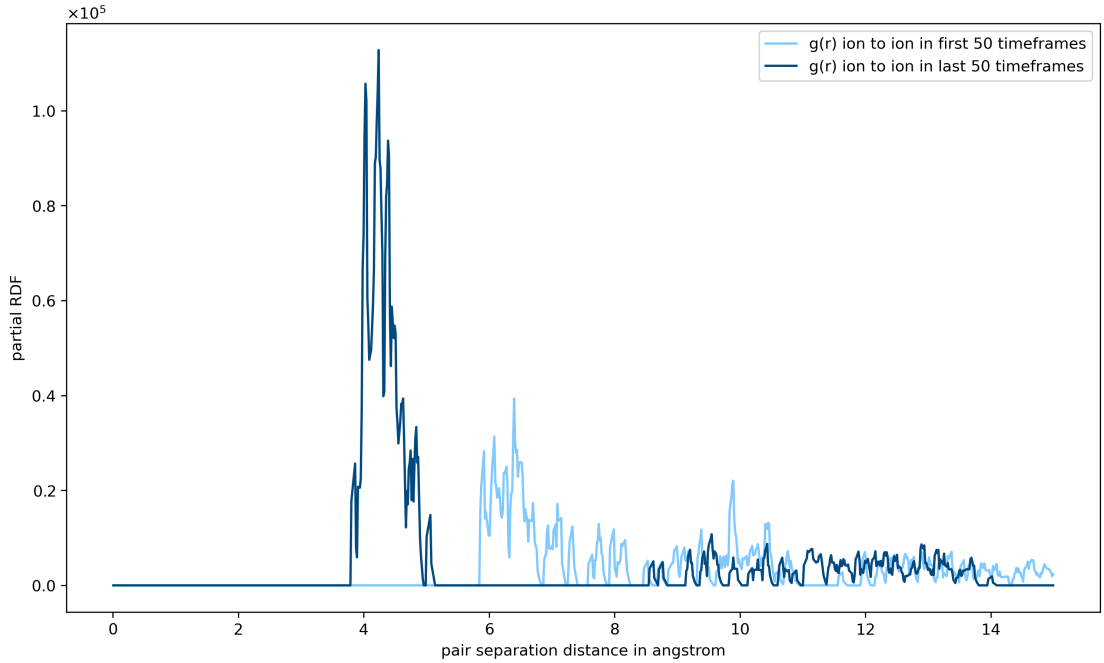

Figure 3.20: Partial radial distribution function of the ion-ion-distance before and after the collision for the methanol / water droplet. The first frame of the simulation is shown in light blue and shows a maximum at around 6 Å. The last frame is shown in dark blue. A new maximum is visible at around 4 Å. The distance between the ions decreases after the collision event transfers energy onto the droplet.

As expected, this phenomenon can also be reproduced for a droplet with a different solvent system (cf. Figure 3.21). Here, an acetonitrile / water droplet was analyzed with the same method as explained above. The ions are positioned closer to each other after the collision event in this simulation run also. They move from 7 Å to 5 Å.

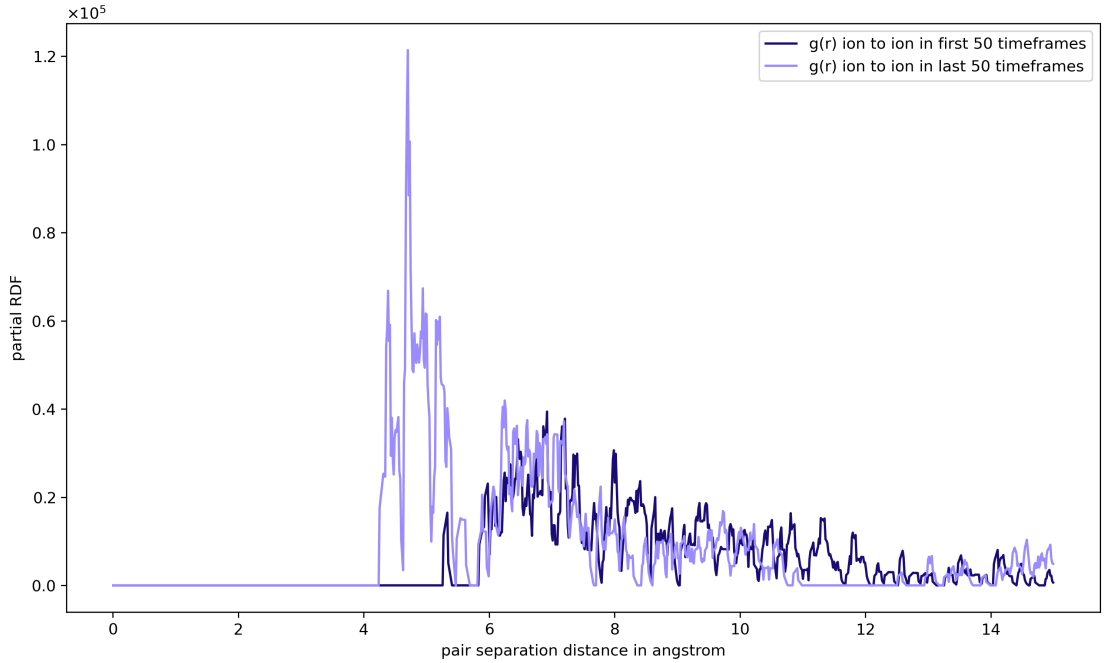

Figure 3.21: Partial radial distribution analysis of the ion-ion-distance before and after the collision of ammonium (modeled as unified particle) with the acetonitrile / water droplet. Again, the distance between the ions is decreasing after the collision event (light purple lines).

Although the simulated collision events did not lead to disintegration of the droplets, they influence the behavior of the droplets significantly. A single projectile increases the internal temperature of the droplet. It rotates due to the impulse transfer during the event and successive translation, and it even influences the distance between the molecules within the droplet as the coordination analysis showed.

3.4.2 Relaxation time estimation

By simulating multiple collision events, it became clearer how the energy of a collision with a projectile is distributed and how stable the droplets are. Still, the relaxation time of the droplet in which the collision energy is fully distributed over all particles in the droplet is still unknown. This is an important parameter to assess the kinetics of the effective temperature increase in the droplet due to collisions. The relaxation time of the droplets can be estimated by single collision event simulations: The droplet is cut

in two halves by their positions: One half is facing towards the impact site and the other is oriented away from it. As mentioned above, LAMMPS can record energies for every simulated particle and every timestep. The kinetic energies during the collision event can now be analyzed for the two halves separately. Obviously, the half facing towards the projectile should exhibit a sudden increase in total energy first. The kinetic energy of the half oriented away from the collision center can only increase due to the distribution of the collision energy by the interactions of droplet particles with each other. Figure 3.22 illustrates this simulation approach, where the separation of the droplet in two halves is indicated by the different colors of the simulated particles.

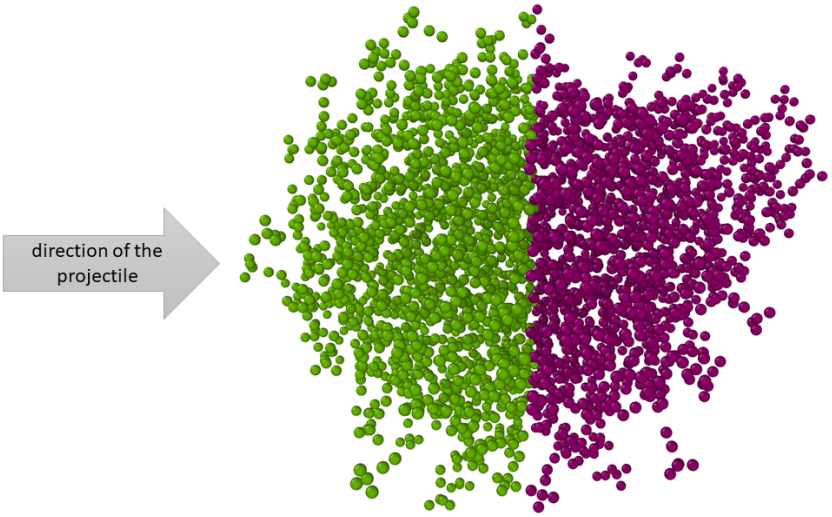

Figure 3.22: Representation of a simulated droplet to show how the molecules of the droplet were segmented to allow the estimation of the relaxation time. The projectile is facing the ”towards half” (green). The “away half” is shown in purple. The energy of the projectile is considered to be fully distributed over the droplet, when the mean kinetic energy of the two halves have converged to the same value.

The green half is directed towards the projectile and is called “towards half” in the following. The purple half is considered the “away half”. The estimated relaxation time of the droplets is defined as the time the collision energy is distributed to the upper

half of the droplet, which is facing away from the collision site. The energies of the two halves converges to a similar value over time which indicates a full distribution. Figure 3.23 depicts the mean kinetic energy of the particles of the droplet over the simulated time. The droplet in consideration is comprised of 440 water, 334 acetonitrile and 7 lithium ions. This leads to a m/z 3090, which is similar to actual droplet signatures observed in the Bruker ion trap. As explained above, the colliding particle is initialized with a velocity according to 20 eV kinetic energy. It collides with the droplet at around 50 ps. The energy of the lower half (dark green) increases with a steep step in the same fashion as shown before. Obviously, the mean kinetic energy of the upper half (light green) does not show a sudden energy step. It rather increases slowly until it converges with the mean kinetic energy of the lower half. This leads to a relaxation time of approximately 25 ps for this collision event. To put this timescale in perspective: Picoseconds is the range for hundreds of vibrations of a molecules. A vibration for a small molecule like HCl is reported as 8.95×10^{13} Hz, which is roughly 0.01 ps [100]. Therefore, the simulation results indicate that single collision events with high kinetic energies are distributed within approximately 100 vibrations of the molecules of the droplet, which is still considerably fast.

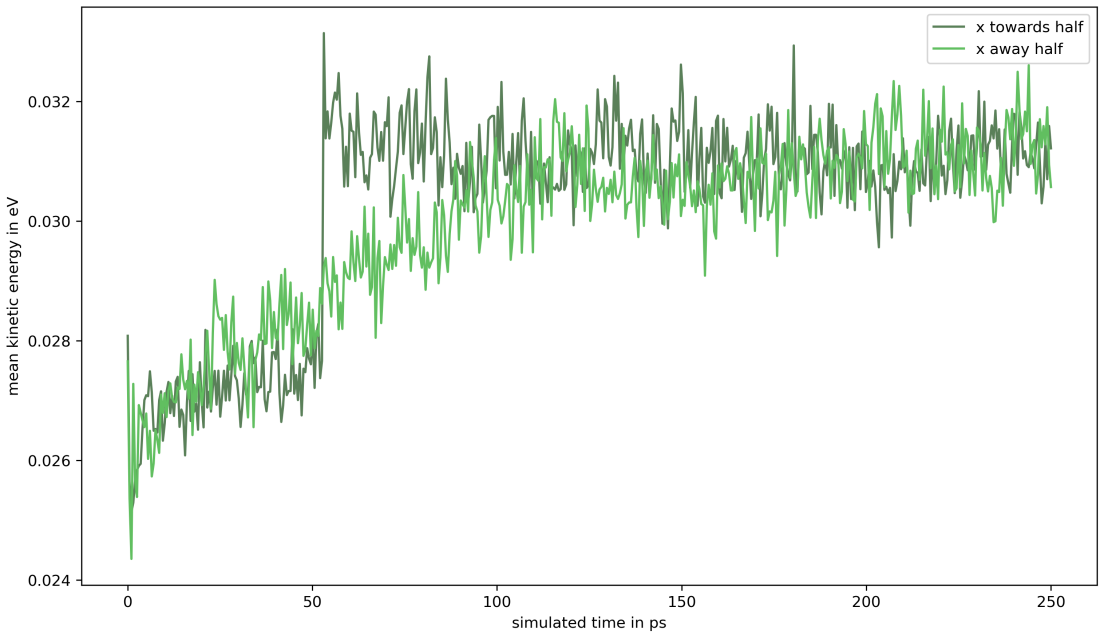

Figure 3.23: Relaxation time estimation for an acetonitrile / water droplet. The projectile had a kinetic energy of 20 eV and hits the droplet at 50 ps. The average kinetic energy of the droplet molecules is plotted against the simulated in ps. The average kinetic energy of the two halves converges after approximately 25 ps.

Figure 3.24 shows the same analysis of energy as shown above, but it includes the mean potential energy (upper right) and the sum of the kinetic and the potential energy (bottom). The potential energy does not show the collision with the projectile and is therefore not useful for relaxation time estimation. This is not surprising, as the projectile only experiences a kinetic energy increase in the simulation run, which is then transferred to the droplet. To ensure that the calculation and estimation is still correct, the mean kinetic and mean potential energy for both halves is summed and depicted as well. It shows a similar energy trajectory as shown for the previous collision simulations of the total energy (cf. Figure 3.15). The total energy does not show the energy drift at the beginning of the simulation. The mean kinetic energy shows such a drift up until the projectile hits the droplet (around 50 ps of simulated time). The reason behind this drift at the beginning of the simulation is still unclear, but it seems to be an artifact of the droplet cut in half as the potential energy halves show this drift also.

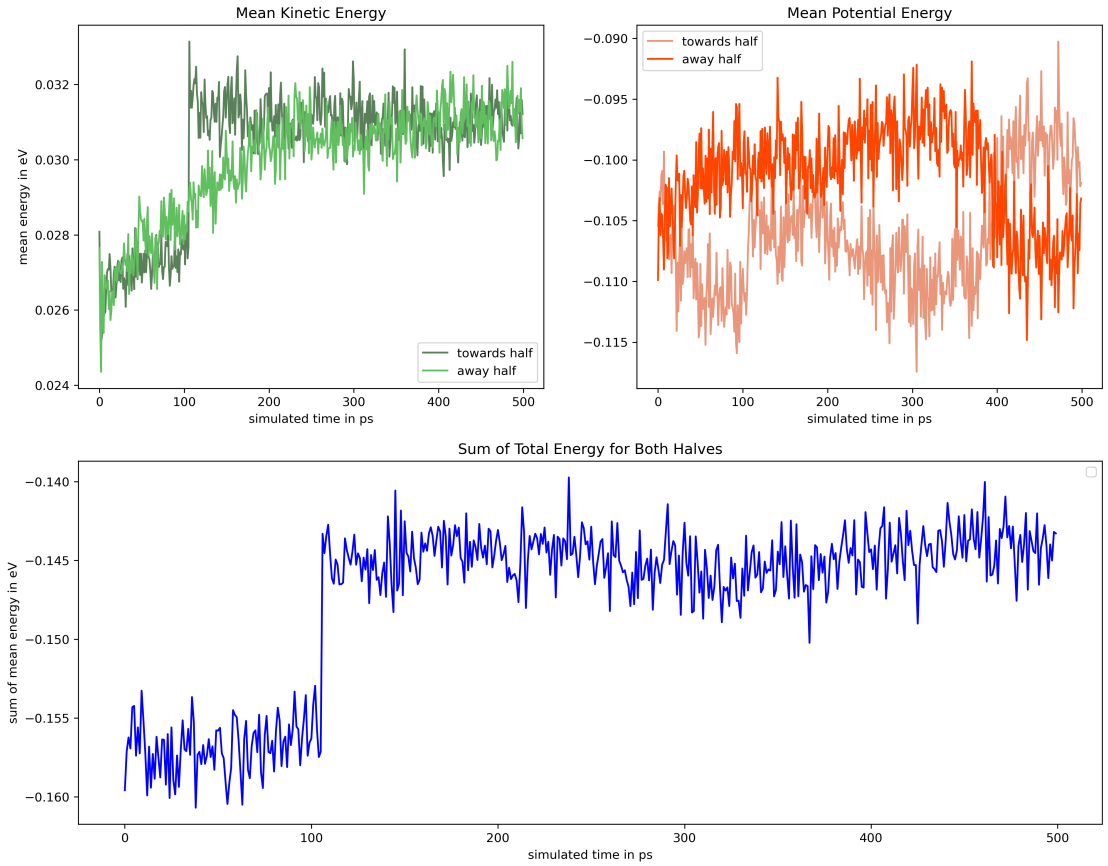

Figure 3.24: Depiction of kinetic, potential, and total energy of the same droplet. The potential energy cannot be used for this analyzation as the collision with the projectile cannot be seen as an increase in the potential energy.

If the kinetic energy of the projectile is increased to 45 eV) the apex at the collision event is sharper than before (cf. Figure 3.25). Again, the mean kinetic energies of the two halves converge after approximately 25 ps, although it fluctuates slightly after the collision. The relaxation time does not increase with higher kinetic energy of the projectile. Even this high kinetic energy brought by the projectile can be distributed within hundreds or thousands of molecular vibrations.

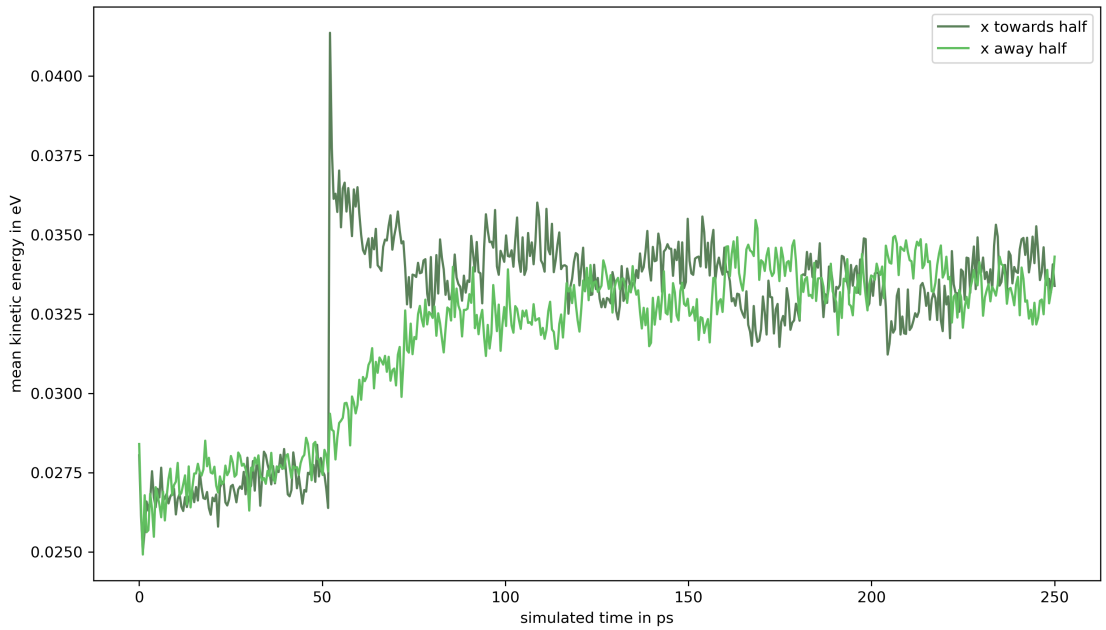

Figure 3.25: Relaxation time estimation for an acetonitrile / water droplet. The projectile had a kinetic energy of 45 eV and hits the droplet at 50 ps. The average kinetic energy of the droplet molecules is plotted against the simulated time in ps. The average kinetic energy of the two halves converges after 25 ps, but the mean kinetic energy of the half which is directed away from the collision fluctuates heavier than seen before (cf. Figure 3.23).

This estimation was repeated for larger droplets. A collision with a droplet with a m/z of 4642, consisting of 827 water, 655 acetonitrile and 9 ammonium ions, was simulated. The overall shape of the time dependent average kinetic energies of the two halves appears nearly identical to the simulation results with smaller droplets (cf. Figure 3.26). However, the relaxation time is longer. The average kinetic energies of the droplet segments converge 50 ps after the collision event. The transport of the energy by collision requires a longer time due to the larger average distances within the droplet the energy has to be transferred over. Still, the order of magnitude for the relaxation time is in the same range as of hundreds of molecular vibrations.

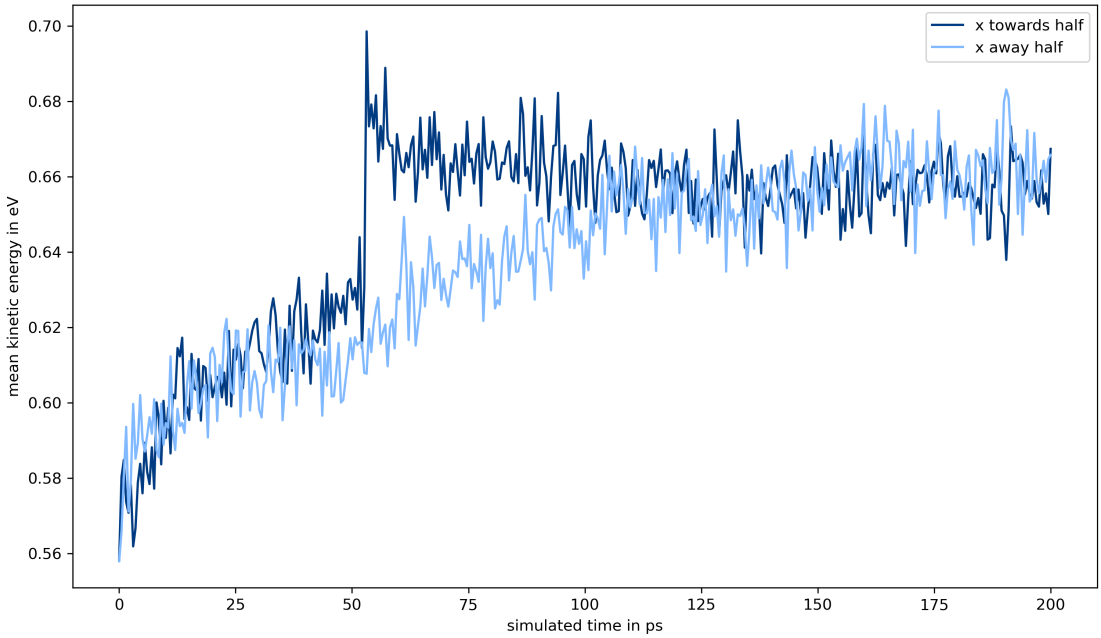

Figure 3.26: Relaxation time estimation for a larger acetonitrile / water droplet. The projectile had a kinetic energy of 20 eV and hits the droplet at 50 ps. The mean kinetic energy of the two halves converges after approximately 50 ps.

The kinetic energy of the projectile was increased to 45 eV in a second collision simulation of the larger droplet. Figure 3.27 depicts the mean kinetic energies for the droplet segments in this simulation run. Again, the mean kinetic energy of the two halves converges. However, the relaxation time increases to 150 ps (at 200 ps simulated time). The droplet needs longer to distribute the energy fully on all particles. It seems as if the half that is directed away from the collision even exhibits a slight energy drift at the end of the simulation.

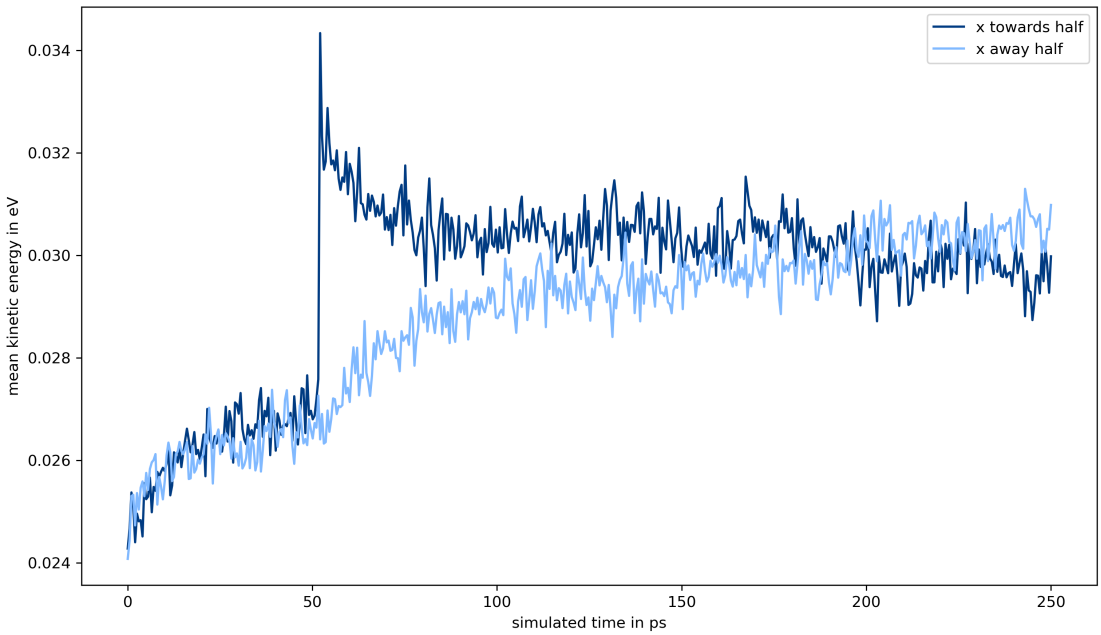

Figure 3.27: Relaxation time estimation for the larger acetonitrile / water droplet. The projectile had a kinetic energy of 45 eV and hits the droplets at 50 ps. The kinetic energy of the projectile is distributed at the end of the simulation run. Approximately after 150 ps (200 ps simulated time) the energy of the two halves converges. The half directed away from the collision shows a slight energy drift at the end of the simulation.

A droplet with a m/z 4679 consisting of 889 water, 961 methanol and 10 ammonium ions was simulated to further investigate the dependency of the general relaxation behavior on the chemical composition of the droplets. Due to the structural differences of the solvent molecules, the distribution of the energy due to intermolecular interaction within the droplet could be different. However, the relaxation time estimation for the methanol droplet leads to the same general conclusion as before (cf. Figure 3.28): With a projectile which has a kinetic energy of 20 eV, the kinetic energy is fully distributed within 50 ps after the collision event. This is, again, a very short time frame in comparison to the collision frequency between droplets and neutral background gas particles for example.

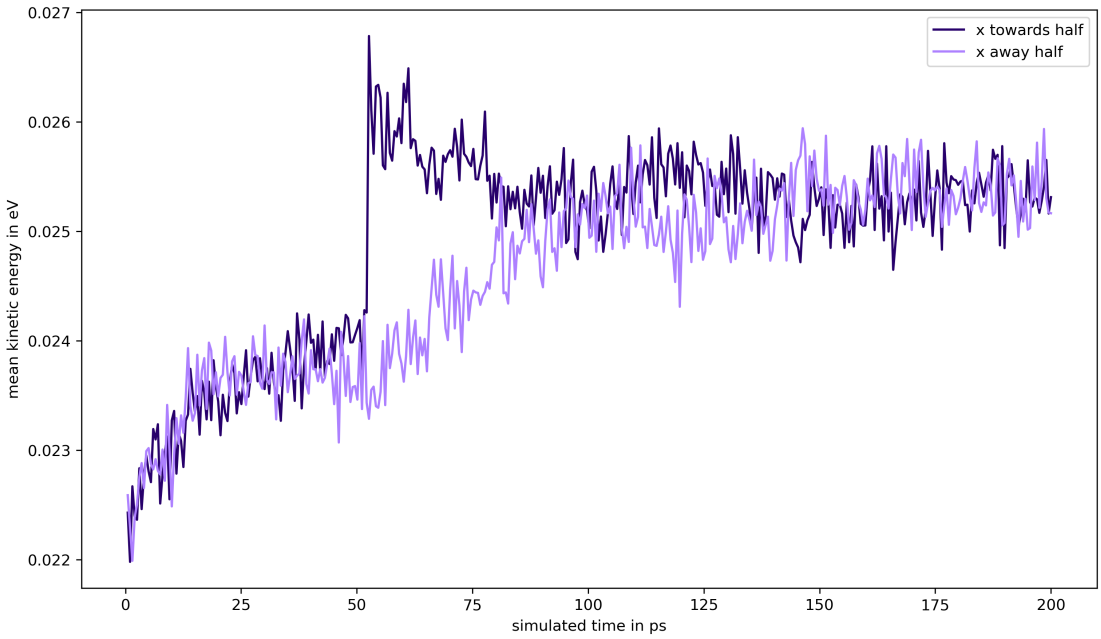

Figure 3.28: Relaxation time estimation for a methanol / water droplet: The projectile had a kinetic energy of 20 eV and hits the droplet at 50 ps. After 50 ps the kinetic energy of the projectile is fully distributed.

The kinetic energy of the projectile was also increased to 45 eV in a second simulation run. Similarly, to the results of the acetonitrile / water droplet, the mean kinetic energies of the two halves are converging after 100 ps (cf. Figure 3.29). The droplet needs a longer time to fully distribute the energy of the collision (cf. Figure 3.28).

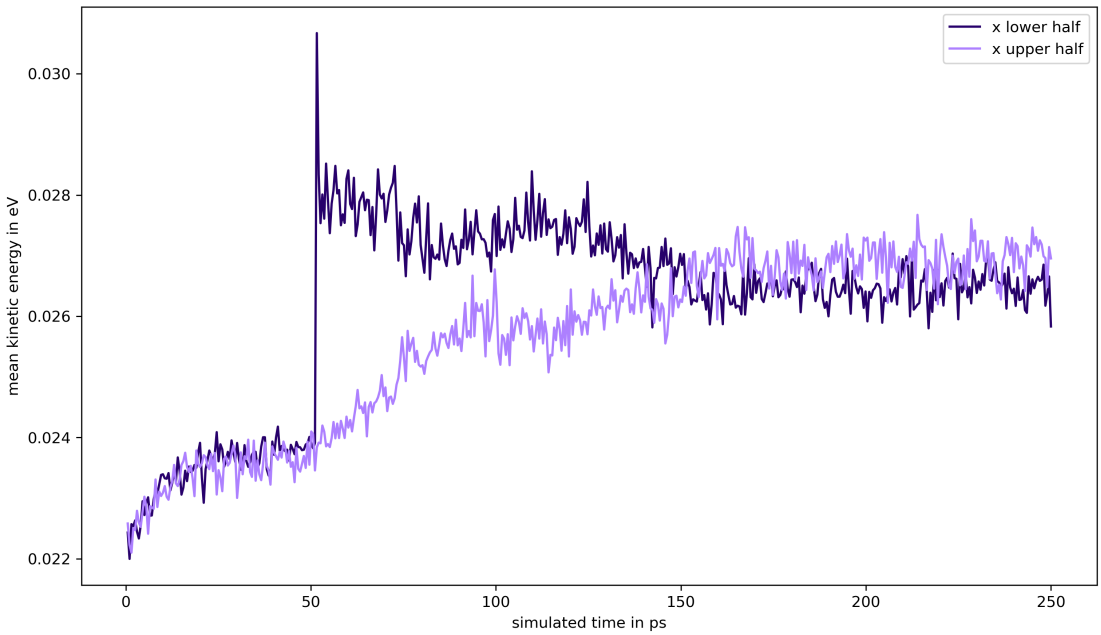

Figure 3.29: Relaxation time estimation for a methanol / water droplet: The projectile had a kinetic energy of 45 eV and hits the droplet at 50 ps. The increased kinetic energy of the projectile is fully distributed at the end of the simulation run. The relaxation time can be estimated at 100 ps (150 ps simulated time).

The small relaxation time for the droplets indicates a reason for their high stability. The droplet only needs a short time frame to distribute the energy of a collision fully. Even with higher collision energies, the droplet is able to distribute the energy within roughly 100 ps. As the relaxation time frame is estimated as this short interval, actual collisions of droplets with the background gas particles, which typically occur with a significantly lower collision frequency at the reduced pressures in MS vacuum stages, can be considered as a heating process of the charged droplets. The particles in the droplet are able to relax between two collision and the energy is evenly distributed. The droplets are therefore able to take up a large amount of energy due to the even distribution of the energy on many internal degrees of freedom.

3.4.3 Disintegration due to collisions

As described above, the simulated charged droplets generally exhibit a substantial stability: The relaxation time of a single impactor is estimated in picosecond range and the droplets stays intact as particle aggregates and even keep their overall shape. This leads to the question on how much energy through collision the droplets can accumulate before they begin to disintegrate and how the structure and coordination of the droplet is influenced right before the disintegration. The methanol / water droplet described before with a m/z 4679 was again taken to investigate this aspect. The droplet was simulated to collide with 100 argon projectiles with approximately 1 eV each. The projectiles were initialized with a specific force (0.1 (kcal/mol)/Å) randomly around the droplet. The collision energy of the projectile was estimated by the farthest possible distance to the droplet with the equation [100]:

$$W = F \cdot s \tag{3.1}$$

With W = work, F = force and s = distance. The longest possible distance to the droplet is the border of the simulation box. The border is approximately 250 Å from the droplet positioned. With this calculation the maximum value of the collision energy can be estimated. To ensure collisions between the projectiles and the droplet, they are constantly dragged into the center of mass of the droplet during the simulation. This means, that a collision with molecules of the droplet leads to no reflection off of the surface, as it was the case in the simulations shown before, but they are dragged even further into the droplet. The purpose of this simulation setup was to give a first rough limit of energy accumulation and a certain disintegration. The result in terms of total energy is shown in Figure 3.30. The total energy accumulation is 600 eV. This is due to the fact that the projectiles are forced into the droplet and are not reflected off the surface. Again, a collision did not follow physical conditions: The projectiles were simply forced further into the droplet even if they collided with another molecule.

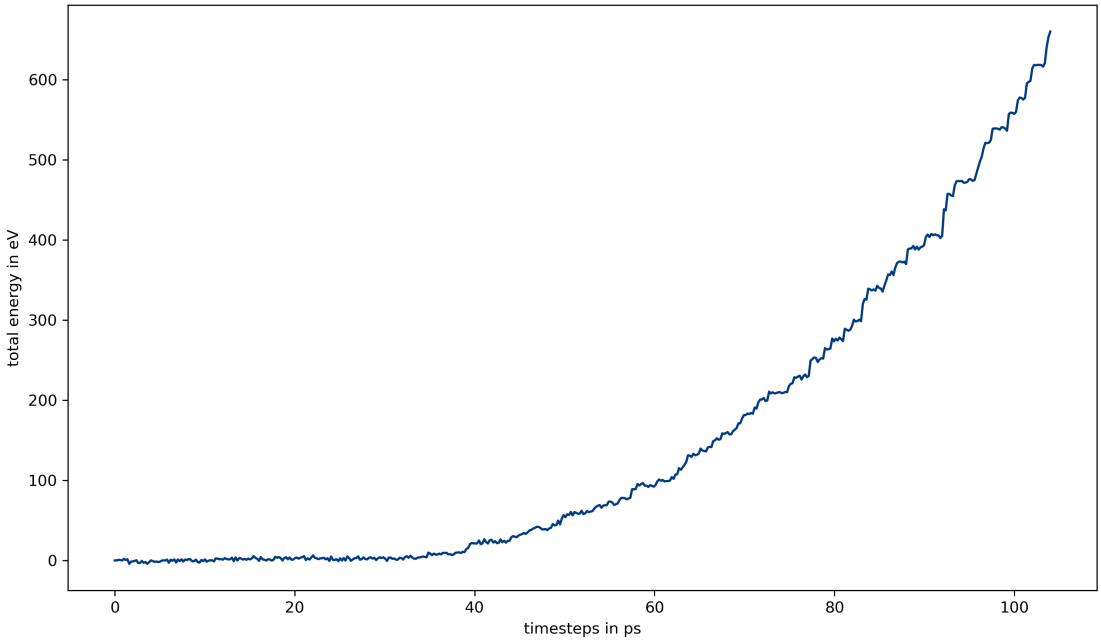

Figure 3.30: Total energy accumulation for 100 collisions with argon projectiles dragged into the center of mass of a methanol / water droplet. The droplet starts to lose shape at the end of the simulation run (100 ps).

The droplet begins to lose shape at the end of the simulation at around 105 ps. This is shown in Figure 3.31. The droplet is colored according to a cluster ID, which is assigned by a cluster analysis done with OVITO. It defines clusters in terms of molecular aggregates by the distance between particles in the clusters. In the following results the search radius for the cluster segmentation was set to 10 Å. The largest cluster is colored in green. In the last frame of the simulation, which is shown in Figure 3.31, the droplet can be considered as still intact by its visual appearance. Only a few molecules have detached from its surface and are therefore identified as individual clusters by the cluster analysis. This is surprising considering the substantial increase in the total energy visible in Figure 3.30.

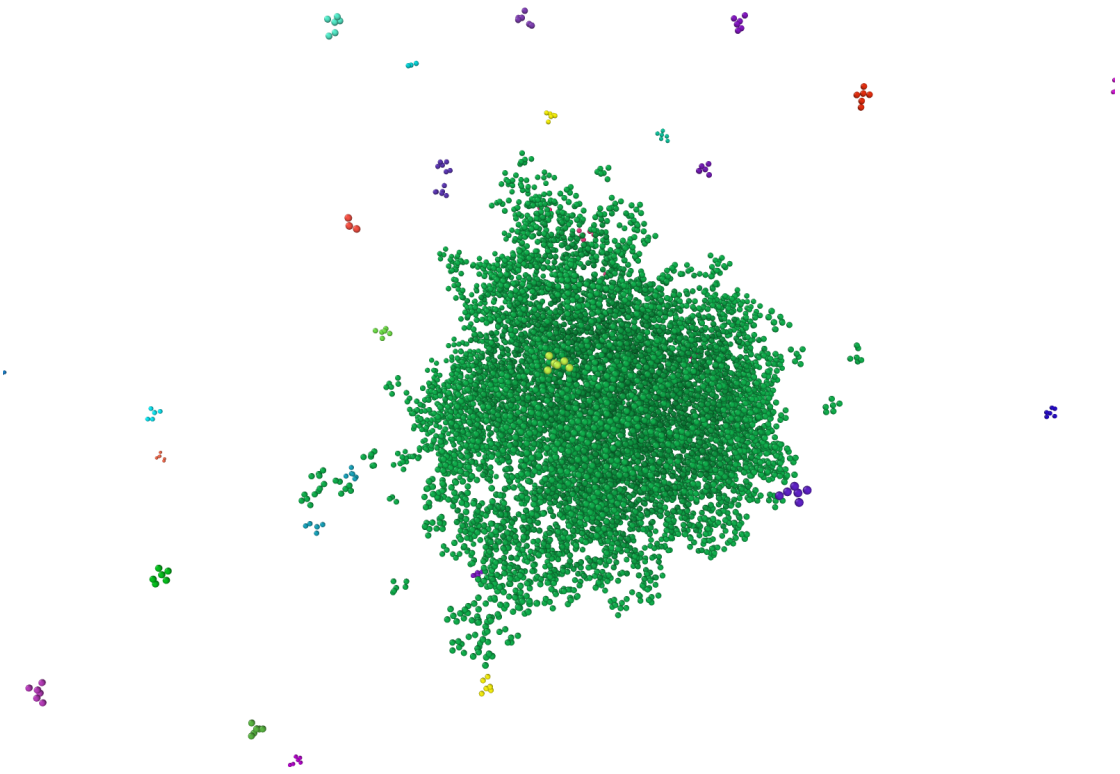

Figure 3.31: Droplet at the end of the simulation after collision of 100 projectiles with a kinetic energy of approximately 1 eV. towards the center of mass of the acetonitrile / water droplet. Despite the substantial total energy accumulation of 600 eV, the droplet is just starting to disintegrate.

In contrast, full disintegration of simulated droplets can be observed in subsequent simulation runs, if the kinetic energy of the colliding projectiles is increased as presented in Figure 3.32. Cluster analysis was repeated for these simulation runs also; the identified clusters are colored according to their cluster IDs in Figure 3.32. An interesting pattern of fragmentation into different sized clusters becomes apparent: The droplet does break apart in a whole spectrum of different sized clusters also including very small clusters and even single molecules but does not disintegrate into single molecules exclusively.

(a) (b)

Figure 3.32: Droplets after 100 projectiles with higher kinetic energies are dragged into the center of mass of the acetonitrile / water droplet. Left: 5 eV projectile energy, right: 10 eV projectile energy.

Figure 3.33 shows the total energy accumulation in the acetonitrile / water droplet after multiple collisions with projectiles with different kinetic energies. Although the simulations with high kinetic energy terminated early due to a numerical error in which a pair of atoms is distancing themselves too much between two timesteps, the energy accumulation for the disintegration simulations exhibit similar general behavior. The interactions between a pair of atoms are accounted for in a so-called neighbor list, which is missing an entry, if this error occurs. The simulation is immediately stopped. The simulation runs considering projectiles with higher kinetic energies show steep steps in the total energy. These are occurring when the droplet breaks apart into larger fragments. As mentioned above, this breakup is visible in Figure 3.32: In both renderings clearly show a larger cluster (in pink) which was formed by the droplet fragmenting in larger pieces.

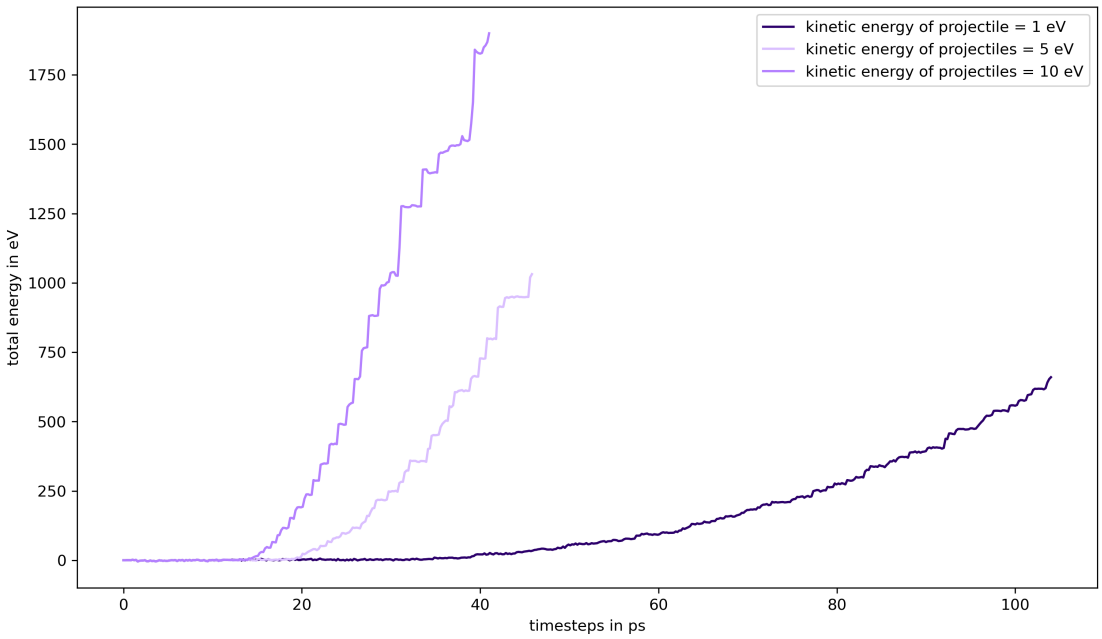

Figure 3.33: Comparison of the total energy after different projectiles are dragged into the center of mass of the droplet. The simulation run in dark purple shows the collision with the lowest kinetic energy. The droplet is nearly intact after the run ends. If the kinetic energy of the projectiles is increased, the droplets disintegrate due to the accumulated energy. The simulation runs with 5 and 10 eV terminate early, due to a numerical error in which the atoms are moving unphysical between two timesteps.

The disintegration simulations lead to the question if the fragmentation of the droplets is occurring in specific reproducible pattern. If a specific pattern arises due to the energy accumulation and fragmentation, the clusters can be categorized and further analyzed.

3.5 Droplet fragmentation

As demonstrated by the collision simulations, with a certain amount of energy accumulated into the droplets they begin to fragment into molecular clusters. The collision frequency is much smaller than the estimated relaxation time (cf. Figure 3.23), which leads to the suggestion that collisions with the particles is leading to a heating of the droplet. To mimic the energy accumulation from collisions, an external numerical thermostat was applied to the simulated droplets which heats them up with a specific heating rate. The first results with this simulation setup were promising: different temperatures applied on the molecules of the droplet lead to variations to the cluster patterns.

3.5.1 External heating: Relaxation and rescale

In the simulations presented before, projectiles transferred energy to the droplet through collisions. Writing the simulation input for the collision simulation becomes tedious if multiple projectiles are used. In the collision simulations leading to complete disintegration of the droplets, the numerical instabilities in the simulation with fully fragmented droplets made it difficult to compare long simulation runs. A simpler method would be to describe the accumulation the molecules of the droplets without the simulation of individual collisions with external particles. This can be achieved by a numerical thermostat: It increases the velocities of the atoms contained in the droplet by a certain amount corresponding to a defined temperature the particle ensemble should exhibit as a whole. This was done in linear temperature ramps for different end temperatures: 400 K, 600 K, 800 K and 1000 K starting from 300 K each for simulations of 150 ps total simulated time. The temperature increase induces the fragmentation process of the droplets. The fragmentation pattern is analyzed by a cluster analysis as described above performed with OVITO. The droplet consisted of 440 water, 334 acetonitrile molecules and 7 charges (Li ions). Figure 3.34 shows the number of identified clusters over the simulated time for the different heating rates. The cutoff radius for the cluster analysis was 10 Å again. Molecules found within this specified search radius of each other are considered a cluster. Obviously, the droplet is considered to be one large cluster initially. By applying the thermostat, the droplet begins to fragment,

and the number of clusters increases at higher temperatures. The fragmentation process begins with small molecules leaving the droplet. After a certain temperature is reached, the droplet breaks apart in larger fragments. This temperature is estimated around 500 K. This behavior was visible in different trajectories of the droplets. In addition, the steps shown in Figure 3.35 were roughly at 500 K. The pronounced steps visible in this diagram are discussed in detail in the following. That is the reason why the fragmentation process for the heating ramp to 400 K only entails single molecules leaving the droplet.

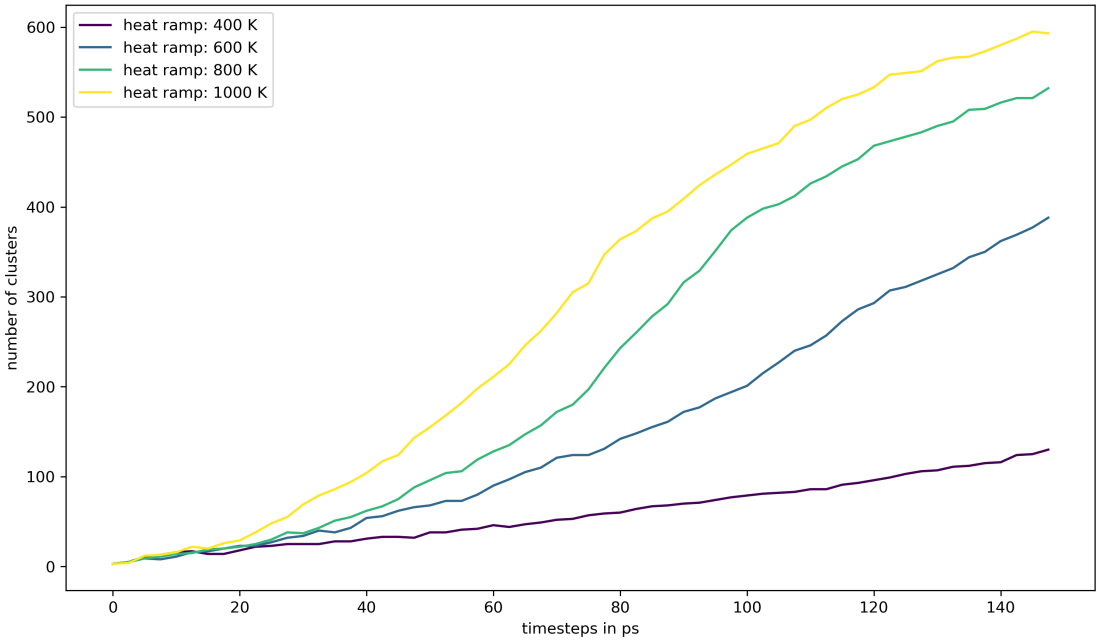

Figure 3.34: Analysis of the number of clusters of an acetonitrile / water droplet with 800 molecules in total for different heat ramp simulations. The darkest color is the lowest end temperature of the heat ramp (400 K). The droplet starts to disintegrate into larger fragments at 500 K.

That the droplet is breaking apart in large fragments and does not “evaporate” molecule by molecule becomes apparent by analyzing the number of molecules in the largest cluster (cf. Figure 3.35). As described above, when a certain temperature is reached (around 500 K) the droplet exhibits a fragmentation process into large fragments. This becomes visible in Figure 3.35: A large step is observable in the largest

cluster size with a heating ramp to 600 K. This rapid change of the molecule number in the largest cluster is the consequence of a larger fragment leaving the main droplet which is essentially a breakup of the main droplet in to at least two fragments. These characteristic large steps in the size of the largest cluster are visible for all heating ramps above 500 K.

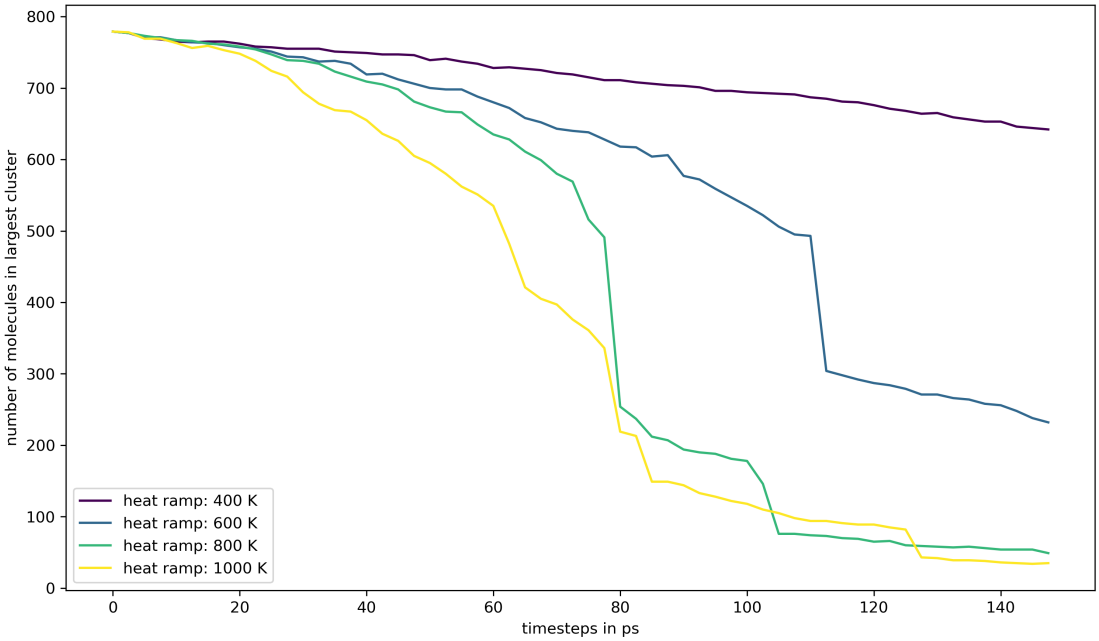

Figure 3.35: Analysis of the number of molecules within the largest cluster for an acetonitrile / water droplet. Again, the darkest color shows the simulation run for the lowest end temperature (400 K). The large steps visible in the plot show the disintegration of the droplet into large fragments as the number of molecules is drastically changing.

Figure 3.36 shows a visualization of the fragmentation process of the droplet for the heating to 600 K. The largest cluster is colored in green. On the left side the droplet is shown before it breaks apart. Notably, the droplet already has almost split into two mass centers which are still connected by a comparably thin filament. In the right panel, the split is complete. The fragment leaving the main droplet is colored pink. However, the two cluster are nearly the same size, therefore the process is essentially a breakup in two halves. Such events occur frequently with heating ramps set to high temperatures.

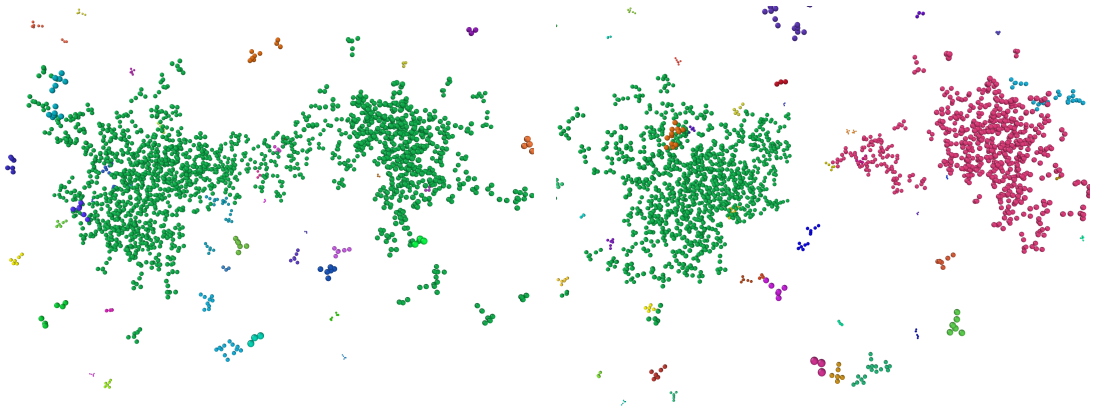

(a) (b)

Figure 3.36: Visualization of a typical droplet split event of an acetonitrile / water droplet (440 water, 334 acetonitrile molecules, 7 charges, m/z 3095) droplet. Left: The droplet immediately before breaking apart (timestep: 108 ps), right: The droplet fragmented in two larger cluster (timestep: 111 ps).

The simulation droplet fragmentation with linear heat ramps with a thermostat was done for different droplets to investigate chemical effects on this process. The organic solvent was changed and the ratio of water and organic solvents was varied as well. The overall results were very similar: If the droplet is heated up with an external thermostat, specific fragmentation patterns appear. As expected, the composition of the droplet has an influence on these patterns.

3.5.2 Simulated mass spectra from cluster patterns

As explained above, the different heating ramps and compositions of the droplet lead to specific fragmentation patterns that can be investigated further. The heating ramp simulations were repeated multiple times to analyze the fragment clusters statistically. The appearing fragments can be categorized: fragments containing charges and uncharged fragments. The charged neutral fragment clusters were not considered in detail, as they would not appear in a mass spectrum and can therefore not be compared with experiments on a mass spectrometer. In contrast, a histogram of the fragments containing charges represents is essentially a simulated fragment mass spectrum. Since the individual simulation runs for such an analysis have to be independent from each

other, the velocity distribution of the molecules was initiated with different random seeds. The heating ramp simulation to 400 K for the droplet consisting of water / acetonitrile and lithium charges (440 water, 334 acetonitrile molecules, 7 charges, m/z 3095) was repeated for 100 simulation runs. The last frame of each simulation run was analyzed with the cluster analysis tool from OVITO as described above. The number of clusters were counted and categorized by the calculated m/z of the clusters. Figure 3.37 shows the resulting histogram / simulated mass spectrum. Interesting to note is that a double peak structure at m/z 2500 is visible which was also the case in the experiments with acetonitrile as solvent.

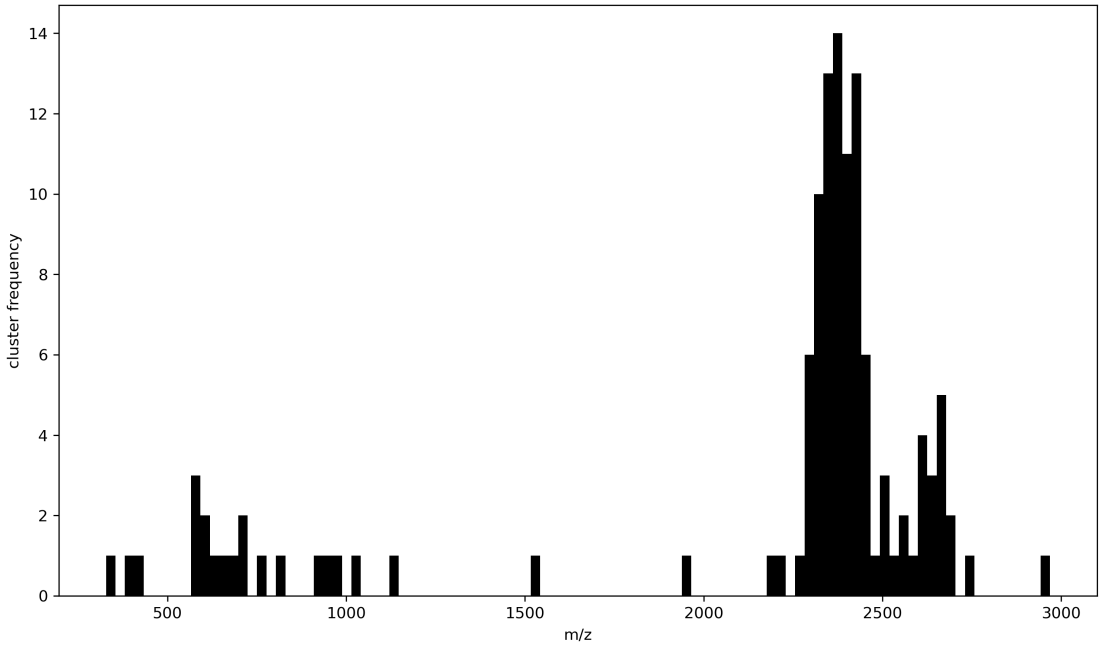

Figure 3.37: Simulated mass spectrum derived from a cluster analysis of the last frames heating ramp simulation. End point of the heating ramp of the acetonitrile / water droplet was 400 K. The MD simulation was repeated 100 times to increase the statistical sample size for the analysis of the cluster pattern.

If a mass spectrum from the Bruker amaZon QIT is compared to the simulated one the surprising similarities of the double peak structure become apparent. The mass spectra shown in Figure 3.38 share the same x-axis. Although the double peak structure in

the simulated spectra is much broader, the overall appearance is similar: The main intensity is at the double peak structure in the simulation and the experiment. At lower and higher masses only small peaks are visible.

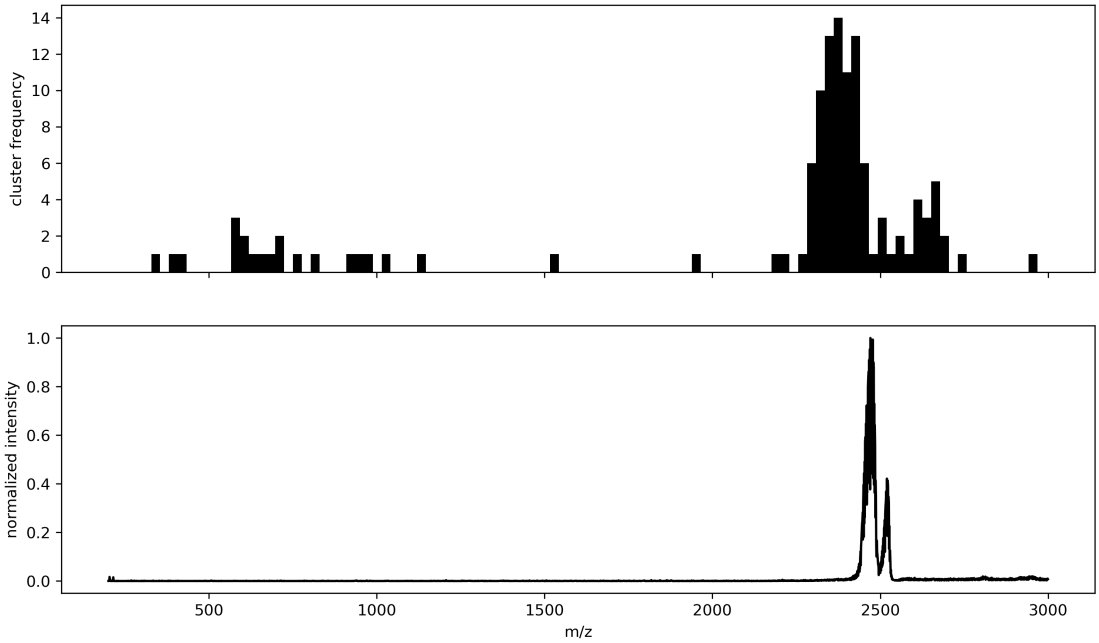

Figure 3.38: Comparison of simulated (top) and experimental (bottom) mass spectrum. The spectra share the same m/z-axis. The solvent system was acetonitrile and water. The double peak structure at 2500 is visible in both spectra, although it is broader in the simulated spectrum.

The described simulation approach was repeated for methanol as solvent. The simulated droplet consisted of 512 methanol molecules, 512 water molecules with 9 Li charge carriers, the resulting m/z was 2218. The results are shown in Figure 3.39. It shows the statistically analysis of the methanol / water droplet heating ramp simulation for 400 K. Again, a pronounced double peak structure appears, though it is shifted slightly to smaller m/z. In the low m/z range, around m/z 500, a significantly larger number of fragment signals as the acetonitrile / water droplets exhibited can be observed.

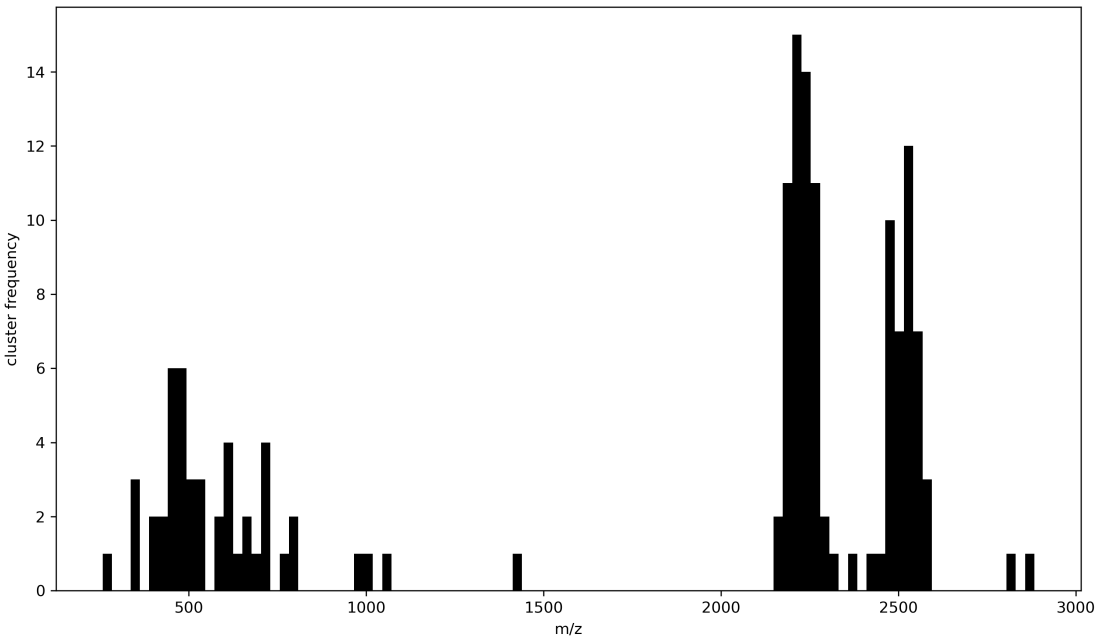

Figure 3.39: Simulated mass spectrum derived from a cluster analysis of the last frames of heating ramp simulations. End point of the heating ramp of the methanol / water droplet was 400 K. The simulation was repeated 100 times to increase the statistical sample size for the analysis of the cluster pattern.

Figure 3.40 shows a comparison of the heating ramp simulation with the results of an experiment with methanol as a solvent. Some similarities between the two mass spectra can be observed. Although a strong pronounced double peak structure around the isolation window cannot be observed in the experiments, the main intensity can again be found at the isolation window of m/z 2500. However, in comparison to the spectra of the acetonitrile / water system (cf. Figure 3.37), the left side of the isolated peak is shifted slightly below the isolation window. This is reflected in the simulated mass spectrum. The main intensity of the double peak structure in the simulations is appearing below m/z 2500.

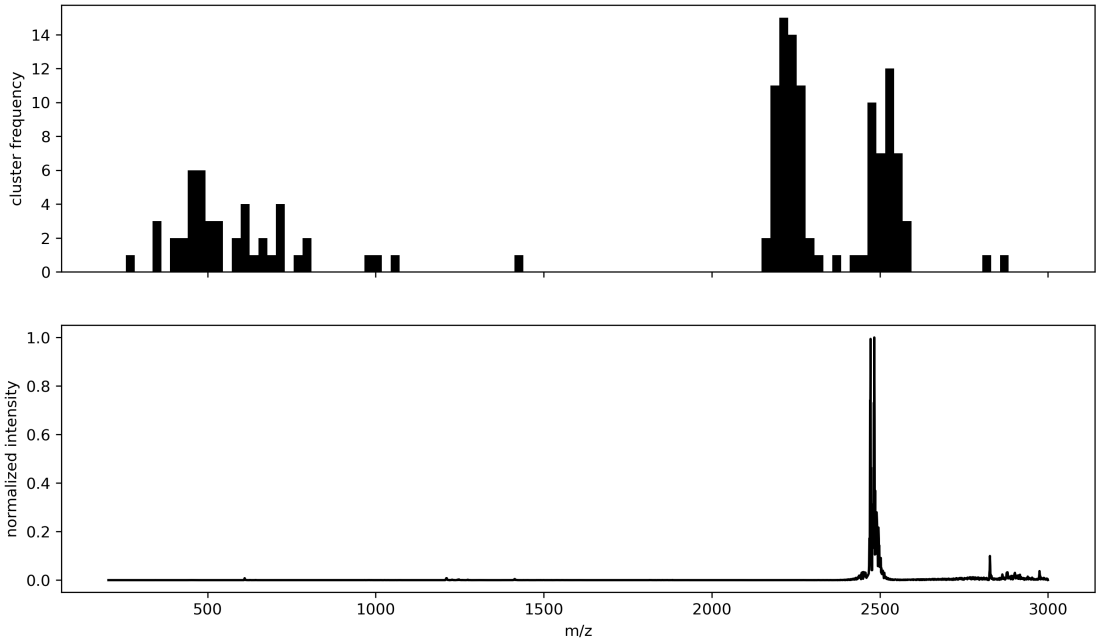

Figure 3.40: Comparison of simulated (top) and experimental (bottom) mass spectrum. The spectra share the m/z x-axis. The solvent system was methanol and water. Again, a pronounced double peak structure is visible in the simulated mass spectrum while a narrower peak structure can be observed in the experimental mass spectrum.

The similarities between the simulated and the experimental mass spectra are surprising, as the droplet composition and ending temperatures of the heating ramps were chosen arbitrarily. Even the distribution of intensities in the double peak structure (cf. Figure 3.38) is similar in the simulation and the experiment. This is encouraging evidence that MD simulations are actually able to reproduce the conditions found in a real mass spectrometer. If the end temperature of the heating ramp is increased, the simulated mass spectra lose their double peak structure and the increased fragmentation of the droplets becomes apparent: If the droplet is heated up to 600 K, the observed charged fragments are much smaller. This is reflected in the simulated mass spectrum shown in Figure 3.41. The intensity maximum of the simulated mass spectrum is around m/z 500 for the acetonitrile / water system with a second local maximum around m/z 1700.

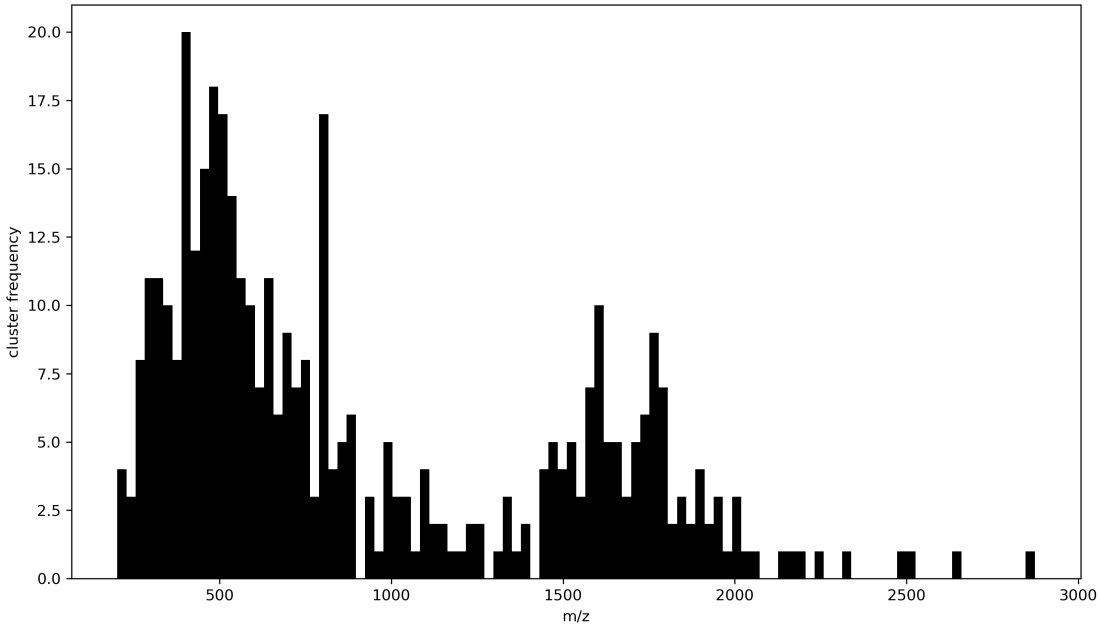

Figure 3.41: Simulated mass spectrum derived from a cluster analysis of the last frame of a heating ramp simulation. End point of the heating ramp of the methanol / water droplet was 600 K. The simulation was repeated 100 times to to increase the statistical sample size for the analysis of the cluster pattern.

The temperature was increased even more in another set of simulations. In Figure 3.42 the maximum of number of clusters is found at even lower m/z for a simulation with an end temperature of 800 K. The obvious reason is that the droplet is fragmenting more rapidly with smaller resulting fragments. The simulated mass spectra for the higher ending temperatures show drastic differences to the experimental mass spectra, which leads to the idea that the simulation of the heating ramp of 400 K represents the reality of ESI experiments more closely.

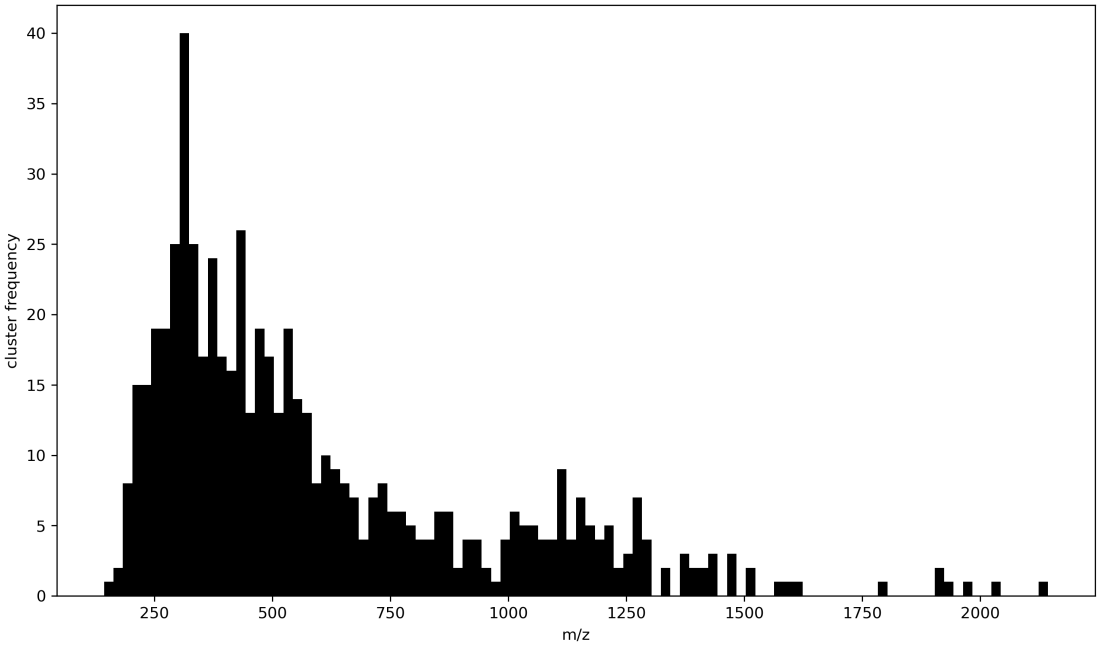

Figure 3.42: Simulated mass spectrum derived from a cluster analysis of the last frame of a heating ramp simulation. End point of the heating ramp of the methanol / water droplet was 800 K. The simulation was repeated 100 times to increase the statistical sample size for the analysis of the cluster pattern.

This underlines the surprising results of the comparison between the heating ramp simulations to 400 K and the experimental data: The simulated mass spectra show qualitative similarities compared to the experiments.

3.6 Mobility calculations

The MD simulations gave deeper insight into charged droplets, their structure, stability and fragmentation dynamics. As the experiments show, the droplets enter the MS vacuum stages regardless of counter measurements, like drying gas or the declustering potential. The aspiration of droplets is understandable if they have a similar mobility as a simple clustered analyte or larger molecules like the steroid mentioned before in section 1.3. Simple mobility calculations give a first estimation of the mobility of charged droplets and allow to assess if these aggregates are likely penetrating the vacuum regions of the MS instruments. For this, some results of the aforementioned MD simulations were used as an estimation of size and charge density of the charged droplets as these parameters are necessary input information for mobility calculations. Considering that the MD simulations led to surprising comparability between experiments and simulations, the use of these parameters seem like a promising approach. As the ions are moving through the background gas, their transport is directed by external forces like the applied electric field and gas flows and their electric mobility and molecular diffusion. Additionally, the ion-dipole, ion-induced dipole and quadrupolar moment interactions influences the empirical mobility of ions [36]. As the mobility is dependent on the interactions of the ion with the background gas, the choice of an appropriate collision model is important. A common and comparably simple approach is the hard-sphere collision model, in which the colliding particles are considered as impenetrable spheres which are reflected upon collision with no additional interaction potential [36]. In other models the interactions between colliding particles are calculated with additional potentials like the 12,6-Lennard-Jones-potential. IMoS (**I**on **Mo**bility **S**oftware) is one of multiple codes available to calculate mobility and collision cross sections of ions [101–104]. The collision model can be freely chosen in IMoS, depending on the desired accuracy and computational costs. IMoS calculates the ion mobility from modeled collision cross sections with the Mason-Schamp equation [101, 104, 105].

3.6.1 IMoS calculations of charged droplets

IMoS calculation results are important information, as they could contribute to the understanding why charged droplets from ESI are penetrating deeply into mass spec-

trometer vacuum stages. As first validation of the general approach, the collision cross section (CCS) calculated by IMoS for different droplets is compared to the simple geometrical cross section of the individual droplet. The geometrical cross section for a collision of a pair of gas particles is defined as [100]:

$$\sigma = \pi(d^2), d = \frac{1}{2}(d_a + d_b) \tag{3.2}$$

With σ as the cross section and d_a as the diameter of molecule a and d_b as diameter of molecule b. Since in a collision of a droplet with the background gas, the diameter of the background gas particle (molecule a) is magnitudes smaller than the diameter of the droplet (molecule b), the background gas particle diameter (molecule a) becomes insignificant and can be left out of the calculation. Thus, only the radius of the droplet matters for the geometrical collision cross section. The calculations with IMoS were done for two droplets, which were simulated with LAMMPS in advance to determine the geometrical structure of the droplets. The particle coordinates of the relaxed droplet (discussed in section 3.3) can be used as input for the cross section (CCS) calculations. From the different approaches IMoS offers, a trajectory method was selected to calculate the CCS, in which the interactions of the background gas and collision gas (N_2) were accommodated with additional 12,6-Lennard-Jones-potentials. The interaction potentials for all possible pairs of atoms are listed in an additional database file of the IMoS package, which defines essentially a special purpose classical force field. Figure 3.43 shows exemplary collisions of the neutral background gas, nitrogen in this case, with the droplet simulated with the trajectory method. The gas particles are not simply reflected: The trajectories of the gas particles are influenced by the assumed Lennard-Jones and ion-induced potential for the different atom types. The potential is described by the following equation [106]:

$$\Phi(x,y,z) = 4\epsilon \sum_{i=1}^{n} \left[\left(\frac{\sigma}{r_i}\right)^{12} - \left(\frac{\sigma}{r_i}\right)^{6} \right] - \frac{\alpha}{2}\left(\frac{ze}{n}\right)^2 \cdot \left[\left(\sum_{i=1}^{n} \frac{x_1}{r_1^3}\right)^2 + \left(\sum_{i=1}^{n} \frac{y_1}{r_1^3}\right)^2 + \left(\sum_{i=1}^{n} \frac{z_1}{r_1^3}\right)^2 \right] \tag{3.3}$$

The distance between a gas molecule and an atom is given by $r_i = x, y, z$. α describes the polarizability which dictates the ion-induced potential. ϵ and σ are the Lennard-Jones parameters, which are in accordance with the well-depth of the potential.

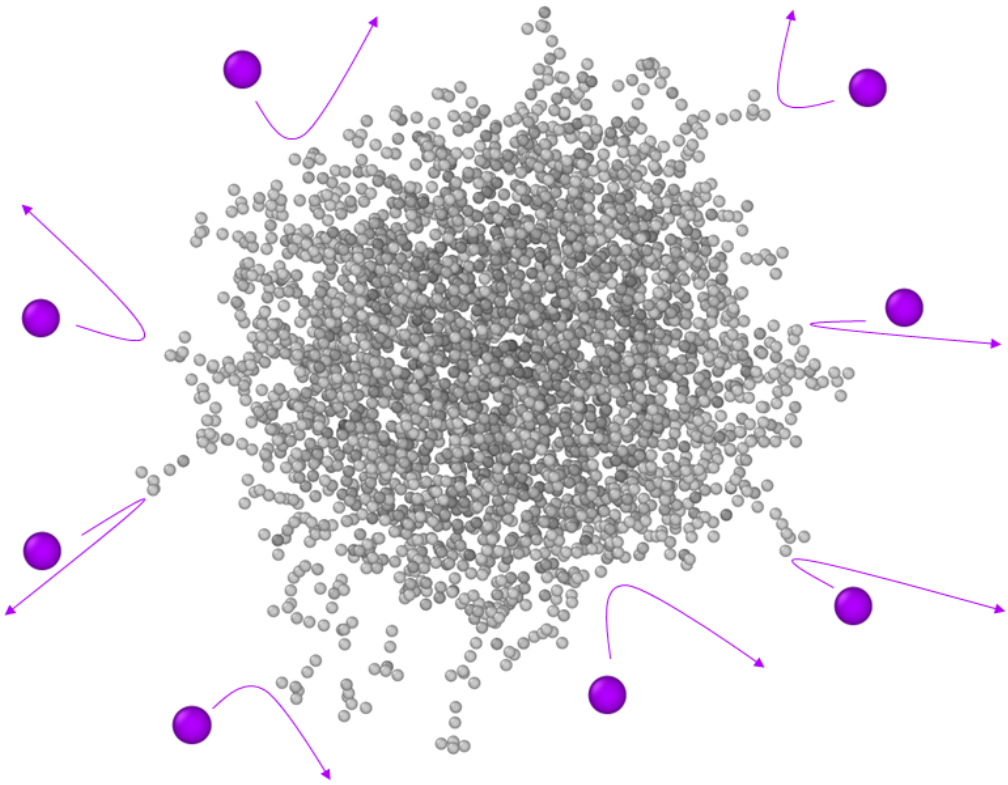

Figure 3.43: Schematic representation of the collision model used in IMoS: The approaching colliding neutral background gas particles (in violet) are not simply reflected off of the surface by specular reflections but result from inter molecular interaction potentials defined by a classical force field.

At first, a droplet consisting of 440 water and 334 acetonitrile molecules and charged with 7 lithium ions was investigated. This gives a total mass of 21 663 u and m/z 3095. The CCS calculated by IMoS for this droplet equates to 3416 $Å^2$. The geometrical cross section calculated by the radius of the droplet, assuming it has a perfect spherical shape, equates to 2114 $Å^2$. For this geometrical assumption the diameter in all three directions was averaged, as the droplet has a slightly larger extent in the x-direction. This calculation was repeated for another droplet: Here, a larger acetonitrile / water

droplet was investigated. It contained 827 water molecules, 655 acetonitrile molecules and 9 ammonium-ions as charges. The mass of this droplets is 41 903 u, divided by the number of charges this equates to m/z 4656. With IMoS the CCS equates to 5907 Å^2. Again, the geometrical cross section was also calculated by the averaged diameter of the droplet. This equates to a cross section of 2903 Å^2. The results are collected in Table 3.1. The collision cross sections calculated by IMoS are substantially larger than the geometrically estimated cross sections. This underlines the requirement for the usage of approaches like the trajectory method to get realistic CCS values. It could be assumed that in the realm of the ESI droplets, which are rather large in comparison to simple analytes, the simple estimation is efficient enough. However, the CCS would be substantially underestimated. The reason behind the higher CCS calculated by IMoS could be the influence of the charges in the droplet. They are not shielded and affect the interaction potential of the droplet, and thus enlarge the effective collision surface.

Table 3.1: Cross section calculations for two droplets

	CCS by IMoS	Simple cross section equation
Droplet with m/z 3095	3416 Å^2	2114 Å^2
Droplet with m/z 4656	5907 Å^2	2903 Å^2

IMoS also calculates the mobility from the determined CCS with the Mason-Schamp equation [36, 105]:

$$K = \frac{3}{16}\frac{q}{N}\left(\frac{2\pi}{\mu k T_{\text{eff}}}\right)^{1/2}\frac{1}{\sigma} \tag{3.4}$$

With K as the mobility, q is the charge of the ion, N is the density of the background gas, k the Boltzmann constant, T_{eff} is the ambient temperature and σ the collision cross section. Ambient temperature (304 K) was set as background temperature in the software for both droplets. The reduced mobility is calculated as discussed in section 1.3. The results are given in Table 3.2. The mobility and reduced mobility for the smaller droplet is slightly higher than the values for the larger droplet. A higher mobility equates to a higher drift velocity through the background gas in an applied electric field. Reduced mobilities in the range of 0.53-3.37 cm^2/Vs are tabled for ambient pressure by Shumate et al. for a variety of small molecular analytes like alcohols, amino acids and larger aromatic systems [38]. The mobilities calculated for the droplets are in the same

order of magnitude.

Table 3.2: Mobility calculation done with IMoS tabled for two droplets

	Mobility by IMoS	Reduced mobility K_0
Droplet with m/z 3090	0.46 cm^2/Vs	0.41 cm^2/Vs
Droplet with m/z 4642	0.34 cm^2/Vs	0.31 cm^2/Vs

Therefore, the CCS and mobility calculations for the two droplets strongly support the notion that droplets are indeed able to enter the mass spectrometer and even make it to the mass analyzer. The high number of charges allow them to be transported in the same fashion as bare, small molecular analytes.

3.7 Conclusions - Simulations

In the previous chapter an overview of MD simulations of charged droplets was given. LAMMPS proved to be a valuable tool to investigate the characteristics different charged droplets with approximately 1000 to 2000 solvent molecules and up to 10 charges in total. A workflow for the simulations was established. The initial configuration of simulation runs and force field parameters was generated with support of the software moltemplate. The simulation data analysis with OVITO and different custom python scripts is promising. Thus, the critical parameters for the simulations of droplets could be identified starting with the shape of the aggregates. After applying a thermostat to the simulated particles in the block shaped starting configuration in initial relaxation calculations, the particles transformed into a spherical droplet. The results from such relaxation simulations were the starting point for the following investigations. Different known basic parameters, like the influence of the Rayleigh Limit to the shape and stability of the droplets, were reproduced within LAMMPS simulations. It was possible to successfully simulate different typical solvent systems that are used in ESI experiments with the established workflow. The high stability of the charged droplets was verified with collision and energy transfer simulations: The collision with single or a few projectiles only increased the internal energy of the droplet and did not lead to disintegration. The relaxation time of the energy distribution within the droplets was estimated: The kinetic energy of a single projectile is distributed fully within a few tenth of picoseconds, which is two orders of magnitudes higher than vibrations of a molecule like HCl [100]. The fast energy distribution could be one of the reasons why the droplets survive the ion source and enter the mass spectrometer. A limit for the energy accumulation could be established by applying an external numerical thermostat to the simulated droplets. The simulated mass spectra, which resulted from fragment cluster pattern analysis, showed surprising similarities to experimental mass spectra. Notably, a double peak structure close to the isolation window of the Bruker ion trap spectra could be qualitatively reproduced. The cluster patterns resulted from disintegration simulations with different heating ramps. The cluster were categorized and statistically analyzed. For two different solvent systems the simulated mass spectra show behavior with qualitative similarities to experimental results. Mobility calculations with IMoS using the droplet structures derived from LAMMPS simulations show that droplets have collision

cross sections similar to comparably small bare molecular analyte ions. The collision cross sections and thus calculated mobilities gave further supporting information as to why the droplets are able to surpass the ion source and even reach the mass analyzer region. All in all, MD simulations with LAMMPS seem to give results which are comparable to experiments and widely accepted phenomenon like the Rayleigh Limit. Proceeding works could use MD simulations to widen the understanding of the dynamic of these aggregates.

4 Outlook

As discussed above, proceeding works are needed to deepen the understanding of the droplets. Experimental works could entail the characterization of the spraying conditions. An optical analysis of the spray within an ion source or a specially built chamber could be done. This could be achieved by the use of an optical particle counter (OPC) or a laser scattering device, which is a specific measurement system for sprayed particles and droplets. Planned spatially resolved laser ionization within of an actual Bruker ESI ion source seems promising to characterize the spraying condition [107]. The coupling of a HPLC (high performance liquid chromatography) to a Bruker ion trap give also very similar droplet signatures as described in this work. The use of a HPLC system to feed the liquid analyte solution into the ion source seems to stabilize the spraying conditions, which is in accordance with discussions with different instrument manufacturers. The pump of the HPLC system is just more stable than a simple syringe pump. The experimental possibilities to further investigate charged droplets originating from electrospray seem to be virtually limitless due to the variety of parameters and systems that can be considered. Therefore, this work was only the beginning of the investigation into charged droplets. Additionally, the workflow for MD simulations with LAMMPS established in this work could be extended which would lead to further understanding of the droplets. Especially the simulated mass spectra could be examined in more detail. The repeated simulation runs take a long time to give statistical profound data. Therefore, different solvent systems could not be fully investigated in this work, which gives much room for further work. In addition, the chemical variation of the simulated droplets could be widened by considering different analytes or solvents. First results of a proceeding work established that thermometer ions and their fragments can be simulated within different droplets [108]. The structure of the different species leads to different dynamical behavior for the thermometer ions. Furthermore, the disintegration pattern of the droplet could be investigated. This could lead to a prediction of the

fragment pattern in the actual mass spectra. With every question this work answered about the existence of the charged droplets, it seemed that two or three more questions came about. This work is only the beginning of the research into charged droplets as it leaves enough room for further investigations.

Abbreviations

ESI	electrospray ionization
MS	mass spectrometry / mass spectrometer
PDA	phase doppler anemometry
CRM	charge residue model
IEM	ion evaporation model
DMS	differential mobility spectrometer
API	atmospheric pressure ionization
Quad	quadrupole
RF	radio frequency
DC	direct current
LMCO	low mass cutoff
CID	collision induced dissociation
CE	collision energy
QIT	quadrupole ion trap
accu time	accumulation time
ICC	ion charge control
APCI	atmospheric pressure chemical ionization
TIC	total ion count / total ion chromatogram
EIC	extracted ion count
MD	molecular dynamic
LAMMPS	large-scale atomic/molecular massively parallel simulator
OPLS	optimized potentials for liquid simulations
AA	all-atoms

UA	united-atoms
SMD	steered molecular dynamic
RDF	radial distribution function
IMoS	ion mobility software
CCS	collision cross section
OPC	optical particle counter

List of Tables

List of Figures

Bibliography

[1] M. Dole et al. “Molecular beams of macroions”. In: *The Journal of Chemical Physics* 49.5 (1968), pp. 2240–2249. DOI: 10.1063/1.1670391.

[2] M. Yamashita and J. B. Fenn. “Electrospray ion source. Another variation on the free-jet theme”. In: *Journal of Physical Chemistry* 88.20 (1984), pp. 4451–4459. DOI: 10.1021/j150664a002.

[3] C. M. Whitehouse et al. “Electrospray Interface for Liquid Chromatographs and Mass Spectrometers”. In: *Analytical Chemistry* 57.3 (1985), pp. 675–679. DOI: 10.1021/ac00280a023.

[4] T. R. Covey, B. A. Thomson, and B. B. Schneider. “Atmospheric pressure ion sources”. In: *Mass Spectrometry Reviews* 28.6 (Nov. 2009), pp. 870–897. DOI: 10.1002/mas.20246.

[5] R. B. Cole. *Electrospray and MALDI Mass Spectrometry*. Ed. by R. B. Cole. Second Edi. Hoboken, New Jersey: John Wiley and Sons, Inc., 2010.

[6] E. de Hoffmann and V. Stroobant. *Mass Spectrometry Principles and Applications*. Tech. rep.

[7] J. Fenn. “Electrospray Wings for Nanoscale Elephants”. In: *2006 Sixth IEEE Conference on Nanotechnology*. Vol. 1. IEEE, 2006, pp. 1–1. DOI: 10.1109/NANO.2006.1716997.

[8] P. Kebarle and U. H. Verkerk. “Electrospray: From Ions In Solution To Ions In The Gas Phase, What We Know Now”. In: *Mass Spectrometry Reviews* 28 (2009), pp. 898–917. DOI: 10.1002/mas.

[9] V. Kertesz and G. J. Van Berkel. “Minimizing analyte electrolysis in an electrospray emitter”. In: *Journal of Mass Spectrometry* 36.2 (2001). DOI: 10.1002/jms.122.

[10] N. B. Cech and C. G. Enke. “Practical implications of some recent studies in electrospray ionization fundamentals”. In: *Mass Spectrometry Reviews* 20.6 (2001). DOI: 10.1002/mas.10008.

[11] J. Lin et al. “Study on properties of wooden capillary electrospray ionization mass spectrometry”. In: *Rapid Communications in Mass Spectrometry* 34.5 (2020), pp. 1–6. DOI: 10.1002/rcm.8600.

[12] G. I. Taylor and A. D. McEwan. “The stability of a horizontal fluid interface in a vertical electric field”. In: *Journal of Fluid Mechanics* 22.1 (1965), pp. 1–15. DOI: 10.1017/S0022112065000538.

[13] J. Fernández de la Mora. “The Fluid Dynamics of Taylor Cones”. In: *Annual Review of Fluid Mechanics* 39.1 (2007), pp. 217–243. DOI: 10.1146/annurev.fluid.39.050905.110159.

[14] M. Cloupeau and B. Prunet-Foch. “Electrohydrodynamic spraying functioning modes: a critical review”. In: *Journal of Aerosol Science* 25.6 (1994), pp. 1021–1036. DOI: 10.1016/0021-8502(94)90199-6.

[15] M. Cloupeau. “Recipes for use of EHD spraying in cone-jet mode and notes on corona discharge effects”. In: *Journal of Aerosol Science* 25.6 (1994), pp. 1143–1157. DOI: 10.1016/0021-8502(94)90206-2.

[16] K. Tang and A. Gomez. “Generation by electrospray of monodisperse water droplets for targeted drug delivery by inhalation”. In: *Journal of Aerosol Science* 25.6 (1994), pp. 1237–1249. DOI: 10.1016/0021-8502(94)90212-7.

[17] I. Marginean et al. “Flexing the Electrified Meniscus: The Birth of a Jet in Electrosprays”. In: *Analytical Chemistry* 76.14 (2004), pp. 4202–4207. DOI: 10.1021/ac049817r.

[18] G. Meesters et al. “Generation of micron-sized droplets from the Taylor cone”. In: *Journal of Aerosol Science* 23.1 (1992), pp. 37–49. DOI: 10.1016/0021-8502(92)90316-N.

[19] K. L. Kaiser. *Electrostatic Discharge*. CRC Press, 2005.

[20] J. N. Smith, R. C. Flagan, and J. L. Beauchamp. “Droplet Evaporation and Discharge Dynamics in Electrospray Ionization”. In: *The Journal of Physical Chemistry A* 106.42 (2002), pp. 9957–9967. DOI: 10.1021/jp025723e.

[21] R. L. Grimm and J. L. Beauchamp. “Evaporation and Discharge Dynamics of Highly Charged Multicomponent Droplets Generated by Electrospray Ionization”. In: *The Journal of Physical Chemistry A* 114.3 (2010), pp. 1411–1419. DOI: 10.1021/jp907162w.

[22] A. Gomez and K. Tang. “Charge and fission of droplets in electrostatic sprays”. In: *Physics of Fluids* 6.1 (1994), pp. 404–414. DOI: 10.1063/1.868037.

[23] A. Wortmann et al. “Shrinking droplets in electrospray ionization and their influence on chemical equilibria”. In: *Journal of the American Society for Mass Spectrometry* 18.3 (2007), pp. 385–393. DOI: 10.1016/j.jasms.2006.10.010.

[24] A. Venter, P. E. Sojka, and R. G. Cooks. “Droplet Dynamics and Ionization Mechanisms in Desorption Electrospray Ionization Mass Spectrometry”. In: *Analytical Chemistry* 78.24 (2006), pp. 8549–8555. DOI: 10.1021/ac0615807.

[25] M. A. Abbas and J. Latham. “The instability of evaporating charged drops”. In: *Journal of Fluid Mechanics* 30.4 (1967), pp. 663–670. DOI: 10.1017/S0022112067001685.

[26] J. W. Schweizer and D. Hanson. “Stability limit of charged drops”. In: *Journal of Colloid and Interface Science* 35.3 (1971), pp. 417–423. DOI: 10.1016/0021-9797(71)90141-X.

[27] D. C. Taflin, T. L. Ward, and E. J. Davis. “Electrified droplet fission and the Rayleigh limit”. In: *Langmuir* 5.2 (1989), pp. 376–384. DOI: 10.1021/la00086a016.

[28] E. Davis and M. Bridges. “The rayleigh limit of charge revisited: light scattering from exploding droplets”. In: *Journal of Aerosol Science* 25.6 (1994), pp. 1179–1199. DOI: 10.1016/0021-8502(94)90208-9.

[29] X. Feng, M. J. Bogan, and G. R. Agnes. “Coulomb Fission Event Resolved Progeny Droplet Production from Isolated Evaporating Methanol Droplets”. In: *Analytical Chemistry* 73.18 (2001), pp. 4499–4507. DOI: 10.1021/ac0101555.

[30] M. Peschke, U. H. Verkerk, and P. Kebarle. “Features of the ESI mechanism that affect the observation of multiply charged noncovalent protein complexes and the determination of the association constant by the titration method”. In: *Journal of the American Society for Mass Spectrometry* 15.10 (2004), pp. 1424–1434. DOI: 10.1016/j.jasms.2004.05.005.

[31] A. P. Bruins, T. R. Covey, and J. D. Henion. “Ion spray interface for combined liquid chromatography/atmospheric pressure ionization mass spectrometry”. In: *Analytical Chemistry* 59.22 (1987), pp. 2642–2646. DOI: 10.1021/ac00149a003.

[32] F. Zarrin, S. Kaufman, and J. Socha. “Droplet size measurements of various nebulizers usingdifferential electrical mobility particle sizer”. In: *Journal of Aerosol Science* 22.SUPPL. 1 (1991), S343–S346. DOI: 10.1016/S0021-8502(05)80108-9.

[33] M. S. Wilm and M. Mann. “Electrospray and Taylor-Cone theory, Dole’s beam of macromolecules at last?” In: *International Journal of Mass Spectrometry and Ion Processes* 136.2-3 (1994), pp. 167–180. DOI: 10.1016/0168-1176(94)04024-9.

[34] R. Juraschek, T. Dülcks, and M. Karas. “Nanoelectrospray—More than just a minimized-flow electrospray ionization source”. In: *Journal of the American Society for Mass Spectrometry* 10.4 (1999), pp. 300–308. DOI: 10.1016/S1044-0305(98)00157-3.

[35] Lord Rayleigh F.R.S. “XX. On the equilibrium of liquid conducting masses charged with electricity”. In: *The London, Edinburgh, and Dublin Philosophical Magazine and Journal of Science* 14.87 (1882), pp. 184–186. DOI: 10.1080/14786448208628425.

[36] G. A. Eiceman and Z. Karpas. *Ion Mobility Spectrometry*. 1994.

[37] C. Bylda et al. “Rapid Quantification of Digitoxin and Its Metabolites Using Differential Ion Mobility Spectrometry-Tandem Mass Spectrometry”. In: *Analytical Chemistry* 87.4 (2015), pp. 2121–2128. DOI: 10.1021/ac503187z.

[38] C. Shumate, R. St. Louis, and H. Hill. “Table of reduced mobility values from ambient pressure ion mobility spectrometry”. In: *Journal of Chromatography A* 373.C (1986), pp. 141–173. DOI: 10.1016/S0021-9673(00)80211-3.

[39] B. A. Thomson and J. V. Iribarne. “Field induced ion evaporation from liquid surfaces at atmospheric pressure”. In: *The Journal of Chemical Physics* 71.11 (1979), pp. 4451–4463. DOI: 10.1063/1.438198.

[40] J. Fernandez de la Mora. “Electrospray ionization of large multiply charged species proceeds via Dole’s charged residue mechanism”. In: *Analytica Chimica Acta* 406.1 (2000), pp. 93–104. DOI: 10.1016/S0003-2670(99)00601-7.

[41] V. Znamenskiy, I. Marginean, and A. Vertes. “Solvated Ion Evaporation from Charged Water Nanodroplets”. In: *The Journal of Physical Chemistry A* 107.38 (2003), pp. 7406–7412. DOI: 10.1021/jp034561z.

[42] J. V. Iribarne and B. A. Thomson. “On the evaporation of small ions from charged droplets”. In: *The Journal of Chemical Physics* 64.6 (1976), p. 2287. DOI: 10.1063/1.432536.

[43] L. Konermann. “A simple model for the disintegration of highly charged solvent droplets during electrospray ionization”. In: *Journal of the American Society for Mass Spectrometry* 20.3 (2009), pp. 496–506. DOI: 10.1016/j.jasms.2008.11.007.

[44] L. Konermann, A. D. Rodriguez, and J. Liu. “On the Formation of Highly Charged Gaseous Ions from Unfolded Proteins by Electrospray Ionization”. In: *Analytical Chemistry* 84 (2012), pp. 6798–6804.

[45] S. Consta, M. I. Oh, and A. Malevanets. “New mechanisms of macroion-induced disintegration of charged droplets”. In: *Chemical Physics Letters* 663 (2016), pp. 1–12. DOI: 10.1016/j.cplett.2016.08.001.

[46] L. Konermann et al. “Unraveling the Mechanism of Electrospray Ionization”. In: *Analytical Chemistry* 85.1 (2013), pp. 2–9. DOI: 10.1021/ac302789c.

[47] Y. Kang, B. B. Schneider, and T. R. Covey. “On the Nature of Mass Spectrometer Analyzer Contamination”. In: *Journal of the American Society for Mass Spectrometry* 28.11 (2017), pp. 2384–2392. DOI: 10.1007/s13361-017-1747-3.

[48] A. A. Shvartsburg. *Differential Ion Mobility Spectrometry*. CRC Press, 2008. DOI: 10.1201/9781420051070.

[49] B. B. Schneider et al. “Differential mobility spectrometry/mass spectrometry history, theory, design optimization, simulations, and applications”. In: *Mass Spectrometry Reviews* 35.6 (2016), pp. 687–737. DOI: 10.1002/mas.21453.

[50] K. V. Barylyuk et al. “Fragmentation of benzylpyridinium “thermometer” ions and its effect on the accuracy of internal energy calibration”. In: *Journal of the American Society for Mass Spectrometry* 21.1 (2010), pp. 172–177. DOI: 10.1016/j.jasms.2009.09.023.

[51] J. E. Carpenter et al. “How Hot are Your Ions Really? A Threshold Collision-Induced Dissociation Study of Substituted Benzylpyridinium “Thermometer” Ions”. In: *Journal of the American Society for Mass Spectrometry* 28.9 (2017), pp. 1876–1888. DOI: 10.1007/s13361-017-1693-0.

[52] M. M. Sharaf El-Din et al. “Validated liquid chromatography–tandem mass spectrometry method for simultaneous determination of clopamide, reserpine and dihydroergotoxine: Application to pharmacokinetics in human plasma”. In: *Journal of Pharmaceutical and Biomedical Analysis* 125 (2016), pp. 236–244. DOI: 10.1016/j.jpba.2016.03.051.

[53] A. R. Katritzky et al. “Kinetics and mechanism of nucleophilic displacements with heterocycles as leaving groups. 26. Collisionally activated dissociation of N-alkylpyridinium cations to pyridine and alkyl cations in the gas phase”. In: *Journal of the American Chemical Society* 112.7 (1990), pp. 2471–2478. DOI: 10.1021/ja00163a001.

[54] J. H. Gross. *Mass Spectrometry: A Textbook*. Springer Berlin Heidelberg, 2004.

[55] P. E. Miller and M. B. Denton. “The quadrupole mass filter: Basic operating concepts”. In: *Journal of Chemical Education* 63.7 (1986), p. 617. DOI: 10.1021/ed063p617.

[56] C. Reichardt. “Empirical Parameters of the Polarity of Solvents”. In: *Angewandte Chemie International Edition in English* 4.1 (1965), pp. 29–40. DOI: 10.1002/anie.196500291.

[57] R. T. Kelly et al. “The ion funnel: Theory, implementations, and applications”. In: *Mass Spectrometry Reviews* 29.2 (2009), n/a–n/a. DOI: 10.1002/mas.20232.

[58] R. R. Julian, S. R. Mabbett, and M. F. Jarrold. “Ion funnels for the masses: Experiments and simulations with a simplified ion funnel”. In: *Journal of the American Society for Mass Spectrometry* 16.10 (2005), pp. 1708–1712. DOI: 10.1016/j.jasms.2005.06.012.

[59] T. Kim et al. “Design and Implementation of a New Electrodynamic Ion Funnel”. In: *Analytical Chemistry* 72.10 (2000), pp. 2247–2255. DOI: 10.1021/ac991412x.

[60] C. Markert et al. “Observation of charged droplets from electrospray ionization (ESI) plumes in API mass spectrometers”. In: *Analytical and Bioanalytical Chemistry* (2021).

[61] K. P. Vollhardt and N. E. Schore. *Organische Chemie*. 3. Auflage. Weinheim: Wiley-VCH, 2000.

[62] C. E. Mortimer and U. Müller. *Chemie*. 10. Auflag. Stuttgart: Georg Thieme Verlag KG, 2010.

[63] M. Thinius. “Kinetic energy measurements for ion dynamics studies in API-MS and Modeling of an FT-QIT”. In: (2021).

[64] B. J. Alder and T. E. Wainwright. “Studies in Molecular Dynamics. I. General Method”. In: *The Journal of Chemical Physics* 31.2 (1959), pp. 459–466. DOI: 10.1063/1.1730376.

[65] A Rahman. “Correlations in the Motion of Atoms in Liquid Argon”. In: *Physical Review* 136.2A (1964), A405–A411. DOI: 10.1103/PhysRev.136.A405.

[66] L. Konermann et al. “How to run molecular dynamics simulations on electrospray droplets and gas phase proteins: Basic guidelines and selected applications”. In: *Methods* 144 (2018), pp. 104–112. DOI: 10.1016/j.ymeth.2018.04.010.

[67] C. L. Brooks et al. “Classical molecular dynamics”. In: *The Journal of Chemical Physics* 154.10 (2021), p. 100401. DOI: 10.1063/5.0045455.

[68] B. J. Alder and T. E. Wainwright. “Phase Transition for a Hard Sphere System”. In: *The Journal of Chemical Physics* 27.5 (1957), pp. 1208–1209. DOI: 10.1063/1.1743957.

[69] R Hentschke, E. M. Aydt, and B Fodi. *Molekulares Modellieren mit Kraftfeldern Einführung in die Theorie und Praxis der Computersimulation molekularer Systeme*. 1996.

[70] R Car and M Parrinello. “Unified Approach for Molecular Dynamics and Density-Functional Theory”. In: *Physical Review Letters* 55.22 (1985), pp. 2471–2474. DOI: 10.1103/PhysRevLett.55.2471.

[71] R. Iftimie, P. Minary, and M. E. Tuckerman. “Ab initio molecular dynamics: Concepts, recent developments, and future trends”. In: *Proceedings of the National Academy of Sciences* 102.19 (2005), pp. 6654–6659. DOI: 10.1073/pnas.0500193102.

[72] S. Stephan et al. “MolMod – an open access database of force fields for molecular simulations of fluids”. In: *Molecular Simulation* 45.10 (2019), pp. 806–814. DOI: 10.1080/08927022.2019.1601191.

[73] B. L. Eggimann et al. “An online parameter and property database for the TraPPE force field”. In: *Molecular Simulation* 40.1-3 (2014), pp. 101–105. DOI: 10.1080/08927022.2013.842994.

[74] H. Berendsen, D van der Spoel, and R van Drunen. “GROMACS: A message-passing parallel molecular dynamics implementation”. In: *Computer Physics Communications* 91.1-3 (1995), pp. 43–56. DOI: 10.1016/0010-4655(95)00042-E.

[75] B. R. Brooks et al. “CHARMM: A program for macromolecular energy, minimization, and dynamics calculations”. In: *Journal of Computational Chemistry* 4.2 (1983), pp. 187–217. DOI: 10.1002/jcc.540040211.

[76] E. Lindahl, B. Hess, and D. van der Spoel. “GROMACS 3.0: a package for molecular simulation and trajectory analysis”. In: *Journal of Molecular Modeling* 7.8 (2001), pp. 306–317. DOI: 10.1007/s008940100045.

[77] B. R. Brooks et al. “CHARMM: The biomolecular simulation program”. eng. In: *Journal of Computational Chemistry* 30.10 (2009), pp. 1545–1614. DOI: 10.1002/jcc.21287.

[78] J. C. Phillips et al. “Scalable molecular dynamics on CPU and GPU architectures with NAMD”. In: *The Journal of Chemical Physics* 153.4 (2020), p. 044130. DOI: 10.1063/5.0014475.

[79] A. P. Thompson et al. “LAMMPS - a flexible simulation tool for particle-based materials modeling at the atomic, meso, and continuum scales”. In: *Computer Physics Communications* 271 (2022), p. 108171. DOI: 10.1016/j.cpc.2021.108171.

[80] M. D. Hanwell et al. “Avogadro: an advanced semantic chemical editor, visualization, and analysis platform”. In: *Journal of Cheminformatics* 4.1 (2012), p. 17. DOI: 10.1186/1758-2946-4-17.

[81] A. I. Jewett et al. “Moltemplate: A Tool for Coarse-Grained Modeling of Complex Biological Matter and Soft Condensed Matter Physics”. In: *Journal of Molecular Biology* 433.11 (2021), p. 166841. DOI: 10.1016/j.jmb.2021.166841.

[82] W. L. Jorgensen and J. Tirado-Rives. “The OPLS Potential Functions for Proteins. Energy Minimizations for Crystals of Cyclic Peptides and Crambin”. In: *Journal of the American Chemical Society* 110.6 (1988), pp. 1657–1666. DOI: 10.1021/ja00214a001.

[83] W. L. Jorgensen, D. S. Maxwell, and J. Tirado-Rives. “Development and Testing of the OPLS All-Atom Force Field on Conformational Energetics and Properties of Organic Liquids”. In: *Journal of the American Chemical Society* 118.45 (1996), pp. 11225–11236. DOI: 10.1021/ja9621760.

[84] S. J. Weiner et al. “An all atom force field for simulations of proteins and nucleic acids”. In: *Journal of Computational Chemistry* 7.2 (1986), pp. 230–252. DOI: 10.1002/jcc.540070216.

[85] W. L. Jorgensen and J. D. Madura. “Temperature and size dependence for Monte Carlo simulations of TIP4P water”. In: *Molecular Physics* 56.6 (1985), pp. 1381–1392. DOI: 10.1080/00268978500103111.

[86] W. L. Jorgensen et al. “Comparison of simple potential functions for simulating liquid water”. In: *The Journal of Chemical Physics* 79.2 (1983), pp. 926–935. DOI: 10.1063/1.445869.

[87] H. J. C. Berendsen et al. “Interaction Models for Water in Relation to Protein Hydration”. In: *Intermolecular Forces*. 1981, pp. 331–342. DOI: 10.1007/978-94-015-7658-1_21.

[88] C. J. de Grotthuss. “Memoir on the decomposition of water and of the bodies that it holds in solution by means of galvanic electricity”. In: *Biochimica et Biophysica Acta - Bioenergetics* 1757.8 (2006), pp. 871–875. DOI: 10.1016/j.bbabio.2006.07.004.

[89] L. Konermann and S. Kim. “Grotthuss Molecular Dynamics Simulations for Modeling Proton Hopping in Electrosprayed Water Droplets”. In: *Journal of Chemical Theory and Computation* 18.6 (2022), pp. 3781–3794. DOI: 10.1021/acs.jctc.2c00001.

[90] R. Lustig. “Statistical thermodynamics in the classical molecular dynamics ensemble. I. Fundamentals”. In: *The Journal of Chemical Physics* 100.4 (1994), pp. 3048–3059. DOI: 10.1063/1.466446.

[91] E. M. Pearson, T. Halicioglu, and W. A. Tiller. “Laplace-transform technique for deriving thermodynamic equations from the classical microcanonical ensemble”. In: *Physical Review A* 32.5 (1985), pp. 3030–3039. DOI: 10.1103/PhysRevA.32.3030.

[92] B. Isralewitz, M. Gao, and K. Schulten. “Steered molecular dynamics and mechanical functions of proteins Isralewitz, Gao and Schulten 225”. In: *Current Opinion in Structural Biology* 11 (2001), pp. 224–230.

[93] E. Polak and G. Ribiere. “Note sur la convergence de méthodes de directions conjuguées”. In: *Revue française d’informatique et de recherche opérationnelle. Série rouge* 3.16 (1969), pp. 35–43. DOI: 10.1051/m2an/196903R100351.

[94] A. Stukowski. “Visualization and analysis of atomistic simulation data with OVITO–the Open Visualization Tool”. In: *Modelling and Simulation in Materials Science and Engineering* 18.1 (2010), p. 015012. DOI: 10.1088/0965-0393/18/1/015012.

[95] W. G. Hoover. “Canonical dynamics: Equilibrium phase-space distributions”. In: *Physical Review* 31.3 (1985), pp. 1695–1697.

[96] S. Nosé. “A molecular dynamics method for simulations in the canonical ensemble”. In: *Molecular Physics* 52.2 (1984), pp. 255–268. DOI: 10.1080/00268978400101201.

[97] C. Polaczek. “Investigation of ion-solvent interactions in electrospray ionization mass spectrometry”. thesis. Wuppertal: Bergische Universität Wuppertal, 2021.

[98] N. Agmon. “The Grotthuss mechanism”. In: *Chemical Physics Letters* 244.5-6 (1995), pp. 456–462. DOI: 10.1016/0009-2614(95)00905-J.

[99] A. Malevanets et al. “Landau–Ginzburg theory for ‘star’-shaped droplets”. In: *Molecular Physics* 116.21-22 (2018), pp. 2892–2900. DOI: 10.1080/00268976.2018.1513174.

[100] P. Atkins. *Physikalische Chemie*. 3 corr. Weinheim [u.a.]: Wiley, 2001.

[101] C. Larriba and C. J. Hogan. “Free molecular collision cross section calculation methods for nanoparticles and complex ions with energy accommodation”. In: *Journal of Computational Physics* 251 (2013), pp. 344–363. DOI: 10.1016/j.jcp.2013.05.038.

[102] C. Larriba-Andaluz et al. “Gas Molecule Scattering and Ion Mobility Measurements for Organic Macro-ions in He versus N2 Environments”. In: *Physical Chemistry Chemical Physics* 17.22 (2015), pp. 15019–15029. DOI: 10.1039/C5CP01017A.

[103] C. Larriba and J. Fernandez de la Mora. “The Gas Phase Structure of Coulombically Stretched Polyethylene Glycol Ions”. In: *The Journal of Physical Chemistry B* 116.1 (2012), pp. 593–598. DOI: 10.1021/jp2092972.

[104] C. Larriba-Andaluz and C. J. Hogan. “Collision cross section calculations for polyatomic ions considering rotating diatomic/linear gas molecules”. In: *The Journal of Chemical Physics* 141.19 (2014), p. 194107. DOI: 10.1063/1.4901890.

[105] E. W. McDaniel and E. A. Mason. *The mobility and diffusion of ions in gases*. Wiley, 1973, pp. 1–381.

[106] T. Wu et al. “Optimization of long range potential interaction parameters in ion mobility spectrometry”. In: *The Journal of Chemical Physics* 148.7 (2018), p. 074102. DOI: 10.1063/1.5016170.

[107] M. Lorenz et al. “The distribution of ion acceptance in atmospheric pressure ion sources: Spatially resolved APLI measurements”. In: *Journal of the American Society for Mass Spectrometry* 19.3 (2008), pp. 400–410. DOI: 10.1016/j.jasms.2007.11.021.

[108] L. Grashoff et al. *Molecular Dynamic Simulation of ESI droplet fragmentation in MS vacuum stages*. Tech. rep. Maastricht: IMSC 2022, 2021.